Predicting Reduced Beam Section (RBS) Connection Performance in Steel Moment Frames

A thesis submitted in partial fulfilment of the requirements for the degree of Doctor of Philosophy

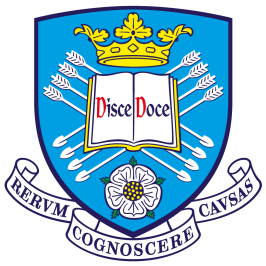

The University Of Sheffield.

Written By:

THOMAS ALEXANDER HORTON

The University of Sheffield
Faculty of Engineering
Department of Civil and Structural Engineering

Submission date:
August 12, 2021

Dedication

This thesis submitted in partial fulfilment of the requirements for the degree of Doctor of Philosophy, is dedicated in loving memory to my Grandpa ***Peter John Allmand-Smith*** who died August 15th 2011. Grandpa was an eccentric entrepreneur who invented the Stormguard^{TM} Sill. He was an engineering genius who has inspired me to pursue a career in Civil and Structural Engineering through academia.

Abstract

Reduced Beam Section (RBS) connections are widely adopted within seismic design codes for steel moment resistant frames. Accurate cyclic representations for RBS connections are important for the design and retrofitting of connections. Research has shown that the geometry of RBS connections affects its non-linear cyclic hysteresis. Currently, there is no method available which can accurately represent non-linear strength and stiffness degradation for any size RBS without the need for full finite element or experimental tests for calibration purposes.

In this research, a more efficient design methodology for RBS connections is proposed by investigating the geometries which define the RBS connection. Then a detailed and comprehensive database of highly accurate cyclic hysteretic models of 1480 different RBS connections is presented. This database should prove useful in better understanding the seismic performance of RBS connections. Using this database, calibrated models which could accurately predict the non-linear cyclic behaviour including stiffness and strength degradations were developed. Using this calibrated data set, highly accurate and reliable neural networks were trained and developed that are capable of predicting the full cyclic hysteresis of any RBS connection; given the geometries which define the connection as an input. A mode accuracy of 98% for these networks was achieved. Following on from this work, a proof of concept for the application of this work for the design and assessment of steel moment resistant frames was investigated, by utilizing the deep learning neural networks to predict the local RBS connection hysteretic models. Finally, the potential for additive printing (3D printing) in the design of future connections has been suggested through a critical literature review.

The results from this research clearly show that the three geometrical parameters which define the RBS connection influence the seismic design parameters of the connection. Design equations to predict the effects the key seismic design parameters have on RBS connections compared with a corresponding full steel connections has been proposed. Interestingly, the sections could be categorised into two sets depending on their buckling characteristics after being subjected up to a performance-based design loading criteria corresponding to collapse prevention. This database was used to calibrate improved models capable of representing RBS non-linear hysteresis. Comparisons between these calibrated parameters and the values predicted from equations available in literature gave significant differences. The differences were a result of 1) the regressional equations available in literature were based on a limited number of data points 2) a number of different types, sizes and shapes of RBS configuration were in the database and 3) the cut which defines the RBS geometry was not taken into account. Consequently, a set of deep learning neural networks enabled the non-linear cyclic hysteresis incorporating strength and stiffness degradation to be predicted for any section given the section properties and RBS geometry of the connection as an input. A proof of concept shows how the models developed in Chapter 4 would prove useful in the design and assessment of steel moment resistant frames. To conclude this research, the realistic implementation of how this work can be applied to the potential use of additive printing through a critical literature review has been presented. Finally, future work and recommendations have been suggested.

Research Contribution

An extensive analytical study was carried out into the performance of fully welded steel Reduced Beam Section (RBS) connections. As a result of the research work undertaken, the following journal papers have been prepared for submission for publication:

Journal Papers

Published

Horton, T., Hajirasouliha, I., Davison B., and Ozdemir, Z., 2021. More Efficient Design of Reduced Beam Sections (RBS) for Maximum Seismic Performance. *Journal of Constructional Steel Research*

Horton, T., Hajirasouliha, I., Davison, B., Ozdemir, Z., and Abuzayed, I., 2021. Development of More Accurate Cyclic Hysteretic Models to Represent RBS Connections. *Journal of Engineering Structures*

Submitted and Under Peer Review

Horton, T., Hajirasouliha, I., Davison B., and Ozdemir, Z., 2021. Accurate Prediction of Cyclic Hysteresis Behaviour of RBS Connections Using Deep Learning Neural Networks. *Submitted to: Journal of Engineering Structures, 15/03/2021.*

Ready for Submission

Horton, T., Hajirasouliha, I., Davison B., and Ozdemir, Z., 2021. The Potential for 3D Printed Connections in the Design and Retrofitting of Steel Structures. *Intending to Submit to: Journal of Advances in Structural Engineering, date tbc.*

Acknowledgements

I would like to extend acknowledgements to Dr. Iman Hajirasouliha, Professor Buick Davison and Dr. Zuhal Ozdemir for their extended support during this research.

I would like to thank the ongoing support of my Mummy throughout my academic life. She never stops supporting me.

The unconditional love and support from my Fiancé during this research has made completing it possible. I couldn't imagine a life without her.

Table of Contents

List of Figures

List of Tables

List of Symbols

a Parameter defining RBS geometry, distance from column face to start of RBS

as Strain hardening ratio

b Parameter defining RBS geometry, width of RBS

b Hardening parameter, defines rate of change of yield surface

b_f Width of the beam flange

C_k Hardening parameter, kinematic hardening modulus

c Parameter defining RBS geometry, depth of RBS

d Depth of the beam

E_{diss} Energy dissipated

I_{RBS} Second moment of area of the RBS

I_{FS} Second moment of area of the full section

$K0$ Initial elastic stiffness

$K1$ Pre-capping stiffness

L Length of the beam

M_y Yield moment or Effective yield moment

M_c Peak moment or Capping moment strength

M_r Residual moment

M_f Moment that develops at the column face

M_{pr} Moment that develops at the plastic hinge

m Gradient of the straight line used in equation 2.6 & 2.7

Q Hardening parameter, maximum size of yield surface

S_h Distance from column face to centre of RBS

t_f Width of the flange

t_w Width of the web

V_{RBS} Shear force acting at the RBS

V_u Shear force acting at the face of the column

$Y1$ Distance 1 used for minimization in equation 2.5

$Y1'$ Distance 1' used for minimization in equation 2.5

$Y2$ Distance 2 used for minimization in equation 2.5

$Y2'$ Distance 2' used for minimization in equation 2.5

α_1 Coefficient 1 for equation 2.3

α_2 Coefficient 2 for equation 2.3

β_1 Coefficient 1 for equation 2.7

β_2 Coefficient 2 for equation 2.7

$P\delta$ P-Delta effects during non–linear analysis

δ Displacement

δ_u Ultimate displacement of the beam at load point

δ_y Yield displacement of the beam at load point

γ_k Hardening parameter, Rate at which C_k changes

κ Ratio of effective yield moment to residual moment

λ_{web} Slenderness of the web

λ Deterioration parameter for the mIK model

μ Ductility

θ_u Ultimate rotation

θ_y Yield rotation

θ_p Pre-capping rotation

θ_{pc} Post capping plastic rotation

rad Radians

List of Acronyms

bVal	b value
CJP	Complete joint penetration weld
CP	Collapse prevention
cVal	c value
DL	Damage limitation
FE	Finite Element
FR	Flange Reduction
FS	Full section
IO	Immediate occupancy
KDP	Key design parameter
LS	Life safety
MCE	Maximum considered earthquake
mIK	modified-Ibarra-Krawinkler
NN	Neural Network
NC	Near collapse
PGA	Peak ground acceleration
R	Statistical regression value to represent spread of data
RBS	Reduced Beam Section
SMF	Steel moment frame

SMA Smart memory alloy

SHS Square hollow section

SD Significant damage

WHP Hourglass shaped energy dissipation pins

WUF-B Welded flange bolted web connections

WUF-B Welded unreinforced welded web connection

WUF Welded unreinforced flange connection

Chapter 1

Introduction

1.1 Research Motivation

The 1994 Northridge and 1995 Kobe Earthquakes induced many unanticipated brittle fractures to occur at the welded beam to column connections in moment resistant frames (SAC Joint Venture, 2000d,b). Although no steel buildings collapsed, significant repair costs were incurred to fix the brittle fractures in the steel frames (Engelhardt and Sabol, 1997). During the 1994 Northridge and 1995 Kobe Earthquakes an estimated combined property damage and economic loss of $120 billion and $160 billion respectively, occurred as a result of the natural disaster (SAC Joint Venture, 2000b; Rose and Lim, 2002; Sawada and Shimizutani, 2008). In the years following the aftermath of these earthquakes, developments in the Reduced Beam Section (RBS) connection were quickly adopted in the American and European design standards due to their stable energy dissipation capacity and ability to protect the columns and beam-column connections in the frame.

However, a critical review of Reduced Beam Section (RBS) connections used within seismic design, show that while RBS connections are widely adopted within the European and American seismic design guides and recommendations, the geometry and shape of the RBS connections which affect its seismic performance are not considered in the design of these connections. There is no systematic design methodology which controls the seismic performance of RBS connections by using the key geometrical parameters. Previous research has shown that the performance of a frame can be quantified by the damage sustained during non-linear analysis. By varying the RBS geometry, this can affect the seismic capabilities of RBS connections, thus providing scope to improve the frames performance.

Currently, there is a lack of accurate methods to predict the seismic behaviour of RBS connections. Preliminary studies have shown that modifying the RBS can affect the seismic performance of RBS connections by up to 20%. The widely accepted modified-Ibarra-Krawinkler (mIK) model cannot accurately capture the non-linear behaviour of RBS connections with varying RBS geometry. The mIK model has many limitations which include: full cyclic experimental results are needed for calibration to get accurate models, equations to predict the mIK parameters are based on a wide range of connection types and RBS geometry which effects its cyclic hystereis are not taken into account.

Subsequently, the cyclic performance of steel connections affects the seismic performance of steel moment resistant frames. There is no accurate method for predicting and representing the cyclic hysteresis performance of steel RBS connections while taking into account the geometries of the RBS connection. While previous research has shown that RBS connections affect the performance of steel moment resistant frames (in terms of connection rotational damage and drifts), the affects of varying the RBS connection geometry on the performance of steel frames has not been investigated. In addition, there is currently no performance-based optimization frame work for improving the performance

of RBS steel moment frames under non-linear dynamic analysis. The aim of this research is to provide a more accurate method of modelling and predicting the non-linear cyclic hysteresis of RBS connections and to provide a proof of concept method for the future application of these improved models in a performance-based optimized design.

1.2 Background Review

1.2.1 The development of RBS connections

Following the aftermath of the 1994 Northridge and 1995 Kobe earthquakes, America's Federal Emergency Management Agency (FEMA) sponsored the SAC Joint Venture to investigate these failures. The SAC Joint Venture was formed with a specific goal of investigating the brittle fractures in steel connections as a results of the earthquake and developing new design approaches and repair methods to help limit the damage in future steel framed buildings. The SAC Joint Venture was formed of three organizations: Structural Engineers Association of California (SEAOC), Applied Technology Council (ATC) and the Consortium of Universities for Research in Earthquake Engineering (CUREE) (SAC Joint Venture, 1994). As a result, state-of-the-art recommendations were produced for seismic evaluation and upgrading of pre-Northridge buildings, as well as recommended seismic design criteria for new buildings (SAC Joint Venture, 2000b). The SAC Joint Venture concluded that the brittle fractures in pre-Northridge welded beam to column connections arose due to large stress concentrations as a result of the shape and type of connection, defects in the welds and low weld toughness (SAC Joint Venture, 2000d,b). In order to prevent these brittle fractures in welded connections it was recommended that the pre-Northridge connection should be upgraded. This can be achieved by modifying the shape of the connection by using Reduced Beam Section (RBS) connections or semi-rigid connections, to reduce stress concentrations. Alternatively adding reinforcement such as new weld replacements with improved toughness, welded haunched or cover plate connections or by other acceptable strengthening means (SAC Joint Venture, 2000b; BSI, 2005).

Pre-Northridge beam-column connections initially consisted of welded-flange-welded-web connections but soon changed to welded-flange-bolted-web connections (WUF-B[1]) shown in Figure 1.1, due to extensive research and economical advantages in construction. The WUF-B has: complete joint penetration (CJP) welds for the beam flange to column face for transfer of bending moment, shear plates bolted to the beams web for transfer of shear forces, doubler plates to control the panel zone yielding and continuity plates to prevent local damage to column flange as well as ensuring uniform stress in the beam flanges.

[1]The WUF-B was pre-qualified in the Uniform Building Code (UBC, 1997), and was considered to be an ideal connection for seismic performance. (The UBC has detailed provisions and requirements relating to: fire, life safety, health and safety, construction and building design. It is a tool which aims at preserving public health and safety while providing safe-guards from hazards within the built environment. The UBC adopts provisions for structural design which have been approved by the American National Standards Institutes (ANSI) and is adopted as the base code for most jurisdictions in the United States of America.)

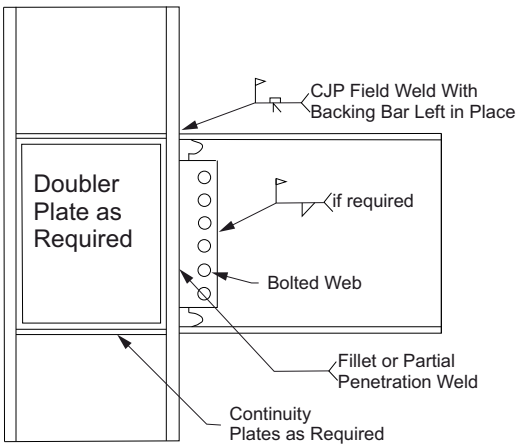

Figure 1.1: Example of a welded-flange-bolted-web (WUF-B) connection

Damage was expected to occur in the WUF-B as yielding and local buckling of the beam. However, it was evident after the Northridge Earthquake that significant brittle fractures occurred in a wide range of steel buildings. The main damages that occurred were:

- CJP weld fractures between the bottom beam flange and column
- Fracture of the column flange behind the CJP weld
- Fracture of the column flange and into the column web

These brittle fractures left the WUF-B connection susceptible to a significant loss in rigidity and strength, leaving the residual flexural strength and rigidity to be resisted by the top CJP weld and bolted shear tab. This left the connection subjected to fracture of the shear tab to column weld and fracture of the shear tab bolt holes.

The main reason for the brittle fractures was the increased stress concentrations at the beam flange to column flange location. Stress concentrations in the pre-Northridge WUF-B connections occurred as a result of the following combinations (SAC Joint Venture, 2000d):

- Bending and shear forces must be transferred from the beam to the column through the welded joints and the shear tab, these combined section properties are less than the beam, resulting in stress concentrations
- Beam flanges carry a large amount of beam shear giving significant increase in stress concentrations
- The centre of the joint between the beam flange and column flange is restrained from movement (mainly in thick beam flanges) this leads to an increase in stress concentrations
- Weak shear panel zone deformations result in kinking of the column flanges next to the beam-flange-to-column-flange joint leading to an increase in stress concentrations
- Presence of weld access holes allows severe stress concentrations to occur
- The increase in beam sizes (beam sizes were increased to reduce the number of connections in a structure leading to smaller labour costs) placed larger stress concentrations on the connection which induced the likelihood of brittle fracture

- A new type of welding process (semi-automatic, self-shielding and flux-cored arc welding) gave a lower notch toughness weld which allowed brittle fractures to initiate more easily in them
- Poor weld quality and practice of leaving the backing bar in place also lead to brittle fractures

As a result of the brittle fractures of the Northridge Earthquake there were two initial schools of thought: 1) reduce the welding defects and the stress concentrations in the areas around the weld by modifying the details of the connection (improving weld access hole) and welding techniques (Figure 1.2) 2) Move the location of the plastic hinge and allow yielding in the beam. The latter has been adopted by modern design codes as the accepted method of seismic design.

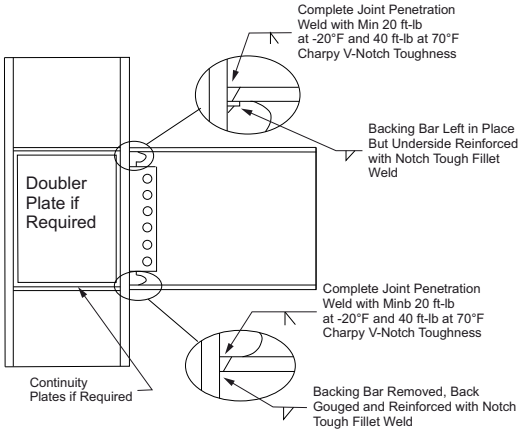

Figure 1.2: Improvements in the welding techniques for the WUF-B connection

FEMA 355D suggested a range of alternative connections to the pre-Northridge earthquake welded flange connection. These are broken into four categories as follows: 1) unreinforced connections 2) strengthened or reinforced connections 3) reduced beam section connections and 4) welded-flange plate connections (SAC Joint Venture, 2000d). These connections were either improvements in the welding or detailing of the connection or suggestions for alternative connections. More details of these connections can be found in SAC Joint Venture (2000d).

In order to provide a highly ductile response and reliable performance, the beam-column assembly can be modified by either strengthening the connection or weakening the beam (BSI, 2004):

1. Strengthening the connection – this forces the plastic hinge to occur in the beam as opposed to the connection. The beam-column connection can be reinforced using: cover plates, ribs, side plates or haunches. Alternative stronger connection detailing can be adopted. Figure 1.3 shows some examples of these types of connections.

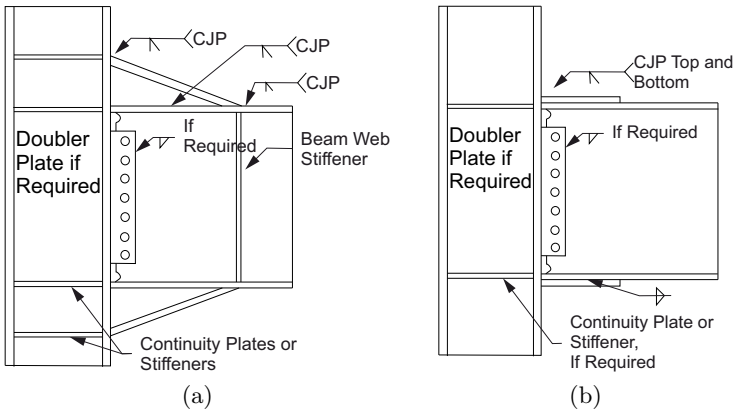

Figure 1.3: Figures to show two common methods of reinforcing the connection (a) Haunched connection (b) Cover plate connection

2. Weakening the beam – Reduced Beam Section (RBS) connections are a favourable method of reducing the strength of the beam to allow plastic hinges to occur in the beam.

Since the 1994 North Ridge Earthquake, researchers investigated many different methods of reinforcing pre 1994 North Ridge earthquake connections to prevent future brittle fractures. It is now widely accepted that by weakening sections of the beam, allowing plastic hinges to form, these brittle fractures can be prevented while at the same time producing very ductile and energy dissipative steel frames (Tong et al., 2016).

Plumier (1990) first proposed RBS connections, shown in Figure 1.4, as an idea to develop safe structures in seismic zones. Specific sections of the beam were weakened in an attempt to provide a stable dissipative zone. These sections of the beam adjacent to the beam-column connection are weakened by trimming the beams flanges. This forces yielding to occur in the reduced section. RBS connections can be: constant, tapered or radius cut, however, radius cut RBS provide the highest rotational capacity.

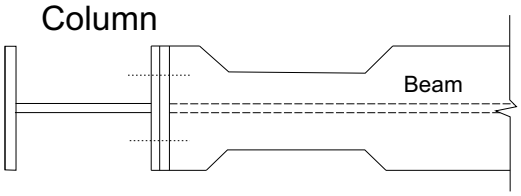

Figure 1.4: The first RBS connections proposed by Plumier (1990)

According to Eurocode 8 (BSI, 2004) clause 6.6.1 (1)P, moment resistant frames should be designed so that plastic hinges form either in the beams or in the beam to column connections. Steel moment resistant frames can provide very ductile systems, which have a good supply of energy dissipation. The current design philosophy in seismic design of steel framed moment resistance buildings allows the energy from the seismic event to be dissipated in the beams. Plastic hinges occur in the beam where the hysteretic behaviour of the steel yielding allows dissipation of some energy. This provides a highly ductile frame to ensure the life safety of the occupants (Sultana and Youssef, 2016b).

RBS connections shown in Figure 1.5 are a simple but effective method of weakening sections of the beam in order to move the damage away from the columns and beam-column connections; and

into the beams. Plastic deformations are allowed to occur in the beams, providing a stable hysteresis for energy dissipation while at the same time protecting the connection from damage and potential failure. For a more detailed review of the current design standards and adopted methods for static and dynamic modelling, refer to Appendix B.

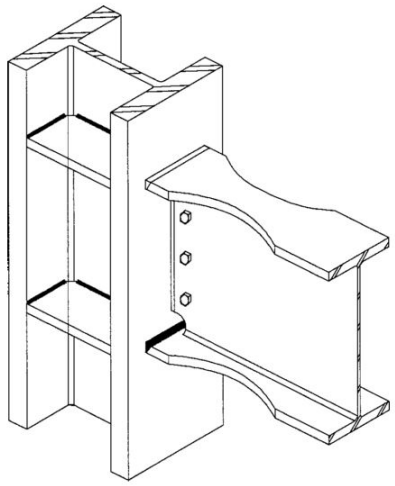

Figure 1.5: An isometric view of an RBS connection (Jones et al., 2002)

1.2.2 Review of RBS and other seismic dissipative connections

Refer to Chapter 2 Section 2.2, Chapter 3 Section 3.2.1 and Chapter 4 Section 4.2.1 for a critical literature review of RBS connections. Refer to Chapter 3 Section 3.2.1 and Appendix A Sections A.4, A.5, A.6 and A.7 for a critical literature review of seismic connections and energy dissipative connections.

1.2.3 RBS in current design

Reduced Beam Section (RBS) connections have become widely adopted in the European and American design guides and standards (refer to Appendix B for a detailed review of these standards). The three main design guides incorporating RBS connections are as follows:

- BS/EN 1998 (BSI, 2004) is the British Standard for seismic design, covering all common and basic structures. The seismic design objectives of BS/EN 1998 (BSI, 2004) in the event of an earthquake is to ensure: 1) Human lives are protected, 2) Damage is limited and 3) Structures important for civil protection remain operational. BS/EN 1998 (BSI, 2004) is made up of 6 parts which cover general design aspects or different types of structures. Part 3 (BSI, 2005) of BS/EN 1998 (referred to as BS/EN 1998-3) covers the design of RBS connections.

- The American design requirements for RBS connections are outlined in ANSI/AISC 358-16 (AISC, 2016b) (Pre-qualified Connections for special and Intermediate Steel Moment Frames for Seismic Applications). This document standardises the design of connections and allows these connections in structural buildings without the need for additional testing. RBS connection design is covered by this code.

- FEMA 350 (SAC Joint Venture, 2000a) provides specific design and performance evaluation procedures for steel framed moment resisting structures. Similarly, this American guide covers the design of RBS connections.

1.3 Scope of Research

This research focuses on predicting and optimizing the performance of RBS connections at both the local and structural frame level. For a better understanding of how the RBS geometries affect its seismic performance, an extensive parametric analysis on the key geometries of RBS is conducted to assess its effects on the cyclic hysteresis. The ability to improve the modified-Ibarra-Krawinkler (mIK) model - capable of representing the RBS cyclic hysteresis - is investigated through a set of deep learning neural networks and algorithms. This set of supervised learning neural networks and algorithms is capable of predicting highly accurate improved mIK models for any size beam and RBS geometry. Finally, a proof of concept at the global frame level has been demonstrated to shown the potential of utilising these methods for improving and optimizing the performance-based design of steel moment resistant frames by varying the RBS geometries.

1.4 Aims and Objectives

The aim of this research is to develop a methodology to enable the optimal performance-based design of RBS connections at the local level, this will then enable multi-criteria performance-based optimization of steel moment resistant frames at the global level. This was achieved by completing the following objectives:

1. Conduct a critical study of the seismic behaviour of moment resistant connections using the concept of Reduced Beam Sections (RBS).
2. Development of a validated non-linear Finite Element (FE) model of a fully Welded Unreinforced Welded Web (WUF-W) connection and conducting a comprehensive analytical study to investigate how the geometries which define the RBS connection effect the key seismic design parameters of RBS connections to be used as benchmark examples.
3. Compile a complete database of cyclic hysteretic responses of RBS connections to assess the influence of the prominent geometries which define the RBS and identify the key design parameters
4. Construct a database of calibrated modified-Ibarra-Krawinkler models for a wide range of steel RBS connections for more accurate design and assessment purposes compared to the existing methods
5. Design a set of deep learning neural networks and classification algorithms to predict the non-linear cyclic hysteresis (utilising the modified-Ibarra-Krawinkler model) for any size RBS connection and RBS geometry
6. Demonstrate the concept of performance-based design optimization in steel moment resistant frames by controlling the geometries of RBS connections
7. Investigate the opportunity for utilising additive manufacturing (3D printing) in the design and optimization of performance-based design of future seismic resistant connections

1.5 Tasks and Methodology

The following methodology is adopted to achieve the objectives:

1. Provide a comprehensive review of the existing research on RBS and seismic connections [Objectives 1 to 7]

2. Develop a detailed Finite Element (FE) model in ABAQUS in order to conduct an extensive parametric analysis on 90 RBS connections to assess the effects of different seismic design parameters for ranges within the recommended upper and lower limits of the geometries which define the RBS. Use the results to develop design equations to predict these seismic design parameters of RBS compared to full section properties [Objective 2]

3. Write a Python macro code in Matlab to create an FE model in ABAQUS of 1,480 different RBS FE models to analyse under a displacement based loading protocol up to $0.07rad$, in order to extract and post-process the results into a database of cyclic hysteresis curves [Objective 3]

4. Conduct an automated calibration process in Matlab on an equivalent spring model of the RBS in OpenSees, in order to determine parameters for the modified-Ibarra-Krawinkler model capable of representing the non-linear cyclic hysteresis of all RBS connections within the database in order to compare these calibrated parameters with the predictive parameters equations in literature [Objective 4]

5. Conduct supervised learning in Matlab using a set of Neural Networks and Classification algorithms which comprise of cascade forward-feed neural networks and a bootstrap aggregating ensemble algorithm learner, to be able to predict highly accurate and improved modified-Ibarra-Krawinkler models for any RBS connection [Objective 5]

6. Provide a proof of concept example of how the highly accurate and improved modified-Ibarra-Krawinkler models can be implemented in a performance-based design optimization methodology in OpenSees for the non-linear dynamic analysis of steel moment resistant frames [Objective 6]

7. Provide a state-of-the-art review of the seismic resistant connections and modern additive manufacturing techniques with the aim to suggest the opportunities for additive manufacturing in the future design and optimization of seismic resistant connections [Objective 7]

1.6 Thesis Layout

This research consists of seven chapters and three appendices briefly summarised in the following subsections.

Chapter 1: Introduction

This chapter provides an overview of this research, focusing on the Research Motivation, Scope of Research and Tasks and Methodology. A general introduction to the problem and critical review of existing literature on RBS connections and seismic dissipative connections has been completed.

Chapter 2: More Efficient Design of Reduced Beam Sections (RBS) for Maximum Seismic Performance

This chapter is aimed at developing more efficient design methodologies for RBS connections by investigating the effect of geometrical parameters of the connections. A brief critical review of RBS connections was conducted. Two detailed validated models of RBS connections were developed in order to carry out an extensive parametric analysis on 90 different specimens. The effect the RBS geometries have on five key seismic design parameters was investigated. Subsequently, practical design equations were proposed to predict the seismic performance of RBS connections compared to a full sections for the five key design parameters.

Chapter 3: Development of More Accurate Cyclic Hysteretic Models to Represent RBS Connections

Chapter 3 presents a database of detailed and accurate improved modified-Ibarra-Krawinkler (mIK) models that can reliably capture the cyclic hysteresis behaviour of RBS connections over a range of RBS geometries. A validated FE model was developed which allowed a comprehensive parametric study of 1480 different RBS connections to develop a full cyclic hysteresis profile. The database was used to conduct a calibration process utilising the bisector method in order to develop a comprehensive database of improved mIK models capable of predicting the non-linear cyclic behaviour of RBS connections. The results from this chapter should prove useful in the seismic design and assessment of RBS connections.

Chapter 4: A set of deep learning Neural Networks for the prediction of accurate modied-Ibarra-Krawinkler parameters for the cyclic hysteretic behaviour of RBS connections

This chapter uses supervised machine learning to train a set of deep learning neural networks and a classification algorithm, which, through a logical flowchart process, are capable of accurately predicting the non-linear cyclic hysteresis for any RBS connection. The extensive database for the full cyclic hysteresis of the connections developed in Chapter 3, was used to train the neural networks and classification algorithm. The results from this chapter will prove useful in the design and assessment of steel RBS frames.

Chapter 5: More Efficient Design of Moment Resisting Steel Frames with RBS Connections

A simple methodology for achieving an efficient performance of steel moment resistant RBS frames by controlling the geometry of the RBS is developed in this chapter. This methodology utilises an automated approach using the set of Neural Networks developed in Chapter 4 which allows a trial and error permutation approach to be adopted. A non-linear model of a four storey Welded-Unreinforced-Flange frame was developed as a benchmark. The performance of this frame was assessed under a strong earthquake. RBS connections were used to provide an improved frame performance in terms of the strong column-weak beam concept. Finally, a more efficient RBS frame design was developed by controlling the cut (geometry) of the RBS connection. The methodology developed in this chapter will prove useful in developing a multi-criteria optimization approach for different performance levels of RBS frames in future work.

Chapter 6: Conclusions and Recommendations for Future Work

This chapter contains the summary of the results followed by recommendations for future work.

Appendix A: The Potential for 3D Printed Connections in the Design and Retrofitting of Steel Structure

Appendix A examines the potential for additive manufacturing (3D printing) to be utilised in the design and retrofitting of steel structures. A critical literature review is presented on the following topics:

- Reduced Flange Section including tapered RBS, conventional RBS and drilled flange connections
- Novel energy dissipative devices and dampers integrated into connections as fuses
- Self centring device - which focuses on the connections ability to self centre after seismic excitations

- Smart Memory Alloys (SMA) incorporated into the connection
- Recent additive printing methods and techniques and how these could be integrated into steel connections in future design

Appendix B: Review of the European and American Standards

This appendix covers a detailed review of the current European and American seismic design standards and guidelines.

Appendix C: Detailed Review of Connection and Frame Modelling

This appendix covers a overview and detailed summary of the connection and frame modelling techniques used in the American design guidelines. A detailed overview on the development of the modified-Ibarra-Krawinkler (mIK) model has been conducted. This expands on the extensive literature review of the non-linear cyclic modelling methods in Chapter 3 Section 3.2.2 and Chapter 3 Section 3.2.3.

Appendix D: American Wide Flange Beams used for the Database

This appendix details the selected American Wide Flange beams used in developing the database covered in Chapter 3.

Chapter 2

More Efficient Design of Reduced Beam Sections (RBS) for Maximum Seismic Performance

More efficient design methodologies for RBS connections are developed in this chapter by investigating the effects of RBS geometrical parameters. This chapter is based on the paper titled: More Efficient Design of Reduced Beam Sections (RBS) for Maximum Seismic Performance, submitted to Journal of Constructional Steel Research dated 25/01/2021. It should be noted this chapter reads as a standalone paper. It may repeat sections previously introduced in this thesis.

2.1 Abstract

Reduced Beam Sections (RBS) are increasingly used in modern construction due to their large rotational capacity and ability to dissipate and absorb large amounts of seismic energy, thus, creating a ductile and stable steel frame system. Currently, in the design of RBS connections, the effect of RBS cutting parameters on the cyclic performance of the beam elements are not taken into account. However, using different RBS geometries for any single beam, compared to its full section, can have up to 30% differences in cyclic behaviour of the connections. The aim of this study is to develop a more efficient design methodology for RBS connections, by investigating the cyclic performance of different beams with a wide range of different flange reductions. First, detailed Finite Element (FE) models of different American Wide Flange RBS connections are developed and validated against two cyclic beam-column sub assembly experiments from literature. The models took into account the non-linear material properties and adopted appropriate modelling techniques for the connection welds, supports and bracing. Then, an extensive parametric analysis on 90 different specimens was undertaken in order to assess how the geometrical parameters which define RBS connections affect the key design parameters including, Yield Moment (M_y), Peak Moment (M_c), Ultimate Rotation (θ_u), Ductility (μ) and Energy Dissipated (E_{diss}). It is shown that the depth (c) and width (b) of the RBS cut are the most influential geometrical design parameters, affecting up to 30% changes in the key performance parameters compared to a full beams section (no RBS present). Finally, based on the results of this study, practical design equations are proposed to predict the seismic performance of RBS connections compared to a full section (no RBS present) as a function of the five key design parameters used in common practice. The proposed equations should prove useful in preliminary design of RBS connections to achieve maximum seismic performance.

2.2 Introduction

The 1994 Northridge and 1995 Kobe Earthquakes induced many unanticipated brittle fractures to occur at the welded beam to column connections in moment resistant frames (SAC Joint Venture, 2000d,b). Although no steel buildings collapsed, significant repair costs were incurred in order to fix the brittle fractures in the steel frames (Engelhardt and Sabol, 1997). During the 1994 Northridge and 1995 Kobe Earthquakes an estimated combined property damage and economic loss of $120 billion and $160 billion respectively, occurred as a result of the natural disaster (SAC Joint Venture, 2000b; Rose and Lim, 2002; Sawada and Shimizutani, 2008). Following the aftermath of these earthquakes, America's Federal Emergency Management Agency (FEMA) sponsored the SAC Joint Venture to investigate these failures (SAC Joint Venture, 1994). As a result, state-of-the-art recommendations were produced for seismic evaluation and upgrading of pre-Northridge buildings, as well as recommended seismic design criteria for new buildings (SAC Joint Venture, 2000b). The SAC Joint Venture concluded that the brittle fractures in pre-Northridge welded beam to column connections arose due to large stress concentrations as a result of the shape and type of connection and defects in the welds and low weld toughness (SAC Joint Venture, 2000d,b). In order to prevent these brittle fractures in welded connections it was recommended that the pre-Northridge connection should be upgraded. This can be achieved by modifying the shape of the connection (for example by using reduced beam section connections or semi-rigid connections) to reduce stress concentrations. Alternatively adding reinforcement can be used such as new weld replacements with improved toughness, welded haunched or cover plate connections or by other acceptable strengthening means(SAC Joint Venture, 2000b; BSI, 2005).

There are a number of pre-qualified connections specified in BS/EN 1998-3 (BSI, 2005), FEMA 350 (SAC Joint Venture, 2000a) and ANSI/AISC 341-16 (AISC, 2016a), which possess a highly ductile and reliable response needed to overcome the risk of brittle fractures. Reduced Beam Section (RBS) connections are a widely adopted method specified in European (BSI, 2005) and American (AISC, 2016b) design codes. At specific locations the beams flanges are trimmed back to provide weakened sections, in order to shift the plastic deformations away from beam-column connections and into the beam in an attempt to provide a stable dissipative zone. Consequently, adequate ductility is provided by the frame to absorb the seismic energy and avoid the risk of brittle fractures occurring, providing a stable dissipative zone.

The first cyclic experiments conduced on RBS connections and reinforced cover plate connections, highlighted the excellent rotational capacities of both types of connections compared to the pre Northridge connections, which were susceptible to brittle fracture (Engelhardt and Sabol, 1997). Subsequent experimental cyclic tests were conducted on a variety of RBS connections by varying the way in which the RBS sections were fabricated (tapered, constant or radius cut) by a number of researchers (Chen et al., 1996; Oh et al., 2015; Chen and Lin, 2013; Roeder, 2002). The results of these studies in general showed that a radius cut RBS provided the highest rotational capacity. These tests also showed that fractures of the RBS initiated at rough edges of the RBS highlighting the need for the RBS cuts to be ground smooth to prevent stress concentrations from occurring. Roeder (2002) compared the cyclic performances of three different connections which included Welded Unreinforced Flange – Welded Web (WUF-W), RBS and Welded Unreinforced Flange – Bolted Web (WUF-B) connections. Results showed that RBS connections can achieve a good seismic performance with larger rotational capacities compared to the WUF-W and WUF-B connections.

Jones et al. (2002) tested eight RBS beam to column connections looking specifically at how the panel zone strength and difference between welded and bolted flanges affected connection performance. It was shown that a stronger panel zone dissipated more energy and produced more stable connections,

with minor differences between bolted and welded connections. In another relevant study Lee et al. (2005) tested a number of bolted and welded connections with strong and weak panel zones in order to asses their cyclic responses. Welded connections provided superior performance compared to the bolted connections due to bolt slippage and brittle failure. Stronger panel zones also allowed a larger overall deformation to occur. Lee and Kim (2007) suggested an improved WUF-B RBS connection which featured a larger shear tab with a diagonal bolt line following the shear load path. This helped to transfer the shear forces to the beams web and avoid a brittle failure. Uang et al. (2000) tested six beam-column sub assemblies to assess the effectiveness of using RBS connections or welded haunches on beam lower flanges to rehabilitate pre-Northridge connections with a concrete slab. They concluded that the application of RBS to the lower flanges of the beam was not enough to prevent brittle fracture of the connections. The effects of a composite slab on the performance and cyclic responses of RBS connections were also studied in several research works (Jones et al., 2002; Lee et al., 2016; Li et al., 2017), which demonstrated that the composite floor enhanced the stability of the connection by a delayed strength degradation.

Eight main factors including the strength, stiffness, RBS geometry and connection assembly which significantly effect the design and response of RBS connections are discussed in depth by Sophianopoulos and Deri (2011). Einabadi et al. (2016) conducted a finite element analysis to determine the optimum geometry for an RBS connection. The geometrical parameters and connection performance were evaluated depending on the energy dissipated, tension in the panel zone and initial stiffness of the load displacement graph. Ohsaki et al. (2009) optimised the shape of a reduced beam section (not following the recommended geometrical parameters) by maximising the energy dissipated as the objective function, with the maximum plastic strain at the welded connection as the constraint. They showed that an optimized RBS shape can significantly improve the energy dissipated by the RBS. Sophianopoulos and Deri (2017) also conducted an optimization on a bolted end plate RBS connection under static loading in order to determine the best possible fabricated connection.

Pachoumis et al. (2009) first compared how the depth of two RBS cuts affected the performance of WUF-F RBS connections, showing that the geometry of RBS connections affects its performance. The connection with the larger cut into its flanges developed earlier web and flange buckling. In order to investigate how the RBS connection geometries controlled the connections cyclic performance further validated finite element models were developed (Pachoumis et al., 2009, 2010). Gilton and Uang (2002) conducted full scale experimental tests on two different wide flange beams with moment connections on the weak axis (web) of the column in order to asses how RBS connections affected their performance. By using a parametric finite analysis, they also showed that the presence of the RBS reduced the strain concentration at the edge of the beam flanges weld. Similarly, Sofias et al. (2014) conducted two full scale RBS connections on extended end plate bolted connections to compare two grades of steel – 430 Mpa and 370 Mpa, respectively. Both connections achieved an acceptable rotational capacity, however, it was concluded that the depth of the RBS cut into the flange (commonly known as the c parameter) should be correlated with the ductility level of the steel grade used.

Han et al. (2012) gathered data from literature for WUF-B RBS connections in order to provide empirical equations that could predict the rotational capacities of WUF-B connections. In an attempt to estimated the rotational capacity of WUF-W RBS, Roeder (2002) used regression analysis. Similarly, fragility functions developed from 71 experimental tests collected in literature were presented by Lignos et al. (2009). These fragility functions estimated the probability of an RBS moment connection reaching or exceeding different damage states.

Novel types of reduced beam flanges have also been suggested in literature. Morshedi et al. (2017) conducted a finite element (FE) parametric analysis on a Double Reduced Beam Section (DRBS).

This connection used two reduced beam sections in series at either end of the beam in order to help reduce the equivalent plastic strain by increasing the plastic hinge region as well as delaying local web buckling and hence strength degradation. A parametric study was also conducted to assess the sensitivity of the DRBS geometries, suggesting optimal geometries for the connection.

RBS sections that utilise drilled holes in the flanges (referred to as Drilled Flanges (DF)) can also provide good seismic performance. Farrokhi et al. (2009) first proposed drilling holes in the cover plates of reinforced WUF-B connections in order to create intentional weak areas. Results showed this alleviated the stress concentrations in the welds and initiated ductile yielding around the holes instead. Vetr et al. (2012) conducted experimental results on DF connections in order to asses the effect of different hole layouts and diameters. Results showed that the DF connections can exhibit adequate rotational capacities, thus making them a viable choice for a moment connection. In a follow up study Atashzaban et al. (2015) optimized DF connections by finding the best location and configuration of drilled holes in order to reduce the Equivalent Plastic Strain (EPEQ) and Rupture Index. Hole configuration of the DF plays a vital role in controlling the performance of the DF connection. Rahnavard et al. (2015) conducted an analytical study and compared how different hole configurations (width, amount and location) affected the cyclic performance compared to WUF and RBS connections. In general, the results of these studies showed that DF connections dissipated more energy compared to RBS connections. Most recently Ahmady Jazany (2018) examined how to improve the performance of DF connections by establishing limits for the hole diameters, centre-to-centre hole spacings, number of holes, beam span-to-depth ratio and grade of steel. They concluded that hole configuration can significantly reduce the EPEQ at the weld and around the drilled holes. The parametric results also showed that the steel grade has a significant impact on the connections performance.

The most important conclusions from literature show that the geometry and shapes of the RBS connection affects how the connection will perform under seismic loading. Similarly, the layout and configuration of the holes in DF connections play an important role in the connections cyclic performance. Currently, representation of the seismic performance of RBS connections using equations or mathematical models does not take into account the effect of RBS geometries. There is also no systematic design methodology available to control the seismic performance of RBS connections, by using the key parameters that define the RBS geometry. While the literature review has shown that the geometries of RBS connections affect its seismic performance, the significance of how the cyclic performance of any beam is effected by varying the RBS geometrical parameters, has not been fully investigated in literature.

The aim of this Chapter is to develop more efficient design methodologies for RBS connections by investigating the effect of geometrical parameters of such connections. First, a validated FE model is developed in ABAQUS using two beam to column sub assemblies. Then a comprehensive parametric study is conducted to investigate the effect of RBS geometries on the cyclic performance of RBS beams using experimentally validated models. This will enable a better understanding how the geometries that define the RBS connection control its seismic performance at the connection level. Finally, new design equations will be developed to predict the affect RBS geometry has on the key design parameters for any RBS connection.

This will be achieved by exploring how the geometries specified in Figure 2.1 affect the main seismic design parameters. These include: Yield Moment (M_y), Peak Moment (M_c), Ultimate Rotation (θ_u), Energy Dissipated (E_{diss}) and Ductility (μ). A new design methodology which utilizes proposed empirical equations will enable designers to predict the key seismic design parameters of any RBS connection using the pre-defined geometrical parameters a, b or c, (within the specified limits). This

will enable the designer to take into account the seismic design performance of the beam to enable maximum energy dissipation and hence better seismic performance within the connection. This will also lay down the basic principles for future work to control the performance of a structure at the frame level, by varying the RBS geometries.

In this Chapter a comprehensive literature review has been conducted, followed by a summary of the current design methodology of RBS connections in Section 2.3. Section 2.4 presents the detailed FE model with an extensive FE parametric analysis in Section 2.5 and results shown in Section 2.6. A detailed discussion of the results in Section 2.7, highlights the key RBS geometries which influence the key seismic design parameters. A summary of the important and key points of this Chapter is concluded with Section 2.8.

2.3 Current design methodology for RBS connections

RBS connections are considered to be pre-qualified in most design guidelines, which means they can be used in the design of steel frames if the specified design and fabrication procedures are followed. This is a result of rigorous testing to ensure they provide a reliable and acceptable behaviour. However, pre-qualified connections are subject to limitations laid out in the applicable design code.

The geometries of RBS connections are specified by three parameters: a, b and c as shown in Figure 2.1. Limits, specific to the applicable code, have been imposed on the RBS geometries, as the pre-qualified experimental tests in literature were conduced over a small and limited range of a, b and c geometries. According to Engelhardt (1999), the geometries of a and b were kept small so as to minimize the moment that develops at the column face (M_f), (Figure 2.2 shows how larger values of a and b increase the S_h value leading to a larger M_f). The limits imposed on the a parameter allow the stress that develops across the RBS to spread uniformly across the flange at the column face, whereas, the limit on the b parameter helps to avoid significantly large inelastic strains in the RBS (Engelhardt, 1999). The c parameter is limited to 25% of the flange width to avoid excessive loss in strength or stiffness (AISC, 2016b; Engelhardt, 1999).

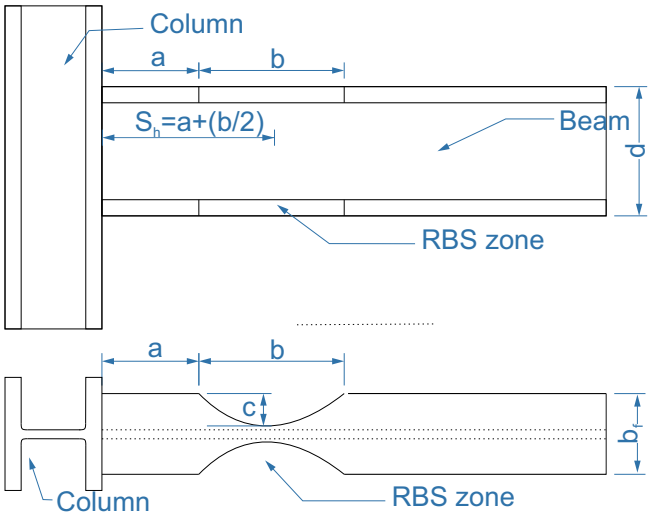

Figure 2.1: Geometric parameters of RBS connections

2.3.1 Design according to BS/EN 1998-3

For RBS connection design, BS/EN 1998-3 (BSI, 2005) specifies three rotational capacities corresponding to three limit states that will be achieved by the connection, if a detailed design procedure is followed. Table 2.1 summaries flexural RBS rotational capacities with their corresponding limit states. A rotation of $0.04rad$ is considered to be a Near Collapse (NC) limit state.

Table 2.1: Rotational capacities of RBS beams corresponding to each limit state according to BS/EN 1998-3

Damage Limitation (DL)	**Significant Damage (SD)**	**Near Collapse (NC)**
0.010rad	$0.025rad$	$0.040rad$

Initial guesses of the geometrical parameters for the RBS connections recommended by BS/EN 1998-3 (BSI, 2005) are given in Table 2.2, where b_f is the width of the beams flange and d is the depth of the beam. According to BS/EN 1998-3 (BSI, 2005), the plastic moment and shear strength of the beam must also be checked. Forces and moments acting at the column face and RBS connection are shown in Figure 2.2. The plastic moment of the beam is checked to ensure it can carry the moment that occurs at the column face M_f as a result of the sum of the moment that develops at the plastic hinge M_{pr} – defined as the centre of the RBS – and the moment due to the shear force acting at the plastic hinge location V_{RBS}. The shear strength of the beam should also be checked. The following defines the symbols in Figure 2.2: S_h is the distance from the centre of the RBS to the column face, a and b are the geometries of the RBS (see Figure 2.1), M_{pr} is the maximum probable moment that occurs at the centre of the plastic hinge (or RBS), V_{RBS} is the shear force that arises at the centre of the plastic hinge from the load combination applied, V_u is the shear force that develops at the face of the column and M_f is the maximum probable moment at the column face used in the design procedure.

Table 2.2: The recommended RBS geometries according to BS/EN 1998-3

RBS Geometries		
a	b	c
$0.60b_f$	$0.75d$	$\leq 0.25b_f$

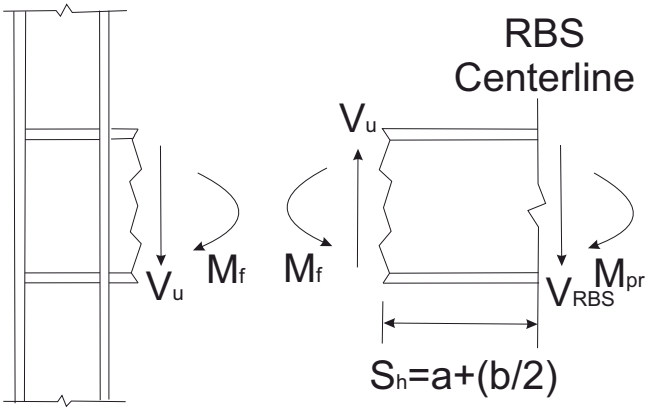

Figure 2.2: A schematic showing the forces and moments arising at the column face and plastic hinge locations.

2.3.2 Design according to ANSI/AISC 358-16 and FEMA 350

Similarly, ANSI/AISC 358-16 (AISC, 2016b) and FEMA 350 (SAC Joint Venture, 2000a) both specify the RBS connection as pre-qualified with the ability to achieve $0.04rad$ of rotation confidently. The design process of RBS connections is the same as BS/EN 1998-3 (BSI, 2005) and summarised in Section 2.3.1. The only difference is that ANSI/AISC 358-16 (AISC, 2016b) and FEMA 350 (SAC Joint Venture, 2000a) specify acceptable ranges for the limits of the a, b and c parameters which are shown in Table 2.3.

Table 2.3: RBS geometry limits defined in ANSI/AISC 358-16

Limits for a	**Limits for b**	**Limits for c**
$0.5b_f \leq a \leq 0.75b_f$	$0.65d \leq b \leq 0.85d$	$0.1b_f \leq c \leq 0.25b_f$

2.3.3 Performance design according to ASCE/SEI 41-17

ASCE/SEI 41-17 (ASCE, 2017a) adopts a performance-based design approach. Three different limit states, which are Immediate Occupancy (IO), Life Safety (LS) and Collapse Prevention (CP), are defined to determine the performance of the connections. RBS connections – defined as fully restrained connections in ASCE/SEI 41-17 (ASCE, 2017a) – are considered deformation controlled in flexure. Through non-linear static and dynamic design procedures, maximum permissible deformations/rotations of the RBS connections can be compared to these performance limits, in order to determine their level of performance. Table 2.4 summarises the acceptance criteria for the three RBS limit states in ASCE/SEI 41-17 (ASCE, 2017a).

Table 2.4: The acceptance criteria of RBS connections for the three limit states according to ASCE/SEI 41-17

Limit States (rad)		
IO	**LS**	**CP**
$0.025 - 0.00015d$	$0.0525 - 0.00023d$	$0.07 - 0.00030d$

2.4 Validation of FE models

2.4.1 ABAQUS finite element modelling

To asses the effects that the RBS parameters a, b and c have on the cyclic behaviour of fully welded connections (WUF-F) a finite element model using the general purpose ABAQUS (ABAQUS, 2016) software is developed. In order to validate the FE model, two full scale sub assemblies from Lee et al. (2005) and Nia et al. (2013), shown in Figures 2.3a and 2.3b respectively, is used. The experimental test carried out by Nia et al. (2013) was a welded unreinforced welded web connection to a box column designed based on ANSI/AISC 341-05 (AISC, 2016a) and ANSI/AISC 360-05 (AISC, 2016c). The connection was designed to represent a medium sized exterior multi-storey connection and contained shear tabs and continuity plates. The continuity plates were fillet welded on three sides and the fourth side was welded with a Complete Joint Penetration weld. The beam flange was groove welded to the box column with the backing bar being fillet welded in place. The beams web was grove welded from one weld access hole to the other. Finally, the shear tab was groove welded to the column flange and fillet welded to the beam web. This shear tab was also used as a backing plate for the Complete Joint Penetration groove weld connecting the beam web to the column flange. Welds used were specified as a minimum Charpy V-notch touchness of 27 J at -29°C. Further details of the connection and

experimental set up can be found in Nia et al. (2013). Likewise, Lee et al. (2005) carried out the experimental tests on a strong panel zone with a welded web. Continuity plates with equal thickness to the beams flange were specified. Welds used for the connection were Charpy V-Notch toughness of 26.7 J at -28.9°C. A strong floor and strong wall was used to mount the connection on and lateral bracing was provided as a distance 2.5m from the face of the column. Further details of the connection and experimental set up can be found in Lee et al. (2005).

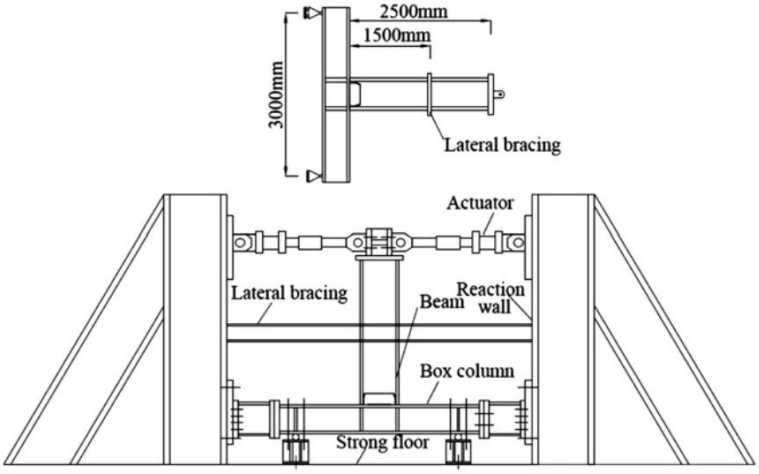

(a)

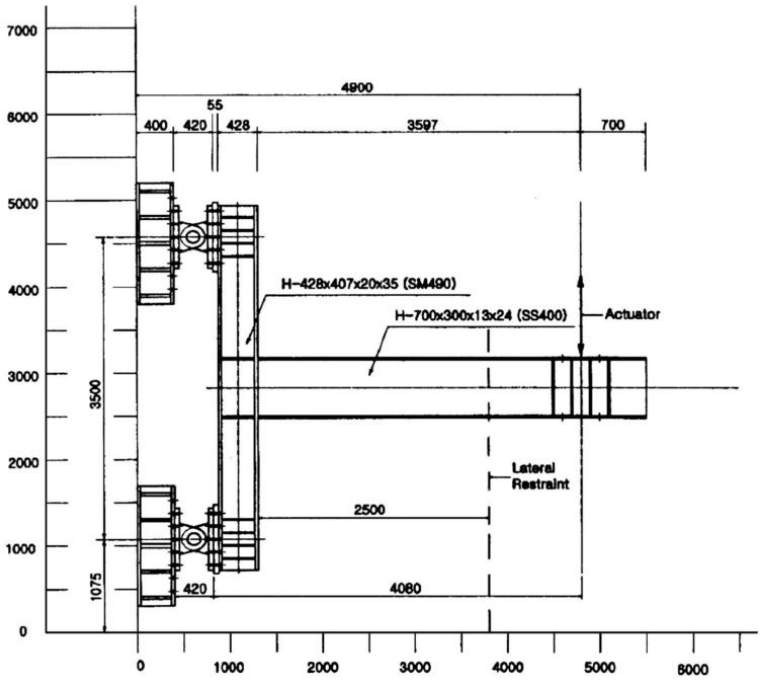

(b)

Figure 2.3: Diagrams of the experimental test set-ups used to validate the finite element model by (a) Nia et al. (2013) and (b) Lee et al. (2005) (Nia et al., 2013; Lee et al., 2005).

The cyclic loading applied in Lee et al. (2005) was in accordance with the SAC loading protocol (SAC Joint Venture, 2000a), while Nia et al. (2013) used the AISC/ANSI 341-05 (AISC, 2016a) loading protocol. As the cyclic loading of the sub assemblies during each cycle was applied slowly, a static-general analysis (with non-linearity accounted for), is adopted in ABAQUS. The "time" period varies

from 0.0 to 1.0 over the adopted 0.01 time step, hence, the "time" increments are fractions of the total period of the step.

In order to reduce the computational time, Reduced Integration Shell S4R elements are used which are capable of capturing the local buckling of the beam web and flanges. The connection and areas of significant buckling and plastic deformation are meshed with a finer mesh in order to produce more accurate results. In areas of the connection where significant local buckling is expected to occur, and in areas of high stress concentrations, the elements are meshed with 20mm mesh dimensions. A transition to a larger course mesh (up to 200mm) in areas where buckling did not occur, is adopted to save computational time. This method of meshing is compared to a model with 20mm mesh throughout, and the results showed no significant differences in the moment verses rotation hysteresis. A mesh convergence study is conducted which showed that for areas of significant importance a 20mm mesh provided highly accurate results while at the same time providing a reasonable model running time. The boundary conditions applied are representative of the respective experimental set ups observed in Lee et al. (2005) and Nia et al. (2013).

In order to model the plasticity behaviour a combined non-linear isotropic and kinematic strain hardening model using the Von Mises yield surface and associated flow rule is used. Calibration of the material properties is based on the coupon test results provided in the respective references Lee et al. (2005) and Nia et al. (2013) in order to define the two pairs of hardening parameters: Q, b and C_k,γ_k. For the first pair, Q defines the maximum size of the yield surface and b defines the rate of change of the yield surface with increasing strain. The subsequent pair C_k and γ_k are defined as the initial kinematic hardening modulus and the rate at which the hardening modulus changes with increasing strains respectively.

2.4.2 Connection DC-M from Nia et al. (2013)

A welded unreinforced flange to box column taken from Nia et al. (2013) is modelled in order to validate the modelling techniques used. The material properties used are based on the mechanical properties of tested steel coupons from Nia et al. (2013), shown in Table 2.5. The tie command is used to model all welds. Kinematic coupling to a reference point was used to simulate the load point and fixed column end arrangements. Buckling of the flanges at 6% in Figure 2.4a is found to be consistent with the buckling of the DC-M specimen in Figure 2.4b at the respective 6% drift. Figure 2.4c shows that very good agreement can be found between the experimental results and FE analysis results.

Table 2.5: Coupon test results from experimental tests Nia et al. (2013)

Location	Yield Strength (Mpa)	Tensile strength (Mpa)	Elongation (%)
Beam flange	252.0	399.6	30.8
Beam web	351.0	482.5	27.5

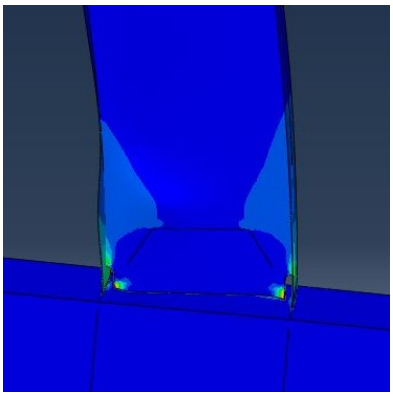

(a)

(b)

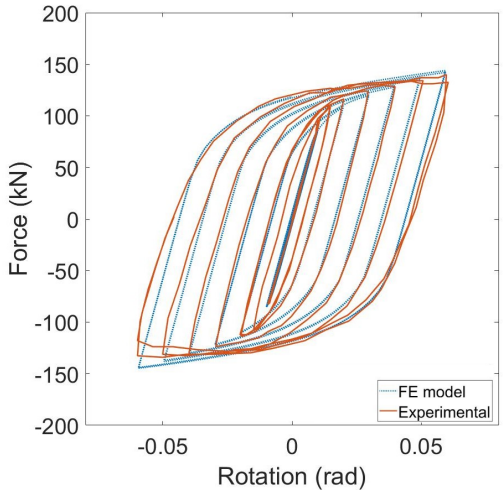

(c)

Figure 2.4: (a) Equivalent Plastic Strain (PEEQ) contour plot from the FE model of the deformation at 6% drift (b) observations of the beam from experimental results (Nia et al., 2013) (c) comparisons of the cyclic hysteric force-rotation curve with that of experimental and numerically observed

2.4.3 Connection DB-700-SW Lee et al. (2005)

A fully Welded Unreinforced Welded Web (WUF-W) RBS connection with a strong panel zone is selected from Lee et al. (2005). Table 2.6 shows the coupon test results taken form Lee et al. (2005) for calibrate the combined hardening parameters. The buckling of the beam flanges from the FE model (Figure 2.5a) is in good agreement with the buckling observed in the experimental results (Figure 2.5b). Figure 2.5c shows the cyclic hysteresis curve obtained from FE analysis compared to the test results. Normalisation of the moment is based on Morshedi et al. (2017). Very good agreement is observed between the FE analysis and the experimental results. The plastic deformation of the RBS connection and the strength degradation of the connection with increasing cycles is captured with a good level of accuracy.

Table 2.6: Coupon test results for the beam

Location	Yield Strength (Mpa)	Tensile strength (Mpa)
Beam flange	304	455
Beam web	364	480

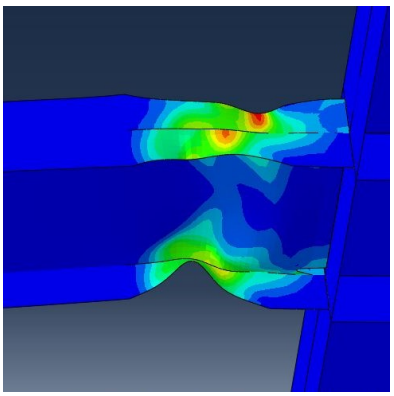

(a)

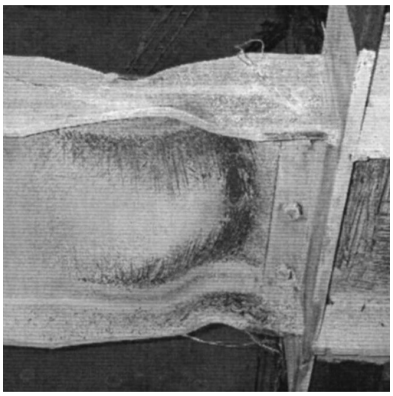

(b)

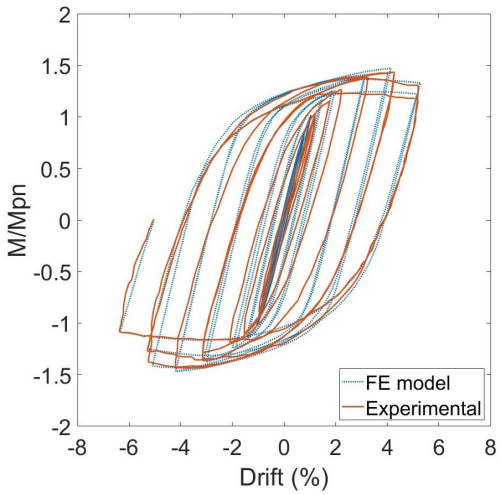

(c)

Figure 2.5: (a) Contour PEEQ plot at 6% drift showing the buckling in the FE model, (b) observed buckling at 6% from the experimental results (Lee et al., 2005) (c) Comparisons of the normalized moment verses drift hysteresis for the finite element and experiment results

2.4.4 Details of the model adopted in the study

In order to asses how the geometries of the RBS connection affect the beams cyclic hysteresis, only the beam is modelled so as to eliminate any effects that the panel zone could have on the connection. Figure 2.6a shows a typical beam modelled which follows exactly the same modelling approaches and techniques mentioned above. The SAC loading protocol (SAC Joint Venture, 2000a) is used in order to assess the connections performance and each beam is loaded up to two cycles of $0.06rad$. Figure 2.6b shows the displacement based loading applied to the beams tip determined based on the beams length.

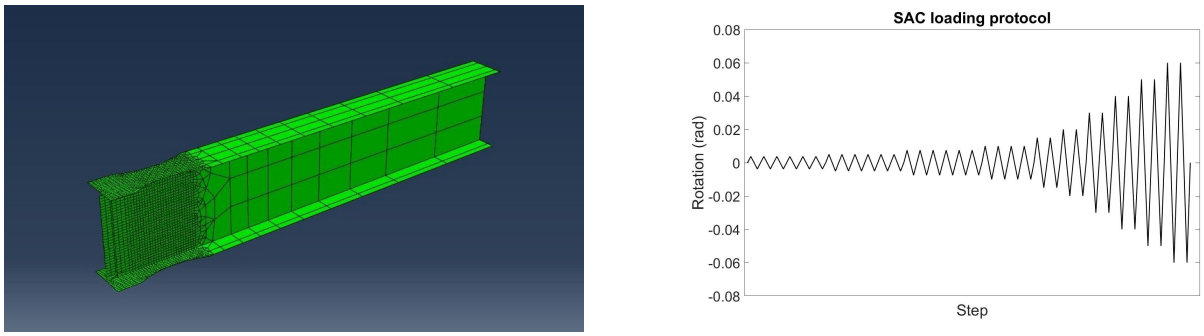

(a) (b)

Figure 2.6: (a) The FE model of the fixed beam used to asses the effects of the RBS geometrical properties on the cyclic performance of the beam (b) the SAC loading protocol applied to the FE model.

2.4.5 Monotonic verses cyclic behaviour

In many studies, the monotonic behaviour of a beam or beam-column connection are used as a rough estimation of the beams cyclic response. However, a complete cyclic hysteresis under an approved loading protocol to asses the effects of cyclic hardening and cyclic degradation provides the true cyclic behaviour. In order to investigate this, the cyclic and monotonic results of a fixed rigid end beam are compared. Figure 2.7 compares an RBS beam loaded to $500mm$ of monotonic tip displacement and the same RBS beam subjected to the cyclic SAC loading protocol up to $0.06rad$.

Figure 2.7 clearly shows that the monotonic result cannot capture the cyclic hardening and strength degradation of the RBS beam. Therefore, the cyclic backbone curve adopted in PEER/ATC-72-1 (Moehle et al., 2010) and shown in Figure 2.7, will be used to represent the strength degradation of the beam for calculating the main seismic design parameters in this study.

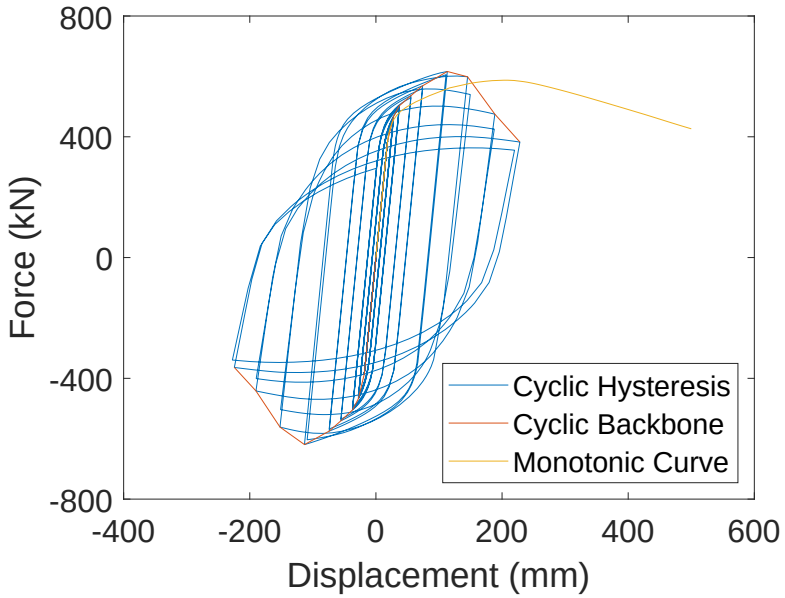

Figure 2.7: Comparisons of the monotonic, cyclic and cyclic backbone results for an RBS beam, highlighting how the cyclic backbone captures the cyclic hardening and strength degradation. Displacement is measured at the tip of the beam.

2.5 Parametric analysis

A comprehensive parametric study of 90 specimens is carried out to assess the effect of different design parameters for ranges within the recommended upper and lower limits of the a, b and c geometries, on the performance of RBS connections. Nine different American Wide Flange Beams ranging from W30X116 to W14X43 are investigated with 10 different variations for each beam. Table 2.7 shows the different beam properties that are modelled and tested by the FE analysis, along with the respective RBS modelling parameters. Figures 2.15a to 2.15i show the cyclic backbone curves for the nine beams cyclically tested for 5 varying cases of the c RBS parameter up to the Ultimate Rotation (defined in Section 2.6).

Table 2.7: The American Wide Flange Beams built in FE models with the corresponding RBS geometrical parameters, (see also Figure 2.1). All dimensions are in mm except beam designations which are in inches.

Beam	d	bf	tw	tf	a	b	c	model	Ref Name	Short Hand
W30X116	762	267	14.4	21.6	0	0	0	2	Full Section	FS
					167	572	27	2.1	20% flange reduction	20%FR
					167	572	37	2.10	28% flange reduction	28%FR
					167	572	47	2.2	35% flange reduction	35%FR
					167	572	57	2.11	43% flange reduction	43%FR
					167	572	67	2.3	50% flange reduction	50%FR
					167	495	47	2.4	smallest b value	>bVal
					167	648	47	2.6	largest b value	<bVal
					134	572	47	2.7	smallest a value	>cVal
					200	572	47	2.9	largest a value	<cVal
W27X114	693	256	14.5	23.6	0	0	0	3	Full Section	FS
					160	520	26	3.1	20% flange reduction	20%FR
					160	520	35	3.10	28% flange reduction	28%FR
					160	520	45	3.2	35% flange reduction	35%FR
					160	520	54	3.11	43% flange reduction	43%FR
					160	520	64	3.3	50% flange reduction	50%FR
					160	450	45	3.4	smallest b value	>bVal
					160	589	45	3.6	largest b value	<bVal
					128	520	45	3.7	smallest a value	>cVal
					192	520	45	3.9	largest a value	<cVal
W27X84	678	253	11.7	16.3	0	0	0	4	Full Section	FS
					158	509	25	4.1	20% flange reduction	20%FR
					158	509	35	4.10	28% flange reduction	28%FR
					158	509	44	4.2	35% flange reduction	35%FR
					158	509	54	4.11	43% flange reduction	43%FR
					158	509	63	4.3	50% flange reduction	50%FR
					158	441	44	4.4	smallest b value	>bVal
					158	576	44	4.6	largest b value	<bVal
					127	509	44	4.7	smallest a value	>cVal
					190	509	44	4.9	largest a value	<cVal
W24X103	623	229	14	24.9	0	0	0	5	Full Section	FS
					143	467	23	5.1	20% flange reduction	20%FR
					143	467	31	5.10	28% flange reduction	28%FR
					143	467	40	5.2	35% flange reduction	35%FR
					143	467	49	5.11	43% flange reduction	43%FR
					143	467	57	5.3	50% flange reduction	50%FR
					143	405	40	5.4	smallest b value	>bVal
					143	530	40	5.6	largest b value	<bVal
					115	467	40	5.7	smallest a value	>cVal
					172	467	40	5.9	largest a value	<cVal

Continued on next page ...

Table 2.7 continued...

Beam	d	bf	tw	tf	a	b	c	model	Ref Name	Short Hand
W24X68	603	228	10.5	14.9	0	0	0	6	Full Section	FS
					143	452	23	6.1	20% flange reduction	20%FR
					143	452	32	6.10	28% flange reduction	28%FR
					143	452	40	6.2	35% flange reduction	35%FR
					143	452	49	6.11	43% flange reduction	43%FR
					143	452	57	6.3	50% flange reduction	50%FR
					143	392	40	6.4	smallest b value	>bVal
					143	513	40	6.6	largest b value	<bVal
					114	452	40	6.7	smallest a value	>cVal
					171	452	40	6.9	largest a value	<cVal
W21X83	544	212	13.1	21.2	0	0	0	7	Full Section	FS
					133	408	21	7.1	20% flange reduction	20%FR
					133	408	29	7.10	28% flange reduction	28%FR
					133	408	37	7.2	35% flange reduction	35%FR
					133	408	45	7.11	43% flange reduction	43%FR
					133	408	53	7.3	50% flange reduction	50%FR
					133	354	37	7.4	smallest b value	>bVal
					133	462	37	7.6	largest b value	<bVal
					106	408	37	7.7	smallest a value	>cVal
					159	408	37	7.9	largest a value	<cVal
W21X62	533	209	10.2	15.6	0	0	0	8	Full Section	FS
					131	400	21	8.1	20% flange reduction	20%FR
					131	400	29	8.10	28% flange reduction	28%FR
					131	400	37	8.2	35% flange reduction	35%FR
					131	400	44	8.11	43% flange reduction	43%FR
					131	400	52	8.3	50% flange reduction	50%FR
					131	346	37	8.4	smallest b value	>bVal
					131	453	37	8.6	largest b value	<bVal
					105	400	37	8.7	smallest a value	>cVal
					157	400	37	8.9	largest a value	<cVal
W18X76	463	280	10.8	17.3	0	0	0	9	Full Section	FS
					175	347	28	9.1	20% flange reduction	20%FR
					175	347	39	9.10	28% flange reduction	28%FR
					175	347	49	9.2	35% flange reduction	35%FR
					175	347	60	9.11	43% flange reduction	43%FR
					175	347	70	9.3	50% flange reduction	50%FR
					175	301	49	9.4	smallest b value	>bVal
					175	394	49	9.6	largest b value	<bVal
					140	347	49	9.7	smallest a value	>cVal
					210	347	49	9.9	largest a value	<cVal
W14X43	347	203	7.7	13.5	0	0	0	10	Full Section	FS
					127	260	20	10.1	20% flange reduction	20%FR
					127	260	28	10.10	28% flange reduction	28%FR
					127	260	36	10.2	35% flange reduction	35%FR
					127	260	43	10.11	43% flange reduction	43%FR
					127	260	51	10.3	50% flange reduction	50%FR
					127	226	36	10.4	smallest b value	>bVal
					127	295	36	10.6	largest b value	<bVal
					102	260	36	10.7	smallest a value	>cVal
					152	260	36	10.9	largest a value	<cVal

2.6 Results

Using the cyclic backbone explained in Section 2.4.5, the Yield Strength (M_y) is determined using the idealised force deformation curve from FEMA 356 (FEMA, 2000). This method uses the first part of the cyclic backbone curve in order to determine the yield point. Figure 2.8a shows how the approximate area above and below the idealised curve and the cyclic backbone curve are balanced in order to determine M_y and its corresponding rotation. The peak strength is determined as the peak value of the cyclic FE results, while the peak rotation is defined as the corresponding rotation to the

peak moment.

The Ultimate Strength (M_u) and Ultimate Rotation (θ_u) are defined as the points on the cyclic backbone curve which corresponds to a 20% loss in the strength from the Peak Strength (M_c) (SAC Joint Venture, 2000a). In this study, the θ_u is defined according to Equation 2.1, where δ is the displacement at the beams load point and L is the length of the beam. Figure 2.8b provides an explanation to how the M_u and θ_u are determined.

$$\theta_u = \delta / L \tag{2.1}$$

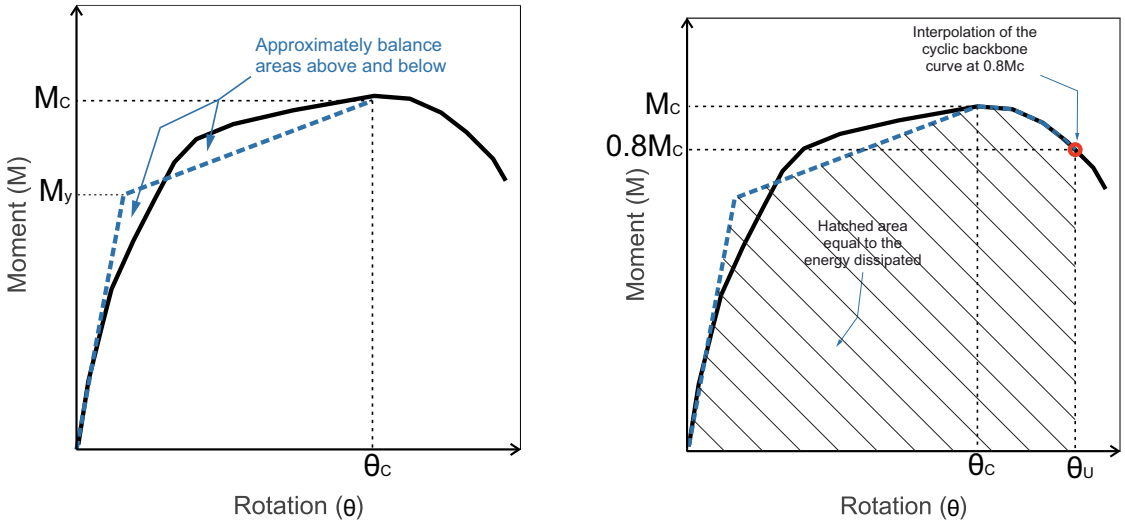

Figure 2.8: (a) Idealised force deformation according to FEMA (2000) to determine Yield and Peak points (b) 20% drop in strength method used to determine the Ultimate points along the cyclic backbone

While investigating how the a, b and c parameters affected the key seismic design parameters it was noted that in general the variation of response parameters for the a and b parameters are small. In order to save computational time, in this section the key seismic design parameter trends for varying a and b cases were based on only three respective varying RBS geometry. To verify the accuracy of this approach, two different RBS beam sections were selected and five variations of different a and b parameter were investigated. The trends for these results, shown in Figures 2.9a and 2.9b, were compared to the trends for RBS beam sections where only three varying cases of a and b parameter had been considered. Both sets of results follow the same trend, thus verifying this approach.

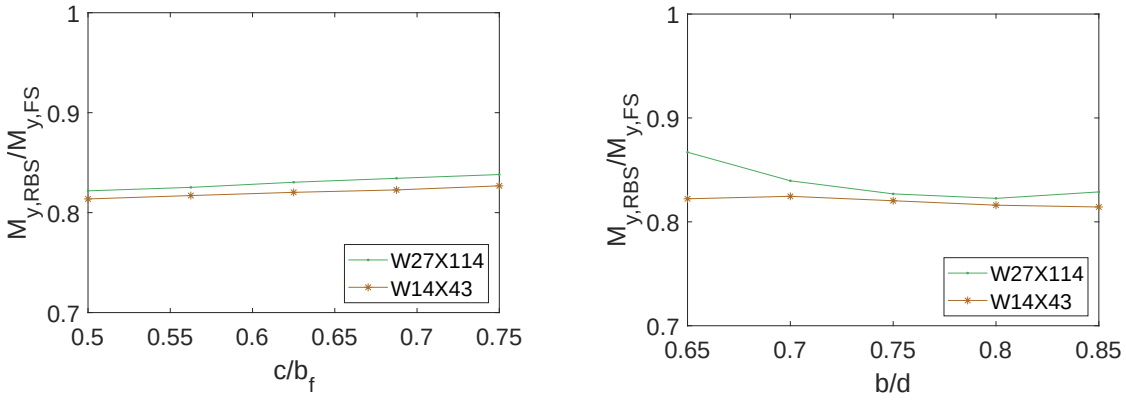

(a) (b)

Figure 2.9: Yield Moment (M_y) trends for W27x114 and W14x43 for varying (a) a parameter and (b) b parameter.

During the comprehensive parametric analysis, while investigating the effects of the RBS geometries on the key design parameters it was important to only change one parameter in order to asses its effects. Therefore, while investigating each of the three parameters (a, b and c) separately the other two parameters are fixed as the average of the upper and lower limits according to Table 2.3

2.6.1 Yield Moment

Figures 2.10a to 2.10c shows how the Yield Moment (M_y) changes with varying a, b and c parameters. The results clearly show that the a and b parameters do not affect the M_y relative to the c parameter, which reduces the moment more than 20% between the two extreme limits. On average, the c parameter reduces the M_y by 27% between the upper and lower recommended values compared to less than 2.0% changes for the a and b parameters.

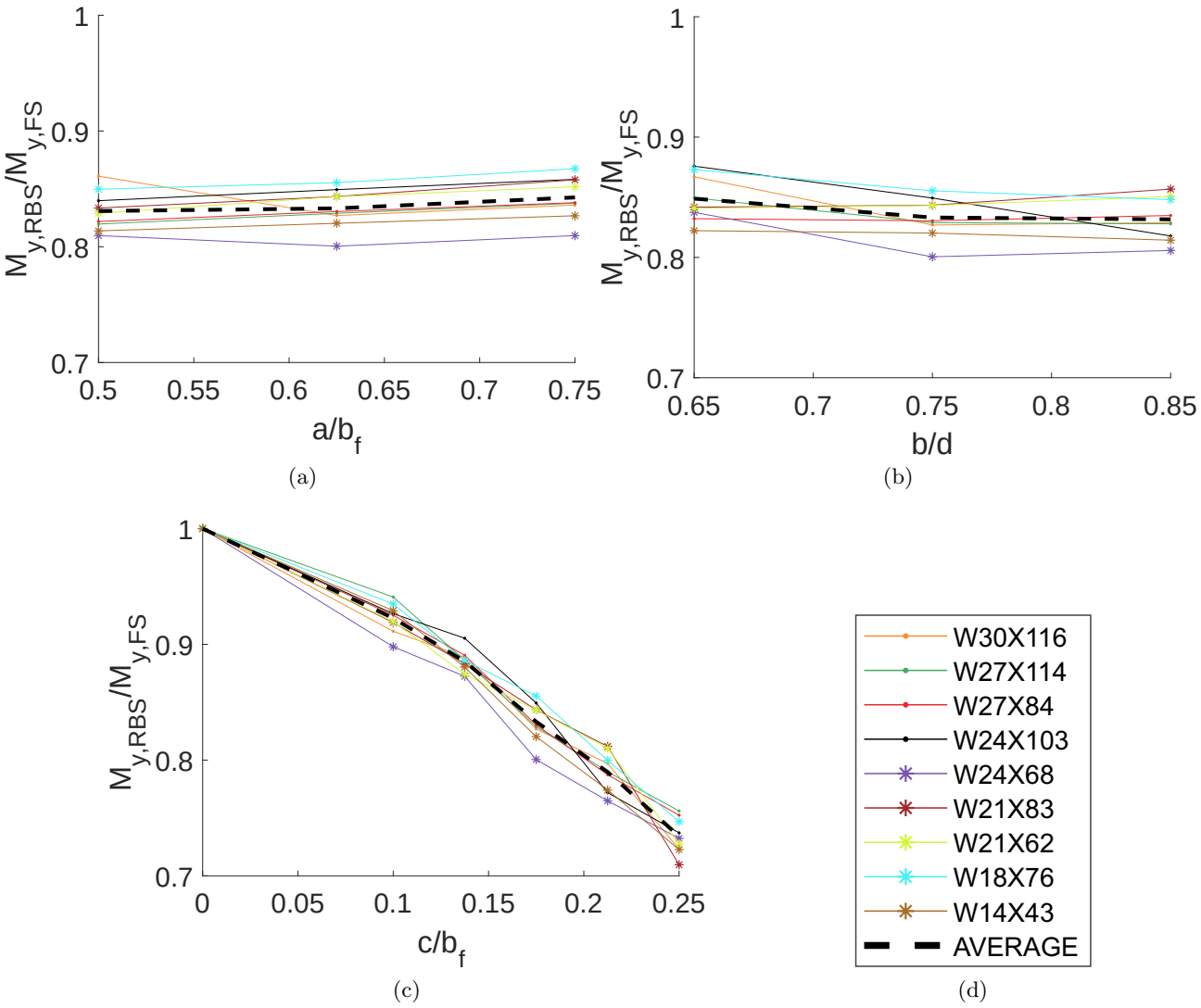

Figure 2.10: The variation of normalized yield moment with respect to (a) parameter a (b) parameter b and (c) parameter c

2.6.2 Peak Moment

The influence of parameters a, b and c on the Peak Moment (M_c) is shown in Figures 2.11a to 2.11c. A reduction of 24% can be observed in Figure 2.11c between the lower and upper limits of the c parameter. Whereas, only 3% changes is observed in the peak moment for the b parameter. Similarly, changes in parameter a has insignificant effect on the estimated peak moment.

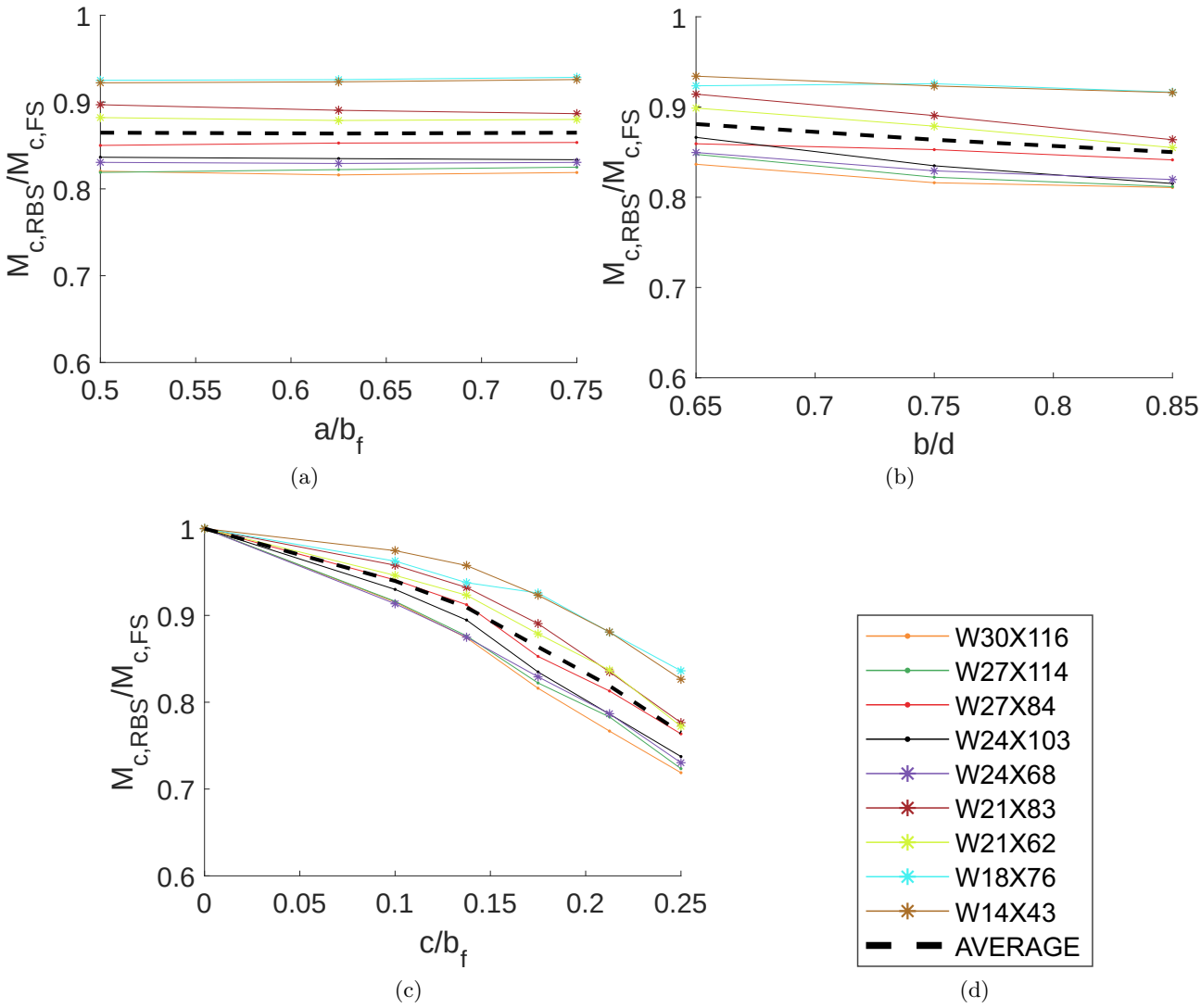

Figure 2.11: The variation of normalized peak moment with respect to (a) parameter a (b) parameter b and (c) parameter c

2.6.3 Ultimate Rotation

The RBS parameters have less of an affect on the Ultimate Rotation (θ_u), compared to M_y and M_c, as shown in Figure 2.12. On average the a parameter has only a 1% influence on θ_u between the upper and lower limits. Interestingly the b parameter appears to be the most influential on θ_u, with 5% reductions in θ_u between lower and upper limits. The c parameter appears to have a smaller influence on average on the θ_u with just over 3% changes of θ_u over the lower and upper limits.

However there are two distinct groups in Figure 2.12c showing completely different trends when the c parameter is increased. The two groups can be clearly classified according to the web slenderness $(d-2t_f)/t_w$ – where the parameters are defined in Figure 2.1. The upper group has a web slenderness smaller than 42, whereas the lower group has a web slenderness larger than 44. Figures 2.11a to 2.11c indicate that the Ultimate Rotation of the beam is also dependent on the web slenderness.

On average for all sections, the RBS has an insignificant influence on θ_u, however, sections W30X116, W27X114, W27X84, and W24X68, with RBS resulted in lower Ultimate Rotations (up to 12% lower)

at the column face compared to full beam sections. These sections have a web slenderness larger than 44, and thus, clearly would resist larger ultimate rotations due to a stiffer beam profile. While sections W24X103, W21X83, W21X62, W18X76, and W14X43, with RBS provide increased Ultimate Rotations at the column face (up to 10% higher). These sections have a web slenderness less than 42 leading to a lower beam stiffness and thus can accommodate larger Ultimate Rotations.

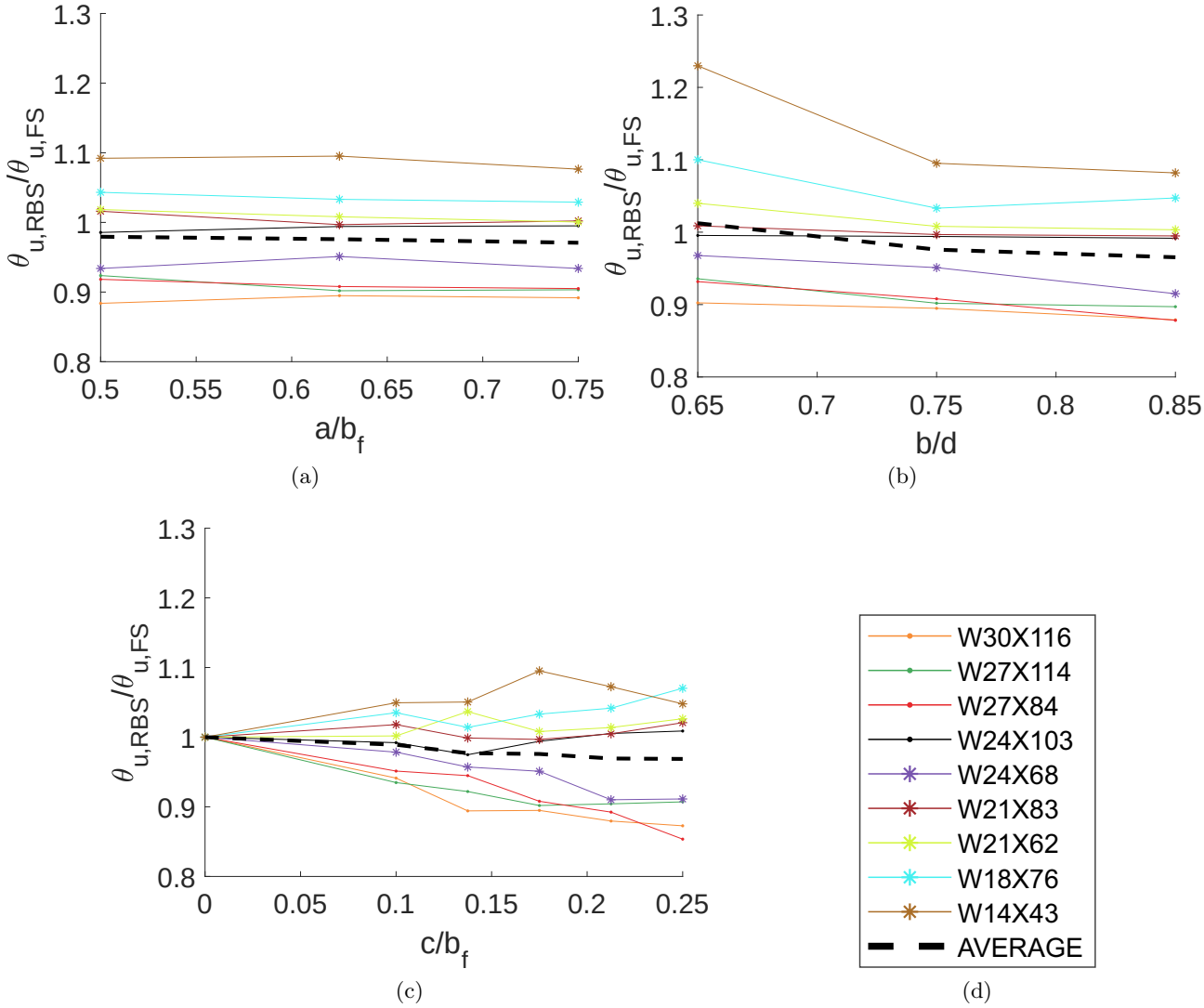

Figure 2.12: The variation of normalized Ultimate Rotation for varying changes with respect to (a) parameter a (b) parameter b and (c) parameter c

2.6.4 Ductility

The ductility (μ) has been calculated following the recommendation in ASCE (2017a), and is defined as follows:

$$\mu = \frac{\theta_u}{\theta_y} = \frac{\delta_u}{L} / \frac{\delta_y}{L} = \frac{\delta_u}{\delta_y} \tag{2.2}$$

where: θ_u is the ultimate rotation, θ_y is the yield rotation, L is the length of the beam, δ_u is the ultimate displacement of the beam at the load point and δ_y represents the yield displacement of the beam at the load point.

The yield rotation (θ_y) is defined as the rotation corresponding to the yield moment, while the ultimate rotation (θ_u) is defined as the rotation corresponding to 80% of the peak moment ($0.8M_c$) as defined is section 2.6. The rotation (θ_u) is calculated using interpolation along the cyclic back bone curve which is defined in Section 2.4.5.

Figure 2.13a shows that the parameter a has very little effect on the beams Ductility (μ), with only 2% changes in μ between the lower and upper limits. Figures 2.13b and 2.13c show that the parameters b and c have more influence, with c being the most prominent. However, the parameter c increases the Ductility with increasing values of c and the parameter b reduces the ductility with increasing values of b. Over all on average, the parameter b causes a 5% reduction between the lower and upper limits and the parameter c infers a 7% increase of ductility between the lower and upper limits.

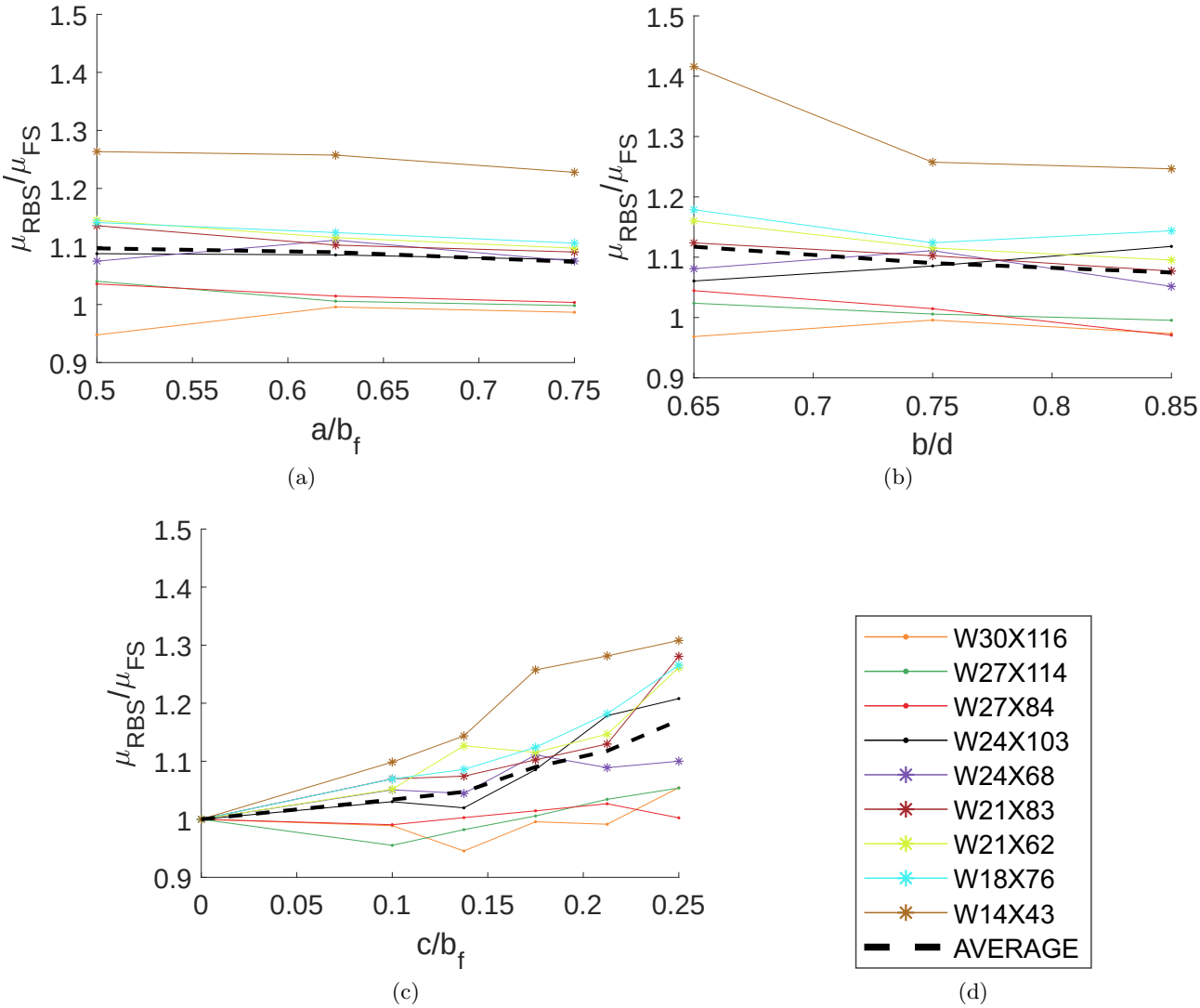

Figure 2.13: The variation of normalized Ductility (μ_{RBS}/μ_{FS}) with respect to the: (a) parameter a (b) parameter b and (c) parameter c

While RBS sections in W30X116, W27X114, and W27X84, provide only 5% increases of ductility, smaller depth sized sections provided up to 30% increases in ductility when RBS sections are used.

2.6.5 Energy dissipation capacity

The energy dissipated (E_{diss}) is defined as the energy under the cyclic backbone curve up to the ultimate rotation as explained in Section 2.6.3 and shown in Figure 2.8b.

Figure 2.14a clearly shows that on average the parameter a has no effect (less that 1% change) on the normalised energy dissipated by the beam. The parameter b has a small influence leading to 7% reductions in the normalised energy dissipation capacity for changes between the lower and upper limits as shown in Figure 2.14b. Figure 2.14c also indicated that the parameter c is the most influential giving changes of 23% in normalised energy dissipation capacity between the lower and upper values of c.

It should be noted that the decrease in energy dissipation corresponding to a decrease in parameter c, shown in Figure 2.14c, can be explained through the definition of the energy dissipation parameter defined in Figure 2.8b. RBS connections with smaller values of parameter c, reduce the capacity of the section which leads to a lower value of yield moment and peak moment, shown in Figures 2.10c and 2.11c respectively. As the ultimate rotation is defined as the rotation corresponding to a 20% reduction in the peak moment (shown in Figure 2.8b), this leads to a reduced calculated value of energy dissipation for the corresponding section.

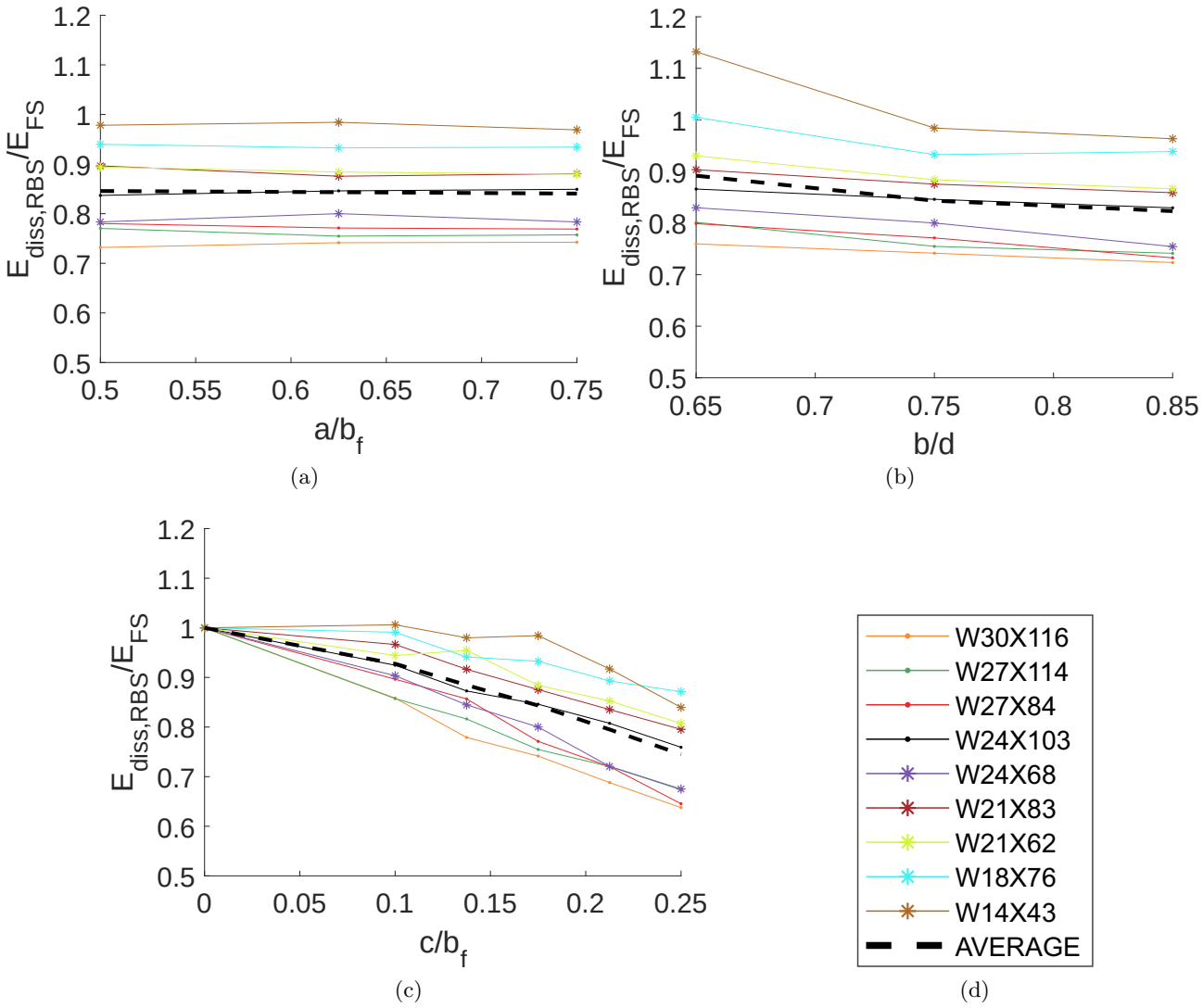

Figure 2.14: The variation of normalized energy dissipation capacity with respect to (a) parameter a (b) parameter b and (c) parameter c

In general, sections W30X116, W27X114, W27X84, and W24X68, provide up to 30% lower normalized energy dissipation capacity for RBS sections compared to the other sections which only provide a decrease of 10% to 15%. Compared to the previous graphs, higher θ_u, M_c and M_y values leads to more energy dissipation in the RBS connections.

2.7 Discussion

2.7.1 Summary of the RBS parameters that have the most influence on the design parameters

Table 2.8 summarises the influence on average of the a, b, and c parameters on the seismic design parameters analysed in Section 2.5. It is shown that the parameter a has insignificant influence on the seismic design parameters of interest. The parameter b also has no significant influence on the M_y or M_c, with small implications on normalised θ_u, μ and E_{diss}. Similar observations can be drawn for the c parameters influence on θ_u and μ. Finally the parameter c is largely influential on the M_y, M_c and E_{diss}, with the E_{diss} seismic design parameter influenced the most by parameter c.

Table 2.8: The percentage influence on average of the RBS geometry on the seismic design parameters

Design Parameter	RBS Parameter		
	a	b	c
M_y	-1%	2%	27%
M_c	0%	3%	24%
θ_u	1%	5%	3%
μ	2%	4%	-17%
E_{diss}	1%	7%	26%

2.7.2 Assessing the adequacy of the beams according to BS/EN 1998-3

BS/EN 1998-3 (BSI, 2005) specifies three minimum rotations that RBS beams must be able to develop at three limit states. Table 2.1 in Section 2.3.1 summaries these required rotational capacities. According to BS/EN 1998-3 (BSI, 2005) the three limit states are characterised as follows:

- Damage Limitation (DL)– the structure has been lightly damaged with negligible permanent drifts. Significant yielding has been prevented with all structural elements retaining strength and stiffness properties.
- Significant Damage (SD) – significant damage has occurred, some lateral residual strength and stiffness is retained but moderate drifts are present and the structure is likely to be uneconomical to repair.
- Near Collapse (NC)– the structure is heavily damaged and has low residual strength, large permanent drifts have occurred and the structure would probably not survive another (moderate) earthquake.

Adequacy of each of the nine beams BS/EN 1998-3 (BSI, 2005) limit states is assessed. Figure 2.15 shows that for all nine beams elastic behaviour occurs below $0.01rad$, indicating that the DL limit state has been achieved.

Figure 2.15 shows that for beams W21X52, W24X68, W27X84, W27X114 and W30X116, an increase in flange reduction for RBS reduces the ultimate rotation. Whereas for W14X43, W18X76, W21X83, and W24X103, increases in flange reduction for the RBS results in larger θ_u. These varying changes in ultimate rotation as a result of the increased flange cut are directly linked with the web and flange slenderness. Sections W14X43, W18X76, W21X83, and W24X103 have a web slenderness less than 42. This indicates a stocky section, where generally buckling of the sections flange is the dominant failure mode. Increasing the RBS cut in these sections allows some of the stresses and strains experienced in the flange to be distributed within the web leading to higher ultimate rotations. Sections W21X52, W24X68, W27X84, W27X114 and W30X116, have a web slenderness larger than 45. These slender sections generally have a dominant failure mode due to buckling of the web. By increasing the cut in the RBS, the slenderness of the flange is reduced dramatically. Given that the dominant buckling failure mode is already within the web, this reduces the ultimate rotation of these sections mainly affected by the web buckling.

Figures 2.15d and 2.15g show the lowest and highest web slenderness values respectively. Figure 2.15g shows how a web slenderness of 55.2 does not meet the NC requirement whereas Figure 2.15d shows how a web slenderness of 38.3 meets the NC requirement.

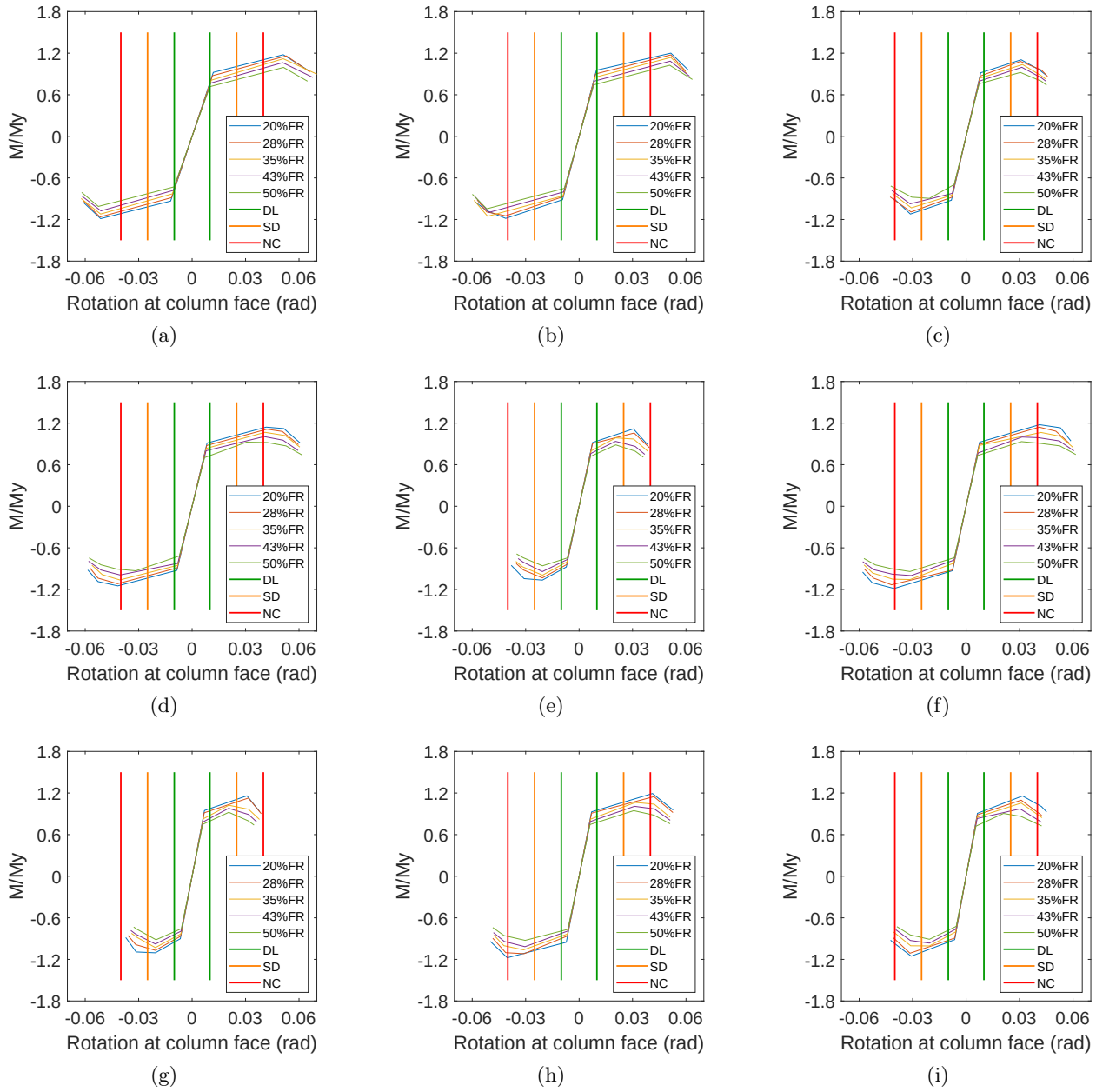

Figure 2.15: Full cyclic backbone curves for (a) W14x43 (b) W18x76 (c) W21x62 (d) W21x83 (e) W24x68 (f) W24x103 (g) W27x84 (h) W27x114 and (i) W30x116, up to the ultimate rotation for each section. The vertical coloured lines show the limit states and can be used to determine the adequacy of each beam achieving the limit states of BS/EN 1998-3

2.7.3 Performance of the beams according to ASCE/SEI 41-17

ASCE/SEI 41-17 (ASCE, 2017a) specifies three Performance Levels – IO, LS and CP – (see Table 2.4 in Section 2.3.1). Table 2.9 summarises the results for assessing the adequacy of the nine beams tested in this study, to meet the ASCE/SEI 41-17 (ASCE, 2017a) performance levels for the rotations that occurred at the column face. Results show that all of the sections in Table 2.7 exceeded an IO performance level of $0.025rad$. In general, the rotation at the column face for each beam reduces for increasing values of the flange reduction. Only RBS sections W24X103, W21X83, W18X76 and W14X43 achieved the LS performance level, and no beams were able to meet the CP performance level.

This indicates that the RBS connections selected in this study are expected to exhibit failure before reaching the CP limits suggested by ASCE/SEI 41-17 (ASCE, 2017a). One of the requirements for RBS connections in ANSI/AISC 358-16 (AISC, 2016b) and FEMA 350 (SAC Joint Venture, 2000a) is the ability to accommodate over 4% inter-storey drift. All of the beams except W27X84 and W24X68 (web slenderness over 54) were able to accommodate the $0.04rad$ of required rotation. This suggests that a web slenderness greater than 54, would not accommodate the ANSI/AISC 3581-16 (AISC, 2016b) and FEMA 350 (SAC Joint Venture, 2000a) 4% inter-storey drift.

Table 2.9: Assessing the adequacy of the beams tested to determine if they achieve ASCE performance levels

Specemin	**Reduction of flange**	**ASCE Performance Level**	**Rotation (θ_u)**	**IO (rad)**	**LS (rad)**	**CP (rad)**
W30X116	20% flange reduction	IO	0.042			
W30X116	28% flange reduction	IO	0.041			
W30X116	35% flange reduction	IO	0.041	0.025	0.052	0.070
W30X116	43% flange reduction	IO	0.039			
W30X116	50% flange reduction	IO	0.039			
W27X114	20% flange reduction	IO	0.050			
W27X114	28% flange reduction	IO	0.048			
W27X114	35% flange reduction	IO	0.048	0.025	0.052	0.070
W27X114	43% flange reduction	IO	0.048			
W27X114	50% flange reduction	IO	0.048			
W27X84	20% flange reduction	IO	0.037			
W27X84	28% flange reduction	IO	0.036			
W27X84	35% flange reduction	IO	0.034	0.025	0.052	0.070
W27X84	43% flange reduction	IO	0.034			
W27X84	50% flange reduction	IO	0.033			
W24X103	20% flange reduction	LS	0.058			
W24X103	28% flange reduction	LS	0.057			
W24X103	35% flange reduction	LS	0.057	0.025	0.052	0.070
W24X103	43% flange reduction	LS	0.058			
W24X103	50% flange reduction	LS	0.057			
W24X68	20% flange reduction	IO	0.038			
W24X68	28% flange reduction	IO	0.035			
W24X68	35% flange reduction	IO	0.035	0.025	0.052	0.070
W24X68	43% flange reduction	IO	0.034			
W24X68	50% flange reduction	IO	0.035			
W21X83	20% flange reduction	LS	0.059			
W21X83	28% flange reduction	LS	0.057			
W21X83	35% flange reduction	LS	0.056	0.025	0.052	0.070
W21X83	43% flange reduction	LS	0.058			
W21X83	50% flange reduction	LS	0.058			
W21X62	20% flange reduction	IO	0.041			
W21X62	28% flange reduction	IO	0.043			
W21X62	35% flange reduction	IO	0.041	0.025	0.052	0.070
W21X62	43% flange reduction	IO	0.042			
W21X62	50% flange reduction	IO	0.042			
W18X76	20% flange reduction	LS	0.058			
W18X76	28% flange reduction	LS	0.057			
W18X76	35% flange reduction	LS	0.059	0.023	0.049	0.065
W18X76	43% flange reduction	LS	0.058			
W18X76	50% flange reduction	LS	0.060			
W14X43	20% flange reduction	LS	0.061			
W14X43	28% flange reduction	LS	0.061			
W14X43	35% flange reduction	LS	0.062	0.025	0.052	0.070
W14X43	43% flange reduction	LS	0.062			
W14X43	50% flange reduction	LS	0.062			

2.7.4 Equations to estimate the seismic design parameters

The data points in Figures 2.10 to 2.14 show that the relationship between a/b_f, b/d and c/b_f to the normalised key design parameters, do not have a tight enough correlation to propose a single equation to predict the effects of these key design parameters for different cases. Analysis of the 90 specimens in the database shows that the second moment of area for each section also influences the structural response of the elements, and therefore, can be used as a design parameter to achieve more consistent results to develop a design formula. Table 2.8 shows that the c geometry of the RBS is most influential for the design parameters considered. Figure 2.16 shows the affects c/b_f has on the normalised Key Design Parameter (KDP) multiplied by the square of the normalised second moment of area for each specific section ($\frac{KDP_{RBS}}{KDP_{FS}} * (\frac{I_{RBS}}{I_{FS}})^2$). In this case the a and b parameter are considered to be the average of the suggested upper and lower limits according to Table 2.3.

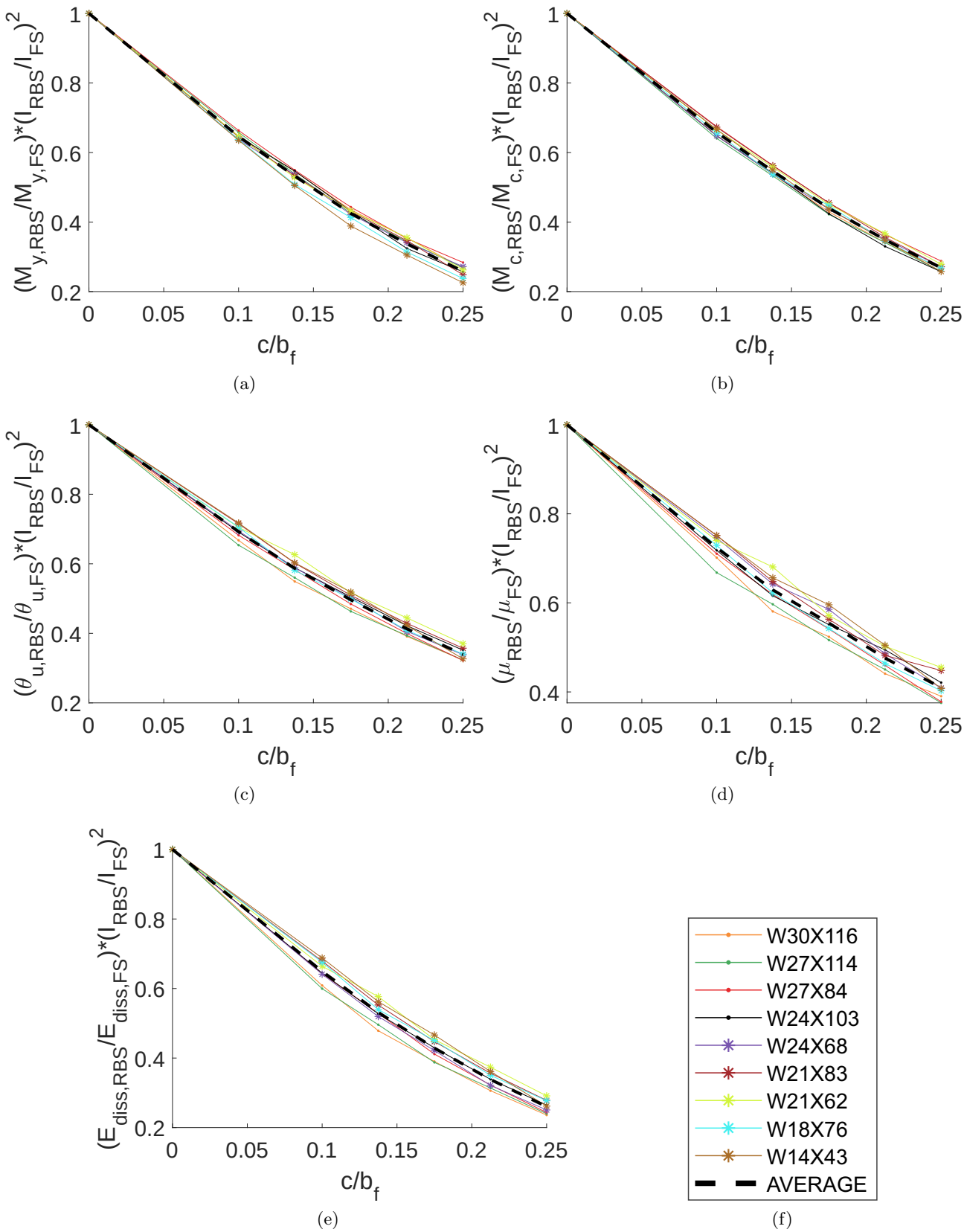

Figure 2.16: Variation of (a) $(M_{y,RBS}/M_{y,FS}) * (I_{RBS}/I_{FS})^2$ (b) $(M_{y,RBS}/M_{y,FS}) * (I_{RBS}/I_{FS})^2$ (c) $(M_{y,RBS}/M_{y,FS}) * (I_{RBS}/I_{FS})^2$ (d) $(M_{y,RBS}/M_{y,FS}) * (I_{RBS}/I_{FS})^2$ and (e) $(M_{y,RBS}/M_{y,FS}) * (I_{RBS}/I_{FS})^2$ with respect to c/b_f

As all axes in Figure 2.16 are dimensionless, quadratic curves can be fitted to the average data lines using the interactive tool MATLAB (The Mathworks Inc, 2019). The general form of these curves are shown in Equation 2.3. These fitted curves provide very good approximations of how the RBS affects the seismic design parameters of a full section (with no RBS present) for any c parameter while keeping the a and b parameter the average of the upper and lower limits. It should be noted that unlike previous data, the results in Figure 2.16 are less scattered and can be used to develop design equations as follows:

$$f\Big(\frac{c}{b_f}, \frac{I_{RBS}}{I_{FS}}\Big) = \Big(\frac{KDP_{RBS}}{KDP_{FS}}\Big) = \left[\alpha_1 \cdot \Big(\frac{c}{b_f}\Big)^2 + \alpha_2 \cdot \Big(\frac{c}{b_f}\Big) + 1.0\right] \cdot \Big(\frac{I_{FS}}{I_{RBS}}\Big)^2 \tag{2.3}$$

where the coefficients α_1 and α_2 are shown in Table 2.10 for each seismic design parameter.

However, if a and b are not considered to be the average of the upper and lower suggested limits, the approxiamtion according to the general Equation 2.3 must be adjusted depending on the influence of the a or b parameters.

When investigating the affects the geometries a and b had on the key design parameters, the c geometry was kept constant, as the average of the upper and lower limits ($35\%FR$) according to Table 2.3 and Table 2.7. When investigating the influence of the a parameter, the b parameter was set at $0.75d$. Similarity, when considering the effects of the b geometry, the a geometry was kept at $0.625b_f$. Therefore, for each key design parameter the influence of the a and b geometry for each section can be normalized for the respective section for the c geometry equal to a 35% flange reduction ($35\%FR$). These graphs are shown in Figures 2.17 and 2.18.

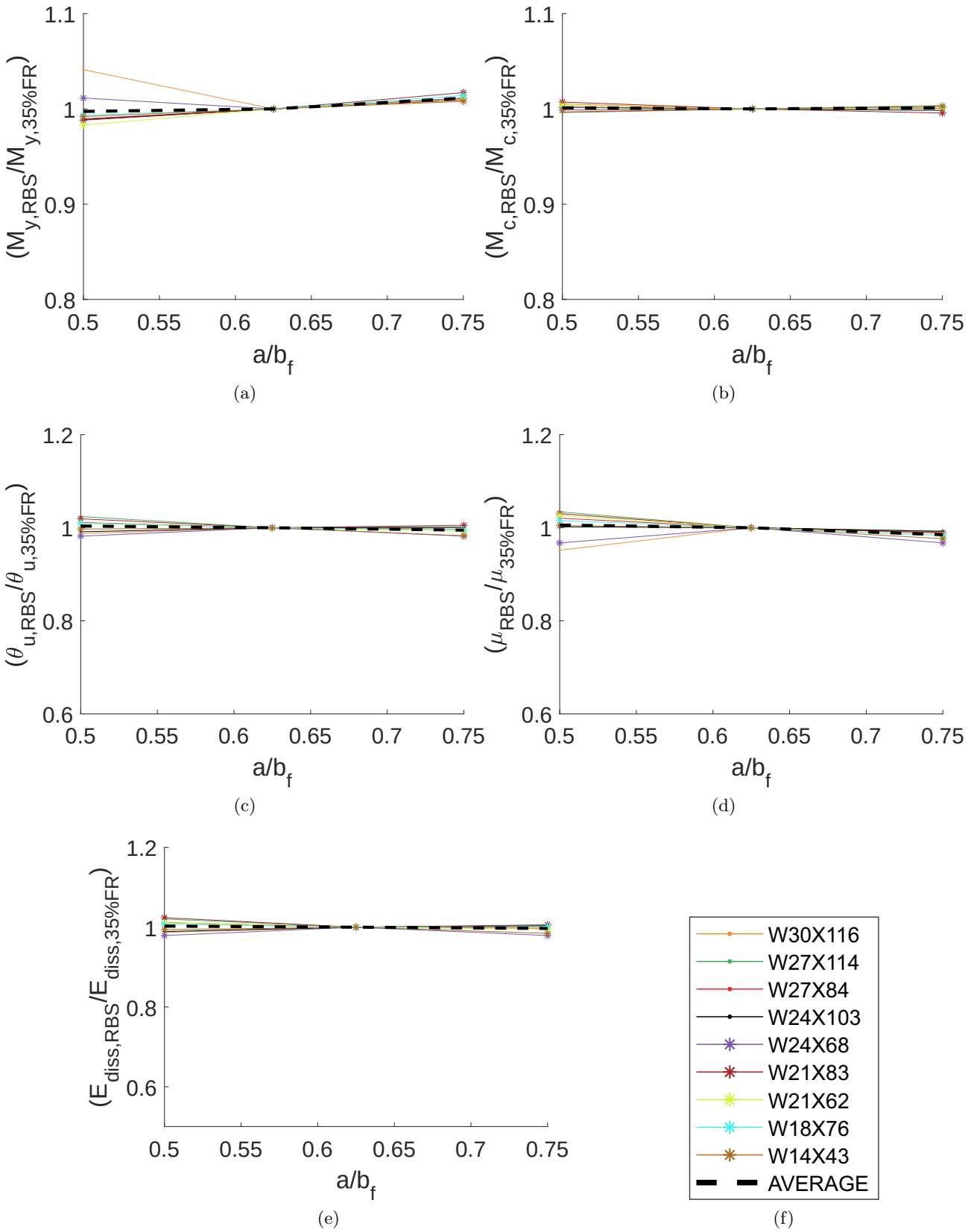

Figure 2.17: Variation of (a) $M_{y,RBS}/M_{y,35\%FR}$ (b) $M_{y,RBS}/M_{y,35\%FR}$ (c) $M_{y,RBS}/M_{y,35\%FR}$ (d) $M_{y,RBS}/M_{y,35\%FR}$ and (e) $M_{y,RBS}/M_{y,35\%FR}$ with respect to a/b_f

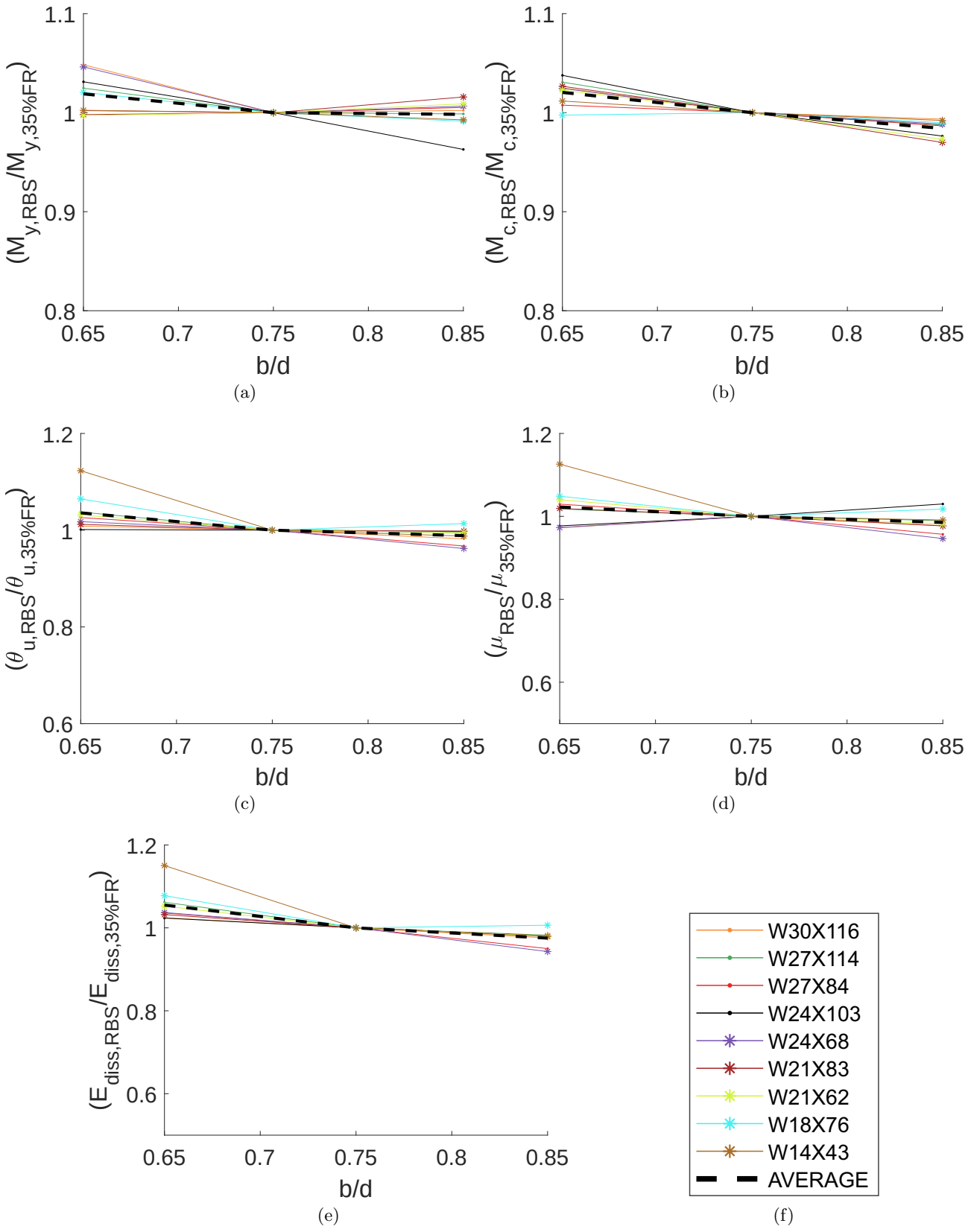

Figure 2.18: Variation of (a) $M_{y,RBS}/M_{y,35\%FR}$ (b) $M_{y,RBS}/M_{y,35\%FR}$ (c) $M_{y,RBS}/M_{y,35\%FR}$ (d) $M_{y,RBS}/M_{y,35\%FR}$ and (e) $M_{y,RBS}/M_{y,35\%FR}$ with respect to b/d

Figure 2.17 shows that the parameter a has insignificant influence on the ratio: $\frac{KDP_{RBS}}{KDP_{35\%FR}}$, with the exception of Figure 2.17a which on average increases the value of the yield moment for increasing values of parameter a by less than 5%. Therefore, when using Equation 2.3 to predict the response of an RBS connection no adjustment needs to be made to take into account the influence of the parameter a and this ratio can assumed to be equal to 1.0. This can be represented by the following equation:

$$f\left(\frac{a}{b_f}\right) = \left(\frac{KDP_{RBS}}{KDP_{35\%FR}}\right) = 1.0 \tag{2.4}$$

Figure 2.18 shows how the parameter b is more influential on the ratio: $\frac{KDP_{RBS}}{KDP_{35\%FR}}$, where noticeable changes can be observed. Therefore, an equation is required which will adjust Equation 2.3 depending on the value of the b parameter within the limits according to Table 2.3 for any section size. The process for determining these equations will be explained by using the key design parameter μ, as an example. If section W24x84 is taken from Figure 2.18d. The straight line which passes through the middle data point $0.75b/d$ is determined based on minimizing the square of the distances $Y1$ to $Y1'$ and $Y2$ to $Y2'$ according to Equation 2.5:

$$\min((Y1 - Y1')^2, ((Y2 - Y2')^2) \tag{2.5}$$

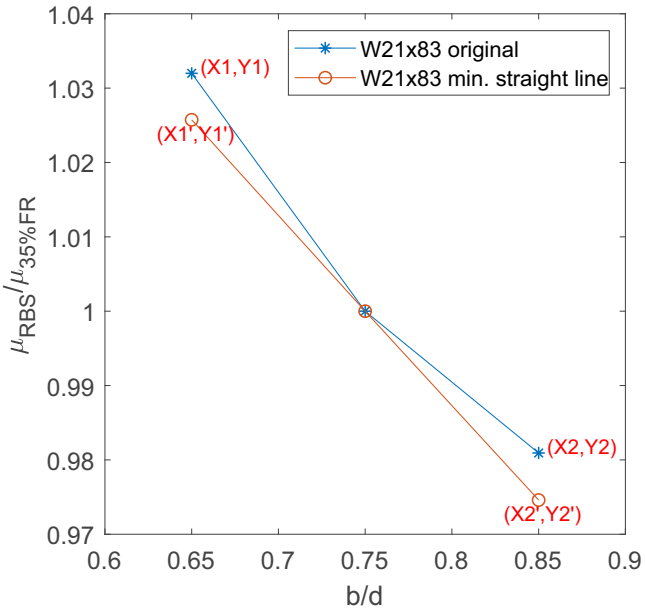

Figure 2.19: Determining the gradient of the straight line used for Equation 2.6 and 2.7

This is done for all sections for each key design parameter. The second moment of area for each full section (I_{FS}) can be plotted against the corresponding slope of each sections straight line (m) for all key design parameters. Log expressions, from Equation 2.6, are fitted to these data points in order to predict the slope of an equivalent straight line for any size section. These graphs are shown in Figure 2.20 for θ_u, μ and E_{diss}.

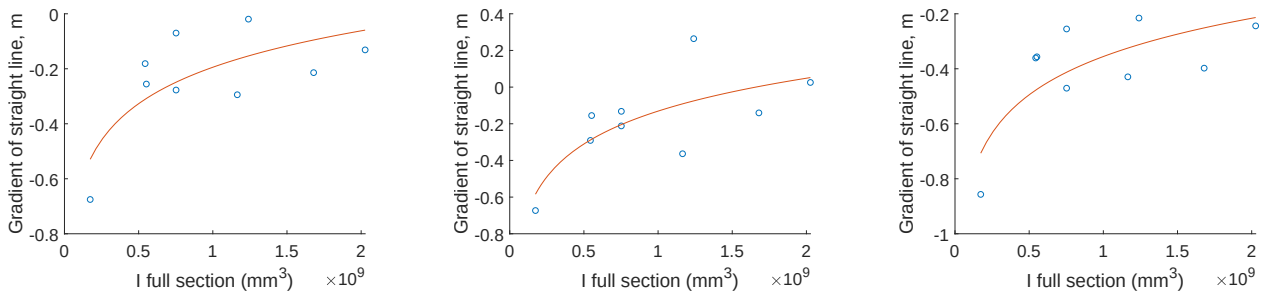

Figure 2.20: Logarithmic expressions used to determine the slope of the straight line for predicting the seismic design parameters for (a) θ_u, (b) μ and (c) E_{diss}.

No correlation or trends are found between the I_{FS} and the slope of the straight line m for key design parameters M_y and M_c. Therefore, the average slope of all section lines is used. Based on Figures 2.18 and 2.20, Equations 2.6 and 2.7 are used to adjust Equation 2.3 based on the influence of the b parameter.

$$f\left(\frac{b}{d}\right) = \left(\frac{KDP_{RBS}}{KDP_{35\%FR}}\right) = m\left(\frac{b}{d} - 0.75\right) + 1.0 \tag{2.6}$$

$$m = \beta_1 \cdot \ln(I_{FS}) + \beta_2 \tag{2.7}$$

where the coefficients m, β_1 and β_2 are shown in Table 2.10 for each seismic design parameter.

To summarise, the influence of the three RBS parameters can be represented by the Equations 2.3, 2.4, 2.6 and 2.7. Equation 2.3 estimates the seismic design parameters for a median set of RBS geometries, while Equations 2.4, 2.6 and 2.7 are correction factors for the influence of the parameters a and b on the median estimate from Equation 2.3. By multiplying these equations together, the ratio of the seismic design parameter of the RBS of interest to the seismic design parameter of the full section can be estimated. The proposed Equation 2.8, and Table 2.10 can be used to predict how the a, b and c parameters affect the seismic design parameters M_y, M_c, θ_u, μ and E_{diss} of RBS sections compared to full sections (no RBS present). Equation 2.8 presents the general equation:

$$\frac{KDP_{RBS}}{KDP_{FS}} = f\left(\frac{c}{b_f}, \frac{I_{RBS}}{I_{FS}}\right) \cdot f\left(\frac{a}{b_f}\right) \cdot f\left(\frac{b}{d}\right) \tag{2.8}$$

Table 2.10: Coefficients for Equations 2.3, 2.4, 2.6 and 2.7

Coefficient	**Key Design Parameters**				
	M_y	M_c	θ_u	μ	E_{diss}
α_1	3.93	3.37	3.07	2.75	3.89
α_2	-3.96	-3.78	-3.41	-3.05	-3.94
m	-0.104	-0.182	n/a	n/a	n/a
β_1	n/a	n/a	0.191	0.259	0.201
β_2	n/a	n/a	-4.16	-5.50	-4.52

The results of this study, in general, should prove useful in the preliminary design and assessment of RBS connections.

2.8 Conclusion

The aim of this Chapter is to develop more efficient design methodologies for the RBS connections by investigating in detail the effect of the key geometric parameters defining an RBS on their seismic performance. An FE model of two different beam column sub-assemblies was validated with two sets of experimental results from literature. The models took into account the non-linear material properties and the appropriate modelling techniques – ties, kinematic-coupling, boundary conditions, constraints – for the connection detailing. The two validated FE models predicted the ultimate strength, failure/buckling modes and loading hysteresis with high accuracy. In order to evaluate the effects of different a, b and c geometries (RBS cut parameters) on RBS connections, a comprehensive parametric analysis was conducted on a total of 90 different specimens. The effects of the three RBS geometries on the seismic design parameters Yield Moment (M_y), Peak Moment (M_c), Ultimate Rotation (θ_u), Ductility (μ) and Energy Dissipated (E_{diss}) were investigated. Based on the results in this Chapter the following conclusions can be drawn:

1. In general, all the three geometric parameters a, b and c, over the recommended ranges in ANSI/AISC 358-16 (AISC, 2016b), have influence over the seismic design parameters considered in this study but with different degrees. The parameter a has very little influence which can be considered negligible, whereas the parameter b has a small effect on the connections performance. However, the parameter c has significant influence over all the five seismic design parameters considered.

2. The adequacy of the beams achieving the three required rotational capacities (DL, SD and NC) for RBS connections according to BS/EN 1998-3 (BSI, 2005) was assessed. Results showed that all beams achieved an elastic state at the DL capacity, however, all but two beams achieved the NC rotational requirement. A direct link between the web slenderness and the ultimate rotation was established, where beams with a web slenderness larger than 54 could not accommodate the NC requirement.

3. The rotations of the beam at the column face were compared to the performance limits of ASCE/SEI 41-17 (ASCE, 2017a). Results showed that all beams achieved the IO level with only 4 beams achieving the LS performance level. None of the beams achieved the CP performance level. All beams apart from W27X84 and W24X68 which have a web slenderness larger than 54, satisfied the ANSI/AISC 358-16 (AISC, 2016b) and FEMA 350 (SAC Joint Venture, 2000a) requirement to accommodate over 4% inter-storey drift.

4. Design equations were developed in order to predict how the RBS geometric parameters a, b and c effect the key seismic design parameters compared to full section properties (no RBS present). Links were determined between the second moment of area, dimensions of the RBS geometries and the beams properties. This is particularly useful for design purposes, as the cyclic performance and seismic design parameters of RBS connections can be estimated without the need for complex and time consuming cyclic experimental or FE analysis.

Chapter 3

Development of More Accurate Cyclic Hysteretic Models to Represent RBS Connections

As a result of the conclusions drawn in Chapter 2 more accurate cyclic hysteresis models for RBS connections were developed in this chapter. This chapter is based on the paper titled: Development of More Accurate Cyclic Hysteretic Models to Represent RBS Connections, submitted to Journal of Engineering Structures dated 07/02/2021[1]*. It should be noted this chapter reads as a standalone paper. It may repeat sections previously introduced in this thesis.*

3.1 Abstract

The concept of Reduced Beam Section (RBS) connections in steel framed buildings have been widely adopted in the European and American Design codes (EN1998-3, ANSI/AISC 358-16 and FEMA 350) as a means of providing safe ductile fuse behaviour in the beam in order to protect the column from any significant damage. However, modelling the hysteretic behaviour of beam-column joints under earthquake excitations can be challenging due to the non-linear complex behaviour as a result of strength and stiffness degradation. Currently there is no comprehensive model available for RBS connections which is capable of considering all the design parameters that affect performance. This chapter presents a database of detailed and accurate modified-Ibarra-Krawinkler models that can reliably capture the cyclic hysteresis behaviour of fully welded RBS connections over a range of different RBS geometries. First a validated Finite Element (FE) model was developed using ABAQUS to accurately predict the cyclic hardening and strength degradation of steel RBS connections by capturing the local web and flange buckling. Then a comprehensive parametric study of 1480 different American wide flange RBS and Full Section (FS) beams loaded to $0.07rad$ of cyclic loading was conducted. These models were created through Python coding which automatically generated and meshed the FE models. These models were subsequently submitted to ABAQUS through the interactive software Matlab for FE analysis. The results of this study should prove useful in seismic design and assessment of RBS connections. The results were used to assess the influence of different RBS design parameters on the structural performance of the connections. It was shown that the conventional method of predicting the modified-Ibarra-Krawinkler model parameters cannot accurately capture the actual hysteresis behaviour of some RBS connections and may lead to unreliable results. The inaccuracy of the conventional equations used to predict the modified-Ibarra-Krawinkler model parameters are a result of the wide range of different RBS connections considered in the multivariable regression analysis used to determine the predictive equations. In this Chapter, only one type of connection is considered

[1] I. Aduzayed contributed to the development of the Python macro code

- welded unreinforced welded web (WUF-W) connection – this removes any variation due to different types of connections exhibiting a range of connection stiffness. The cyclic results from the FE analysis were calibrated with simple equivalent beam representations in the Open System for Earthquake Engineering Simulation programme – OpenSees. This model featured the bilinear modifield-Ibarra-Krawinkler zero length spring in order to capture the cyclic deterioration of the connection. The calibration process utilised the bisector optimization method and was controlled using Matlab. As a result of this work, a comprehensive database of 1480 different beams provides: 1) the beams full cyclic moment-rotation-hysteresis at the plastic hinge location up to $0.07rad$ rotation following the SAC loading protocol, 2) appropriate modifield-Ibarra-Krawinkler parameters to accurately capture the beams cyclic response in OpenSees, for non-linear dynamic analysis. The results of this study should prove useful in seismic design and assessment of RBS connections.

3.2 Introduction

3.2.1 Background

Reduced Beam Section (RBS) connections are widely adopted within seismic resistant steel moment frames in order to 1) combat the risk of brittle fractures in the connections 2) absorb seismic energy through yielding and 3) protect columns from damage. The seismic performance of steel structures has been studied extensively by many researchers (Ibarra and Krawinkler, 2005; Kim and Kim, 2009; Asgarian et al., 2010; Jalali et al., 2011, 2012; Wang et al., 2017; Lemonis, 2018). In general, the results of these studies indicate the good capability of RBS connections achieving these targets.

Full scale tests on steel frames have been conducted by a number of researchers (Chung et al., 2011; Lignos et al., 2011a; Ke and Chen, 2016). Chung et al. (2011) conducted full scale tests on 4 storey two span steel frames with reinforced concrete (RC) slabs under long-period ground motion. The performance of welded unreinforced flange welded web (WUF-W) and welded unreinforced flange bolted web (WUF-B) connections were compared. Test results showed that WUF-B had a lower ductility with WUF-W possessing a larger rotational capacity (up to four times WUF-W). Similarly, Lignos et al. (2011a) conducted two full scale tests on scaled 1:8 4 storey bare steel moment frames in order to get a better understanding for collapse prediction and P-Delta effects in such systems. They successfully calibrated a model to predict the response of the tested structure and highlighted how the deterioration characterises – in particular the post-capping rotational capacity – of critical members in the analytical frame must be accurately represented for collapse prediction. In another study, Wang et al. (2017) used performance-based design to asses a 35 storey pre-Northridge steel moment frame using non-linear response analysis. Probabilistic checks were carried out on collapse prevention (CP) and immediate occupancy (IO) under two hazard levels according to FEMA 351 (FEMA-351, 2000) and FEMA P-58 (Federal Emergency Managment Agency, 2018). Results showed that the buildings failed to meet the CP for both hazard levels considered, where around 30% of the connections failed. The results of their study highlighted the importance of retrofitting existing tall buildings to reduce the amount of damage and inevitable costs following an earthquake.

Ke and Chen (2016) conducted a full scale test on a 2 storey two bay high strength steel moment resistant frame with a novel 2 storey one bay RBS energy dissipating system designed to absorb all damage. Calibrated models for the elements were then used for two 6 storey frame systems – one incorporating the idea of utilizing an RBS energy dissipating system and one without RBS connection – under non-linear dynamic analysis. The RBS energy dissipating system improved the frames performance, sustaining smaller residual and maximum drifts. Kitjasateanphun et al. (2001) compared the effects of two different RBS models on the seismic response of two 3 storey RBS and non-RBS frames. The first model comprised two non-prismatic elements representing the RBS whereas the

second model idealised the RBS as a rotational spring. The affects in the panel zones were investigated using time history analysis. Findings by Kitjasateanphun et al. (2001) showed that the panel zone has a significant influence on the inelastic behaviour of both RBS and non-RBS steel frames. In particular, the distribution of plastic deformation in RBS, beams and panel zones are affected. The two methods of modelling the RBS gave similar results under moderate earthquake excitations, however, it was shown that careful consideration must be given to the modelling methods when the frame is subjected to strong earthquakes. Similarly, Steneker and Lydell (2016) explored through incremental dynamic analysis (IDA) how the effects of detailed and simple (rigid) panel zone modelling affected a 10 storey RBS steel moment resistant frame and concluded that the difference in demand parameters was not significant unless a collapse assessment is required. Jones et al. (2002) also conducted cyclic tests on eight double sided RBS connections looking at strong, medium and weak panel zones. Test results showed that the weak panel zones gave the most stable cyclic response.

Ghassemieh and Kiani (2013) employed non-linear dynamic analysis on 4, 8 and 16 storey RBS frames to investigate the influence of the flexibility of beam to column connections on the frames performance. Inter storey drifts, total drifts, storey shears and shear deformations were considered as quantifying parameters. Non-linear analysis showed that modelling the flexibility of the RBS connection leads to moment redistribution in the beams which decreased the demands in the beams and columns. Shear force in the column and beam ends was reduced as well as the shear demand and distortion in the panel zone. In another study, Nikoukalam and Dolatshahi (2015) conducted a single span single storey finite element analysis to evaluate the performance of RBS fuse shear links with three different span arrangements and concluded that smaller frame span to depth ratios have a higher equivalent plastic strain and shorter plastic hinge lengths. Their findings confirm that the span to depth ratio of steel moment frames can significantly influence the seismic response of steel frames.

The dynamic behaviour of RBS steel moment frames was studied by Chen et al. (1997) and Carter and Iwankiw (1998) in order to demonstrate their higher energy dissipating capabilities compared to pre-Northridge steel frames. The high energy absorbing characteristics of RBS steel frames has been also demonstrated in more recent studies by (Jin and El-Tawil, 2005; Ashrafi et al., 2009; Kildashti and Mirghaderi, 2009; Seo et al., 2010; Nikoukalam and Dolatshahi, 2015; Montuori, 2016; Maleki et al., 2018, 2019). Lignos et al. (2011b) compared non-linear dynamic and non-linear static analysis of 3, 4 and 8 storey three bay special RBS steel moment frames. By comparing storey drifts, shear forces and over turning moments, they concluded that for reliable and accurate quantification of demand parameters non-linear dynamic analysis is necessary. Ashrafi et al. (2009) investigated the effect reduced web sections had on 4, 8 and 16 storey special moment frames using finite element analysis for five different reduced web layout configurations within the frame and concluded that RBS connections can improve the frames performance even though they are not located throughout the structure. Jin and El-Tawil (2005) aimed to develop a better understanding of RBS frame seismic behaviour by modelling 4, 8 and 16 storey frames under non-linear dynamic analysis and reported excellent seismic performance with smaller than anticipated panel zone deformations. Kildashti and Mirghaderi (2009) confirmed the findings by Jin and El-Tawil (2005) through non-linear dynamic analysis of 4 and 8 storey frames with and without RBS connections. The direct comparisons of maximum displacements and inter storey drifts between frames with and without RBS connections showed that the RBS frame performance improved with increasing earthquake ground motion intensity. Their study highlighted that RBS frames reduced the permanent displacements of steel frames which was more prominent for taller frame systems. These results ((Ashrafi et al., 2009; Jin and El-Tawil, 2005; Kildashti and Mirghaderi, 2009)) were confirmed by Montuori (2016).

Seo et al. (2010) proposed a new and improved design method for bolted RBS connections through non-linear time history analysis. Three special moment frames of 3, 9 and 20 stories were evaluated

for two different hazard levels. The life safety (LS) and collapse prevention (CP) performance-based criteria were used for performance assessment. The improved bolted RBS connection achieved a higher CP level compared to the conventional bolted RBS connection. Similarly, Maleki et al. (2018, 2019) investigated the performance of 4 and 16 storey steel moment perimeter frames incorporating welded unreinforced flange (WUF), RBS and drilled flange (DF) connections through incremental dynamic and fragility analysis. The maximum storey drift angle was used to evaluate frame performance. Results showed that the RBS and DF frames sustained three times the intensity measures (a measure of seismic strength) of the WUF frame. The results of Maleki et al. (2018, 2019) highlighted the superior performance of RBS and DF frames when considering the probability of collapse for immediate occupancy (IO) and collapse prevention (CP) performance criteria, while DF frames exhibited the best seismic performance.

Many researches have also conducted frame analysis to investigate the effects of new and novel fuse systems incorporated within the frame system. Nikoukalam and Dolatshahi (2015) conducted single span single storey FE analysis to evaluate the performance of an RBS and a novel hybrid shear fuse link under cyclic loading. Results showed that the RBS and novel shear link gave similar responses, with the novel shear link providing a higher ductility capacity in the frame. These findings were also confirmed by Mahmoudi et al. (2019). A similar study carried out by Kalehbasti and Dolatshahi (2018) investigated a novel shear fuse incorporated within a moment resisting frame. Two 1 storey one bay frames were compared, one utilizing the novel shear fuse and one with ordinary RBS connections and showed that the novel shear fuse had a smaller damage index and expended lower damage for increasing drifts compared to the RBS frame. However, the RBS frame did dissipate more energy at the cost of suffering larger strength loss compared to the shear fuse. Two, 6 storey steel moment frames incorporating self centring moment resistant mechanisms and ordinary welded RBS connections were also compared by Guan et al. (2018) using incremental dynamic analysis. The RBS frame showed 40% larger lateral load carrying capacity and provided a higher collapse resistance, but sustained larger lateral drifts compared to the self centring frame.

3.2.2 Modelling the cyclic behaviour of RBS connections

In order to assess the collapse of structures using simulated programs and software such as OpenSees (Mazzoni et al., 2007; McKenna, 2011), it is essential to be able to accurately represent the cyclic behaviour of steel beams and beam-to-column connections for the non-linear dynamic analysis of frames. Representation of a beams local flange and web buckling using an appropriate non-linear model is essential for predicting the beams inelastic behaviour and to capture the stiffness and strength degradation for cyclic and dynamic analysis. Jalali et al. (2012) compared the performance of 3, 7 and 15 storey perimeter moment frames which incorporated and disregarded strength degradation of the connections. As expected, ignoring strength degradation of the connections led to underestimates of the buildings performance and unrealistic estimations of safety. This was especially prominent for performance-based design considering the Collapse Prevention (CP) criteria. Bravo-Haro and Elghazouli (2018) also conducted incremental dynamic analysis on 54 multi-storey frames, specifically considering the effects of degrading or non-degrading models within the frame systems. Results showed that for the frame systems that incorporated degradation, residual drifts are considerably higher. The drift demand also increased with the number of stories with concentrated demands in the lower levels. Bravo-Haro et al. (2018) conducted a similar study but investigated the chord rotations in the beams, and showed that the frame systems incorporating degradation captured the concentrated seismic demands which led to the development of early plastic mechanisms. They concluded that the influence of degradation is significant at both the design level and collapse prediction of frame systems. In another relevant study, Tsitos et al. (2018) investigated 12 steel moment resistant frames under incremental dynamic analysis, with and without degradation effects incorporated in the frames

behaviour. The findings highlighted again the importance of having models that can accurately predict the strength degradation of connections for evaluating the frame performance.

According to Bosco and Tirca (2017), there are currently three widely adopted methods for modelling the non-linear behaviour of beams and beam-column-connections. These are 1) a non-linear beam model with distributed plasticity across the beam length, 2) a non-linear beam model with concentrated plasticity within a finite plastic hinge length and 3) an elastic beam model with concentrated non-linear rotational springs at either end.

A common way to model the non-linearities of a beam is using a non-linear beam model with distributed plasticity across the beam length. In this model, a force-based beam column element is integrated to determine the non-linear material response. In the distributed plasticity method, plastic hinges can form anywhere along the beam where the moment is at a maximum and the beams fibres enter the non-linear range. The behaviour of the section or beam is based on the original fibre model by El-Tawil and Deierlein (1998). Scott and Fenves (2006) provide an example of the distributed plasticity model, by using a force based beam-column element using the standard Gauss-Labatto integration rule, allowing the plasticity to initially spread through the element. They found that for the hardening section behaviour, the element response, in general, converged. However, for softening section behaviour and at localised deformations, a unique solution may not exist which leads to a loss of objectivity. This is due to the response of the element changing based on the number of integration points rather than the length of the element.

In order to overcome the loss of objectivity as described in Bosco and Tirca (2017) and Scott and Fenves (2006), Scott and Fenves (2006) suggested that the beam should be modelled as three pieces, with concentrated plasticity within a finite plastic hinge length. They developed a new two point Gauss-Radu plastic hinge integration method that can provide exact integration for an element with a linear curvature distribution. Push over analysis results of a simple frame from Scott and Fenves (2006) showed that this new plastic hinge integration method can be used to accurately model the behaviour of the element. These findings led to a finite length hinge model that used a plasticity formulation with specified hinge sections at the ends of the beam. This method is referred to as *Beam With Hinges* and has been applied in many finite element software packages such as OpenSees effectively.

Bosco and Tirca (2017) and Deierlein et al. (2010) proposed two general methods to determine the behaviour of the non-linear *Beam With Hinges* as either: having non-linear moment curvature relationships or explicit fibre section integrations that enforce the assumption that plane sections remain plane. Comparisons of these different plastic hinge integration methods can be found in Scott and Fenves (2006). Ribeiro et al. (2015) provided a good example of a plastic hinge integration method that uses the moment curvature behaviour in distributed plasticity formulations, where similar to Scott and Fenves (2006), the modified Gauss-Radau integration method is used. Bosco and Tirca (2017) also used a fibre cross section discretization at the plastic hinge along with the modified Gauss-Radu integration method to capture the strength and stiffness deterioration for a sections flanges.

In the case of an elastic beam model with concentrated non-linear rotational springs at either end, the rotational springs are usually modelled with phenomenological models (Chisari and Rizzano, 2018). There are many different types of advanced phenomenological models that are useful for defining hysteretic relationships that can replicate the non-linear attributes of a connection or beam including the yielding, strength degradation, stiffness degradation, softening and pinching phenomena. The most common eight phenomenological models are 1) Takeda model by Takeda et al. (1970), 2) Basic Hysteretic model based on the modified Colugh model by Mahin and Bertero (1976) (Mahin

and Bertero (1976) modified the origional Clough model proposed by Clough and Johnston (1966)), 3) Bouc-Wen model by Bouc (1967) and later modified by Wen (1976), 4) Ramberg-Osgood model by Ramberg and Osgood (Ramberg and Osgood, 1943), 5) Richard-Abbot model (Richard and Abbott, 1975), 6) Pivot model by Dowell et al. (1998), 7) SHM Sivaselvan-Reinhorn model (Sivaselvan and Reinhorn, 2000) which is a variation of the model proposed by Bouc (1967) and modified by Wen (1976) and 8) Ibarra-Krawinkler model by Ibarra et al. (2005).

3.2.3 The modified Ibarra-Krawinkler hysteretic model

In this study, the modified Ibarra-Krawinkler (mIK) model is adopted to simulate the cyclic response of RBS connections. More information about this method is provided in the next section. Chisari and Rizzano (2018) highlight the four widely accepted numerical phenomenological models implemented in software packages as the simple hysteretic, Bouc-Wen, Sivaselvan-Reinhorn and modified Ibarra-Krawinkler. Three different sets of tests on both hot rolled and cold formed steel were performed in order to compare the different models to these experimental results more details of the experimental results can be found in D'Aniello et al. (2012). The four different models were calibrated to the experimental results using a calibration procedure based on the minimization of response misfit, presented in Chisari et al. (2017).

In literature, the most widely adopted method for modelling steel moment frames at the element or global level is the concentrated non-linear rotational spring method incorporating the Ibarra-Krawinkler phenomenological model (Lignos et al., 2011b). Previous work carried out by Ibarra et al. (2005) showed that existing concentrated non-linear spring models for representing the hysteretic behaviour of elements were not able to incorporate strength degradation with increasing cycles. As a result, Ibarra et al. (2005) developed a new model which could capture the four main deterioration models of a cyclic hysteresis, including, Basic Strength Deterioration, Post-Capping Strength Deterioration, Unloading Stiffness Deterioration and Accelerated Reloading Stiffness Deterioration. Three variations of the modified Ibarra-Krawinkelr (mIK) model named Bilinear, Peak-Orientated and Pinching were developed, Ibarra et al. (2005). The most appropriate and widely used model to represent hot rolled steel beam-column connections at the local and global level is the mIK Bilinear model, which has been implemented recently by the following researchers (Lignos et al., 2011b; Ghassemieh and Kiani, 2013; Ke and Chen, 2016; Lemonis, 2018; Tsitos et al., 2018; Bravo-Haro and Elghazouli, 2018; Maleki et al., 2019).

The mIK model by Lignos and Krawinkler (2007) was an improvement on the original Ibaara-Krawinkler model with more sophisticated ways used to define the models parameters (more details of these improvements can be found in (Lignos and Krawinkler, 2007; Lignos, 2008; Ibarra and Krawinkler, 2005; Lignos and Krawinkler, 2012).) The mIK model has strength bounds established by a monotonic backbone curve. From this initial backbone curve, the models cyclic hysteretic performance (strength degradation with increasing cycles) is defined by a set of rules depending on the model selected (bilinear, peak-orientated or pinching). The rate of deterioration for the four different modes (basic strength deterioration, post-capping strength deterioration, unloading stiffness deterioration and accelerated reloading stiffness deterioration) are controlled based on specified parameters. However, the parameters which define the mIK model need to be taken as an initial estimate and calibrated with cyclic experimental data (Lignos and Krawinkler, 2012).

Lignos (2008) describes how the parameters which define the mIK model can be estimated using multivariable regression analysis equations determined from a database of experimental results (Lignos and Krawinkler, 2007). This database was produced by Lignos and Krawinkler (2007), and has over 200 steel experimental results obtained from literature. A Matlab tool produced by Lignos and

Krawinkler (2007) calibrated the experimental results against the mIK model in order to determine the model parameters. Two different categories of connections were defined in order to determine three different sets of multi-variable regression equations, covering both conventional and RBS. However, the equations proposed by Lignos (2008) are based on a range of different connection types and experimental set ups taken from literature (shown in Appendix A of (Lignos and Krawinkler, 2012)). Even though the data is split into two different categories (each category is split into two sub categories depending on the depth of the beam), these categories have too many variables and varying parameters which will affect the connections response to cyclic loading. The first category, defined as RBS connections, incorporates a wide range of different connection types and configurations as well as different RBS flange reduction geometries.

The existing data for RBS connections only accounted for 73 out of the 200+ experimental results from the database (Lignos and Krawinkler, 2007, 2011), showing the limited number of data which the regressional equations in (Lignos, 2008) are based on. The equations proposed by Lignos (2008) are only based on the size of RBS from the experimental tests considered, and therefore, do not consider the RBS geometrical parameters which can effect their cyclic hysteresis behaviour (Horton et al., 2021b). These equations that represent the parameters for the mIK model cannot be applicable for sections not included in the experimental tests, and may lead to unreliable results and potentially affect the performance of the designed system (Horton et al., 2021b).

3.2.4 Research significance

This study aims to address research gaps identified in the previous section by developing a better understanding about the hysteretic behaviour of RBS connections, leading to more accurate representative models. A comprehensive analytical study is conducted using experimentally validated detailed finite element models to investigate the effects of RBS geometric parameters on the structural performance of the connections. To achieve this, 1480 individual RBS beam sections were analysed under cyclic loading up to $0.07rad$. The database of cyclic results for the finite element study, was then calibrated with simple zero-length spring models representing the cyclic behaviour of the RBS through the modified-Ibarra-Krawinkler (mIK) model. This database of calibrated mIK parameters (which define the beams cyclic behaviour) was analysed extensively, and the influence of the key RBS geometrical parameters on the calibrated mIK values was investigated. The efficiency of the highly accurate calibrated parameters in this study were then demonstrated by comparisons with predictive parameters using the widely adopted equations suggested by Lignos and Krawinkler (2011). It is shown that ignoring the effects of RBS geometric parameters in the existing models can lead to very inaccurate predictions.

In this Chapter an extensive literature review has been conducted, followed by a summary of the widely adopted method of representing the cyclic performance of RBS connections in Section 3.3. Section 3.4 presents the validated FE model including the methodology used for an extensive parametric study into the cyclic response of 1480 different beam specimens. Section 3.5 presents the results of this extensive parametric study. The results from this parametric analysis were calibrated with a simple mIK model and discussed in detail in Section 3.6. A discussion on the effects of RBS geometries on these cyclic results and comparison with the existing models are given in Section 3.7. A summary of the key points in this Chapter can be found in Section 3.8.

3.3 Methodology

3.3.1 Basics of the modified Ibarra-Krawinkler (mIK) Bilinear model

The mIK Bilinear model, which will be considered in this study, has an initial strength bound defined as the backbone curve of the model as shown in Figure 3.1a. This backbone curve is represented by three strength parameters and four deformation parameters listed in Table 3.1 (explained in more detail in Sections 3.3.2 to 3.3.5)). Using this backbone curve as the initial strength bound, the set of rules defined by the Bilinear model (Ibarra et al., 2005) controls the hysteretic behaviour of the model through three different deterioration modes. These deterioration modes (shown in Figure 3.1b) for the Bilinear model, are defined as Basic Strength Deterioration, Post-Capping Strength Deterioration and Unloading Stiffness Deterioration. These modes can be activated once the yield point for the model has been surpassed and energy has been dissipated. In this study the mIK Bilinear model will be utilised for non-linear dynamic analysis using OpenSees Software (Mazzoni et al., 2007; McKenna, 2011).

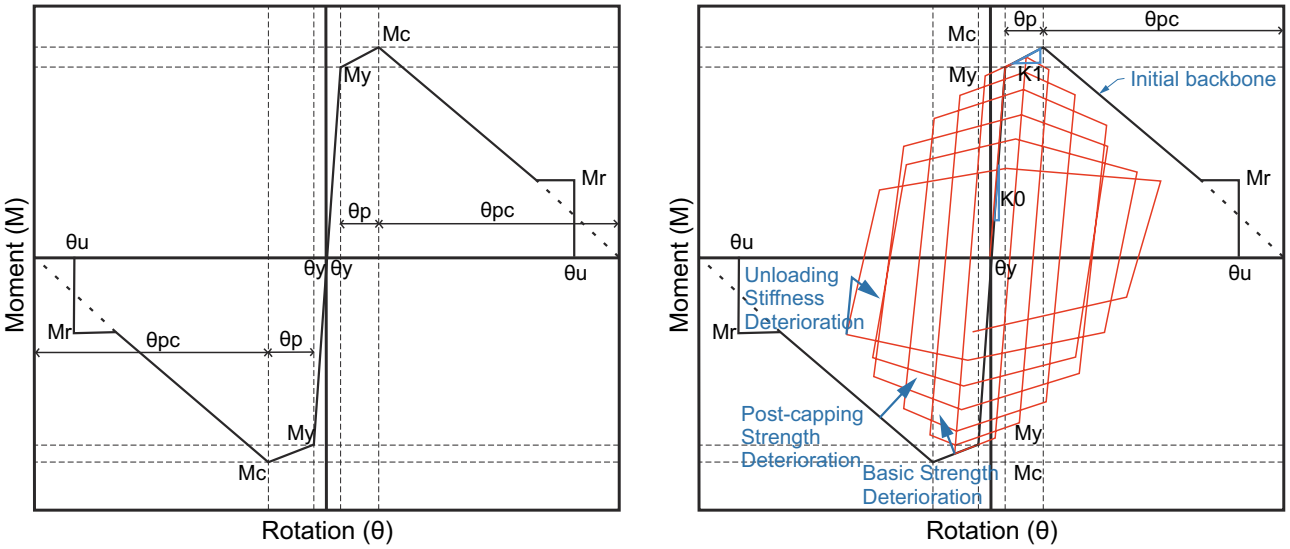

Figure 3.1: (a) Backbone curve used to define the initial strength bounds of the mIK model, and (b) Depiction of the three deterioration modes for the mIK bilinear model

Table 3.1: Definition of the mIK parameters which define the backbone curve

Symbol	Definition
M_y	Effective yield moment
M_c	Capping moment strength
$M_r = \kappa \cdot M_y$	Residual moment
θ_y	Yield rotation
θ_p	Pre-capping plastic rotation
θ_{pc}	Post capping plastic rotation
θ_u	Ultimate rotational capacity
$K0$	Initial elastic stiffness
$K1$	Pre-capping stiffness

3.3.2 The Effective Yield Moment and Capping Moment Strength

The mIK model cannot replicate kinematic hardening of the steel during the cyclic analysis. Therefore, in order to account for the kinematic hardening effects, the Yield Moment and Peak Moment of the RBS connection are increased by a factor. These values are defined as the Effective Yield Moment (M_y) and Capping Moment Strength (M_c), respectively, and are shown in Figure 3.1b.

3.3.3 Initial elastic stiffness

The Initial Elastic Stiffness ($K0$) is defined as the Effective Yield Moment (M_y) divided by the Yield Rotation (θ_y) as shown in Equation 3.1.

$$K0 = \frac{M_y}{\theta_y} \tag{3.1}$$

3.3.4 Strain hardening ratio

The Strain Hardening Ratio (as) of the model is defined as the ratio of the Pre-Capping Stiffness ($K1$) to the $K0$. Equation 3.2 shows how the strain hardening ratio is calculated.

$$as = \frac{K1}{K0} = \frac{\frac{M_c - M_y}{\theta_p}}{K0} = \frac{M_c - M_y}{K0 \cdot \theta_p} \tag{3.2}$$

3.3.5 Cyclic deterioration parameters for the three deterioration modes

For the three modes of deterioration – Strength, Post-Capping Stiffness and Unloading Stiffness – a defined parameter, λ, controls the rate at which each specific mode deteriorates with increasing cycles. This parameter has a value ≥ 0. A value of exactly zero would disable this mode of deterioration. Values larger than zero will enable the specific mode of deterioration, the larger the λ parameter the slower the rate of the deterioration mode. It should be noted that each of the three modes can have its own specific deterioration parameter. However, for simplicity in this Chapter, the same deterioration parameter is adopted for all deterioration modes.

3.3.6 RBS connections and geometry

ANSI/AISC 358-16 (AISC, 2016b) specifies acceptable ranges of geometries which define the RBS connection dimensions. These ranges, shown in Table 3.2, are based on the beam depth (d) and the width of the beam flange (b_f). Figure 3.2 shows how the geometries of RBS connections are defined for a typical I beam to column connection.

Table 3.2: The RBS geometry limits taken from ANSI/AISC 358-16, parameters a, b and c are defined in Figure 3.2

RBS geometry	Limits
a	$0.5b_f \leq a \leq 0.75b_f$
b	$0.65d \leq b \leq 0.85d$
c	$0.1b_f \leq c \leq 0.25b_f$

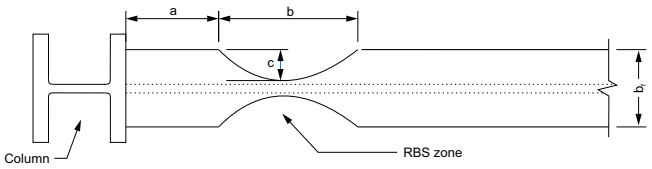

Figure 3.2: The geometries which define a typical beam-column RBS connection

Previous work carried out in Chapter 2 has shown that the geometries a, b and c have influence over the key seismic design parameters – Yield Moment (M_y), Peak Moment (M_c), Ultimate Rotation (θ_u), Ductility (μ) and Energy Dissipated (E_{diss}). The a parameter influence was considered to be negligible, while the b parameter had a small affect on connection performance. These preliminary results showed that the c parameter has the most significant influence over the key seismic performance parameters of RBS connections. Therefore, in this study, the effects of the b and c RBS geometries on the cyclic hysteresis of Welded Unreinforced Flange Welded Web (WUF-W) RBS connections will be extensively investigated.

3.4 Finite Element (FE) analysis

In this study the welded unreinforced welded web (WUF-W) connection is assume to be connected to an infinitely strong column which represents a very strong panel zone. Therefore, in order to asses the beams response under cyclic loading, the beams boundary conditions were fully fixed at one end and free at the other end (point of contraflexture) to replicate this connection. Figure 3.3 represents the general modelling procedures used for this numerical study.

It should be noted that for modelling the global response of a connection the panel zone effects should be taken into account using a suitable model such as the widely adopted scissors model (Gupta and Krawinkler, 1999; Ibarra and Krawinkler, 2005). However, in this chapter, the focus is restricted to the influence of the reduced beam section geometry on connection response. Therefore, the effects of the panel zone or column behaviour were deliberately excluded in order to isolate the effect of RBS geometry changes. By modelling the RBS to a fixed boundary, the effects of varying the RBS geometry can be clearly seen without the potentially beneficial effects of the column or panel zone affecting the response. It should be noted that a similar approach has been widely used by other researchers to assess the structural behaviour of connections (Mojtabaei et al., 2021; Phan et al., 2020; Ye et al., 2020).

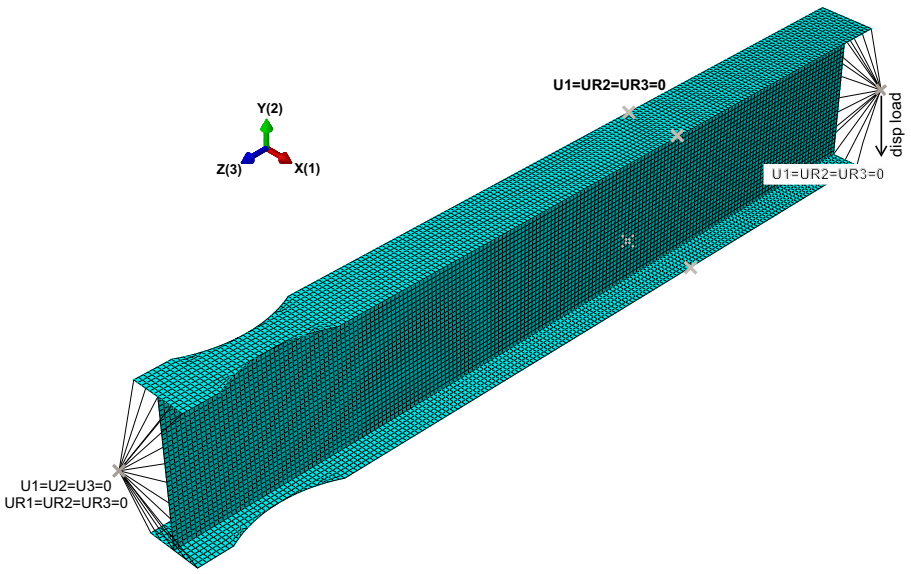

Figure 3.3: Example of the adopted FE model for an RBS connection showing the relevant boundary conditions

Reduced Integration (four noded) Shell S4R elements were used to model each beam section. Each model was meshed with a $20mm$ meshing size throughout the entire beam section. This did increase the computational time compared to adopting a coarser mesh in areas where buckling did not occur,

however, for simplicity of Python coding to automatically generate the models, the same mesh was adopted throughout the section. Lateral restraints in the form of boundary conditions were applied to the edge flange nodes at a distance of 2500mm from the fixed end as shown in Figure 3.3. This prevented potential out of plane buckling of the section during the analysis. A static-general analysis with non-linearity accounted for was selected for all the FE models, this was due to the assumption that the loading was applied slowly. All nodes at the tip of the beam were coupled to a reference point. A displacement based load, following the SAC loading protocol (SAC Joint Venture, 2000a), was applied to this reference point.

A combined model consisting of non-linear isotropic and kinematic strain hardening using the Von Mises yield surface and associated flow rule was adopted to capture the plasticity behaviour of the section. Calibration of the two pairs of parameters which define the model were based on the coupon test results provided in Nia et al. (2013) and Lee et al. (2005). The first pair of parameters – Q and b – define the maximum size of the yield surface and the rate of change of the yield surface respectively. For the second pair of parameters, C_k defines the initial kinematic hardening modulus and γ_k defines the rate of change of C_k with increasing strains. The effects of geometrical imperfections were considered to be negligible for hot rolled steel sections.

3.4.1 Validation of model

In order to validate the FE model, two full scale beam-column sub assemblies were modelled in the general purpose non-linear finite element (FE) software package ABAQUS. The specimens DC-S and DB700-SW were selected from Nia et al. (2013) and Lee et al. (2005), respectively. Specimens DC-S and DB700-SW were loaded according to SAC loading (SAC Joint Venture, 2000a) and AISC loading (AISC, 2016a) up to $0.06rad$, respectively.

The DC-S connection by Nia et al. (2013) was a built up welded unreinforced welded web connection to a box column. The connection consisted of continuity plates which were connected to the box column by fillet and complete penetration welds. The beams web and flanges along with the shear plate were groove welded to the column. The shear plate was fillet welded to the beam web. These welds were all modelled with appropriate tie commands. Figure 3.4a shows the connection set along with the dimensions. The same FE modelling techniques described in Section 3.4 were implemented. The material properties were taken from the mechanical properties obtained from coupon tests (Nia et al., 2013). Good agreement with the tests results can be observed in Figure 3.4b, which compares the force-rotation hysteresis of the test and FE model. Comparisons between the FE model and experimental tests at 6%, shown in Figures 3.4c and 3.4d, shows the local buckling of the flange being captured.

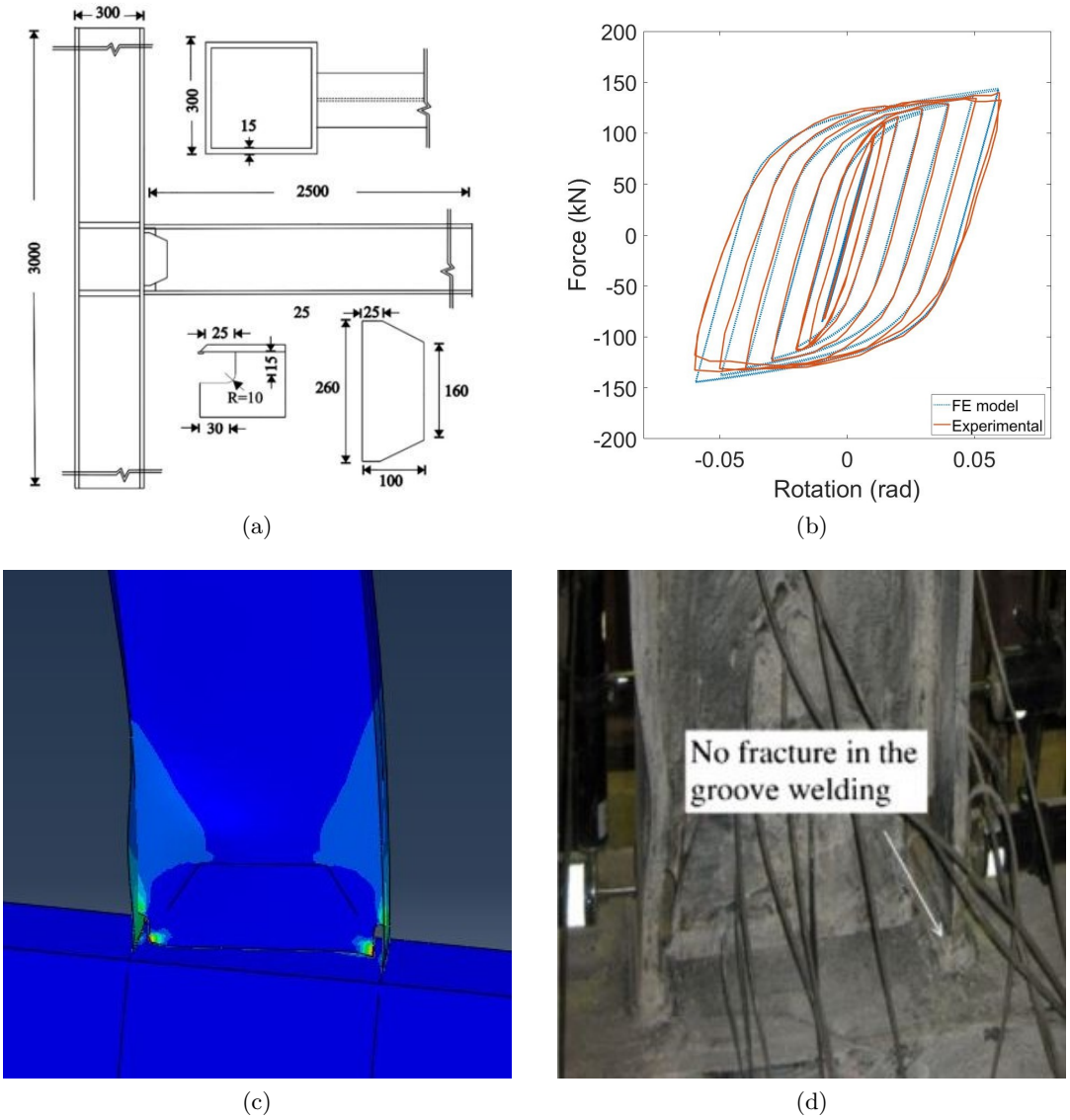

(a) (b)

(c) (d)

Figure 3.4: (a) Connection set up of the DC-S specimen tested by Nia et al. (2013), (b) Comparisons of the force-rotation between the FE model and experimental results, (c) Local buckling of the flange in the FE model, and (d) Observed buckling of the flanges at 6% drift from the experimental tests.

The DB700-SW fully welded unreinforced welded web (WUF-W) reduced beam section (RBS) tested in Lee et al. (2005) was also modelled in order to verify the FE models capability of predicting the strength degradation via local buckling at the plastic hinge region. It should be noted that the local buckling does not prevent the development of a plastic hinge/zone. The test set up consisted of a H700x300x13x24 beam welded to a H428x407x20x35 column. Complete penetration welds were used for connecting the flanges of the beam to the column, while fillet welds were used for connecting the flanges to the beam web. Figure 3.5a shows the full beam-column sub assembly. This connection was modelled following the procedures mentioned in Section 3.4. Combined hardening parameters were determined from the mechanical properties of the coupon tests by Lee et al. (2005). Figure 3.5b compares the moment-rotation graphs obtained in this study and the experimental results of the DB700-SW connection reported by Lee et al. (2005). The results are normalised to the plastic moment of the section (M_{pn}). Very good agreement can be found between the FE model and experimental data, which shows that the strength degradation of the connection could be accurately captured.

Figure 3.5c also shows how development of the plastic hinge, due to local web and flange buckling, is consistent with the buckling observed in the experimental tests shown in Figure 3.5d at 6% drift.

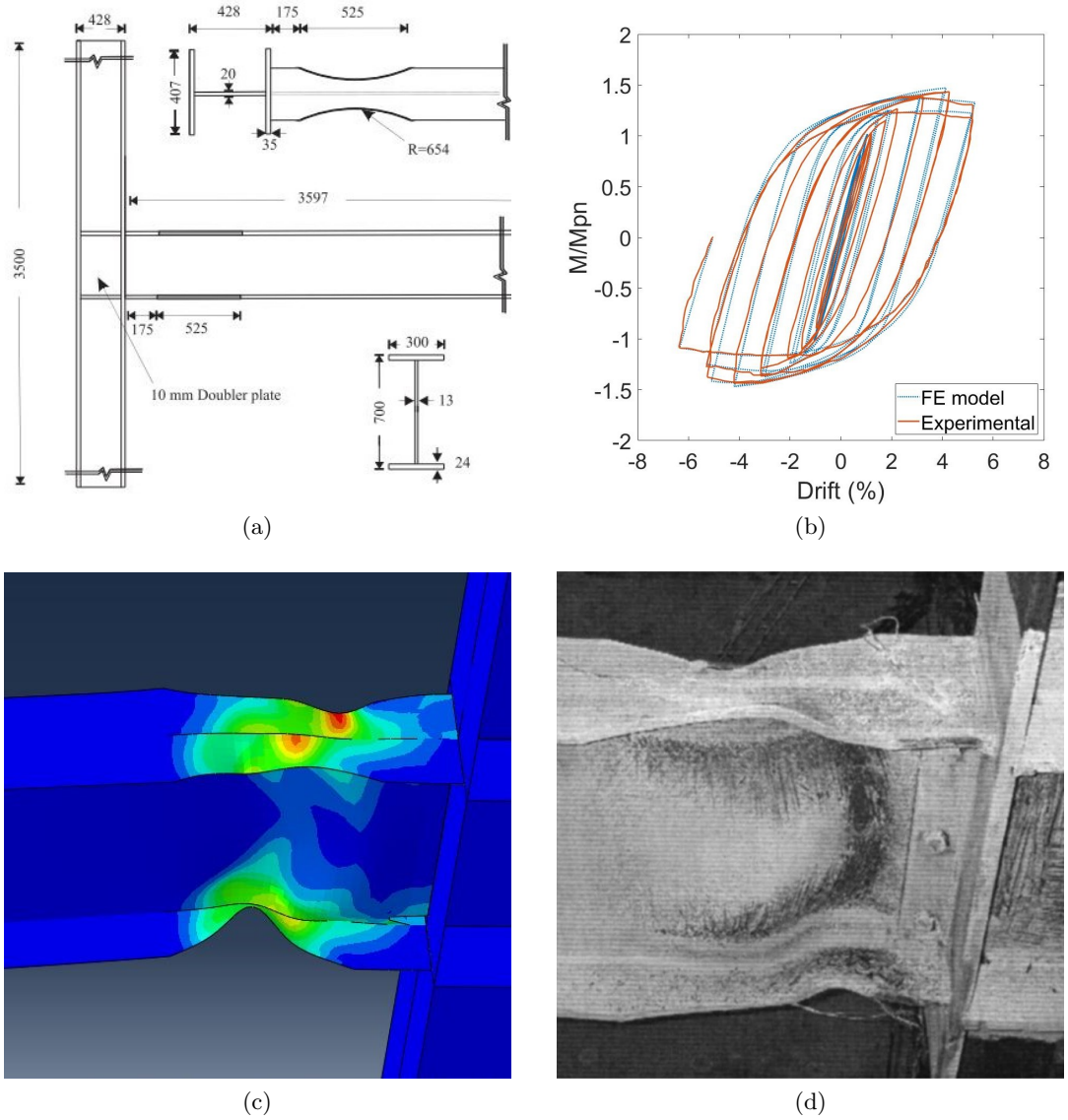

(a) (b)

(c) (d)

Figure 3.5: (a) Connection set up DB700-SW WUF-W connection tested by Lee et al. (2005), (b) Comparisons of the normalized moment rotation between the FE model and experimental results, (c) Buckling of the flanges in the FE model, and (d) Similar buckling observed in the experimental results by Lee et al. (2005)

3.4.2 Comprehensive parametric analysis

In order to asses the effects the b and c RBS geometrical parameters have on the cyclic hysteresis behaviour and calibrated parameters of the modified-Ibarra-Krawinkler (mIK) model, an extensive parametric study was conducted on 1480 different beam specimens. Table D.0.1 in Appendix D shows the 148 different American Wide Flange Beams that were selected for the analysis. For each beam section (shown in Table D.0.1), nine different RBS beams and one full beam section (no RBS present) were analysed. These nine different sizes of RBS beam were based on the recommended AISC limits in (AISC, 2016b) and are shown in Table 3.3.

Table 3.3: Different RBS geometries for each beam section modelled in the parametric analysis

American Wide Flange	RBS Geometry		
	a	b	c
Section 1	0	0	0
Section 2	$0.625b_f$	$0.65d$	$0.175b_f$
Section 3	$0.625b_f$	$0.70d$	$0.175b_f$
Section 4	$0.625b_f$	$0.80d$	$0.175b_f$
Section 5	$0.625b_f$	$0.85d$	$0.175b_f$
Section 6	$0.625b_f$	$0.75d$	$0.100b_f$
Section 7	$0.625b_f$	$0.75d$	$0.138b_f$
Section 8	$0.625b_f$	$0.75d$	$0.175b_f$
Section 9	$0.625b_f$	$0.75d$	$0.213b_f$
Section 10	$0.625b_f$	$0.75d$	$0.250b_f$

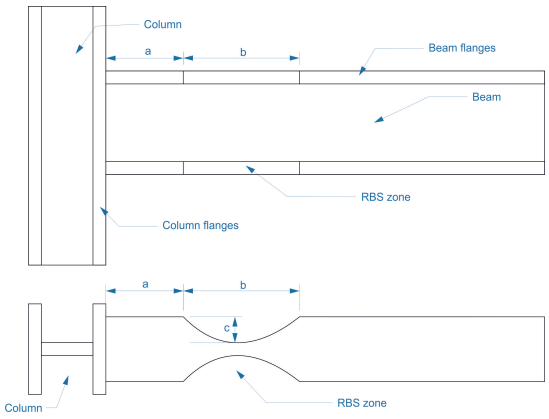

Figure 3.6: Definition of RBS geometries

A Python macro script was developed that could automatically generate the FE model for any specific beam section where values of d, b_f, t_f and t_w were specified along with its corresponding RBS parameters (a, b and c). By defining an input file containing the 1480 different section properties for analysis, the interactive tool MATLAB was used to generate a FE model for each section (using the coded Python macro script) and submit to ABAQUS for FE analysis. MATLAB automatically extracted the results of each beam and saved them to a database for further analysis.

3.5 Parametric analysis results

The cyclic hysteresis results for each beam section were presented as moment-rotation graphs at the location of the plastic hinge (at a distance of $a + b/2$ from the face of the column). In general, the database could be split into two main groups, buckling or non-buckling sections. The sections were categorized on whether they buckled or did not buckle under the displacement based loading up to two cycles of $0.07rad$. Figure 3.7 shows two general examples for these classifications in the database. Figure 3.7a clearly shows how the beam section does not buckle and continues to harden after yielding up to a loading of $0.07rad$. Whereas, Figure 3.7b demonstrates buckling occurs after kinematic hardening up to the peak moment. After this, a reduction in strength of the section with increasing cycles was observed.

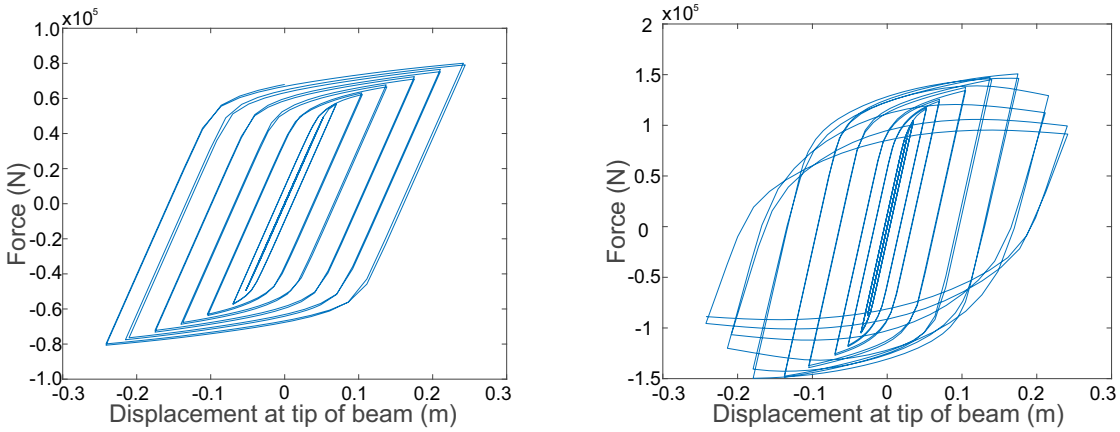

(a) (b)

Figure 3.7: (a) Specimen taken from the database to show how non-buckling was categorised, and (b) An example of a model from the database to demonstrate buckling of a section

3.5.1 Influence of the c parameter on the buckling behaviour

The buckling behaviour of the sections in the database can be categorized into different groups using the slenderness of the web (λ_{web}) for each section according to BS/EN 1993 (British Standards Institute, 2005). By considering sections from the database where only influence of the c parameter was considered (sections 6, 7, 8, 9 and 10 from Table 3.3), Figure 3.8a shows how sections with a web slenderness (λ_{web}) less than 24.0 did not buckle. In general, Figure 3.8b shows sections with a $24.01 < \lambda_{web} < 34.0$ tended not to buckle, whereas sections with a $34.01 < \lambda_{web} < 47.0$ tended to buckle (shown in Figure 3.8c). Figure 3.8c also suggests that for $34.01 < \lambda_{web} < 47.0$, the larger the c geometry the more likely the section is to buckle. Figure 3.8d shows how all sections with a $\lambda_{web} > 47.01$ buckled. Generally, the sections with a larger λ_{web} had a greater chance of developing local buckling as expected.

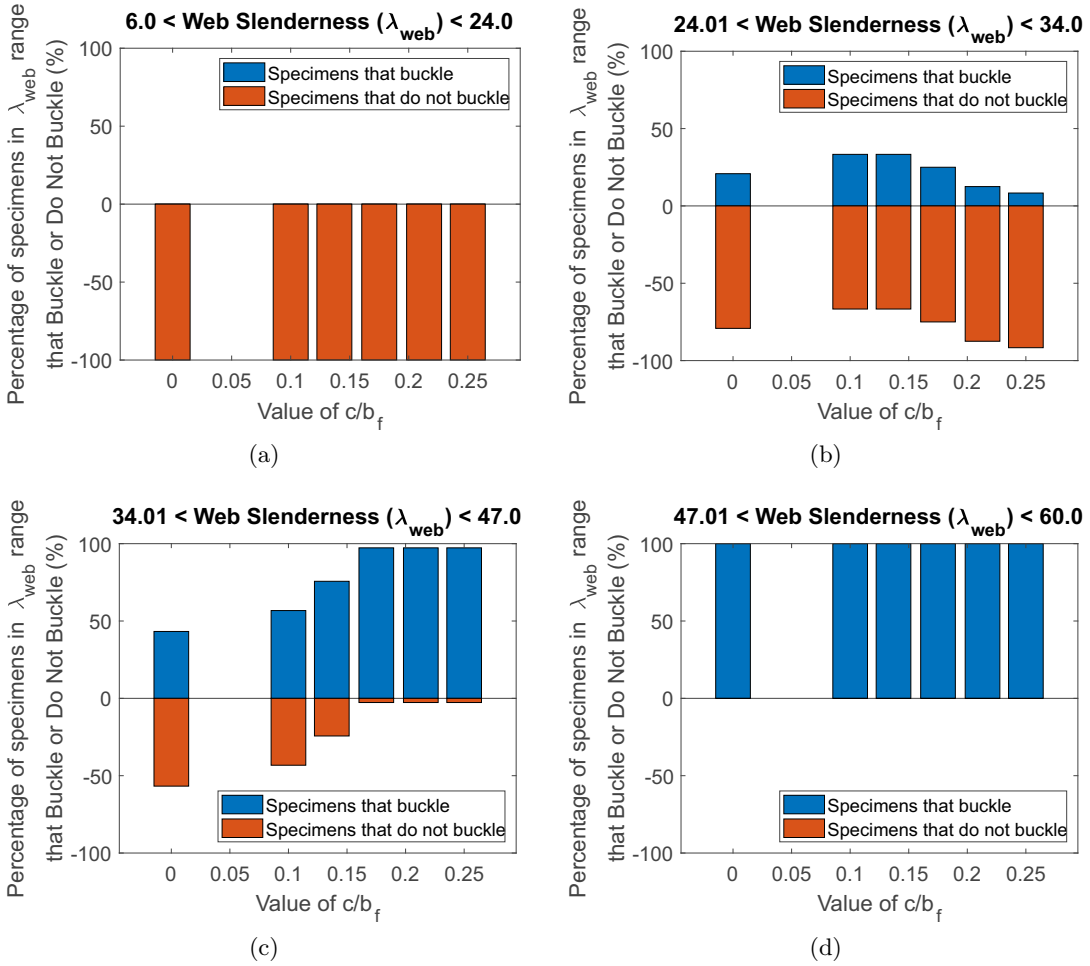

Figure 3.8: Categorization of database specimens – where the influence of c geometry has been considered – for (a) $6.0 < \lambda_{web} < 24.0$, (b) $24.01 < \lambda_{web} < 34.0$, (c) $34.01 < \lambda_{web} < 47.0$, and (d) $47.01 < \lambda_{web} < 60.0$ with respect to c/b_f

3.5.2 Influence of the b parameter on the buckling behaviour

By considering only the effect of the b geometry on the specimens from the database (sections 1, 2, 3, 4 and 8 from Table 3.3 – keeping $c/b_f = 1.75$), they can be grouped into 4 different groups depending on the slenderness of the web. Figures 3.9a to 3.9d show how many specimens in each group buckled for varying values of b/d – a measure of the length of the RBS cut – for each web slenderness group. In general, similar to the previous case, the bar charts show that for a larger λ_{web} the specimens are more likely to buckle.

In general, the results of this study indicate that the influence of the RBS geometry tends to have no effect on whether the specimens buckle except for beams with $34.01 < \lambda_{web} < 47.0$. Figures 3.8c and 3.9c suggest that for $34.01 < \lambda_{web} < 47.0$ the presence of an RBS cut with varying b and c values is more likely to buckle compared to a full section beam (no RBS present). This can be attributed to the fact that generally sections with a larger web slenderness have a dominant failure mode due to buckling of the web, and by cutting the flanges on these sections, the stresses and strains are increased within the web leading to buckling at a lower load level.

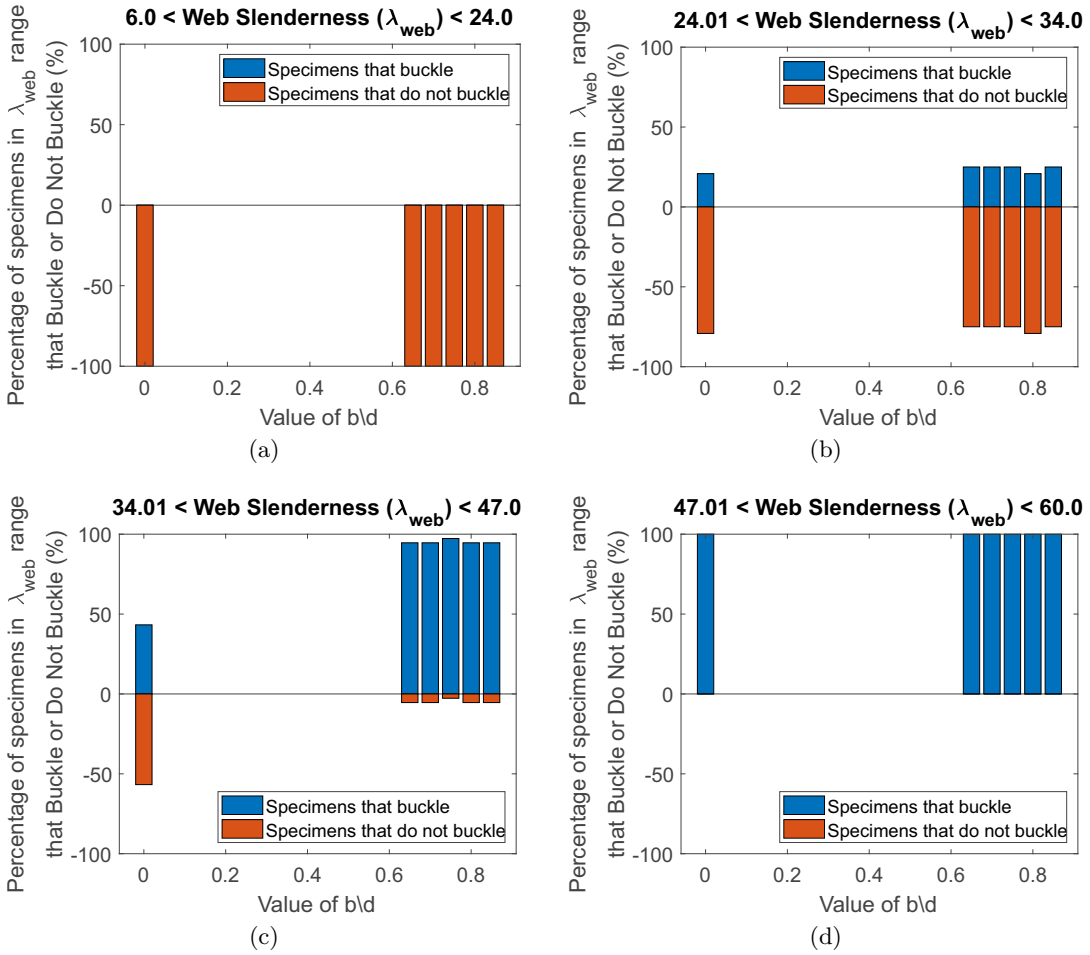

Figure 3.9: Analysis of the database only considering the influence of geomtry b to categorize the buckling behaviour for λ_{web} ranges (a) $6.0 < \lambda_{web} < 24.0$, (b) $24.01 < \lambda_{web} < 34.0$, (c) $34.01 < \lambda_{web} < 47.0$, and (d) $47.01 < \lambda_{web} < 60.0$ with respect to the value of b/d

3.5.3 Ultimate rotation of the specimens

The Ultimate Rotation (θ_u) for each connection was defined according to FEMA 350 (SAC Joint Venture, 2000a). The value of θ_u was taken as the corresponding rotation when a 20% drop in strength from the Peak Strength was reached on the sections cyclic skeleton backbone curve (using the same method described in Chapter 2). In some cases a 20% drop was not achieved after the $0.07rad$ of displacement based loading was completed. So, in order to determine the θ_u, the cyclic skeleton backbone curve was extrapolated until a 20% drop was reached. However, in a few cases, the section had not lost enough strength to be able to extrapolate the cyclic skeleton backbone curve to determine a reliable approximation for θ_u. These cases were disregarded from Figure 3.10 along with the sections that did not buckle. Figure 3.10 shows some general trends for the θ_u for all RBS and full section (FS) beams in the database. In general, it can be noted that the θ_u does not change significantly over the range of sections in the database.

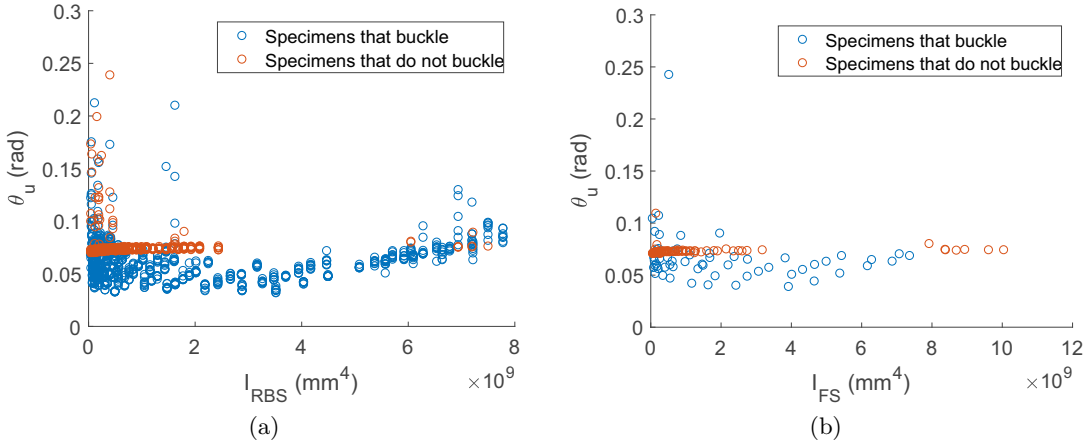

Figure 3.10: The Ultimate Rotation (θ_u) at the RBS location for variations in the (a) I_{RBS} for all RBS sections and (b) I_{FS} for all full sections (FS)

3.6 Calibration of results with bilinear modified-Ibarra-Krawinkler (mIK) model in OpenSees

In this section equivalent mIK spring models are calibrated in order to generate simplified models which are capable of representing the strength degradation of RBS sections in the database. For each of the 1480 different beam sections in the database subjected up to $0.07rad$ of cyclic displacement based loading, an equivalent simple beam model using the program *Open System for Earthquake Engineering Simulation* – OpenSees (Mazzoni et al., 2007) was generated. This model consisted of an elastic beam section with the same elastic mechanical properties as the respective FE model and a mIK Bilinear zero length spring which represented the RBS of the beam. This type of concentrated spring modelling has been used widely by many researchers (Maleki et al., 2018; Guan et al., 2018; Bravo-Haro and Elghazouli, 2018; Tsitos et al., 2018; Lignos et al., 2011b).

The same boundary conditions and displacement based loading that was implemented in the FE model was used. Figure 3.11 shows the adopted simple model. An interactive script was developed in Matlab (The Mathworks Inc, 2019) using the bisector method to calibrate the models automatically. In beam sections where buckling did not occur under the loading applied, the mIK parameters could be taken directly from the cyclic hysteresis, further explanation is given in Section 3.6.2. However, in the buckling cases, the mIK values for θ_{pc}, λ and as (defined in Equation 3.2) needed to be calibrated – more details are provided in Section 3.6.3.

Conventional mIK models aim to capture the cyclic behaviour by changing the monotonic backbone curve using parameters to predict the envelope of the actual cyclic response. However, in this study the actual cyclic response of the beam from a validated FE model has been used directly. Using the cyclic envelope directly will lead to a more reliable and accurate model for use in non-linear dynamic analysis, especially in the case of elements with stiffness and strength degradation.

3.6.1 Modelling assumptions

As the beam specimens used in the FE analysis are bare steel beams, the positive and negative sides of the cyclic hysteresis can be assumed to be symmetric for simplicity. According the ASCE/SEI 41-17 (ASCE, 2017a), the acceptance criteria for the plastic rotations of reduced beam sections for collapse prediction (CP) is given as $0.07 - 0.00030d$, where d is the depth of the beam. Therefore,

for simplicity, in non-linear dynamic analysis if the rotations are larger than $0.07rad$ one can assume collapse or failure of the connection when analysing a frame under seismic excitations. Using $0.07rad$ as the maximum damage criteria for RBS connections under CP, each simple beam model in OpenSees was loaded up to a displacement base loading of $0.07rad$ according to the SAC loading protocol. As mentioned before, there were two general categories of sections in the database sections that buckled or sections that did not buckle after $0.07rad$ of loading. In cases where the sections buckled, θ_u was taken as described in Section 3.5.3. In cases where the sections did not exhibit buckling after the $0.07rad$ loading cycle was completed, θ_u was taken $0.07rad$ as rotations larger than this value can be considered to have failed in terms of the required structural performance.

Appropriate values for the other parameters that define the mIK Biliner model were taken based on common modelling assumptions used by other researchers (Ibarra and Krawinkler, 2005; Lignos and Krawinkler, 2011). The c empirical parameter (reasonable values between 1.0 and 2.0 (Ibarra and Krawinkler, 2005)), which defines the rate of deterioration, was taken as 1.0 after Ibarra and Krawinkler (2005); Lignos and Krawinkler (2011). A unit value would enforce a constant rate of deterioration whereas a higher value (up to 2.0) would speed up deterioration in later cycles while slowing down the rate of deterioration in earlier cycles. The elastic stiffness amplification factor – nFactor – helps to avoid numerical instability problems and minimize problems with a changing moment gradient in the beam during non-linear dynamic analysis and spurious damping moments. The nFactor for this study was taken as 10.0 after Ibarra and Krawinkler (2005). Different rates of deterioration can be considered in the positive and negative side of the cyclic hysterisis by controlling the parameter D which has a range of $0 < D^{+/-} \leq 1$. In this study D is considered to be 1.0 ($D = 1.0$) since the cyclic hysterisis response is symmetric in both directions. The residual strength ratio κ for both directions has been taken as 0.4 after Lignos and Krawinkler (2011). However, generally for all connections in this database, the θ_u is achieved before the residual strength of the connection is reached. Therefore, this assumption does not effect the presented results.

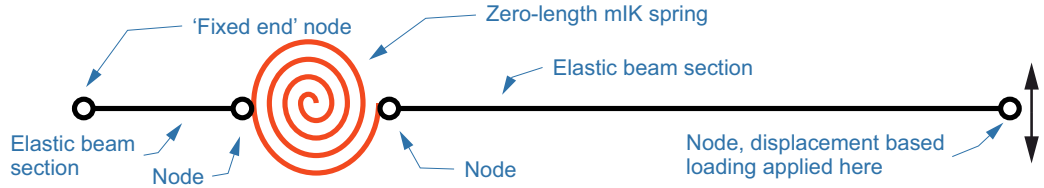

Figure 3.11: The equivalent zero-length spring model for a typical section from the database

In the following sections, more detailed information is provided on the calibration process for the buckling and non-buckling cases.

3.6.2 Non-Buckling case

For the non-buckling cases the mIK parameters can be taken directly from the cyclic hysteresis. As the specimens in this group do not exhibit buckling the deterioration mode (λ) can be set to zero ($\lambda = 0.0$). The other values of θ_p, θ_u, as and $K0$ shown in Figure 3.1 and Equation 3.2 could be taken directly from the hysteresis curves. The values for θ_{pc} could be set to arbitrary values because the connection was considered to have failed at θ_u before it reached this part of the model. Examples of three different calibrated non-buckling beams are shown in Figure 3.12.

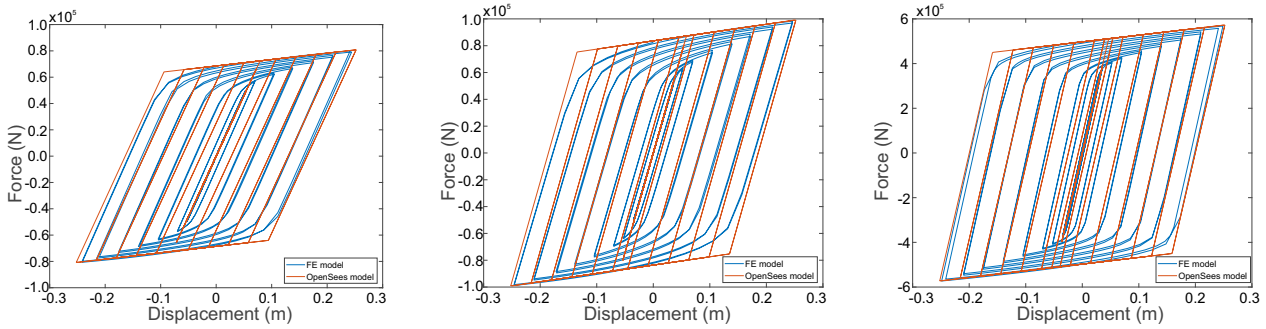

Figure 3.12: Examples of 'calibrated' models taking mIK values straight from the cyclic hysteresis for non-buckling cases, showing (a) W8x48, (b) W10x54, and (c) W18x119, American Wide Flange Sections.

The calibrated as and θ_p values are shown in Figure 3.13 with respect to the web slenderness. Not much scatter can be seen which shows that as and θ_p are practically independent from h/t_W for this category of RBS connections.

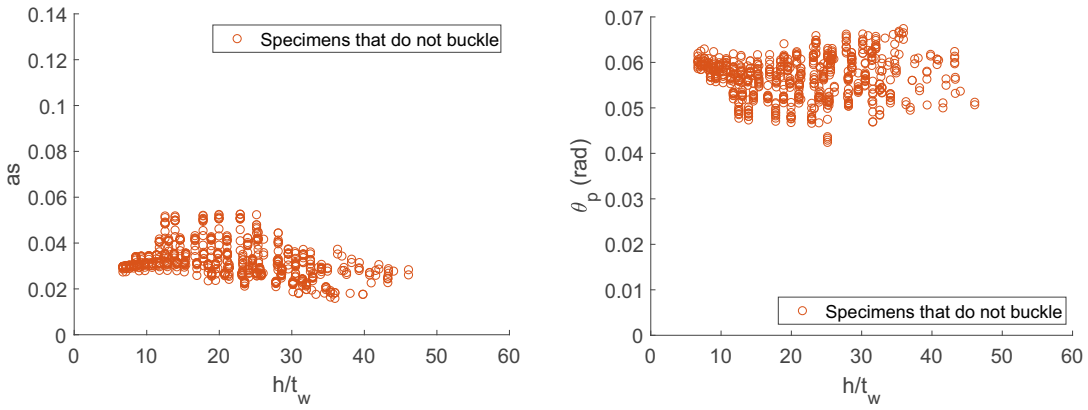

Figure 3.13: Values of mIK for non-buckling specimens for (a) as, and (b) θ_p with respect to h/t_w.

3.6.3 Buckling case

In the buckling cases of RBS beams, an interactive Matlab programme (The Mathworks Inc, 2019) was used to calibrate λ, as and θ_{pc} mIK parameters using the bisector method to converge on the optimal values. Firstly, the λ parameter was calibrated. To do this, the first loop of the cycle where θ_u occurred was extracted from the cyclic FE hysteresis. This loop was then used to match the corresponding first loop of the θ_u cycle in the OpenSees model within a 5% tolerance. Subsequently, the strain hardening ratio, as, was calibrated by adjusting the M_c value (M_y, $K0$, and θ_p in Equation 3.2 are taken directly from the FE results) to within a 5% tolerance. Finally, the θ_{pc} value was calibrated by adjusting the post capping stiffness and comparing the corresponding residual strength of the beam at the θ_u rotation for both models. Examples of three different calibrated buckling beams are shown in Figure 3.14.

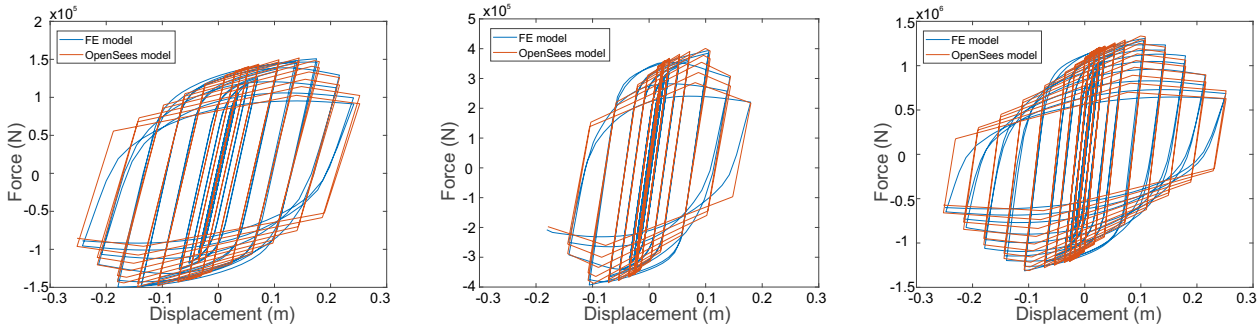

Figure 3.14: Examples of calibrated buckling sections for (a) W16X50, (b) W27x84 and (c) W36x210, American Wide Flange Sections.

In order to demonstrate this bisector calibration process, beam specimen W18X35 with average RBS geometries a, b and c was selected for a step by step example. Initial estimates of all parameters were chosen based on the validated FE results of the corresponding beam section. As discussed above, the λ parameter was calibrated first. An upper–bound, middle–bound and lower–bound solutions of λ was estimated. In order to determine a best fit, the first loop of the cycle where θ_u occurred was extracted from the cyclic FE hysteresis and used as a means of measure. In order to determine a best fit, a selected number of force and displacement values between the FE model and OpenSees model were minimised. Figures 3.15a, 3.15b and 3.15c below show the initial upper–bound, middle–bound and lower–bound results respectively for the first iteration. Figure 3.17a shows the fit of last loop of the cyclic hysteresis extracted for the middle–bound where θ_u occurred for the first iteration.

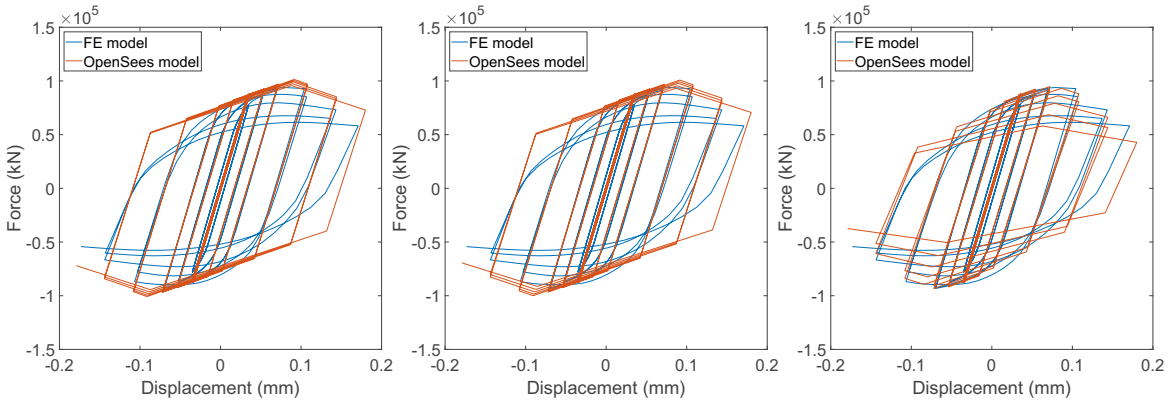

Figure 3.15: (a) Upper–bound, (b) middle–bound and (c) lower–bound solutions for the first iteration of calibration for RBS W18X35.

Figure 3.15 clearly shows that the solution lies between the middle–bound (Figure 3.15b) and the lower–bound (Figure 3.15c). Therefore, in the next iteration step, the middle–bound for the first iteration becomes the upper–bound for the second iteration, the lower–bound for the first iteration is still the lower–bound for the second iteration and a new middle–bound is selected for the second iteration. The bisector iteration process is thus repeated until a tolerance of within 5% is achieved for the fit of the last loop of the cyclic hysteresis. In this case, 5 iterations were required to achieve the specified tolerance.

Results for iteration 2 (Figures 3.16a, 3.16b and 3.16c), 3 (Figures 3.16d, 3.16e and 3.16f), 4

(Figures 3.16g, 3.16h and 3.16i) and 5 (Figures 3.16j, 3.16k and 3.16l) are shown in Figure 3.16. The fit of last loop of the cyclic hysteresis extracted for the middle–bound where θ_u occurred, for the respective iterations is shown in Figure 3.17.

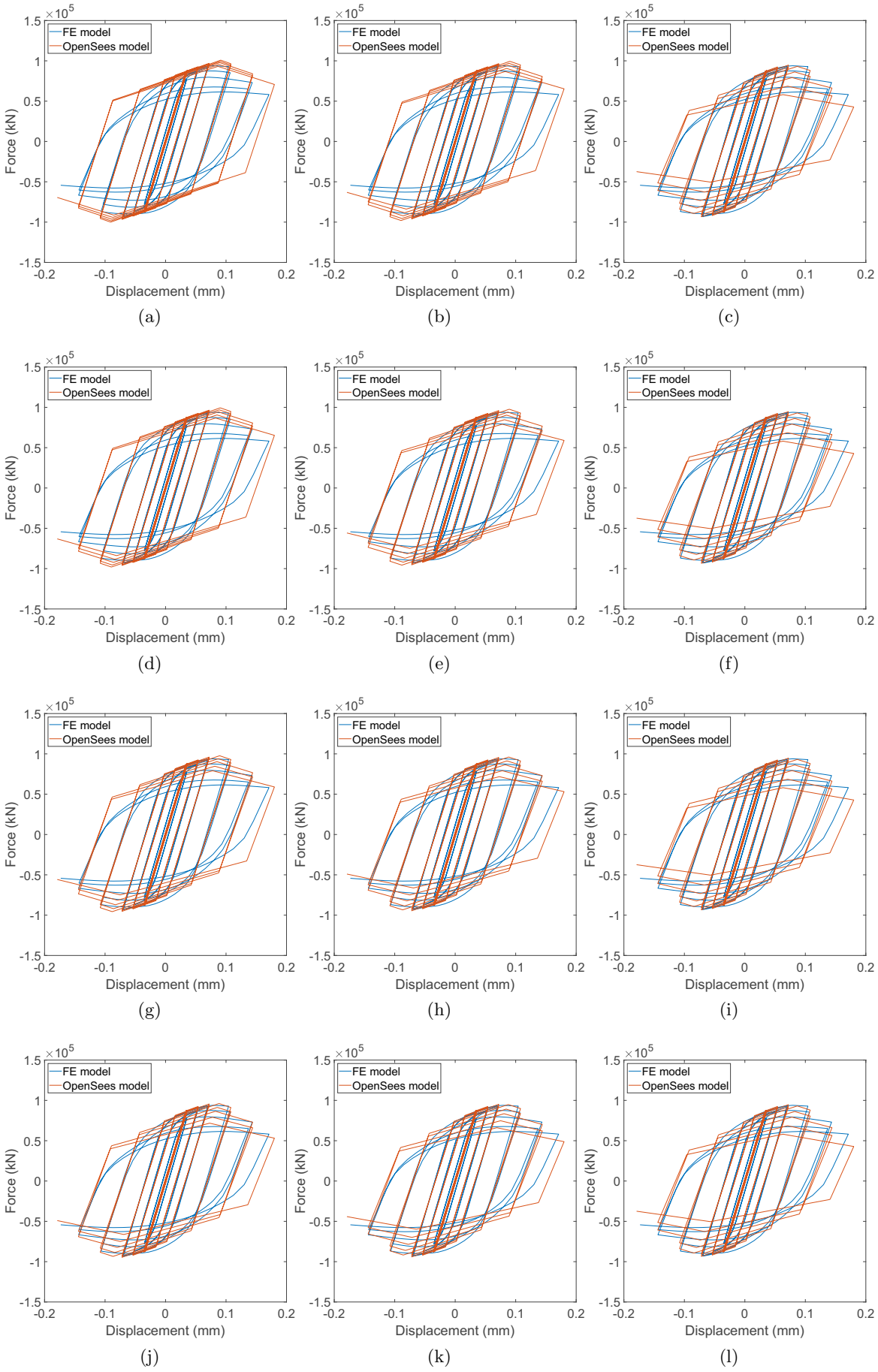

Figure 3.16: Upper–bound, middle–bound and lower–bound respective solutions for iteration No. (a)-(c) 2, (d)-(f) 3, (g)-(i) 4 and (j)-(l) 5.

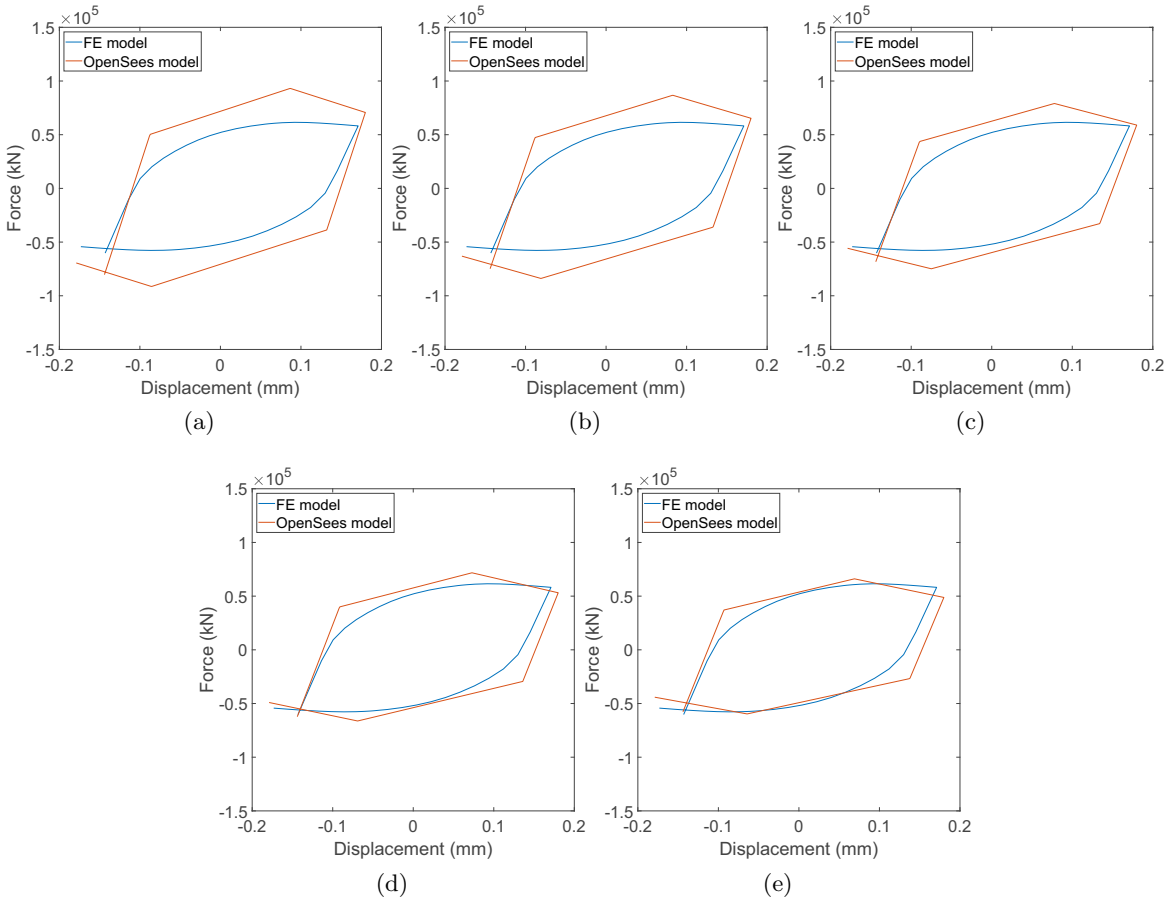

Figure 3.17: Fit of the middle–bound last cyclic loop for iteration No. (a) 1, (b) 2, (c) 3, (d) 4 and (e) 5.

Following from the calibration of the λ parameter, the strain hardening ratio, as, was to be calibrated to within a 5% tolerance. However, the initial estimate of as was already within the 5% tolerance and thus did not require calibration. Finally, calibration of the θ_{pc} was conducted by adjusting the post capping stiffness and comparing the corresponding residual strength of the beam at the θ_u rotation for the FE model and OpenSees model. Step by step graphs of the last loop of the hysteresis cycle for calibration of the θ_{pc} value are shown in Figure 3.18. Again, a tolerance of within 5% was adopted. The calibrated W18x35 beam model is shown in Figure 2.18e.

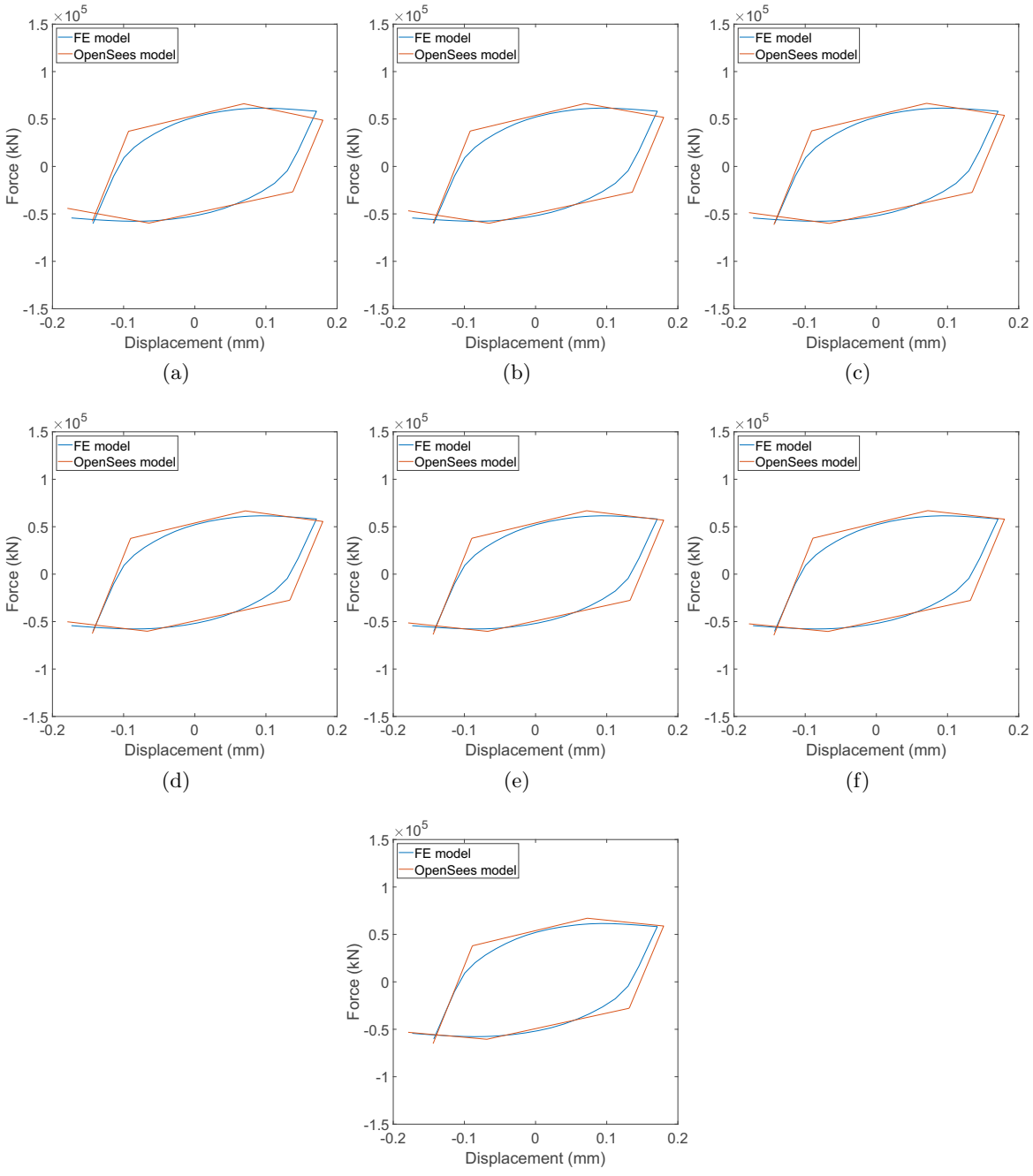

Figure 3.18: Fit of the last cyclic loop during the θ_{pc} calibration for iteration No. (a) 1, (b) 2, (c) 3, (d) 4, (e) 5, (f) 6 and (g) 7.

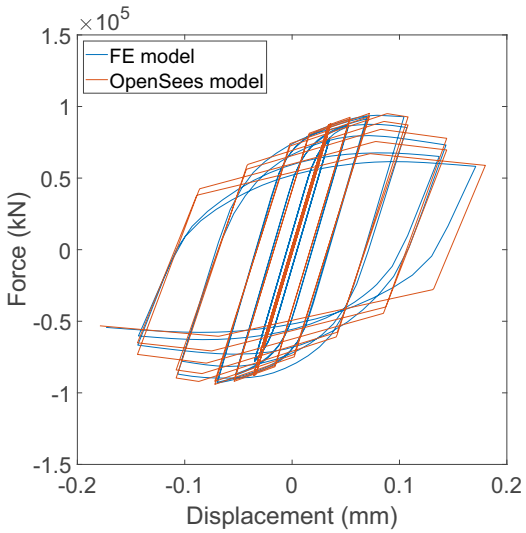

Figure 3.19: Comparisons between the FE model and OpenSees model for the final calibrated RBS W18X35 beam section with average a, b and c geometries with respect to Table 3.3

Scatter plots for the calibrated values of λ, as, θ_{pc} and θ_p for buckling cases are presented in Figure 3.20. Figure 3.20a shows a general exponential trend of λ with respect to h/t_w. According to Figures 3.8 and 3.9, as the web slenderness (h/t_w) increases, the beam specimens are more likely to buckle. Looking at the buckling behaviour from the detailed database results, in general, the sections with a larger web slenderness have shorter cyclic hardening period tending to buckle in earlier cycles. These sections experience more loading cycles post buckling and as a result lose more strength in later cycles. The difference between the peak moment and ultimate moment is much larger compared to a specimen which buckles later on in the displacement based loading protocol. Hence, a smaller value of λ is generally required for beams with a larger web slenderness. The general exponential trend shows that with a stockier web, the λ value required is much larger as the specimen tends to buckle in later cycles with a much smaller proportion of strength being lost.

Figure 3.20b shows a clear increasing trend of as with web slenderness. This suggests that the more slender the beams web the stronger the section behaves in earlier cycles before buckling. Figure 3.20c also shows that, in general, the influence of the web slenderness has a small effect on the post capping rotation. It can be seen from Figure 3.20d that for RBS sections that buckle, in general the stockier the section the larger the cyclic hardening period is, while the more slender the section is the smaller the amount of cyclic hardening that occurs. This can be linked to Figures 3.8 and 3.9 which suggest that the stockier the section the larger the cyclic hardening period. This leads to a much smaller chance of the section buckling within the $0.07rad$ of displacement based loading that was applied.

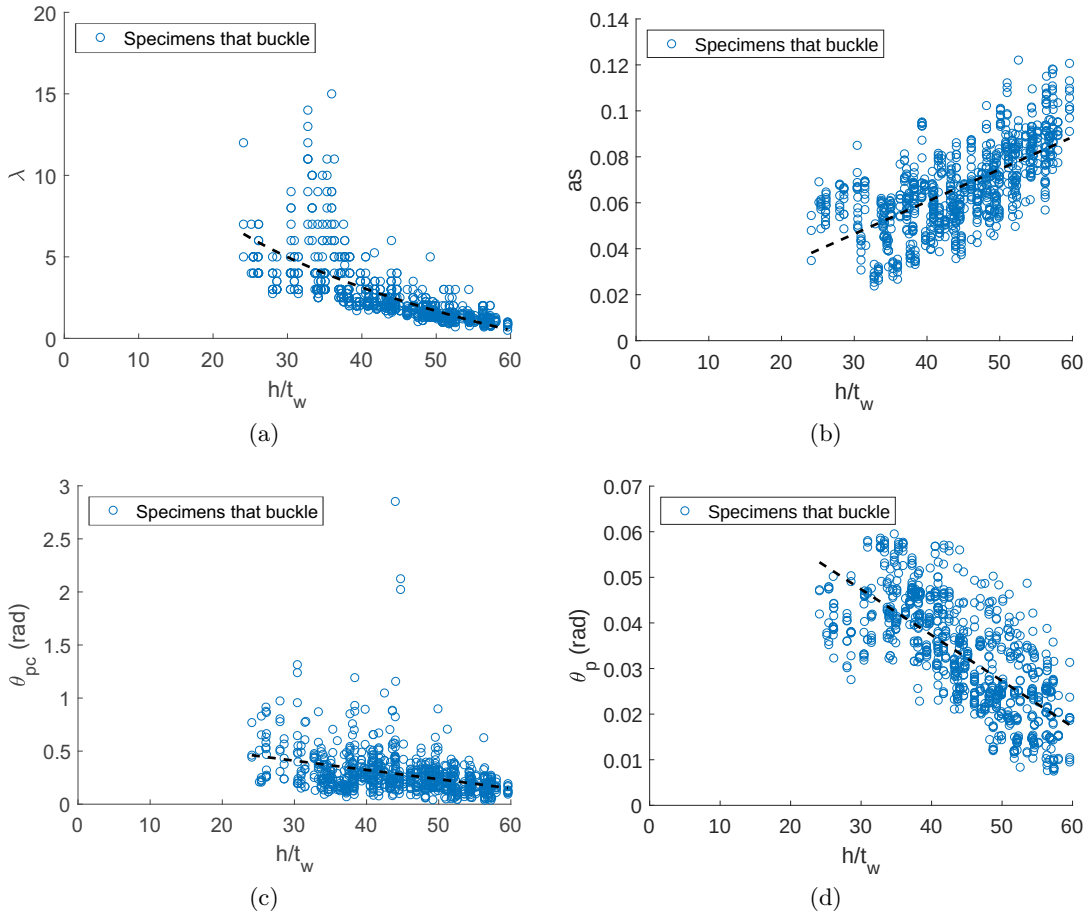

Figure 3.20: The calibrated mIK values for the bucking cases showing (a) λ, (b) as, (c) θ_{pc}, and (c) θ_p, with respect to h/t_w of the beam.

3.6.4 mIK parameters common to non-buckling and buckling case

Parameters common to both the buckling and non-buckling specimens are shown in Figure 3.21. Figure 3.21a shows the general trend for θ_p against the web slenderness. It is clear that in general for a larger web slenderness the beam specimens tend to have a shorter amount of cyclic hardening and hence θ_p. However, for non-buckle beams, the values of θ_p could be misleading since the rotation at which the beams truly buckle is not clear, and therefore, θ_p values cannot be accurately determined. Therefore, these sections could exhibit larger values of θ_p, while in this study the ultimate rotation of any non-buckle beams has been taken as $0.07rad$ as discussed before. However, for non-linear dynamic analysis only the performance of the beam up to the Collapse Prevention (CP) criteria which is roughly $0.07rad$ of rotation for an RBS section, is of interest. Any rotations larger than this are considered to have failed and the θ_u criteria holds true. Figure 3.21b shows a clear inverse trend of the θ_p with respect the the web slenderness. This highlights that the effects of as with increasing web slenderness, are dependent on whether the sections buckles or does not buckle.

A clear trend for both buckle and non buckle specimens can be seen for the initial elastic stiffness ($K0$) with respect to the second moment of area of the full section of the beam (I_{FS}) from Figure 3.21c. A slightly larger spread of data can be observed with increasing I_{FS}. However for the value of the effective yield moment (M_y), two separate clear trends for the buckle and non buckle cases with respect to the second moment of area of the RBS section (I_{RBS}) can be seen from Figure 3.21d. For the non buckle trend in Figure 3.21d, the I_{RBS} values of non buckle scatter points that are larger

than $4E10^9 mm^4$ are considered outliers and have been disregarded from the fitting of the non buckle trend line. These trends can be linked to the θ_p values. As non buckle specimens tend to have a larger kinematic hardening period reflected from the larger θ_p values, this results in the need to increase the yield moment of the section to the effective yield moment of the section by a much larger amount. This is a necessary requirement for the mIK model, which enables the kinematic hardening of the section to be accounted for. This is why there are two clear trends for the effective yield moment of the sections.

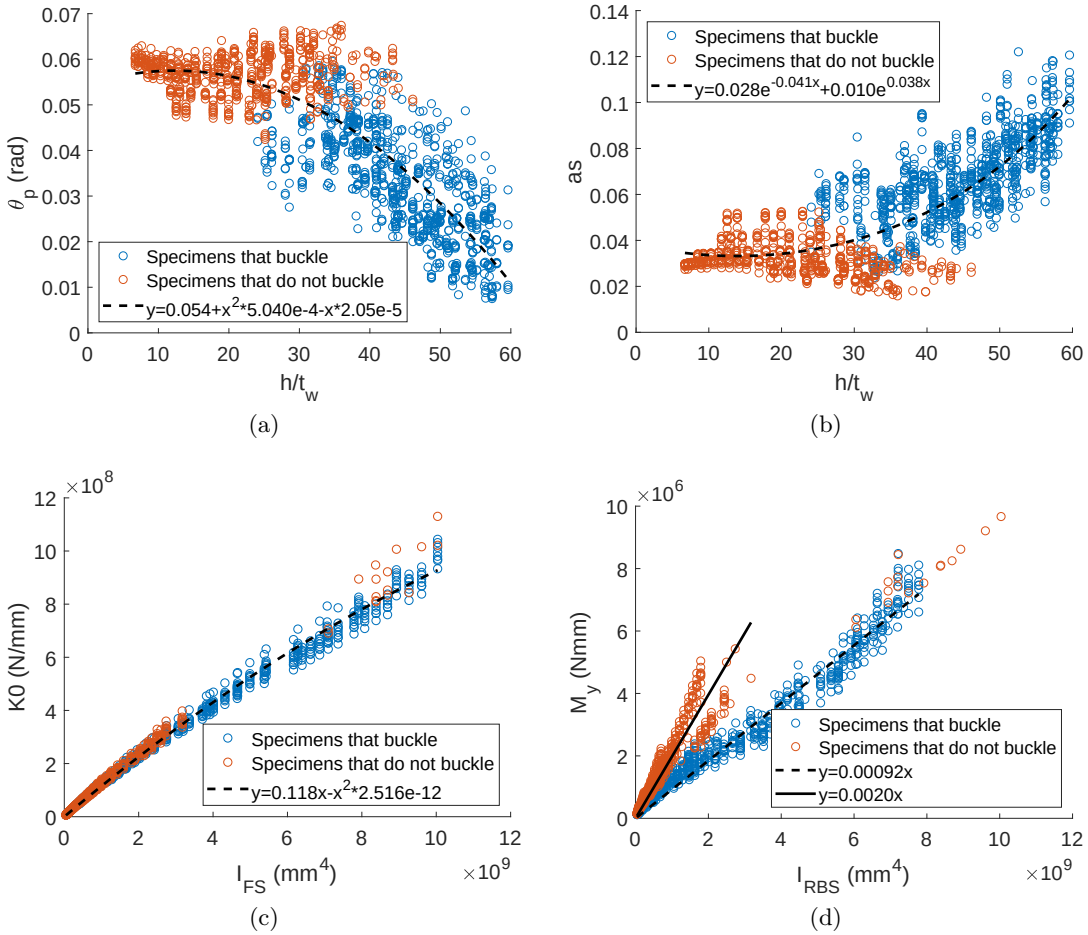

Figure 3.21: Scatter plots for mIK data of (a) θ_p, (b) as, (c) $K0$ and (d) M_y with respect to h/t_w in (a) and (b), I_{FS} in (c) and I_{RBS} in (d)

3.7 Effects of the c and b parameters on the calibrated mIK values

3.7.1 Effects of the c parameter

The general effects of the c parameter on $K0$, M_y, θ_p and as for buckle and non-buckle cases and θ_{pc} and λ for buckle cases only, are shown in Figure 3.22. In order to asses only the effects the c parameter has on the mIK parameters, sections 6, 7, 8, 9 and 10 from Table 3.3 have been selected. Figures 3.22a to 3.22d show that non-buckle cases have a tighter scatter with a much smaller range of normalized parameters compared to the buckling cases. However, in all figures the buckling and non-buckling cases follow similar trends. Trend lines have been added to each plot by taking the average of the scatter points for the five different possible ratios of c/b_f and fitting a linear line through these five points.

From Figures 3.22a and 3.22b it is clear that an increase in c/b_f leads to a reduction in the normalized $K0$ and M_y for each section. The c/b_f value has the strongest effect on $M_{y,RBS}/M_{y,FS} * I_{RBS}/I_{FS}$ ratio which has the most significant change over the varying range of c.

Figure 3.22c compares the normalized θ_p values. A clear trend shows that an increased c/b_f value tends to lead to a smaller normalized θ_p ratio. The non-buckle cases have a much tighter scatter compared to the buckle cases and, on average, have slightly larger values compare to the buckle case which have a much greater spread.

Figure 3.22d has a much less obvious trend. On average the normalized $as_{RBS}/as_{FS} * I_{RBS}/I_{FS}$ values reduce with increasing c/b_f but at a much smaller rate. The non-buckle scatter points have a much tighter grouping compared to the buckling points and, in general, have a much smaller normalized ratio. For non-buckle cases the as_{RBS} tends to be smaller than the as_{FS} values, whereas, in general the buckle cases have the opposite trend.

It should be noted, that the concept of normalizing the response parameters based on the I_{RBS}/I_{FS} used in Figures 3.22a to 3.22b, have been adopted based on previous studies in Horton et al. (2021b). These studies showed that using this dimensionless parameter could take into account the effect of the cross section leading to less scattered results.

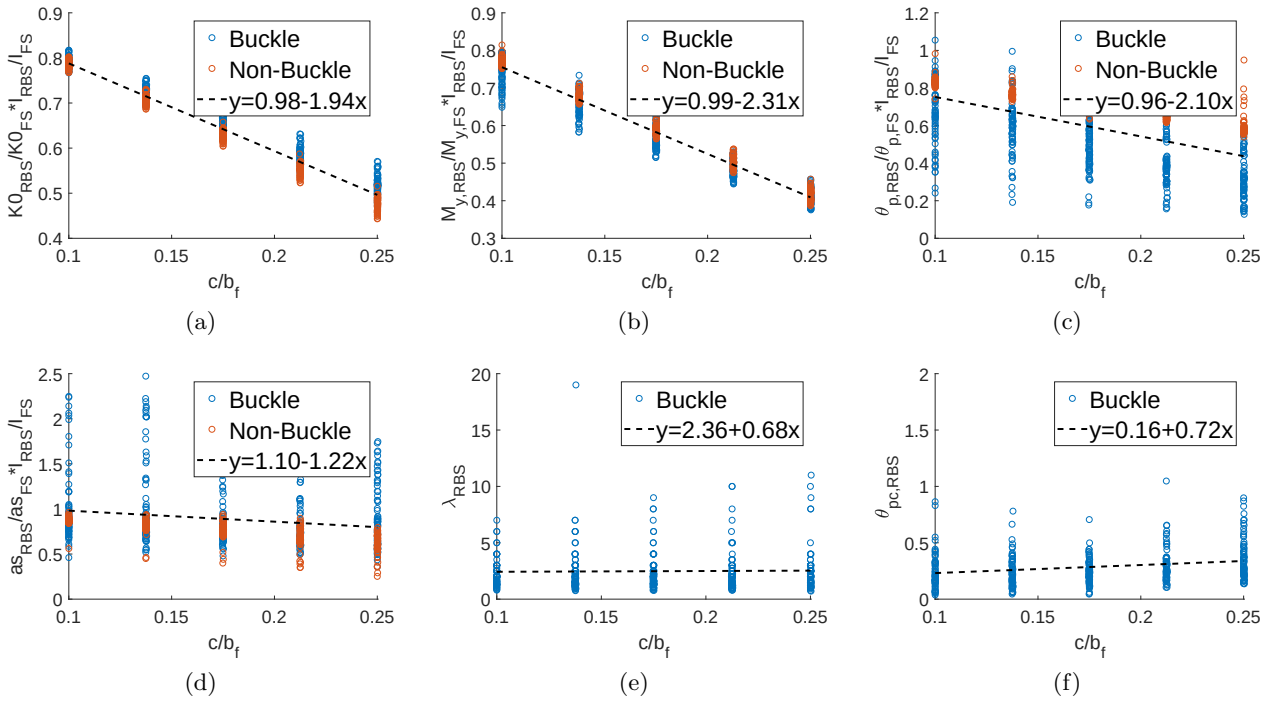

Figure 3.22: Effects of the c geometry for RBS Buckle and Non-Buckle cases for (a) $K0_{RBS}/K0_{FS} * I_{RBS}/I_{FS}$, (b) $M_{y,RBS}/M_{y,FS} * I_{RBS}/I_{FS}$, (c) $\theta_{p,RBS}/\theta_{p,FS} * I_{RBS}/I_{FS}$ and (d) $as_{RBS}/as_{FS} * I_{RBS}/I_{FS}$, (e) λ_{RBS}, and (f) $\theta_{pc,RBS}$ with respect to c/b_f.

Figures 3.22e and 3.22f show the variation of λ_{RBS} and $\theta_{pc,RBS}$ with respect to c/b_f respectively. In general, Figure 3.22e indicates that the range of λ_{RBS} increases as the c/b_f value gets larger. However, on average, the values of λ_{RBS} have very little effect on the c/b_f. In Figure 3.22f the trend is much stronger and shows that with larger c/b_f values the $\theta_{pc,RBS}$ rotation increases. A similar trend is observed in Figure 3.22d for the spread of data with increasing c/b_f values.

3.7.2 Effects of the b parameter

By only selecting sections 2, 3, 4, 5 and 8 from Table 3.3, the effect of the b/d value with respect to normalized mIK parameters and regular mIK parameters can be analyzed. Respective scatter plots are shown in Figure 3.23. By comparing Figures 3.23a and 3.23b to Figures 3.22a and 3.22b directly, it is obvious that the b/d has very little effect on the normalized $K0$ and M_y values. The values of normalized $K0$ and M_y have a much tighter scatter for both buckle and non-buckle sections which suggests that the b/d value has little effect on these parameters.

In contrast, the spread of data in Figure 3.23c is much larger. There appears to be no general trend for the normalized $\theta_{p,RBS}/\theta_{p,FS} * I_{RBS}/I_{FS}$ value. On average, the trend line shows a very small increase in normalized θ_p value with significant scatter for both buckle and non-buckle cases. This shows a very different trend compared to Figure 3.22c for the c/b_f effect. Similarly, Figure 3.23d illustrates a very similar trend to Figure 3.22d with respect to the buckle and non-buckle cases. In general, Figure 3.23d shows that the b/d value has little effect on the normalized as value, however, the RBS non-buckling specimens tend to have smaller as values compared to their respective full section specimens.

Figures 3.23e and 3.23f show the general trend for the effects of b/d on the λ_{RBS} and $\theta_{pc,RBS}$ mIK values. It should be noted that in Figure 3.23f the outliers which are greater than $1.0rad$ have been disregarded for the fitting of the trend line. Again, on average the effects of the b/d can be considered negligible for these mIK values.

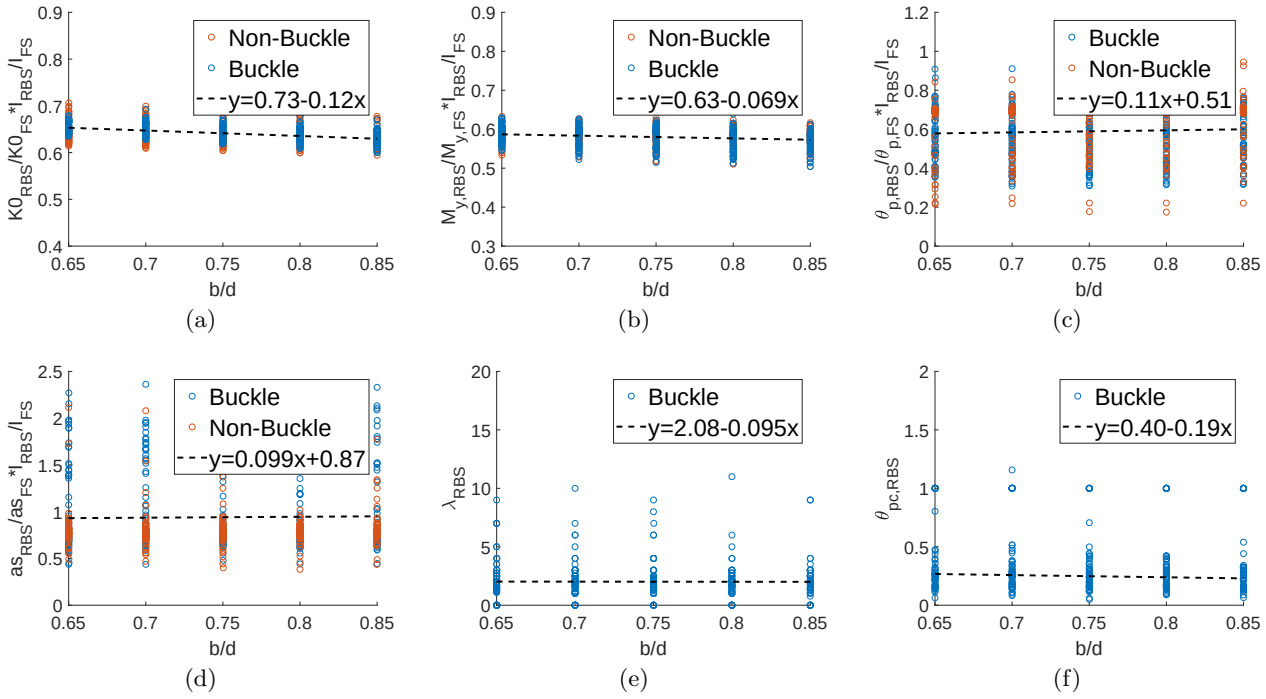

Figure 3.23: Effects of varying the b geometry for RBS Buckle and Non-Buckle cases for (a) $K0_{RBS}/K0_{FS} * I_{RBS}/I_{FS}$, (b) $M_{y,RBS}/M_{y,FS} * I_{RBS}/I_{FS}$, (c) $\theta_{p,RBS}/\theta_{p,FS} * I_{RBS}/I_{FS}$, (d) $as_{RBS}/as_{FS} * I_{RBS}/I_{FS}$, (e) λ_{RBS}, and (f) $\theta_{pc,RBS}$ with respect to b/d.

3.7.3 Comparisons to predictive mIK values from equations

Lignos and Krawinkler (2011) proposed predictive equations which could be used to calculate appropriate mIK parameters for RBS and FS beam connections. In this section, the calibrated values from this extensive FE database have been compared to the values calculated from these predictive equations for both RBS and FS beams.

3.7.4 RBS connections

The first set of equations proposed by Lignos and Krawinkler (2011) is for use in RBS connections, refer to Appendix C for details of the equations. Figure 3.24 compares the values of θ_{pc}, λ and θ_p from the calibrated FE database to Lignos and Krawinkler (2011) predictive equations. It should be noted that only buckling cases are considered in Figure 3.24a. It is clear that the predictive equations by Lignos and Krawinkler (2011) under predict the values of θ_{pc}. The equations predict that the θ_{pc} values have a small range from between $0.1rad$ to $0.5rad$. However, the calibrated database suggests that the range of θ_{pc} is much larger.

Figure 3.24b shows that the predictive equations estimate a similar range (up to around 20) of λ values compared to the calibrated database values. It is clear that the predictive equations from Lignos and Krawinkler (2011) did not consider the buckling behaviour of the sections up to $0.07rad$ of loading. Therefore, when providing values of λ for the mIK model, it is essential that clear assumptions are made during the modelling process. For this database, there are two clear categories of sections – buckling and non-buckling. When considering the values of λ for mIK models it is important to classify the section as buckling or non-buckling so as to assign the appropriate λ value, along with the respective θ_u value. Figure 3.24c compares the mIK buckle and non-buckle RBS values obtained from Lignos and Krawinkler (2011) equations and the corresponding results from the calibrated database. It can be seen that the predictive equations (Lignos and Krawinkler, 2011) generally provide a rough approximation, but it is clear that they do not provide accurate predictions in some cases.

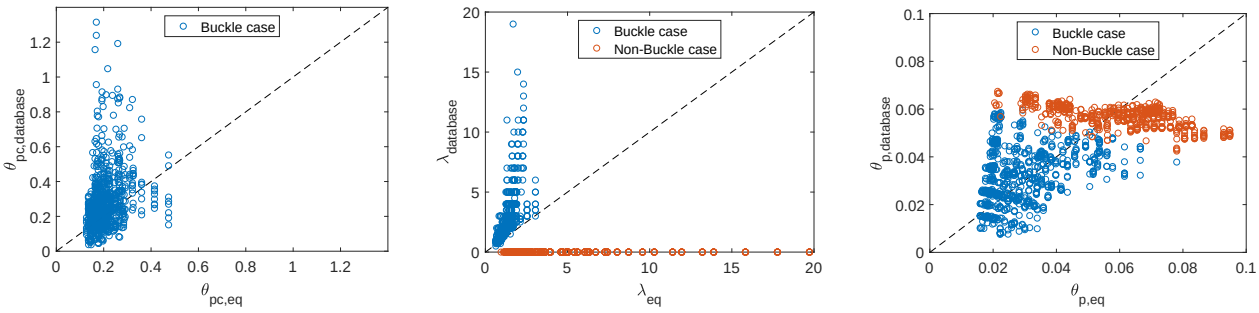

(a) (b) (c)

Figure 3.24: Comparisons of the Lignos and Krawinkler (2011) equations to predict the mIK parameters for RBS connections with the results of the calibrated database for buckling and non-buckling cases: (a) θ_{pc}, (b) λ, and (c) θ_p.

It should be noted that the predictive equations by Lignos and Krawinkler (2011) looked at the monotonic response of the connections and tried to change the parameters that define this backbone curve by using factors to capture the cyclic strength and stiffness degradation as well as amplification factors to capture the kinematic hardening response. The database developed in this study uses the cyclic response directly to specify parameters that define the cyclic hysteresis of the beam and connections directly. While this method may not be appropriate for static analysis, the mIK parameters capture the entire cyclic response of the section with a high level of accuracy. This will play a major

role in being able to model and capture the non-linear dynamic response of structures at the local and global level. It is clear that for defining the mIK parameters, the RBS connection must be first categorised as buckling or non-buckling. This will have a significant effect on what parameters are used when defining the appropriate mIK model.

3.7.5 FS connections

The same problem as above can be concluded for FS connections from Figures 3.25a, 3.25b and 3.25c that show very similar trends with the respective plots in Figure 3.24. These figures again highlight the problem of obtaining the mIK parameters based on the results of monotonic response and ignoring the effects of RBS geometric parameters and the completely different behaviour of buckling and non-buckling elements. However, this Chapter focuses only on the RBS response of sections.

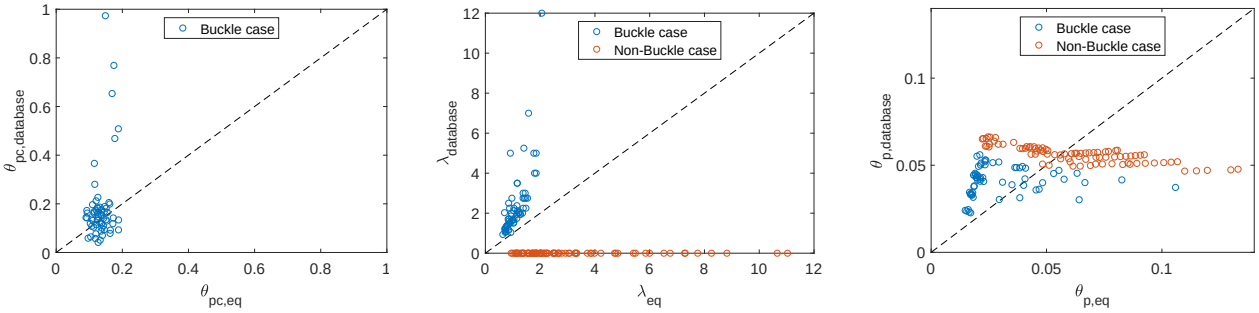

(a) (b) (c)

Figure 3.25: Comparisons of the Lignos and Krawinkler (2011) equations to predict the mIK parameters for other-than-RBS connections with the results of the calibrated database for buckling and non-buckling cases: (a) θ_{pc}, (b) λ, and (c) θ_p

To demonstrate the accuracy of the developed Deep Learning Neural Networks for practical applications, the cyclic behaviour an experimentally validated FE model of the DB700-SW beam specimen tested by Lee et al. (2005) is compared with the results of the mIK model using the predicted parameters. Only the beam from the DB700-SW beam specimen was modelled in accordance with Chapter 2 and 3 to remove any potential beneficial effects of the column or panel zone on the cyclic response. As shown in Figure 3.26, the mIK model could accurately simulate the hysteresis behaviour of the tested connection in terms of initial stiffness, ultimate strength and strength degradation. This demonstrates the efficiency of the developed neural network system for the components outside the training sample set.

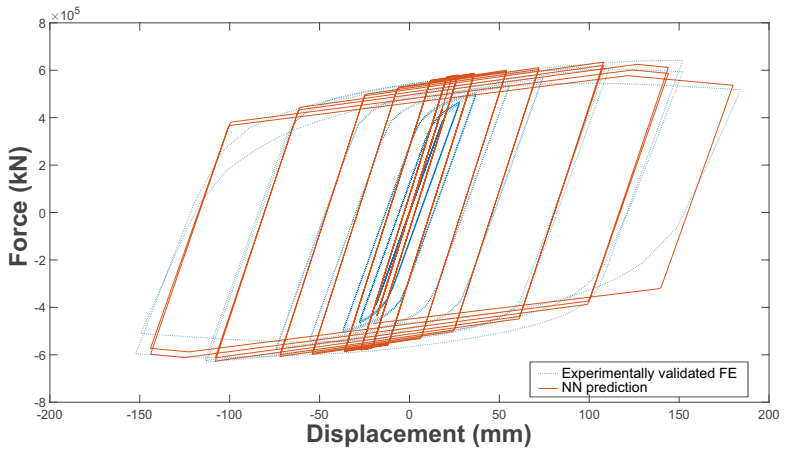

Figure 3.26: Comparisons of the mIK model cyclic response prediction with the experimentally validated FE.

It should be noted that the results of this study are limited to the adopted models and the selected material properties. However, the general conclusions indicate the overall accuracy and reliability of the proposed deep learning Neural Network models to predict the complex non-linear hysteresis behaviour of RBS connections.

3.8 Summary and conclusions

The aim of this Chapter is to provide a better understanding about the cyclic behaviour of fully welded RBS connections and develop a database of detailed and accurate modified-Ibarra-Krawinkler models that can reliably capture the cyclic hysteresis of these connections over a wide range of different RBS geometries. A detailed FE model was first validated using two different sets of experimental beam-to-column assemblies. The developed models captured the cyclic response as well as the web and flange buckling behaviour of the RBS sections through appropriate modelling techniques. A comprehensive FE parametric study of 1480 different American wide flange RBS and FS beams was then carried out. By varying the key RBS geometries, the models were created automatically using a Python macro code in Matlab to create the ABAQUS mode. The FE models were then analysed under SAC proposed displacement based cyclic loading up to $0.07rad$ in ABAQUS and the results were extracted and post processed into a database. Subsequently, these results were calibrated to a simple equivalent beam model utilizing a bilinear modified-Ibarra-Krawinkler zero length spring in OpenSees. The calibration process was implemented in OpenSees and optimised using Matlab. As a result, highly accurate and reliable mIK parameters were defined for 1480 different variations of sections for a wide variety of different RBS geometries. It should be noted that the influence of weld access holes was not taken into account in the models used in this study. On the other hand, the presented results are only applicable for American wide flange fully welded RBS elements. However, the proposed methodology can be easily adopted to develop similar databases for other types of connections (such as Drilled Flange (Atashzaban et al., 2015) and reduced web section (Davarpanah et al., 2020)) and different cross sections. Based on the results from the developed database, the following conclusions can be draw:

1. The cyclic hysteresis results from the FE database can be split into two general categories – sections that buckle or sections that do not buckle. This buckling behaviour is strongly influenced by the slenderness of the beam sections web. Larger web slenderness have a much greater chance of buckling. The c geometry has the most effect in the range $34.01 < \lambda_{web} < 47.0$, where a larger c parameter tends to increase the likelihood of a section buckling. For all other ranges of λ_{web},

the c and b parameters RBS do not appear to have any significant influence on the buckling behaviour of the beam. In general, for these sections the buckling behaviour is controlled by the slenderness of the web, regardless of the RBS geometry.

2. Accurate and reliable bilinear mIK parameters were calibrated for each of the 1480 specimens in the FE database. For buckling cases, the λ and θ_{pc} values were influenced the most by the slenderness of the sections web. The mIK parameters as and θ_p, common to both buckling and non buckling specimens, were also influenced by the web slenderness. A clear linear trend for these mIK parameters could be observed. $K0$ can be considered dependent on the second moment of area of the corresponding section. However, the two different trends for the effective yield moment of buckle and non buckle sections are significantly affected by I_{RBS}. Thus M_y can be considered to be dependent on both the buckling behaviour and I_{RBS} of the section.

3. The influence of the geometrical c and b RBS parameters on the mIK parameters were thoroughly investigated. Results showed that the c parameter effects the $K0$ and M_y values the most. Some influence of the c geometry on the θ_p was also observed, while this parameter had very small effects on the as, λ and θ_{pc} mIK values. The b parameter has practically no influence over the mIK parameters.

4. The predictive mIK values using the widely adopted equations suggested in Lignos and Krawinkler (2011) were directly compared to the mIK database parameters for the 1480 different RBS specimens. The comparisons showed that predictive mIK values under predicted the θ_{pc} and λ values and gave varying results for the θ_p predictions. This highlights that trying to capture the cyclic hysteresis of sections by modifying the monotonic backbone curve after Lignos and Krawinkler (2011) and also ignoring the effects of RBS geometric parameters may lead to very unrealistic results. These issues are addressed in the developed database by directly using the cyclic hysteresis of the sections in order to generate accurate and reliable hysteresis models of RBS elements. The same problem has also been identified for the FS equations presented by Lignos and Krawinkler (2011).

The comprehensive database developed in this study should prove useful in better understanding the structural performance of RBS connections and more reliable design and assessment of such connections for seismic applications.

Chapter 4

Accurate Prediction of Cyclic Hysteresis Behaviour of RBS Connections Using Deep Learning Neural Networks

As a result of the conclusions drawn in Chapter 3, a method to accurately predict the cyclic hysteresis behaviour of RBS has been developed in this chapter. This chapter is based on the paper titled: Accurate Prediction of Cyclic Hysteresis Behaviour of RBS Connections Using Deep Learning Neural Networks, submitted to Journal of Engineering Structures dated 15/03/2021. It should be noted this chapter reads as a standalone paper. It may repeat sections previously introduced in this thesis.

4.1 Abstract

Reduced Beam Section (RBS) connections have been widely adopted in the design of new, and retrofitting of existing steel framed buildings to improve the seismic performance by providing a seismic fuse mechanism through intentionally weakening the beam at the beam-to-column connection interface. The widely adopted modified-Ibarra-Krawinkler model can reliably capture the cyclic hysteresis behaviour of fully welded RBS connections, making it an attractive option for modelling the non-linear behaviour of steel moment resistant frames under earthquake excitations. However, there is currently no reliable or accurate method available to predict the parameters which define the modified-Ibarra-Krawinkler model without appropriate experimental or finite element tests of full scale models of the RBS connection for calibration purposes. This chapter presents, an accurate method of predicting the modified-Ibarra-Krawinkler parameters using a number of different deep learning Neural Networks (NNs) through a logical flow chart process, which provide accurate predictions of the modified-Ibarra-Krawinkler parameters based on the geometrical dimensions of the steel beam and RBS. The proposed networks have been trained based on the database of 1480 finite element cyclic moment-rotation-hysteresis results. First the cyclic moment-rotation-hysteresis results from the selected database were calibrated with simple equivalent beam representations of the finite element models in the OpenSees software. Then a number of different deep learning NNs were developed to predict each of the seven key parameters which define the modified-Ibarra-Krawinkler spring model. Finally, a script was developed through the interactive software Matlab, which can accurately and reliably predict the modified-Ibarra-Krawinkler parameters for any steel beam and RBS geometry without the need for complex and time consuming full scale cyclic experimental tests or finite element analyses. The tool box developed in this study provided over 96% accuracy in predicting the key design parameters, and therefore, should prove useful in the preliminary design and assessment of

steel RBS frames.

4.2 Background

4.2.1 Concept of Reduced Beam Sections

Absorbing seismic input energy within the Reduced Beam Section (RBS) through a fuse like system results in a safe and stable structure which can withstand seismic excitations by protecting the gravity load bearing columns from excessive plastic rotations and failure. While RBS connections have become widely adopted within design codes (BSI, 2005; AISC, 2016b; SAC Joint Venture, 2000a), there is currently no comprehensive model available which is capable of considering all the design parameters that affect the RBS connections performance.

Early cyclic experiments conduced on RBS connections highlighted their excellent rotational capacities compared to the pre-Northridge connections, which were susceptible to brittle fracture (Engelhardt and Sabol, 1997). Cyclic tests conducted by Roeder (2002) showed that RBS connections can achieve a good seismic performance with larger rotational capacities compared to the Welded Unreinforced Flange – Welded Web (WUF-W) and Welded Unreinforced Flange – Bolted Web (WUF-B) connections. Cyclic experimental tests on the fabrication (tapered, constant or radius cut) of RBS connections by Chen et al. (1996); Oh et al. (2015); Chen and Lin (2013) and Roeder (2002) also demonstrated that, generally, highest rotational capacity was achieved by radius cut RBS. The affect of the RBS cut (geometry) on the connections performance was first investigated by Pachoumis et al. (2009). Earlier web buckling and flange buckling was linked with a deeper RBS cut. Validated finite element (FE) models were developed by Pachoumis et al. (2009) and Pachoumis et al. (2010) to investigate this further. The higher energy dissipating capabilities of RBS steel moment frames compared to pre-Northridge steel frames was demonstrated through FE analysis in early studies by Chen et al. (1997) and Carter and Iwankiw (1998). More recently, the energy absorbing characteristics of RBS steel frames has been further investigated by Jin and El-Tawil (2005); Ashrafi et al. (2009); Kildashti and Mirghaderi (2009); Seo et al. (2010); Nikoukalam and Dolatshahi (2015); Montuori (2016); Maleki et al. (2018) and Maleki et al. (2019). Notably, Maleki et al. (2018) and Maleki et al. (2019) used incremental dynamic and fragility analysis to assess the performance of 4 and 16 storey steel moment perimeter frames incorporating welded unreinforced flange (WUF) and RBS connections. Compared to WUF frames, RBS frames exhibited superior seismic performance when considering the collapse prevision (CP) and immediate occupancy (IO) performance-based design levels.

The modified-Ibarra-Krawinkler model by Lignos and Krawinkler (2007) is a widely accepted method adopted by many researchers (Lignos et al., 2011b; Ghassemieh and Kiani, 2013; Ke and Chen, 2016; Lemonis, 2018; Tsitos et al., 2018; Bravo-Haro and Elghazouli, 2018; Maleki et al., 2019) as a way of capturing the non-linear cyclic behaviour of RBS connections. However, there is no accurate and reliable method to enable prediction of the parameters which define the mIK model without the need for complex finite element or experimental models or tests. In one of the relevant studies, Lignos (2008) described how multivariable regression analysis equations determined from a database of experimental results by Lignos and Krawinkler (2007) can be used to estimate the parameters which define the mIK model. However, the equations proposed by Lignos (2008) are based on a range of different connection types and experimental set ups taken from literature. Even though the database used for the regression analysis equations by Lignos and Krawinkler (2007) has been split into two different categories (RBS or conventional), these categories have too many variables and varying parameters which will affect the accuracy of the predicted cyclic response behaviour making them difficult for implementation in practical applications. The first category, defined as RBS connections, incorporates

a wide range of different connection types and configurations as well as different RBS flange reduction geometries. These equations are only based on the general sizes of RBS from the experimental tests considered, and therefore, do not take into account the RBS geometrical parameters which can effect their cyclic hysteresis behaviour (Pachoumis et al., 2009; Horton et al., 2021b). In addition, only 73 out of the 200+ experimental results from the database (Lignos and Krawinkler, 2007, 2011) represented RBS connections, showing the limited number of data which the regressional equations in Lignos (2008) are based on. These equations cannot be applicable for sections not included in the experimental tests, and may lead to unreliable results and potentially affect the performance of the designed system.

The database of highly accurate calibrated mIK parameters in Chapter 3, directly obtained from experimentally validated FE models, gave different results when compared to the parameters predicted through multivariable regression analysis equations in Lignos (2008). These differences are a result of the wide range of different RBS connections considered in the multivariable regression analysis as well as neglecting the effects of RBS cut (geometry) parameters in the proposed design equations. The database from Chapter 3 considered only one type of connection – welded unreinforced welded web (WUF-W) connection – which removed any variation due different types of connections exhibiting a range of connection stiffness. Besides, the effects of RBS geometries are directly included in the developed database. This information is used to train deep learning NNs in this study as will be explained in the following sections.

4.2.2 Applications of Neural Networks in structural design

Deep learning and artificial NNs have recently been increasingly applied to solve complex problems in structural engineering Rafiq et al. (2001). As one of the earlier studies, Adeli and Hung (1995) explained how NNs mimic the biological neural structures of the human brain and central nervous system in order to recognize hidden pattens and classify data. In general, a Neural Network (NN) can map from a set of associated input patters to a set of known output values Rafiq et al. (2001). Multilayered feedforward networks with hidden layers are capable of providing very precise approximations to engineering problems Hornik et al. (1989). Until now, NNs have been used in many areas of structural engineering such as prediction of mechanical or structural values (Guzelbey et al., 2006b; Shahin and Elchalakani, 2008; Tohidi and Sharifi, 2015), assessment of structures (Akbas, 2006; Caglar et al., 2009; Tadesse et al., 2012), assessment of structural damage (Jeyasehar and Sumangala, 2006; Jiang et al., 2006; Bakhary et al., 2007) and structural optimization (Rogers, 1994; Adeli and Park, 1995; Lagaros and Papadrakakis, 2004; Gholizadeh and Mohammadi, 2017).

Rogers (1994) first showed how low cost NNs could be used for computationally expensive structural analysis programming problems. Analysis guidelines were suggested by Rogers for researchers seeking to utilise NNs for structural optimization. Rogers also showed using NNs can produce meaningful optimal design results. Adeli and Park (1995), were one of the first researchers to use a NN dynamics in order to optimize a space truss under multiple loading conditions. They concluded that their proposed optimization technique was suitable for the optimization of large structures after being applied to optimize the weight of four different structures. In another relevant study, Lagaros and Papadrakakis (2004) proposed some improvements to NNs used in optimization of complicated structural problems. Two examples, consisting of a six-storey space frame and a twenty-storey space frame optimization were considered. Results clearly demonstrated that improvements relative to the computational time were achieved through the proper selection of activation property functions. Similarly, Gholizadeh and Mohammadi (2017) proposed efficient methods for seismic performance-based design optimization of steel moment resistant frames using metaheuristic and NN. Various metaheuristic and NN computational performances were compared through optimisation of a three storey and a ten storey steel

moment frame.

NNs have also been utilised for the assessment of structures in order to aid structural design, particularly for complex multi-dimensional problems. Akbas (2006) used NNs to predict the seismic performance of a steel structure. Multi-layered feedforward networks were trained leading to a NN capable of estimating the hysteretic energy demand of steel structures under earthquake ground motions. Caglar et al. (2009) used NNs to present an empirical formulation to predict the base shear of braced and un-braced steel frames and showed that the proposed formulations could predict the base shear more effectively that other empirical models. Similarly, Tadesse et al. (2012) utilised three NNs to predict the serviceability loading deflections in simply supported composite bridges, two span continuous composite bridges and three span continuous composite bridges. The serviceability loadings took into account the flexibility of shear connections, concrete cracking of slabs and shear lag effect in the composite sections.

Other researchers also utilised NNs for the assessment of structural damage in structures. For example, Jeyasehar and Sumangala (2006) developed a feed forward NN for the assessment of damage in pre-stressed concrete beams due to natural frequencies. The NN used static and dynamic data on damaged and undamaged beams. Jiang et al. (2006) used data fusion and NNs in a novel approach in order to identify structural damage. Bakhary et al. (2007) also utilised a used NNs as an efficient tool to estimate the probability of damage. The proposed NN was tested on a steel frame model and also on experimental tests of concrete slabs.

NNs have been utilised in other structural engineering applications as well. Hedayat et al. (2019) used NNs to propose an integrated formula which predicted the minimum strength requirements of steel moment frames at any performance level. They used a bilinear model in Opensees (Mazzoni et al., 2007) to generate force-displacement capacity based displacement curves of varying steel moment frames under a variety of ground motions. NNs were then developed to obtain equations which could be used to estimate the seismic response and performance level for strengthening and retrofitting existing steel frames or designing new steel frames.

In general, large sets of data are required in order to train and test NNs. To achieve this, researchers have widely utilised previous experimental results available in the literature on mechanical properties or behaviour of structural elements. Fonseca et al. (2003) presented a NN which could predict the beam patch load resistance of steel I beams. Guzelbey et al. (2006b) used available experimental data in order to predict the rotational capacity of wide flange beams mitigating the need for numerical or experimental models. Similarly, Guzelbey et al. (2006a) used NNs to predict the web crippling strength of cold formed steel decks. The NN was shown to predict the elastoplastic behaviour of web crippling with a high level of accuracy when compared to experimental results obtained from literature. An extensive parametric study was conducted in order to investigate how geometrical and mechanical parameters of steel sheeting affects the web crippling strength. In another study, Pala (2006) proposed a NN to forecast the elastic distortional buckling stress of cold formed steel C-sections under pure compression or pure bending. Data for the training and testing of the NN was taken from literature. Pala and Caglar (2007) conducted a study to assess the influence of geometrical parameters of cold-formed steel C-sections on the elastic distortional buckling stress through the NN developed in Pala (2006). Pala and Caglar (2007) concluded that due to the complex and cumbersome calculations involved with assessing elastic distortional buckling stress of steel C-sections, NNs are a useful tool for predicting the buckling models of steel C-sections. Shahin and Elchalakani (2008) used multi-layer feed-forward NNs to predict the ultimate pure bending capacity of steel circular tubes. Datasets of 49 fabricated steel circular tubes and 55 cold-formed tubes were used to train the NNs. Four parameters were used as input values for the NN which were shown to accurately predict the

ultimate pure bending of the steel tube sections. Design equations were also presented capable of predicting the ultimate bending capacity of the steel tubed sections.

Where no available data or experimental results exist in literature, validated finite element (FE) models are commonly used to produce large datasets of results necessary to train and test the NN. Gholizadeh et al. (2011) used a back-propagation NN and adaptive neuro-fuzzy inference system in order to estimate the post web buckling critical loads of simply supported castellated steel beams. Sharifi and Tohidi (2014a) also utilised artificial NN to predict the lateral torsional buckling moment capacity of steel I beams with web openings. Their study focused on the stability of damaged bridge beams with web openings under bending loading. In another study, Sharifi and Tohidi (2014b) used artificial NN to predict the ultimate strength of deteriorated steel beams subjected to pitted corrosion. Ultimately a reduction factor, which represented the ultimate strength loss of the steel beam due to pitted corrosion, was predicted using the database of FE models. Tohidi and Sharifi (2015) applied artificial NN to the prediction of the moment capacities of steel I beams subjected to distortion buckling.

4.2.3 Modelling of Reduced Beam Section connections

Modelling the performance of steel moment resistant connections is an important process used in the design or retrofitting of steel frames under seismic excitations. As discussed before, the Reduced Beam Section (RBS) connections are widely used in current design guidelines (BS/EN 1998-3 (BSI, 2005), ANSI/AISC 358-16 (AISC, 2016b) and FEMA 350 (SAC Joint Venture, 2000a)) as a reliable method of absorbing the seismic energy in steel moment frames. In order to accurately represent RBS connections in a non-linear dynamic analysis, an appropriate model which can reliably capture their non-linear cyclic hysteresis behaviour should be adopted by taking into account the strength and stiffness degradation effects.

There are currently several different models which are capable of representing the non-linear behaviour of steel RBS connections. The most widely adopted method, implemented recently by many researchers to represent steel RBS connections, utilises the Bilinear modified-Ibarra-Krawinkler (mIK) (Lignos et al., 2011b; Ghassemieh and Kiani, 2013; Ke and Chen, 2016; Lemonis, 2018; Tsitos et al., 2018; Bravo-Haro and Elghazouli, 2018; Maleki et al., 2019). The Bilinear mIK model captures the Basic Strength Deterioration, Post-Capping Strength Deterioration and Unloading Stiffness Deterioration of the connection through seven parameters which define its cyclic hysteresis shape. Figure 4.1a summarises the parameters which define the model.

Ibarra et al. (2005) first introduced the mIK model which was later improved by Lignos and Krawinkler (2007). Lignos et al. (2010) highlighted that an appropriate analytical model (utilising the mIK model) requires experimental data for model validation, improvement and calibration. Lignos (2008) first proposed new equations to estimate the mIK parameters based on multivariable regression on the database in Lignos and Krawinkler (2007). According to Lignos and Krawinkler (2012), the regression equations in Lignos (2008) gave satisfactory results but need improvements to take into account different geometrical and material properties of the RBS connections. The differences arise due to the type of connection analysed and the varying size and shape of RBS connections. A previous research study in Chapters 2 and 3 also suggests that the size and shape of the RBS cut effects the connections cyclic hysteris, while these parameters are not included in the current design equations. Additionally, the range of RBS connections considered for these regression equations were based on a limited number of experimental tests, and therefore, a larger dataset is required for more accurate and reliable predictions.

Chapter ch:3 compared the predictive equations by Lignos (2008) to a database of mIK parameters calibrated from a wide range of experimentally validated finite element (FE) models of RBS connections. They showed that the required mIK parameters to accurately capture the non-linear behaviour of varying beam and corresponding RBS sizes depend not only on the geometrical parameters which define the RBS steel I section, but also on the geometrical parameters that define the RBS geometries. These accurate mIK models gave different parameters compared to the predictive equations in Lignos (2008).

Currently, the most accurate method to determine the cyclic hysteresis behaviour of RBS connections is to calibrate the key mIK input parameters based on a full cyclic experimental test or a detailed FE cyclic analysis. Both methods are significantly time consuming and either financially or computationally expensive. Consequently, a set of deep learning NNs capable of predicting the full cyclic behaviour of any RBS connection given the geometries defining the RBS and steel I section as an input, is a very attractive solution presented in this Chapter.

Deep learning NN have recently been utilised as a powerful tool for finding hidden patterns within large datasets. The database of 1480 calibrated mIK parameters in Chapter 3, provides a unique opportunity to train a deep learning NN in order to predict accurate mIK parameters to represent the non-linear cyclic hysteretic behaviour of welded unreinforced welded web (WUF-W) connections. The objective of this Chapter is to develop, a set of trained NN which allow researchers and designers to model any RBS connection by defining the geometries of a RBS connection (shown in Figure 4.1b) as an input. This mitigates the need for complex, costly and time consuming detailed finite element (FE) analysis or full scale experimental tests required for calibration of the mIK models. The details of the developed NN are explained in the following sections and their efficiency in predicting the actual hysteresis response of the RBS connections is demonstrated.

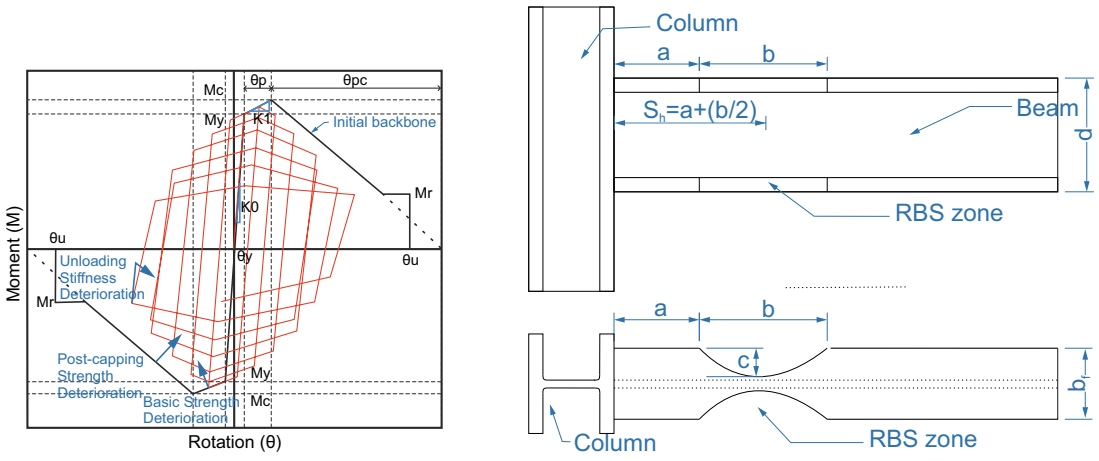

Figure 4.1: (a) Summary of the main mIK parameters and deterioration modes defining the model and (b) Definition of the parameters defining the RBS connection

4.3 Methodology

This study considers the bilinear modified-Ibarra-Krawinkler (mIK) zero length model utilising Basic Strength, Post-Capping Strength and Unloading Stiffness Deterioration in order to accurately capture the non-linear cyclic behaviour of RBS connections (refer to Lignos and Krawinkler (2011) for details of the definitions of each of the parameters which define the mIK model).

4.3.1 Calibrated mIK parameters for database models

For each of the 1480 different beam sections in the selected database from Chapter 3, subjected up to $0.07rad$ of SAC cyclic displacement based loading, an equivalent simple beam model using the program *Open System for Earthquake Engineering Simulation* – OpenSees (Mazzoni et al., 2007) was generated. The simple model consisted of an elastic beam sections with a zero length spring. The elastic beam section has the same elastic mechanical properties as the finite element models from Chapters 2 and 3 used to create the database. The mIK Bilinear zero length spring represents the non-linear behaviour of the RBS connections. This type of concentrated spring modelling has been used widely by many researchers (Maleki et al., 2018; Guan et al., 2018; Bravo-Haro and Elghazouli, 2018; Tsitos et al., 2018; Lignos et al., 2011b). The steel beam has been considered to be symmetric, and therefore, the deformation and strength in the positive and negative direction are the same.

The same boundary conditions and displacement based loading that was implemented in the selected database was used. While building each model by hand would be unrealistic and time consuming, coding of an interactive script in Matlab (The Mathworks Inc, 2019) adopted the bisector method to calibrate the models automatically. Using $0.07rad$ as the maximum damage criteria for RBS connections under Collapse Prevention in accordance with ASCE/SEI 41-17 (ASCE, 2017a), each simple beam model in OpenSees was loaded up to a displacement base loading of $0.07rad$ according to the SAC loading protocol. There were two general categories of sections in the database, sections that buckled or sections that did not buckle up to $0.07rad$ of loading. In cases where the sections buckled, θ_u could be obtained based on the hysteresis curve of the connections. However, in cases where the sections did not exhibit buckling until the loading cycle was completed, θ_u was taken as $0.07rad$. It should be noted that in seismic design applications, the connections are not expected to experience rotations larger than this value.

4.3.2 Results and trends from the calibrated mIK database

The calibrated mIK parameters for each of the database specimens are presented in Figures 4.2 and 4.3. The parameters calibrated for the mIK model are explained briefly in Table 4.1, while Figure 4.1a provides more details of the parameters.

Table 4.1: Definition of the calibrated mIK parameters used in the database

Definition	Symbol	Description	Equation
Effective yield moment	M_y	Strength parameter	-
Capping moment strength	M_c	Strength parameter	-
Yield rotation	θ_y	Deformation parameter	-
Pre-capping plastic rotation	θ_p	Deformation parameter	-
Post-capping plastic rotation	θ_{pc}	Deformation parameter	-
Ultimate rotational capacity	θ_u	Deformation parameter	-
Initial elastic stiffness	$K0$	Stiffness parameter	$K0 = M_y/\theta_y$
Pre-capping stiffness	$K1$	Stiffness parameter	$K1 = (M_c - M_y)/\theta_p$
Strain hardening ratio	as	Stiffness parameter	$as = K1/K0$
Cyclic deterioration parameter	λ	Controls the rate of strength and stiffness deterioration with increasing cycles	-

Figure 4.2 shows the general trends common for specimens that buckle and do not buckle. Figure 4.3 only shows the trends relevant to specimens that exhibit buckling, as they are constant for non-

buckling specimens. The calibrated results clearly show some general trends in the data with respect to the slenderness of the web (h/t_w), second moment of area of the corresponding full section (I_{FS}) and second moment of area of the RBS section (I_{RBS}). The trends presented in Figures 4.2 and 4.3 were the most clear and defined trends with respect to the selected RBS section geometrical properties.

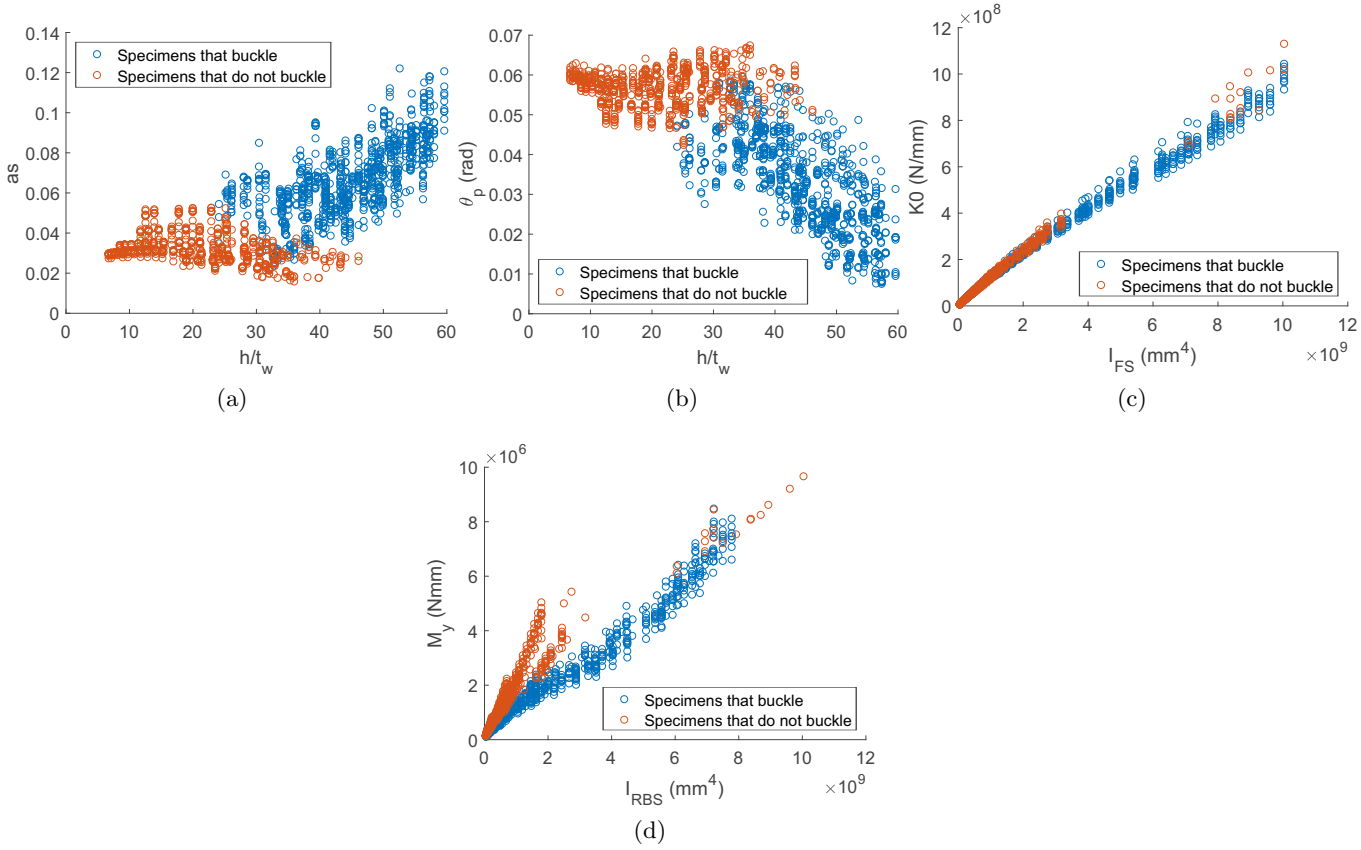

Figure 4.2: Scatter graphs showing the calibrated mIK parameters where buckling and non-buckling characteristics are similar (a) strain hardening ratio (as) and (b) pre-capping plastic rotation (θ_p) against web slenderness (h/t_w), (c) initial elastic stiffness ($K0$) against second moment of area of the corresponding full section (I_{FS}) and (d) effective yield moment (M_y) against second moment of area of the RBS (I_{RBS}).

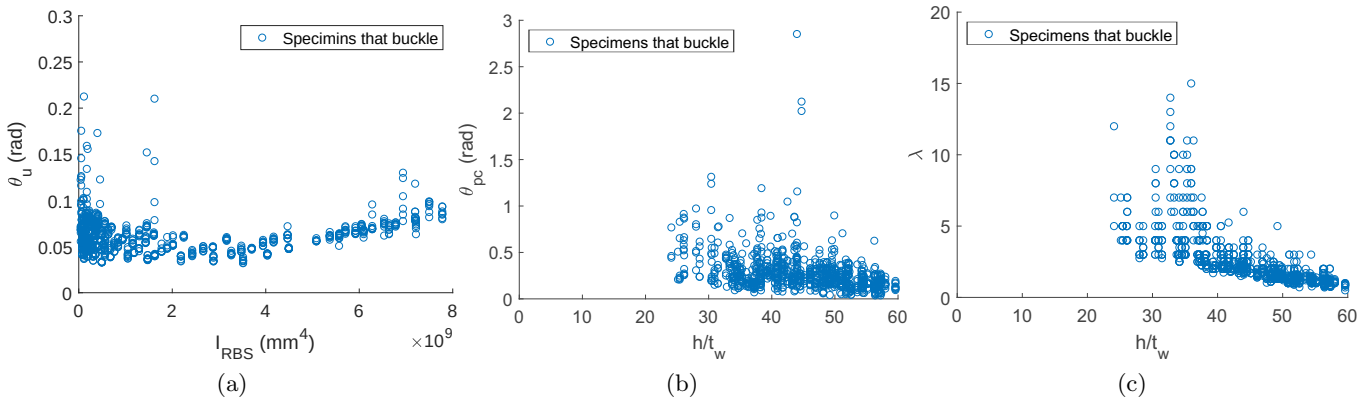

Figure 4.3: Scatter graphs show the calibrated mIK parameters where buckling occurs (a) ultimate rotational capacity (θ_u) against I_{RBS} and (b) post-capping plastic rotation (θ_{pc}) and (c) cyclic deterioration parameter (λ) against h/t_w

4.4 Set of deep learning Neural Network models

In order to predict the mIK parameters for any selected RBS section, using different beam sections and RBS geometries, a set of deep learning NNs and Supervised Machine Learning Classifications have been trained using the database of calibrated mIK results. This set of deep learning NN and Supervised Machine Learning Classifications was completed using the interactive software Matlab (The Mathworks Inc, 2019). As a result, the trained deep learning networks produced complex Matlab functions which were able to accurately predict the relative mIK parameter given the parameters defining the beam section size (b_f, d, t_f and t_w) and RBS geometries (a, b and c) as an input (refer to Figure 4.1b for definitions of these parameters). The flow chart in Figure 4.4 shows the logical procedure implemented and set of deep learning NN and Supervised Machine Learning Classification used to estimate the seven key mIK parameters identified above.

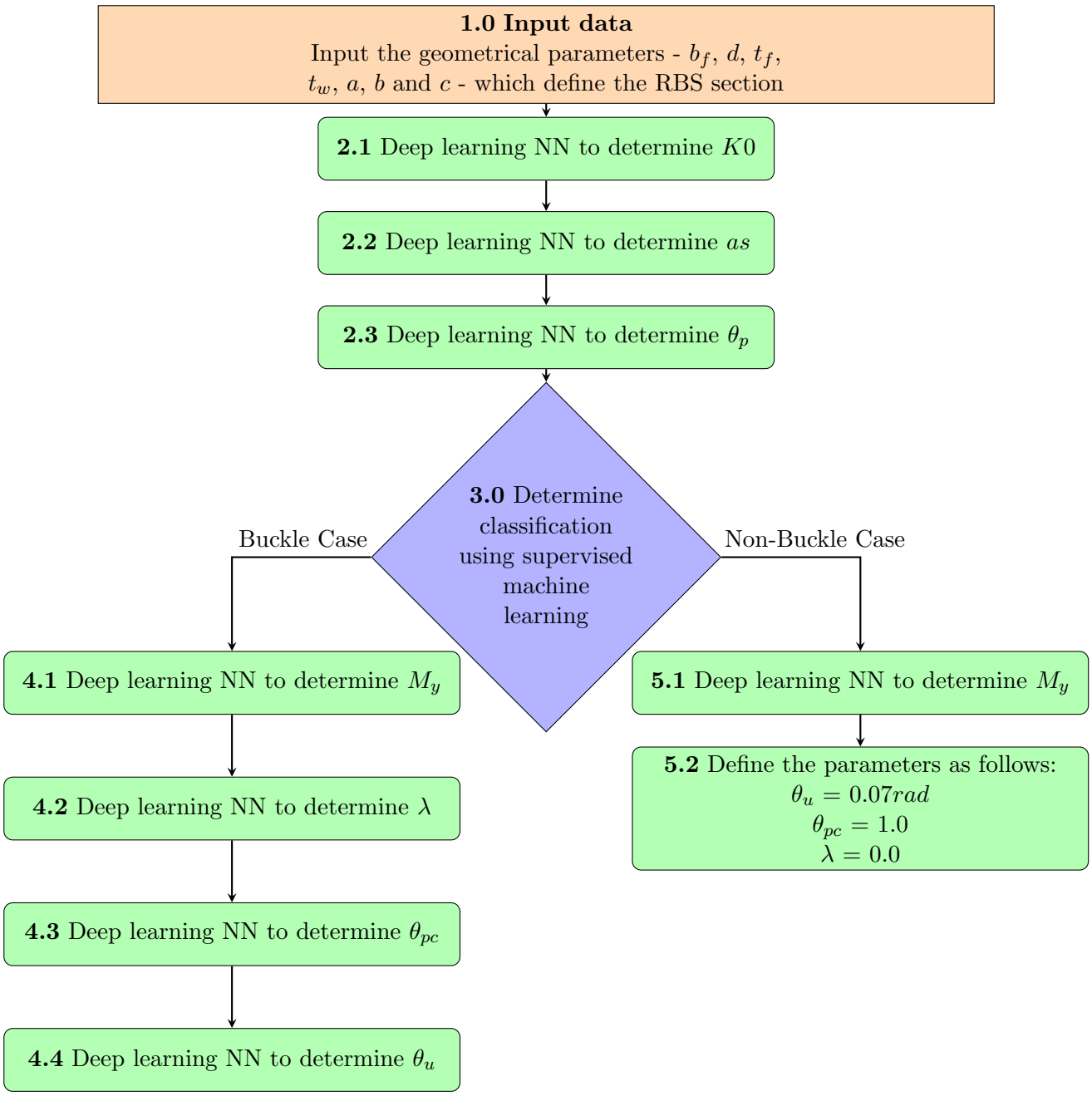

Figure 4.4: Flowchart depicting the logical procedure used to determine the mIK parameters of a RBS connection given the geometrical input data

4.4.1 Summary of Deep learning Neural Networks and classifications used

An interactive script was developed using Matlab (The Mathworks Inc, 2019) following the logical process shown in Figure 4.4, which can accurately predict mIK key parameters for any given geometrical parameters used to define a RBS connection (see Figure 4.1b). Process 1.0 in Figure 4.4 shows the input parameters required. Processes 2.1, 2.2 and 2.3 utilise a deep learning NN which predicts the $K0$, as and θ_p values common to all RBS connections. Process 3.0 distinguishes if the connection will or will not buckle under the applied SAC displacement based cyclic loading up to $0.07rad$. The accuracy of the classification was found to be within 97%. The remaining mIK parameters (M_y, λ, θ_{pc} and θ_u) are then determined depending on the classification during process 3.0. In cases where

buckling occurs, deep learning NNs 4.1, 4.2, 4.3 and 4.4 are used to determine the remaining mIK parameters respectively. If the connection does not buckle, deep learning NN 5.1 is used to determine M_y. The parameters θ_u, θ_{pc} and λ are assigned the value $0.07rad$, $1.0rad$ and 0.0, respectively. It should be noted that since the post capping plastic rotation is never achieved in this case, the value of λ is not needed in the mIK model and hence can be assigned to zero (which deactivates the post capping strength and stiffness deterioration). The post capping plastic rotation (θ_{pc}) is unknown and therefore an arbitrary value of $1.0rad$ (a large plastic number) can be assigned. The ultimate rotation (θ_u) can be also set to $0.07rad$, since any rotations experienced by the connection, beyond this point, can be assumed to have failed in terms of structural performance of the whole structural system. Refer to Section 4.5.1 and Section 4.5.3 for details of the classification algorithm and NN respectively.

4.5 Results and discussion

4.5.1 Classification

The bootstrap aggregating method is a type of bagging ensemble learning, which is based on the familiar decision tree method. As simple decision trees are prone to over-fitting the data, the bootstrap aggregating method is a simple and convenient method of improving the accuracy of a weak decision tree classifier (Breiman, 1996; Efron, 1993). In general, decision tree learning is classed as a weak learner. To train a weak learner effectively, many different bootstrap aggregating replicas of the dataset should be made, and individual decision trees should be grown on these replicas. Each of these bootstrap replicas are obtained by randomly selecting predictors for M observations out of N with replacement, where M is the size of the sample and N is the size of the dataset (Breiman, 1996; Efron, 1993). In order to find the predicted response of the trained bootstrap ensemble, an average of the predictions across the individual grown decision trees should be taken. In general, the bagging predictor aggregation, averages out the multiple bootstrap versions of the learning sets, in order to generate an aggregated predictor. Using an ensemble-bootstrap-aggregating method is a simple way of increasing the accuracy of an existing method (decision trees) by looping the boot strap sample and repeating the aggregation. The prediction or classification is then determined through an average of the separate bootstrap classifications (otherwise known as voting). Figure 4.5 demonstrates how the bootstrap aggregating ensemble algorithm is used in this study (Breiman, 1996; Efron, 1993).

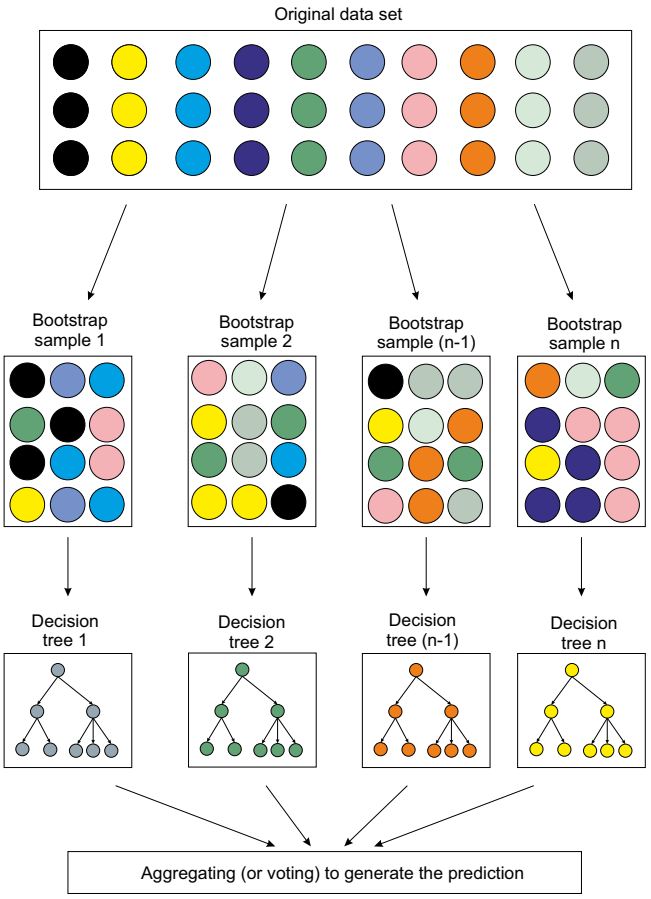

Figure 4.5: Bootstrap aggregating ensemble method of tree bagging used in this study

The Statistics and Machine Learning Toolbox in the interactive computer programme Matlab (The Mathworks Inc, 2019) is used to create the supervised ensemble bootstrap aggregating algorithm for classification of process 3.0 in the flowchart in Figure 4.4. A sensitivity analysis on the number of learning cycles and maximum number of splits for the supervised ensemble bootstrap aggregating algorithm was carried out. 30 different learning cycles and a maximum number of splits in the decision tree of 100 produced highly accurate results without compromising the computational time or complexity of the algorithm. The ensemble-bootstrap-aggregating algorithm achieved an accuracy of 96%, shown through a confusion matrix presented in Figure 4.6. This confusion matrix compares the number of sections which the classification algorithm predicted correctly and incorrectly.

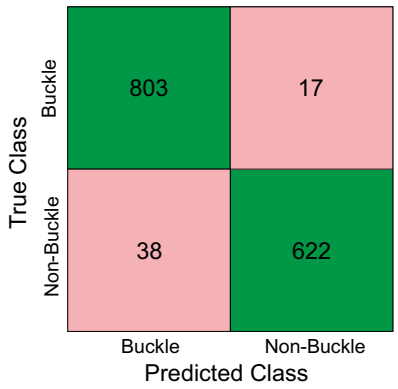

Figure 4.6: Confusion matrix for the classification of the sections

4.5.2 Post capping plastic rotation, Ultimate rotational capacity and Cyclic deterioration parameter of parameters equal to non-buckling cases

Process 5.2 in Figure 4.4 assigns arbitrary values to certain parameters on the condition that the section does not buckle according to process 3.0. As the peak moment and ultimate moment were never reached during the cyclic loading protocol in these cases, the post capping plastic rotation, ultimate rotation and cyclic deterioration parameters could not be defined. However, appropriate values must be assigned to these parameters in order to define the mIK model. Take for example the calibrated mIK model shown in Figure 4.7. It is shown that the post capping plastic rotation, ultimate rotation and cyclic deterioration parameters are not practically needed when defining the cyclic hysteresis of the RBS connection in this case since no stiffness and strength degradation is observed. Therefore, arbitrary values of $0.07rad$, $1.0rad$ and 0.0 have been used to define the mIK parameters θ_u, θ_{pc} and λ respectively. Table 4.2 summaries these values for the modelling of non-buckling RBS connections.

It should be noted that in order to find the true values for defining the post capping plastic rotation, ultimate rotation and cyclic deterioration of non-buckling calibrated mIK models, the displacement based cyclic loading protocol used in the FE models should be increased until the ultimate rotation θ_u and corresponding moment (which defines the post capping plastic rotation θ_{pc}) is reached. The ultimate rotation (θ_u) is defined as the point on the cyclic backbone curve which corresponds to a 20% loss in the strength from the peak moment of the hysteresis. However, in the performance-based design of steel structures in ASCE/SEI 41-17 (ASCE, 2017a), $0.07rad$ of rotation is considered to have achieved a Collapse Prevention (CP) design criteria (while the limit state of ASCE/SEI 41-17 (ASCE, 2017a) specifies $0.07 - 0.00030d\ rad$, the upper bound value of $0.07rad$ has been used for simplicity). Therefore, in the performance-based design of steel structures, any structure that can achieve a rotation of $0.07rad$ can be considered to have achieved the CP level. During the non-linear analysis of structures, a steel frame which achieves the CP level is considered to have collapsed and the analysis is terminated. This indicates that using the values proposed in Table 4.2 will not change the mIK model of this type of connections for the practical range required in seismic design applications.

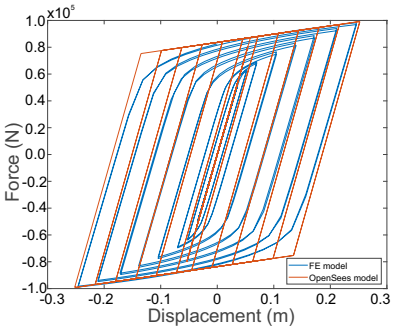

Figure 4.7: Example of a non-buckling calibrated mIK model

Table 4.2: Values assigned to the non-buckling parameters

mIK Parameter	Value assigned
θ_u	$0.07rad$
θ_{pc}	$1.0rad$
λ	0.0

4.5.3 Neural Network

In this study, a cascade forward-feed NN with hidden layers was used for all the deep learning NN in Figure 4.4. Figure 4.8 shows how forward-feed NNs operate. The input layer consists of the input parameters which define the RBS connection (d, b_f, t_w, t_f, a, b and c – shown in Figure 4.1b). The hidden layers are connected with the input layer with modifiable weighted connections. In turn, the hidden layers are all connected to the output layer which produces the desired predicted parameter.

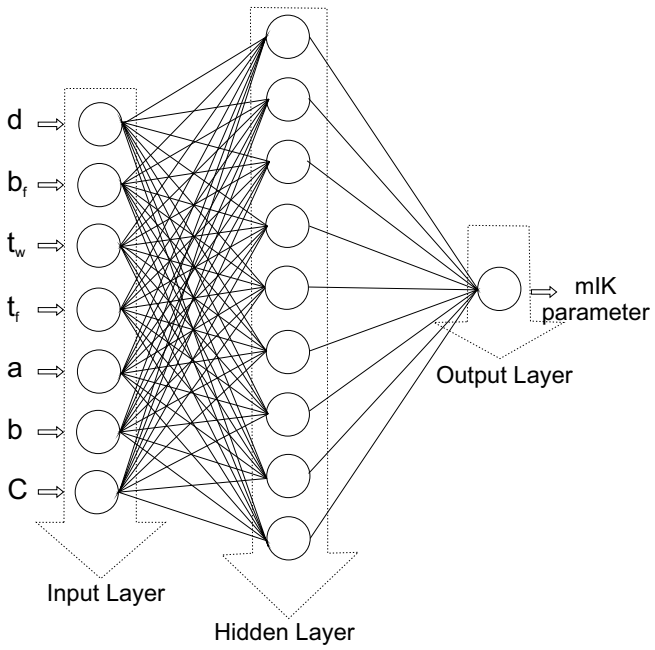

Figure 4.8: Simple depiction of a NN with one hidden layer

A Matlab (The Mathworks Inc, 2019) code was developed to create and train the networks 2.1, 2.2, 2.3, 4.1, 4.2, 4.3, 4.4 and 5.1 from the flow chart in Figure 4.4. As mentioned above, for NN a cascade forward feed network was adopted to train the network. Cascade forward feed networks are similar to feed-forward networks, but they include a connection from the input value and every previous layer into the following layers. A number of different parameters control the training process of the NN. Table 4.3 summarises the parameters which control the cascade forward feed network adopted as a result of trial and error permutations for each network leading to the highest accuracy. 75% of the data from the dataset was used to train the NN and 25% of the data was used to validate the NN.

Four different training functions were tested through trial and error in the cascade forward feed network. The training functions considered were: the Bayesian regularization backpropagation, the Levenberg-Marquardt backpropagation, the conjugate gradient backpropagation with Fletcher-Reeves updates and the Resilient backpropagation (Scales, 1985). The conjugate gradient backpropagation with Fletcher-Reeves updates was adopted for all NN as this gave the most stable accurate networks compared to the other training functions investigated. Refer to Scales (1985) for further details of this training function. This function updated the weight and bias values in accordance with Fletcher-Reeves updates.

The number of hidden layers was kept at four, apart from network 4.3 which when trained with only two hidden layers provided more reliable results compared to four hidden layers. This was because by using four hidden layers the NN was prone to over fitting the data, while reducing the number of hidden layers helped to prevent over fitting and increased the accuracy of the NN. The number of neurons for each hidden layer was self prescribed based on experience from other trained networks. The number of epochs was set to 1000. Distributed parallel computing was utilised in Matlab (The Mathworks Inc, 2019) to help speed up the training time. Four multicore CPU cores were opened up to allow the algorithms to run in parallel. This made full use of all four cores available on the single PC used to train the networks and saved computational power. Many different regulation parameters were tried through the trial and error permutation process. The aim was to have the same regulation parameter across all NNs. However, in the end networks 4.2 and 4.3 required a higher regulation

parameter to provide reliable predictions due to the much larger spread in data.

Table 4.3: Parameters used in the cascade forward-feed NNs

Process No.	mIK Parameter	No. Hidden Layers	No. of neurons per layer	Regulation parameter	No. of iterations
2.1	$K0$	4	60-60-40-40	0.001	10,000
2.2	as	4	60-60-40-40	0.001	10,000
2.3	θ_p	4	60-60-40-40	0.001	10,000
4.1	M_y	4	60-60-40-40	0.001	10,000
4.2	λ	4	60-60-40-40	0.01	10,000
4.3	θ_{pc}	2	60-40	0.2	20,000
4.4	θ_u	4	60-60-40-40	0.001	1000
5.1	M_y (non-buckle)	4	60-60-40-40	0.001	1000

The results for the trained networks 2.1, 2.2, 2.3, 4.1, 4.2, 4.3, 4.4 and 5.1 are shown in Figures 4.9, 4.10 and 4.11. The plotted results compare how accurate the database is at predicting the mIK parameters. The Y-axis for all graphs in Figures 4.9, 4.10 and 4.11 shows the predicted value from the respective network and the X-axis shows the true mIK value from the database. A statistical regression value R, which represents the spread of data from the an x-y line (which would indicate an accuracy of 100%) has been calculated for each network. An R value of 1.0 would indicate that the network can predict the desired result to an accuracy of 100%. A summary of these R values which represent the accuracy of the networks is shown in Table 4.4 in terms of its variation from the true value.

Table 4.4: Values of R which show the accuracy of the networks trained

Network No.	mIK Parameter	R Value
2.1	$K0$	0.99995
2.2	as	0.98878
2.3	θ_p	0.99161
4.1	M_y	0.99989
4.2	λ	0.99407
4.3	θ_{pc}	0.67676
4.4	θ_u	0.98503
5.1	M_y	0.99980

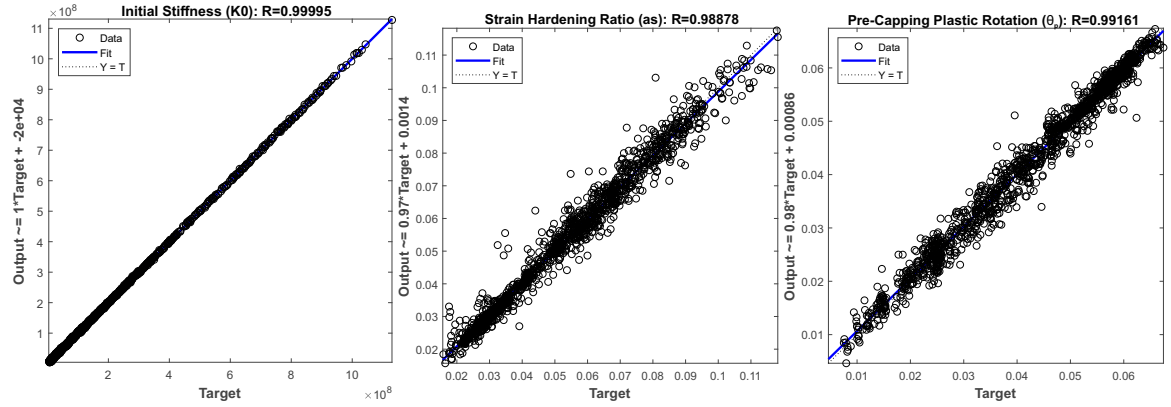

(a) (b) (c)

Figure 4.9: Comparisons of the predicted mIK data with the true mIK data for all sections in the database for networks: (a) 2.1 initial elastic stiffness ($K0$), (b) 2.2 strain hardening ratio (as) and (c) 2.3 pre-capping plastic rotation (θ_p).

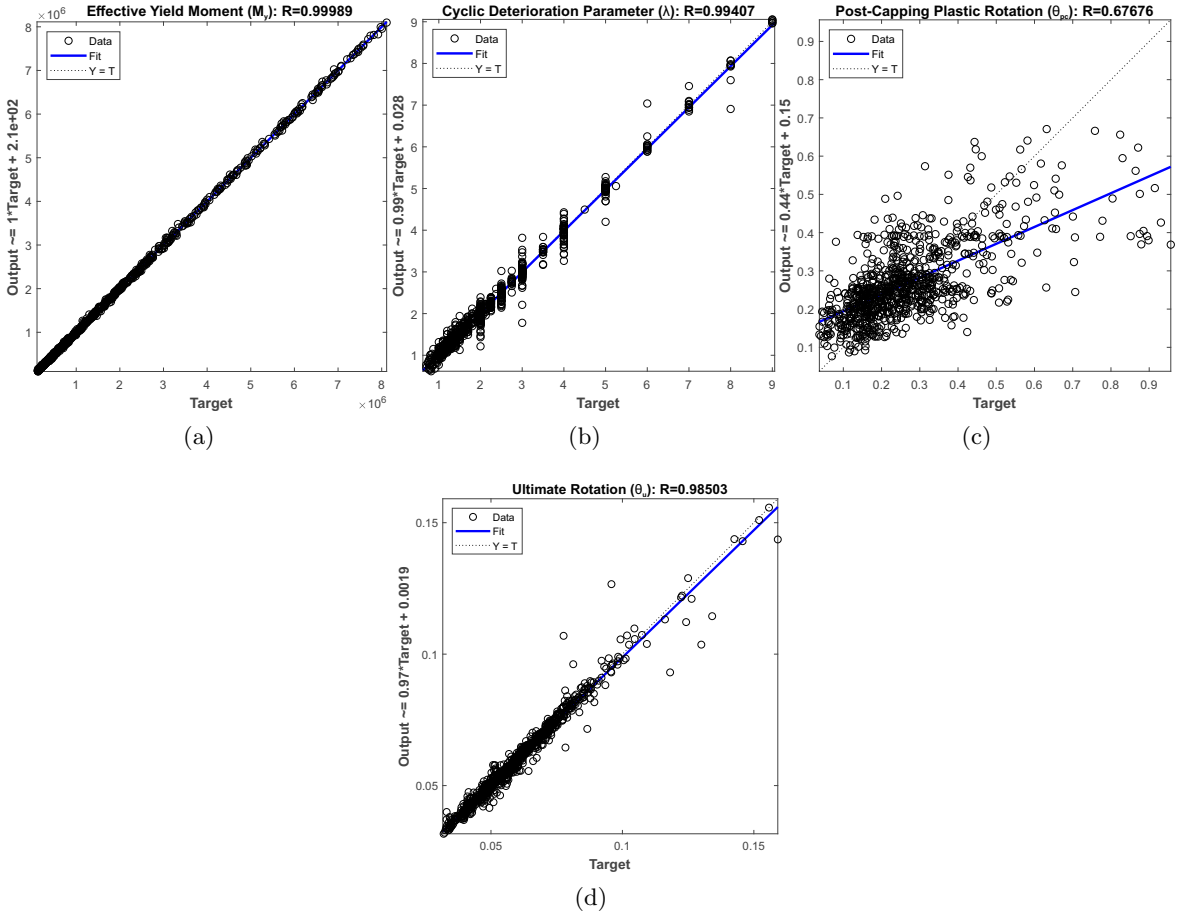

(a) (b) (c) (d)

Figure 4.10: Comparisons of the predicted mIK data with the true mIK data for sections in the database which buckle for networks: (a) 4.1 effective yield moment (M_y), (b) 4.2 cyclic deterioration parameter (λ), (c) 4.3 post capping plastic rotation (θ_{pc}) and (d) 4.4 ultimate rotational capacity (θ_u).

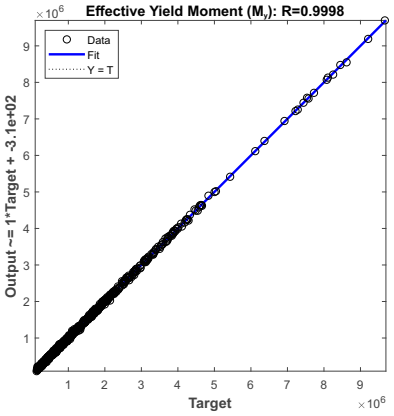

Figure 4.11: Comparisons of the predicted mIK data with the true mIK data for sections that do not buck for networks 5.1 effective yield moment (M_y).

The results in Figures 4.9, 4.10a, 4.10b, 4.10d and 4.11 show that the NN are capable of predicting the non-linear cyclic behaviour of RBS connections to a high level of accuracy. Figure 4.10c shows that the least accurate of the NN was the λ prediction, however, this still gave reasonable results in terms of the R value which corresponds to an accuracy of 68%.

4.6 Conclusions

The aim of this Chapter is to develop a fast and reliable method which can accurately predict the complex non-linear hysteresis behaviour of any RBS connection. Using a comprehensive database of calibrated modified-Ibarra-Krawinkler (mIK) models, used to represent the non-linear cyclic hysteresis behaviour of steel RBS connections, it was shown that general trends can be obtained for the key mIK input parameters with respect to the slenderness of the web, second moment of area of the corresponding full section and second moment of area of the RBS section. However, existing mathematical equations do not take into account the effects of some of these parameters, and therefore, may not lead to accurate predictions. Besides, there is currently no practical method available that is capable of predicting the mIK model parameters for different RBS configurations. To address these issues, in this Chapter a Supervised Machine Learning Classifier and a set of Deep Learning NNs was developed based on the selected database of full cyclic hysteretic behaviour of 1480 RBS connections, calibrated to capture accurately the non-linear cyclic hysteretic behaviour of RBS connections. These deep learning NNs and classifier were developed using the interactive software Matlab (The Mathworks Inc, 2019). The ensemble-bootstrap-aggregating algorithm used for classifying the sections as possessing either buckle or non-buckle characteristics, achieved an accuracy of 96%. A set of cascade forward-feed NNs with hidden layers were also used to predict the mIK parameters achieving a mode accuracy of 98%. Parameters which control the training of the cascade forward-feed networks were established using trial and error permutations. As a result of this research, a practical method is proposed which is capable of predicting improved models that can capture accurately the non-linear cyclic response of any RBS connection only based on the beam and RBS geometries as input information. This mitigates the need for complex, costly and time consuming detailed finite element (FE) analysis or full scale experimental tests generally required to calibrate the mIK model parameters. The set of deep learning neural networks and classifier algorithm developed in this research should prove useful in the practical design and performance assessment of RBS connections and structural systems. The developed framework can be also used as an efficient and low computational cost tool to optimise the design of RBS connections to achieve the best seismic performance.

Chapter 5

More Efficient Design of Moment Resisting Steel Frames with RBS Connections

As a result of the conclusions drawn in Chapter 4 implementation of the method for accurate prediction of the cyclic behaviour of RBS connections has been demonstrated through investigation of a four storey steel moment frame. This chapter aims to provide a proof of concept by building on the work developed in Chapters 2, 3 and 4. Where appropriate, the specific chapters and sections of this research have been referenced appropriately.

5.1 Abstract

Chapters 2, 3 and 4 of this research have demonstrated that RBS connections are a widely adopted method of creating a stable ductile steel frame capable of absorbing larger amounts of seismic energy compared to conventional fully welded connections. The RBS connections can efficiently reduce the seismic demand (e.g. plastic rotations) in the columns and transfer this damage into the beams, thus protecting the critical gravity load carrying system and prevent collapse during strong earthquake events. The results presented in the previous chapters highlighted that the geometries of RBS connections are not currently considered in the design of steel RBS frame systems. Chapter 2 concluded that the c geometry which defines the "cut" of the RBS, has the most significant influence over the key seismic design parameters of RBS connections. In addition, Chapter 3 generated a large dataset of improved calibrated modified-Ibarra-Krawinkler (mIK) models to simulate accurately the nonlinear cyclic behaviour of RBS connections. Finally, Chapter 4 developed highly accurate and reliable deep learning NNs, with an accuracy of 96%, capable of predicting the mIK parameters for any size and geometry of RBS connections given the beam and RBS geometry as an input. The aim of this Chapter is to improve the performance of steel RBS frames by fine tuning the RBS geometry in selected locations within the frame. First a four storey Welded-Unreinforced-Flange (WUF) connection frame (frame 1) was developed as a benchmark. This frame was then subjected to a Maximum Considered Earthquake (MCE) with a Peak Ground Acceleration (PGA) equal to 0.6g. The frame was assessed and the performance of this frame was improved by utilising RBS connections across floors that exhibited plastic rotations in the columns (frame 2). Analysis of this frame under the same MCE indicated an improved performance but still with some design code violations in terms of strong column-weak beam concept. Finally, the performance of this RBS frame was fine tuned by adjusting the RBS cut (geometry) of the connection within the storey level with plastic hinges in the columns (frame 3). An improved frame performance was exhibited under the same MCE and considered to be the practical optimum RBS frame design. This powerful trial and error permutation approach demonstrates how a more efficient performance of RBS steel moment resistant frame can be achieved by controlling the

cut (geometry) of the RBS connection. In order to demonstrate this process a non-linear model of a typical non-linear four storey steel structure was developed in OpenSees. The effects of the non-linear material, P-Delta ($P\Delta$) effects and connection panel zones were all included. The RBS connections in the frame were modelled using the mIK model. A practical performance-based design framework was then developed by providing a link between the NNs developed in Chapter 4 and the OpenSees model to update the parameters of the mIK model based on the selected beam section and RBS geometry. This process was automated and controlled using Matlab. This provided the opportunity to update the design without the need to conduct detailed finite element (FE) analysis in ABAQUS.

5.2 Background

As previously mentioned, the RBS connections can provide a safe and ductile fuse behaviour in the beams in order to protect the columns from significant damage (see Chapter 2 Section 2.2, Chapter 3 Section 3.2.1 and Chapter 4 Section 4.2.1 for a background to RBS connections). Generally, RBS connections are considered to have good capabilities of improving a frames performance, refer to Chapter 3 Section 3.2.1 for a detailed review of frame analysis. In order to accurately represent RBS connections in a non-linear dynamic analysis, appropriate models which can capture their non-linear behaviour should be adopted. The most widely adopted model is the modified-Ibarra-Krawinkler (mIK) model. See Chapter 3 Section 3.2.2 and Section 3.2.3 and Chapter 4 Section 4.2.3 for more information of the methods and models for representing the behaviour of RBS connections.

The aim of this Chapter is to implement and demonstrate the potential of a simple trial and error method for improving the performance of steel moment resistant RBS frames. First, a moment resistant WUF frame (frame 1) based on Maleki et al. (2018) was adopted as a base frame for comparison purposes. Then, the WUF frame was subjected to a MCE equal to $0.6g$ in order to assess its performance. The frames performance was improved by the provision of RBS connections as an alternative to WUF connections. Finally, the performance of the frame was fine tuned by adjusting the geometries of the RBS connection.

The frames were modelled in OpenSees (Mazzoni et al., 2007), which considered non-linear material properties, $P\Delta$ effects of the frame system, detail of the connection panel zone and hysteretic models to capture the cyclic behaviour of WUF and RBS connections. The NNs developed in Chapter 4 were used to develop the necessary parameters for the mIK model depending on the beam and RBS geometries. The model was build using Tcl (Mazzoni et al., 2007) programming language and the analysis process was automated and controlled using Matlab (The Mathworks Inc, 2019) which allowed fast and efficient analysis of the frame system mitigating the need for complex finite element (FE) analysis.

5.3 Methodology

Capacity design of steel moment resistant frames is covered in BS EN 1998-1 (British Standards Institute, 2005) and ASCE/SEI (ASCE, 2017a). Columns must have a larger capacity compared to beams which will allow plastic deformations to occur in the beams and thus protecting the columns. In order to assess the efficiency of the steel moment resistant frame, a performance-based design was adopted using deformation control as the performance indicator. The deformations of the columns were used as an indication of the damage sustained by the frame ASCE (2017a). In this study, the plastic rotations of the columns have been used to quantify the plastic deformation that occurs within the columns. Plastic hinges have been identified in the frame when the maximum rotation experienced by the column whilst subjected to the MCE, exceeds the elastic rotational capacity of the element.

5.3.1 Frame model

In order to investigate the behaviour of steel frames in this research, a four story Welded-Unreinforced-Flange (WUF) frame was adopted from Maleki et al. (2018) and used as a base frame mode. OpenSees (Mazzoni et al., 2007) was used to build the frame model which was coded using TCL programming language. The 4 sotry WUF from Maleki et al. (2018) was designed based on ANSI/AISC360-16 AISC (2016c), ANSI/AISC341-16 AISC (2016a) and IBC IBC (2015). Figure 5.1 shows the frame model adopted. Table 5.1 shows the column and beam sections adopted for the 4 storey frames used in this research. Figure 5.2 and Table 5.2 show the location of these elements in the four storey frame. In order to reduce to complexity of the analysis the frame was assumed to be biaxial symmetry in plan which allowed only one side of perimeter moment frame to be modelled. The perimeter frame adopted was designed to carry one half of the buildings seismic weight.

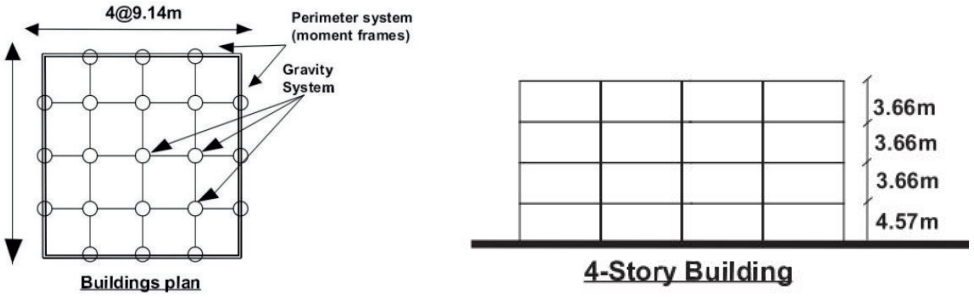

(a) (b)

Figure 5.1: Frame model adopted from Maleki et al. (2018) showing (a) plan of the moment resistant perimeter frame and (b) the elevation of the frame (Maleki et al., 2018).

Table 5.1: Section sizes used to model the four storey frames

Storey Number	Beam Section	Corner Column Section	Intermediate Column Section
1	W33x130	W14x311	W14x233
2	W27x114	W14x311	W14x193
3	W27x94	W14x176	W14x99
4	W24x68	W14x176	W14x99

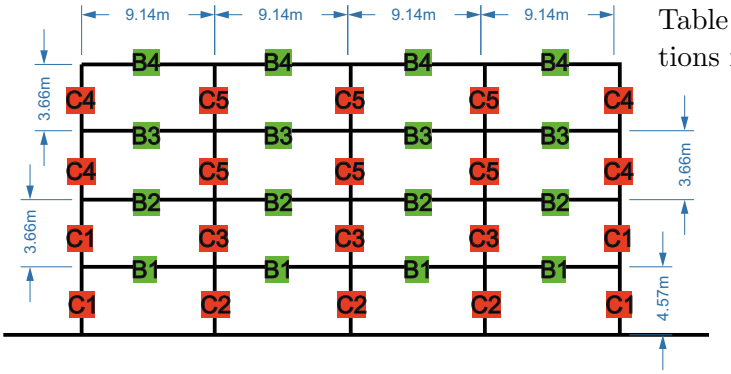

Figure 5.2: Locations of the elements in the typical four storey frame corresponding to the section sizes in Table5.2.

Table 5.2: Section sizes for the element ID locations in Figure 5.2.

Element ID	Section Size
C1	W14x311
C2	W14x233
C3	W14x193
C4	W14x176
C5	W14x99
B1	W33x130
B2	W27x114
B3	W27x94
B4	W24x68

5.3.2 Connection, panel zone and element modelling

Table 5.3: Frame reference and frame types investigated

Frame Reference	Frame Type
Frame 1	WUF
Frame 2	RBS
Frame 3	IMPROVED

The columns were modelled using distributed non-linear behaviour which could capture the plastic hinge formation. Elastic elements were used between the connection spring models to model the beams. In order to model the connection behaviour a concentrated phenomenological spring model was utilised. The WUF connection for frame 1 (refer Table 5.2) was adopted based on the modelling procedures in Moon and Han (2008) and Han et al. (2007). The modelling for the RBS connections in frames 2 and 3 (refer Table 5.2) were adopted based on the modified-Ibarra-Krawinkler (mIK) model (Ibarra et al., 2005). The parameters for the mIK model in frame 2 were adopted based on Maleki et al. (2018) where the c cut (geometry) was assumed to be taken as the average value. The parameters for the mIK model in frame 3 were determined using the NNs developed in Chapter 4 of this research.

In order to model the panel zone and connection joint between the column and beam, the box model, which consists of rigid elements with a zero-length spring to control the shear behaviour of the panel zone was adopted. The equations to model the panel zone were taken from (SAC Joint Venture, 2000c) which took the non-linear behaviour into account. The panel zones were modelled using the adopted techniques from Maleki et al. (2018).

The design loads were adopted from Maleki et al. (2018) and based on ASCE/SEI 7-10 (ASCE, 2010). The self-weight of the beams and columns were lumped at each element connection. To calculate the lumped mass matrix, the formulation $1.0 \cdot \textit{Dead Load} + 0.2 \cdot \textit{Live Load}$ was used. The lumped mass was calculated as half of the member that was framed into the connection. The dead weight and gravity loadings of the structure were assigned to the appropriate nodes and elements in order to represent the transfer of gravity loads accurately. The base of the moment perimeter frame (column elements as ground level) were fixed in both directions, whereas, the base of the leading column which simulates the weight of the gravity frame was pinned at ground level.

A leaning column, modelled as rigid elements is modelled which takes half of the total load acting on the gravity system part of the frame, this leaning column takes $P\Delta$ effects into account. Very small spring stiffness of zero-length-springs were used at the beam column joints to ensure that significant moments were not attracted. Truss elements were axially rigid and connected the leaning column to the frame for transfer of the $P\Delta$ effects. A typical two story one bay extraction from the 4 storey RBS frame (including the leaning column for $P\Delta$ effects) is shown in Figure 5.3.

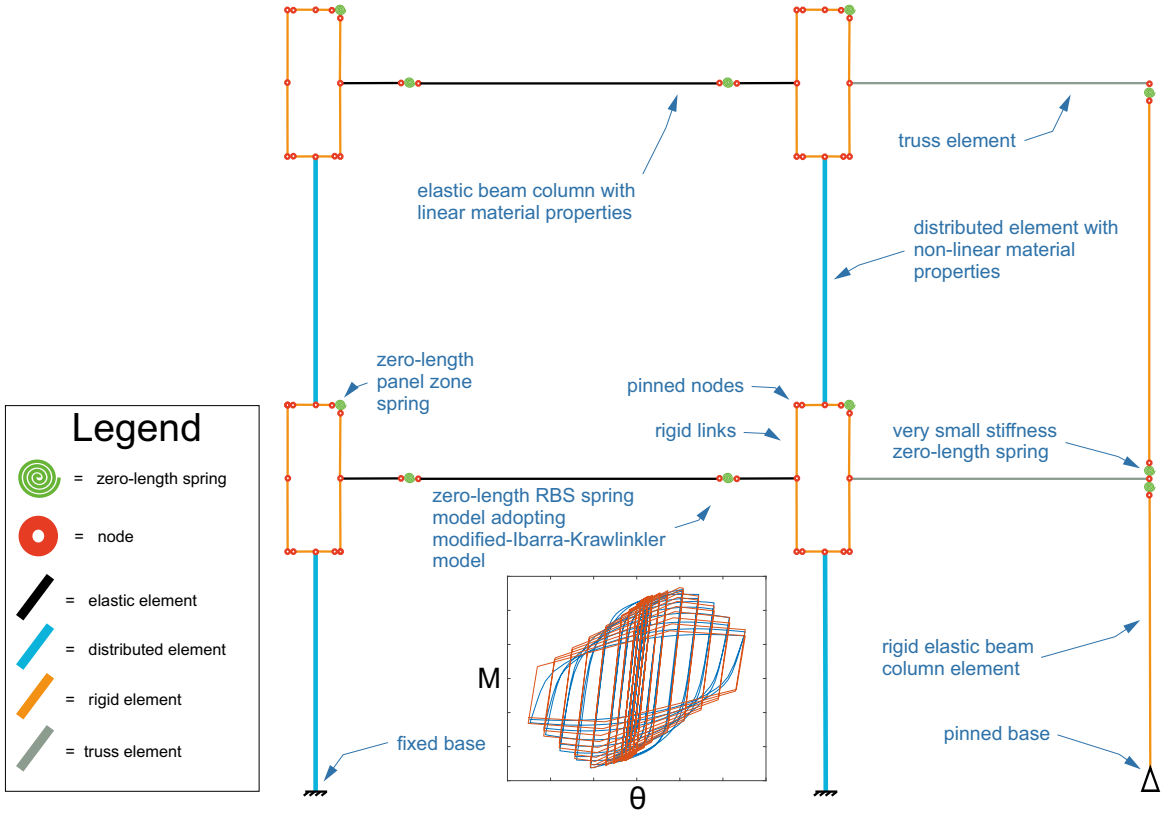

Figure 5.3: Typical two storey one bay extraction from the four frame RBS to demonstrate the modelling techniques used

5.3.3 Plastic hinge length

As the columns distribute the plasticity within the element, the rotation of the columns was determined by calculating the area below the curvature profile of the column within the plastic hinge length. Ten integration points were assigned to the column elements in the model. Equations were used to calculate the plastic hinge length of the columns. These equations taken from Elkady and Lignos (2018) were based on FE database of 50 wide-flange steel columns and achieved an accuracy of 95%.

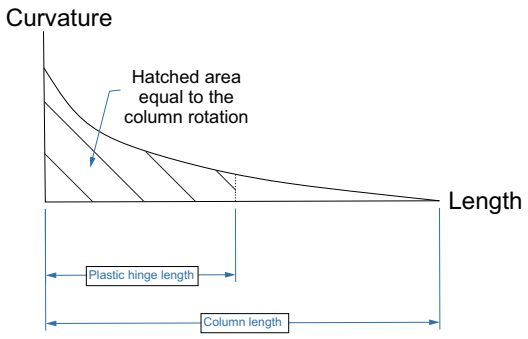

Figure 5.4: Calculation of the rotation of the column defined as the area below the curvature profile of the column between the column end and plastic hinge length

5.3.4 Synthetic earthquake applied

A synthetic earthquake was generated using the software SIMQKE (Vanmarke, 1976). The synthetic earthquake corresponds to a Maximum Considered Eartquake (MCE) corresponding to a Peak Ground Acceleration (PGA) of $0.6g$. This sythetic earthquake was designed to be compatible with the elastic design spectrum of BS EN 1998-1 BSI (2004). As the frame is considered to be symmetric, this earthquake ground motion was applied to both sides of the model respectively in order to determine the maximum demands in all elements

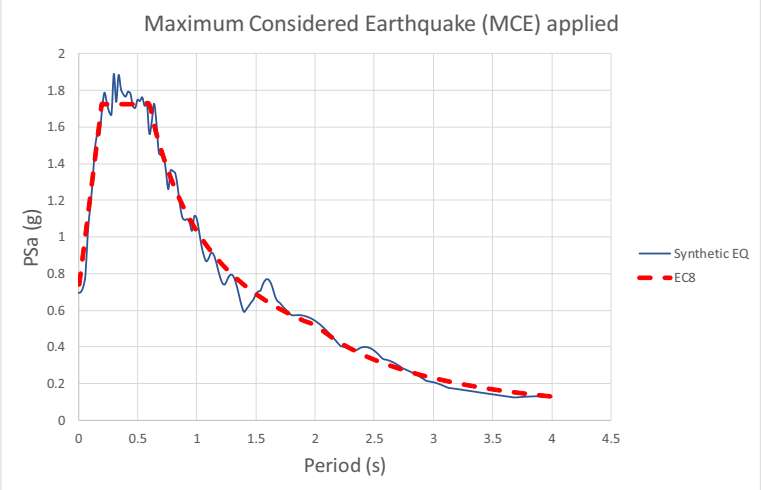

Figure 5.5: Maximum considered earthquake equal to $0.6g$ applied to the model.

5.3.5 Iterative process to achieve the optimum RBS frame

In this study a simple methodology for achieving a more efficient performance of a steel moment resistant RBS frame by controlling the geometry of the RBS is shown in the flowchart pictured in Figure 5.6. This simple methodology utilises a step by step iterative permutation approach until a more efficient result has been achieved.

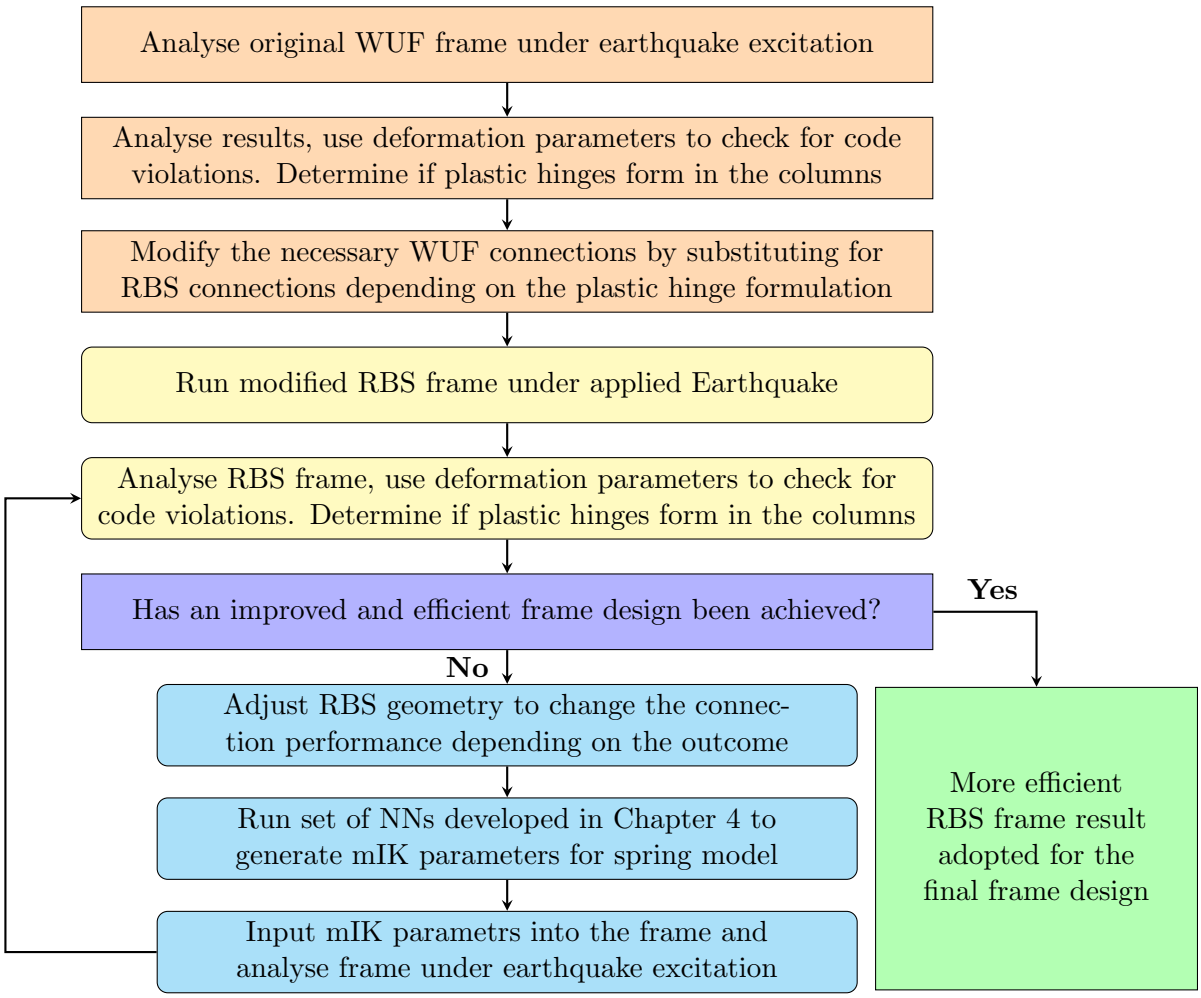

Figure 5.6: Flow chart to demonstrate the iterative design methodology adopted in this study in order to achieve the most efficient result

5.4 Results

The frame periods from the eigenvector analysis for frame 1 (WUF), frame 2 (RBS) and frame 3 (More Efficient) are shown in Table 5.4. As expected, the presence of RBS connections increased the period of the frame. The maximum roof displacement and maximum base shear recorded under the Synthetic MCE are presented in Table 5.4 also.

Table 5.4: Periods for the three frames analysed

Frame Type	Frame Label	Period (s)	Max. Base Shear (kN)	Roof Displacement (m)
WUF	Frame 1	0.649	8195	0.2067
RBS	Frame 2	0.779	5858	0.2359
Optimum	Frame 3	0.780	5895	0.2392

The maximum base shear and inter-storey drift distributions for the three frames are shown in Figure 5.7 below. As expected, the WUF frame experienced larger maximum base shears and less inter storey drift distributions, while the two RBS frames exhibited larger drift distributions and

smaller base shears. This was due to the RBS connections producing a more flexible and less stiff frame compared to the WUF frame.

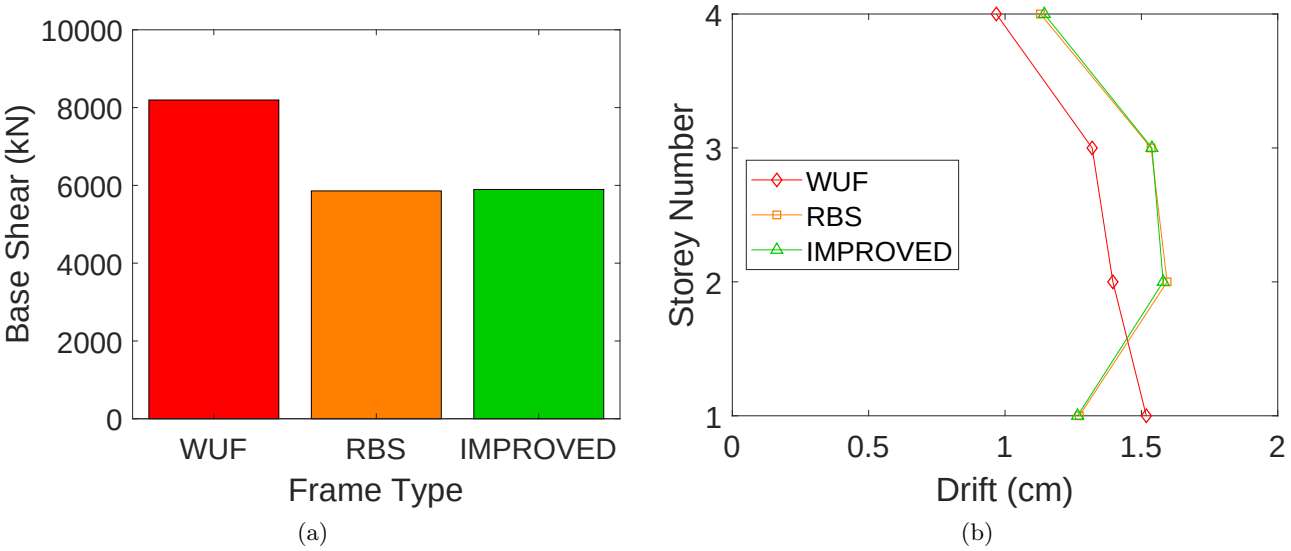

(a) (b)

Figure 5.7: (a) Maximum base shear and (b) the inter story drift distributions, for the WUF, RBS and More Efficient frames under the MCE record.

The simple step by step methodology shown in Figure 5.6 was adopted in order to determine the most efficient frame result. A brief summary of this methdology is shown in Figure 5.8. In order to assess the performance of each frame, a synthetic MCE was applied and the distribution of plastic hinges which developed within the columns was analysed. In order to ensure that the capacity design criteria according to BS EN 1998-1 (BSI, 2004) was satisfied for the frame, no plastic hinges should form within the columns. The plastic hinge distribution throughout the three frames under the Synthetic MCE of 0.6g are presented in Figure 5.9. Details of the connections for each frame are summarised in Table 5.5.

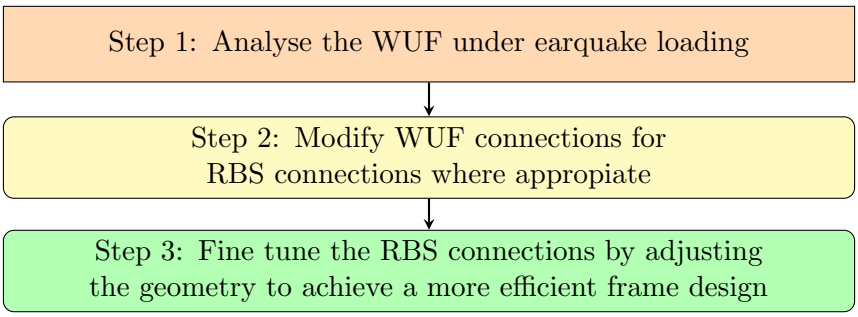

Figure 5.8: Summary of step by step methodology from Figure 5.6

Figure 5.9a presents the distributions of the plastic hinges which formed in the columns of the WUF frame (frame 1) under the MCE. A soft storey failure at the third floor developed. Figure 5.9a shows that plastic hinges form in all columns across floors 1, 2 and 3. The development of these plastic hinges violates the design regulations for a Medium to High ductility level according to BS EN 1998-1 (BSI, 2004).

In order to solve this problem of plastic hinges developing within the columns, RBS connections at all locations in floors 1, 2 and 3 were proposed. No RBS connections were fitted to floor 4 as no plastic hinges in the columns developed at this level. Figure 5.9b shows the distribution of the plastic hinges which formed within the columns for this RBS frame (frame 2). In this case, the RBS connections protected the exterior columns in floor 3 and all the columns in floors 1 and 2. However, plastic hinges still formed within the interior columns of floor 3. This floor suffered from extensive localised damage.

However, in order to solve this problem, the cut (c geometry) for the RBS connections within floor 3, was increased from the average value to the maximum value (according to the limits specified in ANSI/AISC 358-16 (AISC, 2016b) refer to Chapter 2 Section 2.3.2 Table 2.3). Refer to Table 5.5 for a summary of the connections on each floor. The set of NNs developed in Chapter 4 were used to generate the mIK parameters which define the RBS spring model. Figure 5.9c (frame 3) shows that under the MCE EQ, no plastic hinges formed within the columns, thus providing a safe and stable frame which protected the columns. This is considered to be the most efficient frame design. This frame sustained the MCE earthquake without damage in the columns and thus protected the gravity load bearing system.

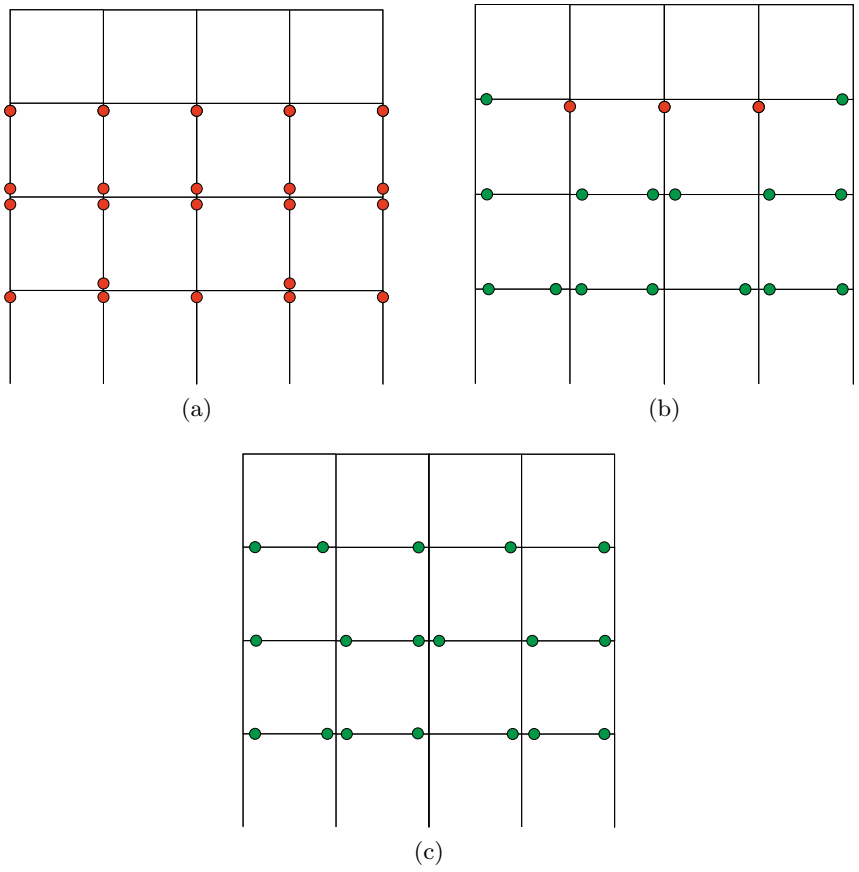

Figure 5.9: The distribution of plastic hinges in the columns (represented by the red circle) and beams (represented by green circles) under the Synthetic MCE for (a) WUF Frame (frame 1) (b) RBS frame (frame 2) and (c) Optimal RBS frame (frame 3).

Table 5.5: Summary of the RBS loactions and sizes adopted for frames 1, 2 and 3. Where c is the depth of cut defining the RBS geometry and b_f is the width of the beam flange.

Frame Type	Frame label	Floor No.	c cut for RBS size
WUF	frame 1	1	No RBS
		2	No RBS
		3	No RBS
		4	No RBS
RBS	frame 2	1	$c = 0.175b_f$ (average)
		2	$c = 0.175b_f$ (average)
		3	$c = 0.175b_f$ (average)
		4	No RBS
More Efficient	frame 3	1	$c = 0.175b_f$ (average)
		2	$c = 0.175b_f$ (average)
		3	$c = 0.25b_f$ (maximum)
		4	No RBS

These results have demonstrated that the frame performance of this WUF frame can simply be improved by replacing the WUF connections with RBS connection. Furthermore, a more efficient steel RBS frame can be achieved by a step by step trial and error system. Fine tuning of the frame was achieved by adjusting the RBS size in order to reach an efficient design by exhibiting a more ductile behaviour.

In current practice, the geometry of an RBS is not considered during the design or structural analysis of RBS frames. The geometry of an RBS can directly effect the beams cyclic performance (at the local level) which directly influences the performance of a steel moment frame (at the global level). Currently, there is no method of predicting the cyclic performance of any RBS given the geometries of the RBS. This chapter has shown how significant the classification algorithm and set of deep learning NNs developed in Chapter 4 are in developing a more efficient RBS frame design compared to WUF and conventional RBS frames. A simple step-by-step permutation trial and error frame design in this chapter has shown the significance and importance the classification algorithm and set of deep learning NNs have on developing more efficient frame designs.

5.5 Scope for future applications

This Chapter has demonstrated how the performance of a moment resistant WUF frame can first be improved by providing RBS connections, subsequently, a better seismic performance can achieved by fine tuning the RBS connections (more specifically adjusting the c cut (geometry) of the connection). Matlab was used to automate the design process, whereby, the non-linear OpenSees RBS model was generated by linking the NNs developed in Chapter 4 by defining the input parameters for the beams and RBS connections. As a result a performance-based design approach for RBS frames was developed and a simple implementation example has been carried out.

This simple trial and error system for achieving a more efficient frame performance, has scope to be applied in future optimization methods to achieve better frame performance. This method to achieve a more efficient solution can be incorporated into multiple permutation steps in larger multi-storey frames in order to improve the frames performance under string earthquake events. In addition, a multi-criteria optimization approach could also be incorporated into this methodology for different performance design levels and a range of damage indication parameters. The development of the classification algorithm and set of deep learning NNs from Chapter 4 can be directly used to

generate the cyclic models required for this methodology. However, it should be noted that this is not in the scope of this research. Refer to Chapter 6 Section 6.2 for potential future applications of this methodology.

5.6 Conclusion

The aim of this study was to develop a simple methodology for the achieving an efficient performance of steel moment resistant RBS frames by controlling the geometry of the RBS. This methodology utilised the set of NNs developed in Chapter 4 as a way of representing the cyclic non-linear behaviour incorporating stiffness and strength degradation of RBS connections for any RBS geometry. Based on the result of this Chapter the following conclusions can be drawn:

1. A simple methodology for achieving a more efficient performance of moment resistant steel RBS frames was developed by utilising a step by step permutation approach. This approach successfully transferred the plastic hinges which formed in the columns into the RBS connections by controlling the geometry of the RBS connections

2. The adequacy of the frame meeting the capacity design principle and medium to high ductility requirements of BS EN 1998-1 (British Standards Institute, 2005) was compared. Frame 1 which consisted of WUF connections violated these design regulations across floors 1, 2 and 3. Frame 2 which utilised RBS connections with a c cut (geometry) equal to average limits specified in BS EN 1998-1 (BSI, 2004) and ANSI/AISC 358-16 (AISC, 2016b) improved the frames performance but still violated the design guidelines within floor 3. Frame 3 consisted of fine-tuned RBS connections within floor 3 which allowed a more efficient frame performance to be achieved which satisfied the capacity design and medium to high ductility requirements in BS EN 1998-1 (BSI, 2004).

Chapter 6

Conclusions and Recommendations for Future Work

6.1 Summary and Conclusions

The main purpose of this research was to carry out an extensive analytical study into the performance of fully welded Reduced Beam Section (RBS) connections. A summary of the main findings and conclusions for each Chapter are summarised in the following sub sections. The main contributions to knowledge are:

- identification of the key design parameters of RBS connections and their influence on the non-linear cyclic performance of the connections
- a database of highly accurate and calibrated models which can accurately capture the cyclic hysteresis of RBS connections
- a method which can accurately predict the complex non-linear hysteresis behaviour of any RBS connection without the need of FE or experimental models
- demonstration of a developed framework which can be also used as an efficient and low computational cost tool to provide a more efficient design of RBS frames to achieve the best seismic performance.

6.1.1 Chapter 2: More Efficient Design of Reduced Beam Sections (RBS) for Maximum Seismic Performance

The aim of this Chapter was to investigate, through an extensive finite element parametric analysis, the affects key geometrical parameters which define an RBS, have on the connections seismic performance. As a result of this analysis, more efficient design methodologies for the RBS connection were developed. With reference to Section 1.4, this chapter was aimed at achieving Objectives 1 and 2.

- Generally, the seismic performance of RBS connections is influenced in different degrees by the three geometric parameters a, b and c. Parameter c has significant influence over all the five seismic design parameters considered. The parameter b has a small effect on the connections performance whereas parameter a has very little influence which can be considered negligible.
- According to the required rotational capacities (DL, SD and NC) for RBS connections according to BS/EN 1998-3 (BSI, 2005), the beams adequacy of achieving these damage states was assessed. The results indicated that the elastic state DL was achieved by all beams, however, the NC rotational requirement was achieved by all but two beams. Direct links between the ultimate

rotation and web slenderness was established. Beams with a web slenderness larger than 54 could not accommodate the NC requirement.

- Performance limits in ASCE/SEI 41-17 (ASCE, 2017a) were used to compare the rotations at the beam and the column face. The results showed that none of the beams achieved the CP performance level and only 4 beams achieved the LS performance level. However, all beams achieved the IO level. Compared to the 4% inter-storey drift requirements of ANSI/AISC 358-16 (AISC, 2016b) and FEMA 350 (SAC Joint Venture, 2000a) all beams satisfied this requirement apart from W27X84 and W24X68.

- To assess how the key seismic parameters of RBS compared to full section properties (no RBS present) were effected by the geometric parameters a, b and c, design equations were developed. Direct links between the beams properties, second moment of area and dimensions of the RBS geometries were established. This is particularly useful in design purposes as the cyclic performance and seismic design parameters of RBS connections can be estimated without the need for complex and time consuming cyclic experimental or FE analysis.

6.1.2 Chapter 3: Development of More Accurate Cyclic Hysteretic Models to Represent RBS Connections

This chapter focused on developing a better understanding for the cyclic behaviour of fully welded RBS connections. In addition, a database of accurate and modified-Ibarra-Krawinkler models that can reliably capture the cyclic hysteresis of RBS connections in a wide range of different RBS geometries was developed. As a result of this chapter, objectives 1, 3 and 4 of Section 1.4 were achieved.

- The database containing the FE cyclic hysteresis results can be split into two general categories – sections that do not buckle or sections that buckle. The buckling behaviour is influenced strongly by the beam section web slenderness. Larger web slenderness have a much greater propensity to buckle. The cyclic hysteresis results from the FE database can be split into two general categories – sections that buckle or sections that do not buckle. This buckling behaviour is strongly influenced by the slenderness of the beam sections web. In the range $34.01 < \lambda_{web} < 47.0$, the c geometry has the most effect where larger values tend to lead to an increased likelihood of section buckling. There appears to be no significant influence from the c and b RBS parameters on the buckling behaviour of beam sections for all other ranges of λ_{web}. Generally, for these sections the buckling behaviour is controlled by the slenderness of the web, regardless of the RBS geometry

- For each of the 1480 specimens in the FE database accurate and reliable bilinear mIK parameters were calibrated. The mIK parameters as and θ_p, common to both buckling and non buckling specimens, were also influenced by the web slenderness. For buckling cases, the λ and θ_{pc} values were influenced the most by the slenderness of the sections web. A clear linear trend for these mIK parameters could be observed. $K0$ can be considered dependent on the second moment of area of the corresponding section. However, the two different trends for the effective yield moment of buckle and non buckle sections are significantly affected by I_{RBS}. Thus M_y can be considered to be dependent on both the buckling behaviour and I_{RBS} of the section.

- The influence of the geometrical c and b RBS parameters on the mIK parameters were thoroughly investigated. Results showed the $K0$ and M_y values were effected the most by the c parameter. Some small influence of the c geometry on the θ_p was also observed, while this parameter had very small effects on the as, λ and θ_{pc} mIK values. Practically, the mIK parameters are not influenced by the b parameter.

- The mIK database parameters for the 1480 different RBS specimens was used to directly compare the predictive mIK values using the widely adopted equations suggested in Lignos and Krawinkler (2011). The comparisons showed that predictive mIK values under predicted the θ_{pc} and λ values and gave varying results for the θ_p predictions. This highlights that ignoring the effects of RBS geometric parameters and trying to capture the cyclic hysteresis of sections by modifying the monotonic backbone curve after Lignos and Krawinkler (2011) may lead to very unrealistic results. The development of the database addressed these issues by directly using the cyclic hysteresis of the sections in order to generate accurate and reliable hysteresis models of RBS elements. The same problem has also been identified for the FS equations presented by Lignos and Krawinkler (2011).

6.1.3 Chapter 4: Accurate Prediction of Cyclic Hysteresis Behaviour of RBS Connections Using Deep Learning Neural Networks

A fast and reliable method which can accurately predict the complex non-linear hysteresis behaviour of any RBS connection was developed as a result of Chapter 5. A practical method is proposed which is capable of predicting improved models that can capture accurately the non-linear cyclic response of any RBS connection based only on the beam and RBS geometries as input information. This mitigates the need for complex, costly and time consuming detailed finite element (FE) analysis or full scale experimental tests generally required to calibrate the mIK model parameters. The set of deep learning NNs and classifier algorithm developed should prove useful in the practical design and assessment of steel RBS frames. Consequently, objectives No. 1 and 5 from Section 1.4 were achieved.

Trends in the key mIK input parameters with respect to the second moment of area of the corresponding full section, second moment of area of the RBS section and slenderness of the web were shown through the comprehensive database of calibrated modified-Ibarra-Krawinkler (mIK) models, used to represent the non-linear cyclic hysteresis behaviour of steel RBS connections. However, existing mathematical equations do not take into account the effects of some of these parameters, and therefore, may not lead to accurate predictions. To address this issue, a Supervised Machine Learning Classifier and a set of Deep Learning NNs was developed based on the selected database of full cyclic hysteretic behaviour of 1480 RBS connections, calibrated to capture accurately the non-linear cyclic hysteretic behaviour of RBS connections. The buckle or non-buckle characteristics possessed by the sections were classified through the ensemble-bootstrap-aggregating algorithm, where an accuracy of 96% was achieved. To predict the mIK parameters achieving a mode accuracy of 98% a set of cascade forward-feed NNs with hidden layers were used. Trial and error permutations were used to establish the parameters which control the training of the cascade forward-feed networks.

6.1.4 Chapter 5: More Efficient Design of Moment Resisting Steel Frames with RBS Connections

The objective of this chapter was to implement the set of deep learning NNs developed in Chapter 4 in a practical design and assessment application at the global frame level. By controlling the geometry of the RBS, a simple methodology for achieving an efficient performance of steel moment resistant RBS frames was developed. The NNs developed in Chapter 4, which are used as a way of representing the cyclic non-linear behaviour incorporating stiffness and strength degradation of RBS connections for any RBS geometry, were incorporated into this methodology. This enabled the referenced objectives 1 and 6 from Section 1.4 to be achieved. The following conclusions can be drawn based on this chapter :

- A step by step permutation approach was utilised for developing a simple methodology for achieving a more efficient performance of moment resistant steel RBS frames. By controlling

the geometry of the RBS connections the plastic hinges could be transferred from forming in the columns to forming in the beams, which is the desired outcome.

- The adequacy of the frames in meeting the medium to high ductility and capacity design principle requirements of BS EN 1998-1 (British Standards Institute, 2005) was compared. These design regulations were violated by frame 1 (WUF frame) across floors one, two and three. Utilising RBS connections with a c cut (geometry) equal to average limits specified in BS EN 1998-1 (BSI, 2004) and ANSI/AISC 358-16 (AISC, 2016b), frame 2 improved the frames performance but still with design guide violations in floor 3. Fine-tuned RBS connections on floor 3 (frame 3) allowed a more efficient frame performance to be achieved which satisfied the capacity design and medium to high ductility requirements in BS EN 1998-1 (BSI, 2004).

6.1.5 Appendix A: The Potential for 3D Printed Connections in the Design and Retrofitting of Steel Structures

An extensive critical literature review was used in Appendix A to propose the future use of additive printing techniques for beam column connections which could allow designers and retro-fitters the freedom to produce a wide range of connections with specified characteristics. As a results the objectives No. 1 and No. 7 from Section 1.4 were achieved.

The range of connections critically reviewed fell into three groups: weakening sections of the beam, fuse type connections and self-centring connections. These effective methods shift the damage away from the column or beam-column-connection and into the beams or replaceable sections of the connection or beam. However, many of these connections still do not solve the problems of a) no efficient design methodology provided that can produce an efficient acceptance criteria, b) no optimal solution has been developed for steel frames where these new connections or innovative methods have been implemented and c) many of the the new connections and innovative methods discussed in Appendix A do not have the flexibility to be easily adjusted. In order to optimize steel frames with replaceable connections, the stiffness and strength (and consequently the energy dissipation) of the connection needs to be easily controlled. For optimization, a large number of the same connections with varying geometries and non-linear dynamic responses need to be produced. Currently, there is no connection that has sufficient flexibility or that can be easily changed and adjusted. Perhaps a solution to this problem lies in developing a concept and framework for an additively printed connection that can dissipate the seismic energy through the yielding of small components within the connection, leading to a lateral displacement (energy absorbing) method for absorbing energy.

Additive printing provides the opportunity to produce a huge range and variety of different connections at no extra cost. Appendix A explores the superior behaviour of 2D and 3D additively printed lattices compared to their solid counter part sections. Lighter, more efficient and stronger shapes of additively printed lattices lead to increased energy absorption; utilising these properties opens up opportunities for connections with designed characteristics and specified performance. The ideal solution would allow additively printed beam-column connections that can be tailored to achieve different performance targets in different parts of the structure by adjusting the geometries of the connection (and consequently the stiffness and strength of the connection which effects the energy absorption characteristics of the connection). This would allow an optimal solution to be achieved which is highly flexible, where the characteristics of each connection can vary significantly.

While this idea may seem unrealistic at this current time, with the speed and rate of developing technology, advances in additive (3D) printing and leaps and bounds in the sophisticated computer technology, could the answer to the future design of optimized seismic connections lie within additive (3D) printing?

6.2 Recommendations for Future Work

As a result of the work completed in this research, the following recommendations for future work have been proposed:

1. A proof of concept method for the performance-based design of steel RBS frames has been demonstrated in Chapter 5, where the set of deep learning NNs developed in Chapter 4 was used to assess the performance of a steel frame. Chapter 4 shows that the performance of the frame in terms of rotational damage can be improved by varying the RBS geometries. There is scope for further investigation for multi-criteria performance-based optimization of steel RBS frames under non-linear dynamic seismic excitations to control the seismic performance under different earthquake intensity levels.

2. The simple trial and error system for achieving an optimum performance, developed in Chapter 5, has scope to be applied in future optimization methods to achieve better frame performance. This method, to achieve a more efficient solution, can be incorporated into multiple permutation steps in larger multi-storey frames in order to improve the frames performance under strong earthquake events. In addition, a multi-criteria optimization approach could also be incorporated into this methodology for different performance design levels and a range of damage indication parameters.

3. A cost analysis for the construction and fabrication of varying RBS connections in a steel moment resistant frame should be conducted. A whole life cycle for implementation of this proposed idea would be beneficial.

4. The potential for 3D printing in the development of future steel connections have been proposed in Appendix A. Further research into how 2D and 3D lattices can be incorporated into connections in order to develop bespoke seismic energy absorbing connections through lateral displacement energy absorbing by yielding of small components within the connection should be researched.

5. In order to develop item 4, representations for the full non-linear cyclic hysteretic behaviour of the potential 3D printed connections could be developed. This would allow scope for the multi-criteria performance-based optimization of steel frame incorporating these 3D printed connections, as developed in Chapter 5 and suggested in item 1 and 2.

Bibliography

ABAQUS
2016. *ABAQUS User's, Theory and Scripting Manuals*. USA: Dassault Systèmes Simulia Corp.

ACSE
2003. ASCE/SEI 31-03: Seismic Evaluation of Existing Buildings. Technical report.

Adeli, H. and S.-L. Hung
1995. *Machine Learning - Neural Networks, Genetic Algorithms and Fuzzy Systems*, new york w edition.

Adeli, H. and H. S. Park
1995. Optimization of space structures by neural dynamics. *Neural Networks*, 8(5):769–781.

Ahmady Jazany, R.
2018. *Improved design of drilled flange (DF) moment resisting connection for seismic regions*, volume 16. Springer Netherlands.

AISC
2016a. ANSI/AISC 341-16: Seismic provisions for structural steel buildings. Technical report.

AISC
2016b. ANSI/AISC 358-16: Prequalified connections for special and intermediate steel moment frames for seismic applications. Technical report.

AISC
2016c. ANSI/AISC 360-16: Spcification for structural steel buildings. Technical report.

AISC
2017. https://www.aisc.org/.

Akbas, B.
2006. A neural network model to assess the hysteretic energy demand in steel moment resisting frames. *Structural Engineering and Mechanics*, 23(2):177–193.

Arisoy, E., S. Musuvathy, L. Mirabella, and E. Slavin
2015. Design and topology optimization of lattice structures using deformable implicit surfaces for additive manufacturing. In *Proceedings of the ASME 2015 International Design Engineering Technical Conferences & Computers and Information in Engineering Conference*, Pp. 1–11.

ASCE
2010. ASCE/SEI 7-10: Minimum Design Loads for Buildings and Other Structures. Technical report.

ASCE
2017a. ASCE/SEI 41-17: Seismic Evaluation and Retrofit of Existing Buildings. Technical report.

ASCE
2017b. http://www.asce.org/.

Asgarian, B., A. Sadrinezhad, and P. Alanjari
2010. Seismic performance evaluation of steel moment resisting frames through incremental dynamic analysis. *Journal of Constructional Steel Research*, 66(2):178–190.

Ashrafi, Y., B. Rafezy, and W. P. Howson
2009. Evaluation of the Performance of Reduced Beam Section (RBS) Connections in Steel Moment Frames Subjected to Cyclic Loading. In *World Congress on Engineering 2009*, volume II, P. 1642.

Atashzaban, A., I. Hajirasouliha, R. A. Jazany, and M. Izadinia
2015. Optimum drilled flange moment resisting connections for seismic regions. *Journal of Constructional Steel Research*, 112(06):325–338.

Autodesk AutoCAD
2019. *AutoCAD Function Reference*.

Baiguera, M., G. Vasdravellis, and T. Karavasilis
2016. Dual seismic-resistant steel frame with high post-yield stiffness energy-dissipative braces for residual drift reduction. *Journal of Constructional Steel Research*, 122:198 – 212.

Bakhary, N., H. Hao, and A. J. Deeks
2007. Damage detection using artificial neural network with consideration of uncertainties. *Engineering Structures*, 29(11):2806–2815.

Banisheikholeslami, A., F. Behnamfar, and M. Ghandil
2016. A beam-to-column connection with visco-elastic and hysteretic dampers for seismic damage control. *Journal of Constructional Steel Research*, 117:185–195.

Bosco, M. and L. Tirca
2017. Numerical simulation of steel I-shaped beams using a fiber-based damage accumulation model. *Journal of Constructional Steel Research*, 133:241–255.

Bouc, R.
1967. Forced vibration ofmechanical systems with hysteresis. In *Proceedings of the fourth Conference on Non-linear Oscillation, Prague, Czechoslovakia,*.

Bravo-Haro, M. A. and A. Y. Elghazouli
2018. Permanent seismic drifts in steel moment frames. *Journal of Constructional Steel Research*, 148:589–610.

Bravo-Haro, M. A., A. Tsitos, and A. Y. Elghazouli
2018. Drift and rotation demands in steel frames incorporating degradation effects. *Bulletin of Earthquake Engineering*, 16(10):1–32.

Breiman, L.
1996. Bagging Predictors. *Machine Learning*, 24:123–140.

Brenne, F., T. Niendorf, and H. J. Maier
2013. Additively manufactured cellular structures: Impact of microstructure and local strains on the monotonic and cyclic behavior under uniaxial and bending load. *Journal of Materials Processing Technology*, 213(9):1558–1564.

British Standards Institute
2005. Eurocode 3 - Design of steel structures. Technical report.

BSI
2004. BS EN 1998-1:2004+A1:2013: Eurocode 8 - Design of structures for earthquake resistance - Part 1. Technical report.

BSI
2005. BS EN 1998-3: Eurocode 8 - Design of structures for earthquake resistance - Part 3. Technical report.

BSSC, ATC, and FEMA
1997. FEMA 273: NEHRP guidelines for the seismic rehabilitation of buildings. Technical Report October.

Caglar, N., M. Pala, M. Elmas, and D. Mercan Eryilmaz
2009. A new approach to determine the base shear of steel frame structures. *Journal of Constructional Steel Research*, 65(1):188–195.

Cao, M., L. Xie, H. Tang, N. Funaki, and S. Xue
2016. Performance Study of an 8-story Steel Building Equipped with Oil Damper Damaged During the 2011 Great East Japan Earthquake Part 2 : Novel Retrofit Strategy. *Journal of Asian Architecture and Building Engineering*, (May):303–310.

Carter, C. J. and N. R. Iwankiw
1998. Improved ductility in seismic steel moment frames with dogbone connections. *Journal of Constructional Steel Research*, 46(1-3):448.

Castiglioni, C. A., L. Calado, I. Vayas, B. Hoffmeister, and R. Goncalves
2012a. Numerical and Experimental Results of Project FUSEIS (Seismic Resistant Composite Steel Frames). (2009).

Castiglioni, C. A., A. Kanyilmaz, and L. Calado
2012b. Experimental analysis of seismic resistant composite steel frames with dissipative devices. *Journal of Constructional Steel Research*, 76:1–12.

CEN
2017. https://www.cen.eu/.

Chan, R. W. K., F. Albermani, and S. M. Williams
2009. Evaluation of yielding shear panel device for passive energy dissipation. *Journal of Constructional Steel Research*, 65:260 – 268.

Chantarapanich, N., A. Laohaprapanon, S. Wisutmethangoon, P. Jiamwatthanachai, P. Chalermkarnnon, S. Sucharitpwatskul, P. Puttawibul, and K. Sitthiseripratip
2014. Fabrication of three-dimensional honeycomb structure for aeronautical applications using selective laser melting: a preliminary investigation. *Rapid Prototyping Journal*, 20(6):551–558.

Chantarapanich, N., P. Puttawibul, S. Sucharitpwatskul, P. Jeamwatthanachai, S. Inglam, and K. Sitthiseripratip
2012. Scaffold library for tissue engineering: A geometric evaluation. *Computational and Mathematical Methods in Medicine*, Pp. 1–14.

Chen, C. C. and C. C. Lin
2013. Seismic performance of steel beam-to-column moment connections with tapered beam flanges. *Engineering Structures*, 48(10):588–601.

Chen, S.-J., J. Chu, and Z. Chou
1997. Dynamic behavior of steel frames with beam flanges shaved around connection. *Journal of Constructional Steel Research*, 42(1):49–70.

Chen, S.-j., J. M. Chu, and C. H. Yeh
1996. Ductile steel beam-to-column connections for seismic resistance. *Journal of Structural Engineering*, 122(11):1292–1299.

Chisari, C., A. B. Francavilla, M. Latour, V. Piluso, G. Rizzano, and C. Amadio
2017. Critical issues in parameter calibration of cyclic models for steel members. *Engineering Structures*, 132:123–138.

Chisari, C. and G. Rizzano
2018. Comparative analysis of cyclic models for steel beams. *Journal of Constructional Steel Research*, 145:315–329.

Chlebus, E., B. Kuźnicka, T. Kurzynowski, and B. Dybała
2011. Microstructure and mechanical behaviour of Ti-6Al-7Nb alloy produced by selective laser melting. *Materials Characterization*, 62(5):488–495.

Chung, Y.-L., T. Nagae, and N. Tomohiro, Matsumiya andMasayoshi
2011. Seismic resistance capacity of beamcolumn connections in high-rise buildings: E-Defense shaking table test. *Earthquake Engineering & Structural Dynamics*, 40(056):605–622.

Clifton, G. C.
2005. *Semi-rigid joints for moment-resisting steel framed seismic-resisting systems*. PhD thesis, University of Auckland.

Clough, R. and S. Johnston
1966. Effect of stiffness degradation on earthquake ductility requirements. In *Proceedings, Second Japan National Conference on Earthquake Engineering*, Pp. 227 – 232.

D'Aniello, M., R. Landolfo, V. Piluso, and G. Rizzano
2012. Ultimate behavior of steel beams under non-uniform bending. *Journal of Constructional Steel Research*, 78:144–158.

Davarpanah, M., H. Ronagh, P. Memarzadeh, and F. Behnamfar
2020. Cyclic behaviour of ellipitical-shapted reduced web section connection. *Structures*, 24:955–973.

Deierlein, G. G., A. M. Reinhorn, and M. R. Willford
2010. Nonlinear Structural Analysis For Seismic Design: A Guide for Practicing Engineers. Technical Report 4.

Deshpande, V. S., M. F. Ashby, and N. A. Fleck
2001. Foam topology: Bending versus stretching dominated architectures. *Acta Materialia*, 49(6):1035–1040.

Dimopoulos, A. I., T. L. Karavasilis, G. Vasdravellis, and B. Uy
2013. Seismic design, modelling and assessment of self-centering steel frames using post-tensioned connections with web hourglass shape pins. *Bulletin of Earthquake Engineering*, 11(5):1797–1816.

Dowell, R. K., F. Seible, and E. L. Wilson
1998. Pivot hysteresis model for reinforced concrete members. *ACI Structural Journal*, 95(5):607–617.

Dubina, D., A. Ciutina, and A. Stratan
2001. Cyclic Tests of Double-Sided Beam-to-Column Joints. *Journal of Structural Engineering*, 2(February):129–136.

Dubina, D., A. Stratan, and F. Dinu
2008. Dual high-strength steel eccentrically braced frames with removable links. *Earthquake Engineering and Structural Dynamics*, 37(07):1703 – 1720.

Efron, B.
1993. *An introduction to the bootstrap*. New York; London: Chapman & Hall.

Einabadi, H., V. Kalatjari, and K. Hossein
2016. Determining the Optimal Geometry of RBS Connection for enhancement of Seismic Behavior of Steel Moment Frames. *Ciência e Natura*, 38(2):1116–1123.

El-Tawil, S. and G. Deierlein
1998. Stress-resultant plasticity for frame structures. *Journal of Engineering Mechanics*, 124(12):1360–1370.

Elkady, A. and D. G. Lignos
2018. Improved Seismic Design and Nonlinear Modeling Recommendations for Wide-Flange Steel Columns. *Journal of Structural Engineering*, 144(9):1–30.

Engelhardt, M. and T. Sabol
1997. Seismic-resistant steel moment connections: developments since the 1994 Northridge earthquake. *Progress in Structural Engineering and Materials*, 1(1):68–77.

Engelhardt, M. D.
1999. The 1999 T. R. Higgins lecture: design of reduced beam section moment connections. *1999 North American Steel Construction Conference(NASCC)*, P. 1999.

Erochko, J., C. Christopoulos, R. Tremblay, and H. Choi
2010. Residual drift response of SMRFs and BRB frames in steel buildings designed according to ASCE 7-05. *Journal of Structural Engineering*, 137(5):589–599.

Evans, A. G., M. Y. He, V. S. Deshpande, J. W. Hutchinson, A. J. Jacobsen, and W. B. Carter
2010. Concepts for enhanced energy absorption using hollow micro-lattices. *International Journal of Impact Engineering*, 37(9):947–959.

Fang, C., M. C. H. Yam, H. Ma, and K. F. Chung
2015. Tests on superelastic NiTi SMA bars under cyclic tension and direct-shear: towards practical recentring connections. *Materials and Structures*, 48(4):1013–1030.

Farmani, M. A. and M. Ghassemieh
2016. Shape memory alloy-based moment connections with superior self-centering properties. *Smart Materials and Structures*, 25(7):1–17.

Farmani, M. A. and M. Ghassemieh
2017. Steel beam-to-column connections equipped with SMA tendons and energy dissipating devices including shear tabs or web hourglass pins. *Journal of Constructional Steel Research*, 135(10):30–48.

Farrokhi, H., F. Danesh, and S. Eshghi
2009. A modified moment resisting connection for ductile steel frames (Numerical and experimental investigation). *Journal of Constructional Steel Research*, 65(10-11):2040–2049.

Federal Emergency Managment Agency
2018. FEMA P-58-1: Seismic Performance Assessment of Buildings. Volume 1 Methodology. Technical Report December 2018.

FEMA
2000. FEMA 356: Prestandard and Commentary for the Seismic Rehabilitation of Buildings. Technical Report 1.

FEMA
2006. FEMA 547: Techniques for the Seismic Rehabilitation of Existing Buildings. Technical report.

FEMA
2009. FEMA P-750: NEHRP Recommended Seismic Provisions for New Buildings and Other Structures. Technical report.

FEMA
2015. FEMA P-154: Rapid visual screening of buildings for potential seismic hazards: A Handbook. Technical Report January.

FEMA
2017. https://www.fema.gov/.

FEMA-351
2000. FEMA-351: Recommended Seismic Evaluation and Upgrade Criteria for Existing Welded Steel Moment-Frame Buildings. Technical report.

Fleischman, R.
2013. NSF Final Report, Development of Cast Modular Components for Steel Construction, Project Findings. Technical report, Civil Engineering and Engineering Mechanics Department, University of Arizona.

Fonseca, E. T., P. C. G. S. Vellasco, S. A. L. D. Andrade, and M. M. B. R. Vellasco
2003. Neural network evaluation of steel beam patch load capacity. *Advances in Engineering Software*, 34:763–772.

Foo, C. C., G. B. Chai, and L. K. Seah
2007. Mechanical properties of Nomex material and Nomex honeycomb structure. *Composite Structures*, 80(4):588–594.

Garlock, M. M., M. Asce, R. Sause, and J. M. Ricles
2007. Behavior and Design of Posttensioned Steel Frame Systems. *Journal of Structural Engineering*, 133(3):389–99.

Ghassemieh, M. and J. Kiani
2013. Seismic evaluation of reduced beam section frames considering connection flexibilit. *The Structural Design of Tall and Special Buildings*, 22(January):1248–1269.

Gholizadeh, S. and M. Mohammadi
2017. Reliability-Based Seismic Optimization of Steel Frames by Metaheuristics and Neural Networks. *J. Risk Uncertanity Eng. Syst., Part A: Civ. Eng*, 3(1).

Gholizadeh, S., A. Pirmoz, and R. Attarnejad
2011. Assessment of load carrying capacity of castellated steel beams by neural networks. *Journal of Constructional Steel Research*, 67(5):770–779.

Gibson, L. J. and M. F. Ashby
1997. *Cellular Solids : Structure and Properties*, 2 edition. Cambridge University Press.

Gilton, C. S. and C.-M. Uang
2002. Cyclic Response and Design Recommendations of Weak-Axis Reduced Beam Section Moment Connections. *Journal of Structural Engineering*, 128(4):452 – 463.

Goswami, S.
2006. On the Prediction of Effective Material Properties of Cellular Hexagonal Honeycomb Core. *Journal of Reinforced Plastics and Composites*, 25(4):393–405.

Guan, X., H. Burton, and S. Moradi
2018. Seismic performance of a self-centering steel moment frame building: From component-level modeling to economic loss assessment. *Journal of Constructional Steel Research*, 150:129–140.

Gupta, A. and H. Krawinkler
1999. Prediction of Seismic Demands for SMRFs with Ductile Connections and Elements. Technical report, Sacramento, CA.

Guzelbey, I. H., A. Cevik, and A. Erklig
2006a. Prediction of web crippling strength of cold-formed steel sheetings using neural networks. *Journal of Constructional Steel Research*, 62(10):962–973.

Guzelbey, I. H., A. Cevik, and M. T. Gogus
2006b. Prediction of rotation capacity of wide flange beams using neural networks. *Journal of Constructional Steel Re*, 62:950–961.

Hamburger, R. O., H. Krawinkler, J. O. Malley, and S. M. Adan
2015. NIST GCR 09-917-3: NEHRP Seismic Design Technical Brief No. 11 Seismic design of steel buckling-restrained braced frames - a guide for practicing engineers. Technical report.

Han, S. W., G. U. Kwon, and K. H. Moon
2007. Cyclic behaviour of post-Northridge WUF-B connections. *Journal of Constructional Steel Research*, 63(3):365–374.

Han, S. W., K. H. Moon, S. H. Hwang, and B. Stojadinovic
2012. Rotation capacities of reduced beam section with bolted web (RBS-B) connections. *Journal of Constructional Steel Research*, 70:256–263.

He, L., T. Togo, K. Hayashi, M. Kurata, and M. Nakashima
2016. Cyclic Behavior of Multirow Slit Shear Walls Made from Low-Yield-Point Steel. *Journal of Structural Engineering*.

Hedayat, A. A., E. Ahmadi Afzadi, H. Kalantaripour, E. Morshedi, and A. Iranpour
2019. A new predictive model for the minimum strength requirement of steel moment frames using artificial neural network. *Soil Dynamics and Earthquake Engineering*, 116(July 2018):69–81.

Hedayati, R., M. Sadighi, M. Mohammadi-Aghdam, and A. A. Zadpoor
2016. Mechanical properties of additively manufactured octagonal honeycombs. *Materials Science and Engineering C*, 69:1307–1317.

Herning, G., M. M. Garlock, J. Ricles, R. Sause, and J. Li
2009. An Overview of Self-Centering Steel Moment Frames. *Structures Congress 2009*, Pp. 1412–1420.

Hornik, K., M. Stinchcombe, and H. White
1989. Multilayer feedforward networks are universal approximators. *Neural Networks*, 2(5):359–366.

Horton, T., I. Hajirasouliha, B. Davison, and Z. Ozdemir
2021a. Accurate Prediction of Cyclic Hysteresis Behaviour of RBS Connections Using Deep Learning Neural Networks. *Submitted to: Journal of Engineering Structures.*

Horton, T., I. Hajirasouliha, B. Davison, and Z. Ozdemir
2021b. More Efficient Design of Reduced Beam Sections (RBS) for Maximum Seismic Performance. *Journal of Constructional Steel Research*, 183.

Horton, T., I. Hajirasouliha, B. Davison, Z. Ozdemir, and I. Abuzayed
2021c. Development of More Accurate Cyclic Hysteretic Models to Represent RBS Connections. *Engineering Structures, In-Press.*

Horton, T. A., I. Hajirasouliha, B. Davison, and Z. Ozdemir
2022. The Potential for 3D Printed Connections in the Design and Retrofitting of Steel Structures. *Indending to Submit to: Journal of Advances in Structural Engineering.*

Hsu, H.-L. and H. Halim
2017. Improving seismic performance of framed structures with steel curved dampers. *Engineering Structures*, 130:99–111.

Hu, J. W., D. K. Kim, and E. Choi
2012. Numerical investigation on the cyclic behavior of smart recentering clip-angle connections with superelastic shape memory alloy fasteners. *Journal of Mechanical Engineering Science*, 227(6):1315–1327.

Ibarra, L. F. and H. Krawinkler
2005. Global Collapse of Frame Structures under Seismic Excitations. Technical Report 152.

Ibarra, L. F., R. A. Medina, and H. Krawinkler
2005. Hysteretic models that incorporate strength and stiffness deterioration. *Earthquake Engineering and Structural Dynamics*, 34(12):1489–1511.

IBC
2015. International Building Code. Technical report.

Inoue, K., K. Suita, I. Takeuchi, P. Chusilp, M. Nakashima, and F. Zhou
2006. Seismic-Resistant Weld-Free Steel Frame Buildings with Mechanical Joints and Hysteretic Dampers. *Journal of Structural Engineering*, 132(6):864–872.

Iqbal, A., S. Pampanin, and A. H. Buchanan
2016. Seismic Performance of Full-Scale Post-Tensioned Timber Beam-Column Connections. *Journal of Earthquake Engineering*, 20(3):383–405.

Jahangiri, A., F. Behnamfar, and M. Jahangiri
2016. Introducing the innovative post-tensioned connection with the rigid steel node. *KSCE Journal of Civil Engineering*, 00(0000):1–9.

Jalali, S. A., M. Banazadeh, A. Abolmaali, and E. Tafakori
2012. Probabilistic seismic demand assessment of steel moment frames with side-plate connections. *Scientia Iranica*, 19(1):27–40.

Jalali, S. A., M. Banazadeh, E. Tafakori, and A. Abolmaali
2011. Seismic performance assessment of steel moment frames with generic Locally Reinforced connections. *Journal of Constructional Steel Research*, 67(8):1261–1271.

Jeyasehar, C. A. and K. Sumangala
2006. Damage assessment of prestressed concrete beams using artificial neural network (ANN) approach. *Computers and Structures*, 84(26-27):1709–1718.

Jiang, S. F., C. M. Zhang, and C. G. Koh
2006. Structural damage detection by integrating data fusion and probabilistic neural network. *Advances in Structural Engineering*, 9(4):445–457.

Jin, J. and S. El-Tawil
2005. Seismic performance of steel frames with reduced beam section connections. *Journal of Constructional Steel Research*, 61(4):453–471.

Jones, S. L., G. T. Fry, and M. D. Engelhardt
2002. Experimental Evaluation of Cyclically Loaded Reduced Beam Section Moment Connections. *Journal of Structural Engineering*, 128(4):441–51.

Kalehbasti, P. R. and K. M. Dolatshahi
2018. Two novel shear fuses in moment resting frames. *Journal of Constructional Steel Research*, 144:198–210.

Kawai, D., Y. Koetaka, K. Suita, K. Inoue, N. Uno, and Y. Fukuchi
2012. Mechanical behavior and design method of weld-free steel structure with knee brace damper using square tube column. In *15th World Conference on Earthquake Engineering (15WCEE)*.

Ke, K. and Y. Chen
2016. Seismic performance of MRFs with high strength steel main frames and EDBs. *Journal of Constructional Steel Research*, 126:214–228.

Kildashti, K. and R. Mirghaderi
2009. Assessment of seismic behaviour of smrfs with RBS connections by means of mixed-based state-space approach. *Structural Design of Tall and Special Buildings*, 18(5):485–505.

Kim, J. and T. Kim
2009. Assessment of progressive collapse-resisting capacity of steel moment frames. *Journal of Constructional Steel Research*, 65(1):169–179.

Kitjasateanphun, T., J. Shen, W. Srivanich, and H. Hao
2001. Inelastic analysis of steel frames with reduced beam sections. *Structural Design of Tall Buildings*, 10(4):231–244.

Kobori, T., Y. Miura, E. Fukuzawa, T. Yamada, T. Arita, Y. Takenaka, N. Miyagawa, N. Tanaka, and T. Fukumoto
1992. Development and application of hysteresis steel dampers. In *Earthquake Enginnering, Tenth World Conference*, Pp. 2341–2346, Balkema, Rotterdam.

Koetaka, Y., P. Chusilp, Z. Zhang, M. Ando, K. Suita, K. Inoue, and N. Uno
2005. Mechanical property of beam-to-column moment connection with hysteretic dampers for column weak axis. *Engineering Structures*, 27(1):109–117.

Köken, A. and A. M. Körolu
2015. Experimental Study on Beam-to-Column Connections of Steel Frame Structures with Steel Slit Dampers. *Journal of Performance of Constructed Facilities*, 29(2):1–11.

Kurata, M., L. He, and M. Nakashima
2015. Steel slit shear walls with double-tapered links capable of condition assessment. *Earthquake Engineering & Structural Dynamics*, 44:1272 – 1287.

Labonnote, N., A. Rønnquist, B. Manum, and P. Rüther
2016. Additive construction: State-of-the-art, challenges and opportunities. *Automation in Construction*, 72:347–366.

Lagaros, N. D. and M. Papadrakakis
2004. Learning improvement of neural networks used in structural optimization. *Advances in Engineering Software*, 35(1):9–25.

Latour, M., V. Piluso, and G. Rizzano
2015. Free from damage beam-to-column joints: Testing and design of DST connections with friction pads. *Engineering Structures*, 85:219–233.

Latour, M. and G. Rizzano
2015. Design of X-shaped double split tee joints accounting for moment-shear interaction. *Journal of Constructional Steel Research*, 104:115–126.

Leblanc, F.
2014. Anything, anyone, anywhere: Toward a cloud-based 3D printing fabrication in architecture. *Rethinking Comprehensive Design: Speculative Counterculture, Proceedings of the 19th International Conference of the Association of Computer-Aided Architectural Design Research in Asia*, (Gershenfeld 2005):1–10.

Lee, C. H., S. W. Jeon, J. H. Kim, and C. M. Uong
2005. Effects of Panel Zone Strength and Beam Web Connection Method on Seismic Performance of Reduced Beam Section Steel Moment Connections. *Journal of Structural Engineering*, 131(12):1854–1865.

Lee, C. H., J. H. Jung, S. Y. Kim, and J. J. Kim
2016. Review of composite slab effect on seismic performance of welded steel moment connections. *Journal of Constructional Steel Research*, 117:91–100.

Lee, C. H. and J. H. Kim
2007. Seismic design of reduced beam section steel moment connections with bolted web attachment. *Journal of Constructional Steel Research*, 63(4):522–531.

Lemonis, M. E.
2018. Steel moment resisting frames with both joint and beam dissipation zones. *Journal of Constructional Steel Research*, 147:224–235.

Leuders, S., M. Thöne, A. Riemer, T. Niendorf, T. Tröster, H. A. Richard, and H. J. Maier
2013. On the mechanical behaviour of titanium alloy TiAl6V4 manufactured by selective laser melting: Fatigue resistance and crack growth performance. *International Journal of Fatigue*, 48:300–307.

Li, R., B. Samali, Z. Tao, and M. Kamrul Hassan
2017. Cyclic behaviour of composite joints with reduced beam sections. *Engineering Structures*, 136:329–344.

Lignos, D. G.
2008. *Sidesway collapse of deteriorating structural systems under seismic excitations.* PhD thesis, Stanford University.

Lignos, D. G., D. Kolios, and E. Miranda
2009. Fragility assessment of reduced beam section steel moment-resisting beam-column connections. *J. of Structural Engineering*, 136(September):1140–1150.

Lignos, D. G. and H. Krawinkler
2007. A Database in Support of Modeling of Component Deterioration for Collapse Prediction of Steel Frame Structures. *Structural Engineering Research Frontiers*, Pp. 1–12.

Lignos, D. G. and H. Krawinkler
2011. Deterioration Modeling of Steel Components in Support of Collapse Prediction of Steel Moment Frames under Earthquake Loading. *Journal of Structural Engineering*, 137(11):1291–1302.

Lignos, D. G. and H. Krawinkler
2012. Sidesway collapse of deteriorating structural systems under seismic excitations. Technical Report 177.

Lignos, D. G., H. Krawinkler, and A. S. Whittaker
2011a. Prediction and validation of sidesway collapse of two scalemodels of a 4-story steel moment frame. *Earthquake Engineering and Structural Dynamics*, 40:807 – 825.

Lignos, D. G., C. Putman, and H. Krawinkler
2011b. Seismic assessment of steel moment frames using simplified nonlinear models. In *3rd EC-COMAS Thematic Conference on Computational Methods in Structural Dynamics and Earthquake Engineering*, number May, Pp. 1 – 18, Corfu, Greece.

Lignos, D. G., F. Zareian, and H. Krawinkler
2010. A Steel Component Database for Deterioration Modeling of Steel Beams with RBS under Cyclic Loading. *Structures Congress 2010*, Pp. 1241–1252.

Lin, Y. C.
2015. Steel sliding-controlled coupled beam modules for advanced resilience of moment resisting frame building systems. *Structures Congress 2015*, Pp. 1423–1434.

Luco, N. and C. A. Cornell
1998. Effects of random connection fractures on the demands and reliability for a 3-story pre-Northridge SMRF structure. In *6th U.S. National Conference on Earthquake Engineering*, Pp. 1–12, Seattle, Washington.

Mahin, S. and V. Bertero
1976. Nonlinear seismic response of a coupled wall system. *Journal of Structural Engineering*, 102(9):1759 – 1980.

Mahmoudi, F., K. M. Dolatshahi, M. Mahsuli, M. T. Nikoukalam, and A. Shahmohammadi
2019. Experimental study of steel moment resisting frames with shear link. *Journal of Constructional Steel Research*, 154:197–208.

Maleki, M., R. Ahmady Jazany, and M. S. Ghobadi
2018. Probabilistic Seismic Assessment of SMFs with Drilled Flange Connections Subjected to Near-Field Ground Motions. *International Journal of Steel Structures*, 358(2000).

Maleki, M., R. A. Jazany, and M. S. Ghobadi
2019. Seismic Fragility Assessment of SMRFs with Drilled Flange Connections using Ground Motion Variability. *KSCE Journal of Civil Engineering*, Pp. 1–14.

Mazzoni, S., F. McKenna, M. H. Scott, and G. L. Fenves
2007. OpenSees command language manual. Technical report.

McCormick, J., H. Aburano, M. Ikenaga, and M. Nakashima
2008. Permissible Residual Deformation Levels for Building Structures Considering both Safety and Human Elements. In *The 14th World Conference on Earthquake Engineering*, Beijing, China.

McKenna, F.
2011. OpenSees: A framework for earthquake engineering simulation. *Computing in Science and Engineering*, 13(4):58–66.

Moehle, J. P., S. A. Mahin, and Y. Bozorgnia
2010. PEER/ATC-72-1 Modeling and Acceptance Criteria for Seismic Design and Analysis of Tall Buildings. Technical Report October.

Mojtabaei, S., J. Becque, and I. Hajirasouliha
2021. Behavior and Design of Cold-Formed Steel Bolted Connections Subjected to Combined Actions. *Journal of Structural Engineering ASCE*, 147(4).

Montuori, R.
2016. The use of Dog-Bone for the Seismic Improvement of Steel MRFs. *WSEAS Transactions on Applied and Theoretical Mechanics*, 11:229–244.

Moon, K. H. and S. W. Han
2008. Seismic performance evaluation of steel moment resisting frames with WUF-B connections. In *AIP Conference Proceedings*, volume 1020, Pp. 1871–1878.

Moradi, S. and M. S. Alam
2015. Feasibility study of utilizing superelastic shape memory alloy plates in steel beam-column connections for improved seismic performance. *Journal of Intelligent Material Systems and Structures*, 26(4):463–475.

Moradi, S. and M. S. Alam
2017. Multi-criteria optimization of lateral load-drift response of posttensioned steel beam-column connections. *Engineering Structures*, 130:180–197.

Morshedi, M. A., K. M. Dolatshahi, and S. Maleki
2017. Double reduced beam section connection. *Journal of Constructional Steel Research*, 138:283–297.

Naeim, F., H. Bhatia, and R. M. Lobo
2001. *The Seismic Design Handbook: Chapter 15 Perfromance Based Seismic Engineering*. Boston: Springer.

Nia, S. Z., M. Ghassemieh, and A. Mazroi
2013. WUF-W connection performance to box column subjected to uniaxial and biaxial loading. *Journal of Constructional Steel Research*, 88:90–108.

Nikoukalam, M. T. and K. M. Dolatshahi
2015. Development of structural shear fuse in moment resisting frames. *Journal of Constructional Steel Research*, 114:349–361.

Nishida, E., B. Song, M. Maguire, D. Adams, J. Carroll, J. Wise, J. Bishop, and T. Palmer
2015. Dynamic compressive response of wrought and additive manufactured 304L stainless steels. In *EPJ Web of Conferences*, volume 94.

Oh, K., K. Lee, L. Chen, S. B. Hong, and Y. Yang
2015. Seismic performance evaluation of weak axis column-tree moment connections with reduced beam section. *Journal of Constructional Steel Research*, 105(10):28–38.

Oh, S.-H., Y.-J. Kim, and H.-S. Ryu
2009. Seismic performance of steel structures with slit dampers. *Engineering Structures*, 31(9):1997–2008.

Ohsaki, M., H. Tagawa, and P. Pan
2009. Shape optimization of reduced beam section under cyclic loads. *Journal of Constructional Steel Research*, 65(7):1511–1519.

Ozdemir, Z., E. Hernandez-Nava, A. Tyas, J. A. Warren, S. D. Fay, R. Goodall, I. Todd, and H. Askes
2016. Energy absorption in lattice structures in dynamics: Experiments. *International Journal of Impact Engineering*, 89:49–61.

Pachoumis, D. T., E. G. Galoussis, C. N. Kalfas, and A. D. Christitsas
2009. Reduced beam section moment connections subjected to cyclic loading: Experimental analysis and FEM simulation. *Engineering Structures*, 31(1):216–223.

Pachoumis, D. T., E. G. Galoussis, C. N. Kalfas, and I. Z. Efthimiou
2010. Cyclic performance of steel moment-resisting connections with reduced beam sections - experimental analysis and finite element model simulation. *Engineering Structures*, 32(9):2683–2692.

Pala, M.
2006. A new formulation for distortional buckling stress in cold-formed steel members. *Journal of Constructional Steel Research*, 62:716–722.

Pala, M. and N. Caglar
2007. A parametric study for distortional buckling stress on cold-formed steel using a neural network. *Journal of Constructional Steel Research*, 63(5):686–691.

Papka, S. and S. Kyriakides
1998. Experiments and full-scale numerical simulations of in-plane crushing of a honeycomb. *Acta Materialia*, 46(8):2765–2776.

Phan, D., S. Mojtabaei, I. Hajirasouliha, T. Lau, and J. Lim
2020. Design and Optimization of Cold-Formed Steel Sections in Bolted Moment Connections Considering Bimoment. *Journal of Structural Engineering*, 146(8).

Plumier, A.
1990. New idea for safe structures in seismic zones. In *Proceedings of IABSE symposium on mixed structures including new materials*, Pp. 431 – 436.

Priestley, M. J. N.
2000. Performance based seismic design. *12th WCEE*, 1(1):1–22.

Rafiq, M. Y., G. Bugmann, and D. J. Easterbrook
2001. Neural network design for engineering applications. *Computers and Structures*, 79(17):1541–1552.

Rahnama, M. and H. Krawinkler
1993. Effects of Soft Soil and Hysteresis Model on Seismic Demands. Technical Report 108.

Rahnavard, R., a. Hassanipour, and N. Siahpolo
2015. Analytical study on new types of reduced beam section moment connections affecting cyclic behavior. *Case Studies in Structural Engineering*, 3:33–51.

Ramberg, W. and W. Osgood
1943. Description of StressStrain Curves By Three Parameters. *National Advisory Committee on Aeronautics, 902, Technical Note.*

Ribeiro, F. L. A., A. R. Barbosa, M. H. Scott, and L. C. Neves
2015. Deterioration Modeling of Steel Moment Resisting Frames Using Finite-Length Plastic Hinge Force-Based Beam-Column Elements. *Journal of Structural Engineering*, 141(2):04014112.

Richard, R. and B. Abbott
1975. Versatile elasto-plastic stress-strain formula. *Journal of Engineering Mechanics*, 101(4):511 – 515.

Ricles, J. M., R. Sause, Y. C. Lin, and C. Y. Seo
2010. Self-Centering Moment Connections for Damage-Free Seismic Response of Steel MRFs. *Structures Congress 2010*, Pp. 955–966.

Roeder, C. W.
2002. Connection Performance for Seismic Design of Steel Moment Frames. *Journal of Structural Engineering*, 128(4):517–525.

Rogers, J.
1994. Simulating Structural Analysis with Neural Network. *J. Comput. Civ. Eng.*, 8(2):252–265.

Rose, A. and D. Lim
2002. Business interruption losses from natural hazards: Conceptual and methodological issues in the case of the northridge earthquake. *Environmental Hazards*, 4(1):1–14.

Ruan, D., G. Lu, B. Wang, and T. X. Yu
2003. In-plane dynamic crushing of honeycombs - A finite element study. *International Journal of Impact Engineering*, 28(2):161–182.

Sabbagh, A. B., M. Petkovski, K. Pilakoutas, and R. Mirghaderi
2012. Development of cold-formed steel elements for earthquake resistant moment frame buildings. *Thin-Walled Structures*, 53:99–108.

SAC Joint Venture
1994. SAC Steel Project.

SAC Joint Venture
2000a. FEMA 350: Recomended seismic deisgn criteria for new steel moment-frame buildings. Technical report.

SAC Joint Venture
2000b. FEMA 354: A Policy guide to steel moment-frame construction. Technical Report November.

SAC Joint Venture
2000c. FEMA 355C - State of the art report on systems perfromance of steel moment frames subject to earthquake ground shaking. Technical report.

SAC Joint Venture
2000d. FEMA 355D: State of the art report on connection perfromance. Technical report.

Sawada, Y. and S. Shimizutani
2008. How do people cope with natural disasters? Evidence from the great Hanshin-Awaji (Kobe) earthquake in 1995. *Journal of Money, Credit and Banking*, 40(2-3):463–488.

Scales, L.
1985. *Introduction to non-linear optimization*. London and Basingstoke: Machillan publishers.

Scott, M. H. and G. L. Fenves
2006. Plastic Hinge Integration Methods for Force-Based BeamColumn Elements. *Journal of Structural Engineering*, 132(2):244–252.

Seo, A. Y., S.-h. Hwang, K.-h. Moon, and S. W. Han
2010. Seismic performance evaluation of the steel moment resisting frames with RBS with bolted web using new moment strength equation. In *International conference on sustainable building asia*, Pp. 683–686, Seoul, Korea.

Shahin, M. and M. Elchalakani
2008. Neural networks for modelling ultimate pure bending of steel circular tubes. *Journal of Constructional Steel Research*, 64(6):624–633.

Sharifi, Y. and S. Tohidi
2014a. Lateral-torsional buckling capacity assessment of web opening steel girders by arti fi cial neural networks elastic investigation. *Front. Struct. Civ. Eng.*, 8(2):167–177.

Sharifi, Y. and S. Tohidi
2014b. Ultimate capacity assessment of web plate beams with pitting corrosion subjected to patch loading by artificial neural networks. *Advanced Steel Construction*, 10(3):325–350.

Shen, Y., C. Christopoulos, N. Mansour, and R. Tremblay
2011. Seismic design and performance of steel moment resisting frames with nonlinear replaceable links. *Journal of Structural Engineering*, 137(10):1107–1117.

Siddique, S., M. Imran, and F. Walther
2017. Very high cycle fatigue and fatigue crack propagation behavior of selective laser melted AlSi12 alloy. *International Journal of Fatigue*, 94:246–254.

Siemens
2013. *PLM Software Inc. NX*.

Sivaselvan, M. V. and A. M. Reinhorn
2000. Mysteretic models for deteriorating inelastic structures. *Journal of Engineering Mechanics*, 126(June):633–640.

Sofias, C. E., C. N. Kalfas, and D. T. Pachoumis
2014. Experimental and FEM analysis of reduced beam section moment endplate connections under cyclic loading. *Engineering Structures*, 59(11):320–329.

Sophianopoulos, D. S. and A. E. Deri
2011. Parameters affecting response and design of steel moment frame reduced beam section connections: An overview. *International Journal of Steel Structures*, 11(2):133–144.

Sophianopoulos, D. S. and A. E. Deri
2017. Steel beam-to-column RBS connections with European profiles: I. Static optimization. *Journal of Constructional Steel Research*, 139:101–109.

Steneker, P. and W. Lydell
2016. Evaluation of the contribution of panel zones to the global performance of moment resisting frames under seismic load. In *Resilient Infrastructure London 2016*, Pp. 1–10, London.

Sultana, P. and M. A. Youssef
2016a. Prediction of local seismic damage in steel moment resisting frames. *Journal of Constructional Steel Research*, 122:122–137.

Sultana, P. and M. A. Youssef
2016b. Seismic performance of steel moment resisting frames utilizing superelastic shape memory alloys. *Journal of Constructional Steel Research*, 125:239–251.

Tadesse, Z., K. Patel, S. Chaudhary, and A. Nagpal
2012. Neural networks for prediction of deflection in composite bridges. *Journal of Constructional Steel Research*, 68:138–149.

Takeda, T., M. Sozen, and N. Nielsen
1970. Reinforced concrete response to simulated earthquakes. *Journal of Structural Engineering*, 96(12):2557 – 2573.

Tan, X. P., Y. J. Tan, C. S. L. Chow, S. B. Tor, and W. Y. Yeong
2016. Metallic powder-bed based 3D printing of cellular scaffolds for orthopaedic implants: A state-of-the-art review on manufacturing, topological design, mechanical properties and biocompatibility. *Materials Science and Engineering C*, 76:1328–1343.

Tancogne-Dejean, T., A. B. Spierings, and D. Mohr
2016. Additively-manufactured metallic micro-lattice materials for high specific energy absorption under static and dynamic loading. *Acta Materialia*, 116:14–28.

The Mathworks Inc
2019. *MATLAB Function Reference*. U.S.: MATLAB and Simulink.

Tohidi, S. and Y. Sharifi
2015. Neural networks for inelastic distortional buckling capacity assessment of steel I-beams. *Thin-Walled Structures*, 94:359–371.

Tong, G., S. Lianglong, and Z. Guodong
2011. Numerical simulation of the seismic behavior of self-centering steel beam-column connections with bottom flange friction devices. *Earthquake Engineering and Engineering Vibration*, 10(2):229–238.

Tong, L., Y. Chen, Y. Chen, and C. Fang
2016. Cyclic behaviour of beam-to-column joints with cast steel connectors. *Journal of Constructional Steel Research*, 116(09):114–130.

Torquato, S., L. V. Gibiansky, M. J. Silva, and L. J. Gibson
1998. Effective mechanical and transport properties of cellular solids. *International Journal of Mechanical Sciences*, 40(1):71–82.

Tsitos, A., M. A. Bravo-Haro, and A. Y. Elghazouli
2018. Influence of deterioration modelling on the seismic response of steel moment frames designed to Eurocode 8. *Earthquake Engineering and Structural Dynamics*, 47(2):356–376.

Tzimas, A. S., A. I. Dimopoulos, and T. L. Karavasilis
2015. EC8-based seismic design and assessment of self-centering post-tensioned steel frames with viscous dampers. *Journal of Constructional Steel Research*, 105:60–73.

Uang, C.-m., Q.-s. K. Yu, S. Noel, and J. Gross
2000. Cyclic Testing of Steel Moment Connections Rehabilited With RBS or Welded Haunch. *Journal of Structural Engineering*, 126(1):57–68.

UBC
1997. UBC 1997 Vol 2. 2.

Valente, M., C. A. Castiglioni, and A. Kanyilmaz
2017a. Numerical investigations of repairable dissipative bolted fuses for earthquake resistant composite steel frames. *Journal of Constructional Steel Research*, 131:275 – 292.

Valente, M., C. A. Castiglioni, and A. Kanyilmaz
2017b. Welded fuses for dissipative beam-to-column connections of composite steel frames: Numerical analyses. *Journal of Constructional Steel Research*, 128:498–511.

Van Bael, S., Y. C. Chai, S. Truscello, M. Moesen, G. Kerckhofs, H. Van Oosterwyck, J. P. Kruth, and J. Schrooten
2012. The effect of pore geometry on the in vitro biological behavior of human periosteum-derived cells seeded on selective laser-melted Ti6Al4V bone scaffolds. *Acta Biomaterialia*, 8(7):2824–2834.

Vanmarke, E. H.
1976. *A Program for Artificial Motion Generation, User's Manual and Dcoumentation*. Cambridge, MA: [publisher unknown].

Vargas, R. E. and M. Bruneau
2006. Seismic Design of Multi-Story Buildings with Metallic Structural Fuses. In *Proceedings of the 8th U.S. National Conference on Earthquake Engineering*, number 280, Pp. 99–104, San Francisco, California, USA.

Vasdravellis, G., T. L. Karavasilis, and B. Uy
2013a. Finite element models and cyclic behavior of self-centering steel post-tensioned connections with web hourglass pins. *Engineering Structures*, 52:1–16.

Vasdravellis, G., T. L. Karavasilis, and B. Uy
2013b. large scale experimental validation of steel post-tensioned connections with web hourglass pins. *Journal of Structural Engineering*, 139(6):1033–1042.

Vasdravellis, G., T. L. Karavasilis, and B. Uy
2014. Design rules experimental evaluation and fracture models for high-strength and stainless-steel hourglass shape energy dissipation devices. *Journal of Structural Engineering*, 140(11).

Vayas, I., P. Karydakis, D. Dimakogianni, G. Dougka, C. A. Castiglioni, A. Kanyilmaz, L. Calado, J. M. Proença, M. Espinha, B. Hoffmeister, T. Rauert, and D. Kalteziotis
2013. Dissipative devices for seismic-resistant steel frames (Fuseis). Technical report.

Vetr, M. G. H., M. Miri, and A. Haddad
2012. Seismic Behavior of a New Reduced Beam Section Connection by Drilled Holes Arrangement (RBS_DHA) on the Beam Flanges through Experimental Studies. In *15th World Conference of Earthquake Engineering*.

Wang, A.-J. and D. L. McDowell
2004. In-Plane Stiffness and Yield Strength of Periodic Metal Honeycombs. *Journal of Engineering Materials and Technology*, 126(2):137–156.

Wang, S., J. W. Lai, M. J. Schoettler, and S. A. Mahin
2017. Seismic assessment of existing tall buildings: A case study of a 35-story steel building with pre-Northridge connection. *Engineering Structures*, 141:624–633.

Wang, W., T. M. Chan, and H. Shao
2015. Seismic performance of beam-column joints with SMA tendons strengthened by steel angles. *Journal of Constructional Steel Research*, 109:61–71.

Wen, Y. K.
1976. Method for random vibration of hysteretic systems. *ASCE Journal of Engineering*, 102(2):249 – 263.

Wendy Gu, X. and J. R. Greer
2015. Ultra-strong architected Cu meso-lattices. *Extreme Mechanics Letters*, 2(1):7–14.

Wolski, M., J. M. Ricles, and R. Sause
2009. Experimental Study of a Self-Centering BeamColumn Connection with Bottom Flange Friction Device. *Journal of Structural Engineering*, 135(5):479–488.

Xu, X., Y. Zhang, and Y. Luo
2016. Self-centering eccentrically braced frames using shape memory alloy bolts and post-tensioned tendons. *Journal of Constructional Steel Research*, 125:190–204.

Xu Bin, S., Y. Yong-Qiang, Y. Peng, and S. Jian-Feng
2012. Development of porous medical implant scaffolds via laser additive manufacturing. *Transactions of Nonferrous Metals Society of China (English Edition)*, 22:181 – 187.

Xue, Q. and C.-C. Chen
2003. Performance-based seismic design of structures: a direct displacement-based approach. *Engineering Structures*, 25(14):1803–1813.

Ye, J., S. Mojtabaei, I. Hajirasouliha, and K. Pilakoutas
2020. Efficient design of cold-formed steel bolted-moment connections for earthquake resistant frames. *Thin-Walled Structures*, 150.

Yeung, S., H. Zhou, H. H. Khoo, and G. C. Clifton
2013. Sliding shear capacities of the Asymmetric Friction Connection. In *2013 NZSEE Conference*, volume 1997, Pp. 1–9.

Zhang, J. and M. F. Ashby
1992. Buckling of honeycombs under in-plane biaxial stresses. *International Journal of Mechanical Sciences*, 34(6):491–509.

Zheng, X., H. Lee, T. H. Weisgraber, M. Shusteff, J. DeOtte, E. B. Duoss, J. D. Kuntz, M. M. Biener, Q. Ge, J. A. Jackson, S. O. Kucheyev, N. X. Fang, and C. M. Spadaccini
2014. Ultralight, ultrastiff mechanical metamaterials. *Science*, 344(6190):1373–1377.

Appendices

Appendix A

The Potential for 3D Printed Connections in the Design and Retrofitting of Steel Structures

This appendix explores the potential application of utilising and retrofitting additively manufactured connections in steel structures. The concept of applying the general principles of Chapter 4 and Chapter 5 into additively manufactured connections is examined. This appendix is based on the paper titled: The Potential for 3D Printed Connections in the Design and Retrofitting of Steel Structures, with the intention of submitting to Journal of Advances in Structural Engineering date tbc. It should be noted this appendix reads as a standalone paper. It may repeat sections previously introduced in this thesis.

A.1 Abstract

European and American design codes specify RBS connections as a method of protecting columns through a capacity based design. The weakened sections of beam in the RBS dissipate the seismic energy through plastic yielding of the beam flanges and web. While RBS connections provide a safe and stable frame performance under earthquakes, they do not solve the problem of 1) large plastic deformations of structural members, 2) large residual storey drifts, 3) high repair costs and 4) loss of serviceability. There are three broad groups of new, novel and interesting connections which have been proposed in literature aimed at solving these problems which include weakening sections of the beam, fuse type connections and self-centring connections. However, many of these methods have a) no efficient design methodology which can provide an efficient acceptance criteria, b) no optimal solution for steel frames which can be implemented using these connections and c) no adaptability of connections to enable easy adjustment of mechanical stiffness and strength properties required for any design situation and optimized solution. This Appendix reviews the current literature and research into steel beam-column connections for seismic design. First, a literature review of Reduced Flange Section connections has been conducted followed by the many different novel dampers and energy dissipation devices, integrated into connections as fuses, self centring connections, and the feasibility of integration of Smart Memory Alloys into beam-column-connections as a means of re-centring damaged frames. Finally, a literature review of additive printing methods and techniques has been completed. The superior behaviour of additively printed 2D and 3D lattices suggests that stronger, lighter and more efficient energy dissipative connections could be produced. As a result of this work, additive printing techniques are proposed for beam column connections which could allow designers and retro-fitters the freedom to produce a wide range and variety of connections with specified characteristics.

A.2 Background

Reduced Beam Section (RBS) connections are included in European (BSI, 2004) and American (AISC, 2016b) design codes. RBS weaken sections of the beam adjacent to the beam-column connection by trimming the beams flanges which forces elastic and plastic yielding to occur in the RBS section. The main advantages of RBS connections are the prevention of brittle fracture occurring in conventional beam-column connections, ability to absorb the seismic energy from an earthquake by yielding at the RBS and provision of a specifically weakened point in order to protect the columns and beam-column welds joints (BSI, 2005; AISC, 2016b).

However, there are four main problems faced by structures incorporating RBS sections in the aftermath of an earthquake: 1) large plastic deformations of structural members, 2) large residual storey drifts, 3) high repair costs and 4) loss of serviceability. While conventional methods of RBS design provide a safe and stable design which prevents the collapse of the structure during an earthquake, often structures are permanently damaged to such an extent that they become unserviceable. Following an earthquake it may be to be more viable to demolish and rebuild structures rather than retrofit and repair. This extensive literature review examines the various retrofitting proposals, improvements to existing connections and new proposed ideas to address these four main problems.

1. **Large plastic deformations of structural members:** Under current design methods for moment resistant steel framed buildings the beams are allowed to form plastic hinges at either end resulting in significant yielding damage to the beam after an earthquake and damage (Sultana and Youssef, 2016b; Moradi and Alam, 2017), not only to the steel structure but also localised damage to building services, which in turn leads to expensive and time consuming rehabilitation consequences (Tong et al., 2016; Valente et al., 2017a,b). Although buildings are designed for a no-collapse and damage limitation requirement under BS/EN 1998 (BSI, 2004), with checks for compliance criteria for the ultimate and damage limitation states, this methodology of design produces large amounts of permanent damage and residual deformations.

2. **Large residual storey drifts:** Farmani and Ghassemieh (2016) noted that significant residual deformations in steel structures after severe earthquakes are a result of plastic hinges forming in the beams and Baiguera et al. (2016) state that residual inter storey drifts need to be better controlled. These residual drifts according to Valente et al. (2017a,b); Banisheikholeslami et al. (2016); Vasdravellis et al. (2013b,a) are difficult to inspect requiring repair that leads to high social-economic losses. Dimopoulos et al. (2013) summarises the social and economic losses associated with the repair of large residual drifts, including high repair costs, loss of building functionality (such as business interruption) and potential building demolition due to large residual inter-storey drifts (Priestley, 2000; Iqbal et al., 2016; Moradi and Alam, 2017).

3. **High repair costs:** The Northridge earthquake led to many beam to column connection failures. According to Castiglioni et al. (2012b,a) large repair costs were required in order to make the steel structures serviceable and advises that steel structures must be simple and cost effective to repair, as structural repairability of members poses a significant problem. Baiguera et al. (2016) and Moradi and Alam (2015) conclude through recent studies that repair costs are not viable when residual drifts are greater than $0.005rad$. Chan et al. (2009) and Xu et al. (2016) note that permanent damage from a serious earthquake is often so large that it is too expensive to repair and in some cases it is more economical and cost effective to demolish and rebuild a severely damaged building than to attempt retrofit or repair (Castiglioni et al., 2012b,a; Lin, 2015; Moradi and Alam, 2017).

4. **Loss of serviceability:** Buildings are designed to Collapse Prevention under a Maximum Considered Earthquake and to Immediate Occupancy under a Design Basis Earthquake (Garlock

et al., 2007). The MCE corresponds to a return period of a 2% probability in 50 years and the Design Basis Earthquake corresponds to a return period of 50% probability in 50 years (Jin and El-Tawil, 2005). A buildings performance can be significantly improved (in relation to the amount of structural damage sustained) by increasing the Immediate Occupancy performance level to achieve a return period of 2% probability in 50 years or the MCE. McCormick et al. (2008) conducted a study to assess the effects that residual drifts have on the occupants of buildings. They concluded that residual drifts of 0.5% ($0.005rad$) are considered as maximum permissible drifts. According to Erochko et al. (2010) if residual drifts of 0.5% are taken as the level beyond which structures are practically usable, then Special Moment Resistant Frames (SMRF) and Buckling-Restrained Braced Frames (ERBF) will not meet this immediate occupancy requirement. This is due to 79% and 60% of the design-level earthquake ground motions applied in Erochko et al. (2010) analyses, caused residual drifts greater than 0.5% in SMF and BRBF respectively. Xue and Chen (2003) highlights that even though a structure is designed against collapse, large amounts of damage may still occur in the building leading to a loss of serviceability.

A.3 Scope of this literature review

Proposals of new ideas for seismic design have been investigated by many researchers and presented in papers throughout literature. A detailed review of these proposals are explored in this Appendix. Many research papers have been produced on seismic resistant steel framed beam column connections that allow plastic hinges, and thus energy dissipation, to occur in either the beam or in the connection itself. Different methods ranging from simple to complex, such as: reduced beam and web sections, self-centring framed connections, self-centring pre-tensioned connections, replaceable fuse type damper connections and smart memory alloys (SMA) have been proposed by many researchers. Many of these methods seek to reduce the residual deformations, inter-storey drifts and larger plastic deformations that occur in both the steel beams and in the building.

Much research have been conducted on dampers located at the vicinity of the beam-column connections as a means to protect structural members from damage through friction or energy dissipation (Hsu and Halim, 2017). Fully welded connections cannot be easily replaced or repaired after a seismic event, thus, bolted connections with replaceable sections offer a more versatile solution (Oh et al., 2009; Köken and Körolu, 2015). Researches have proposed replaceable fuse type connections capable of sustaining multiple cyclic loading and absorbing seismic energy (Vasdravellis et al., 2013b,a). However, replacing dampers in a structure after a large-scale earthquake has proved to be both an economic and operational problem (Jahangiri et al., 2016). Thus, the ideal solution would need to be easily replaceable to minimize repair costs (Valente et al., 2017a,b).

The aim of this Appendix is to carry out an extensive literature into the existing steel seismic beam column connections. Subsequently, a review of some of the additive printing methods and techniques that have recently been conducted. This Appendix proposes the use of additive (3D) printing of parts or whole beam-column-connections in order to produce superior seismic resistant connections and reduce or eliminate plastic deformations in beams, residual storey drifts, high repair costs and loss of serviceability.

A.4 Novel dampers and energy dissipation devices

Web Hourglass Pins (WHP) were first proposed by Kobori et al. (1992). Aa honeycomb damper (Figure A.4.1a) system and an hourglass-shaped damper (Figure A.4.1b) were proposed. The work

showed the development and application of honeycomb dampers and hour glass-shaped dampers to absorb the seismic and vibrational energy in a 29 storey building and indoor ski-slope respectively.

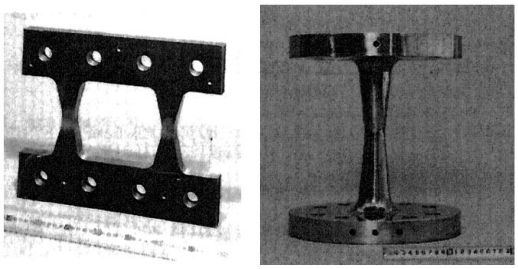

(a) (b)

Figure A.4.1: Novel energy dissipation devices (a) honeycomb damper and (b) Hourglass Pin (WHP) (Kobori et al., 1992)

Experimental results by Kobori et al. (1992) demonstrated excellent energy dissipation capacities with a butterfly shaped hardening characteristics at larger amplitudes of displacement and non-linear analysis showed how the structural displacements, storey drifts, maximum shear forces were reduced in the structures where the dampers were retrofitted.

A.4.1 Experimental evaluation of WHP

Vasdravellis et al. (2014) investigated the behaviour of WHP to evaluate how they performed and their application for use as steel yielding devices. The fracture capacity and the hysteretic behaviour of the hour shaped devices were investigated through testing of three types of steel: 1) HSS high ductility stainless steel carbon grade M1020, 2) SS304 stainless steel austenitic grade 304 and 3) SSD Duplex stainless steel. The yielding behaviour of the WHP is shown in Figure A.4.2. Fracture commonly started from section 1 in cyclic loading. Cracks formed also in sections 2 and 3. Ultimately the connections fractured at section 1.

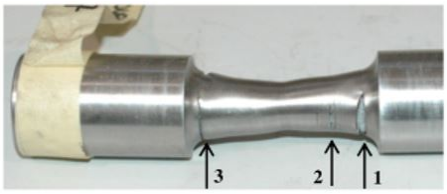

Figure A.4.2: Yielding of a WHP after testing (Vasdravellis et al., 2014)

The results showed that SS304 has the highest ductility followed by SSD with HSS having the least ductility. Monotonic tests showed that the hour glass connections are ductile and do not fracture and cyclic loading showed a stable hysteretic response. The SSD has a more reliable response and hence proved to be the most practical for seismic energy absorption applications. WHPs were noted to achieve a ratio of fracture displacement to yield displacement (ductility), suggesting that WHPs have adequate cyclic ductility and will not produce a sudden drop in strength which can accelerate the collapse of a frame.

A.4.2 WHPS integrated into moment frames

Baiguera et al. (2016) proposed a moment resistant frame (Figure A.4.3a) combined with concentric braces which used the novel hour glass shaped energy dissipative pins (WHP) proposed by Vasdravellis

et al. (2014) at the connection as replaceable fuses (shown in Figures A.4.3b and A.4.3c). The WHP are designed to dissipate energy by yielding of the high post yield stiff WHPs in the locations where plastic hinges are expected to occur in the beams. Experimental results showed that the WHPs produced a uniform distribution of plastic deformation in order to delay fracture and increase energy dissipation. Equations to predict the mechanical characteristics and capacity of the hour glass shaped pins were developed. The beam fuses presented in Baiguera et al. (2016) are designed to follow the same methodology as Shen et al. (2011), where a steel plate was bolted between two beams in order to concentrate and localise the plastic deformation in this plate.

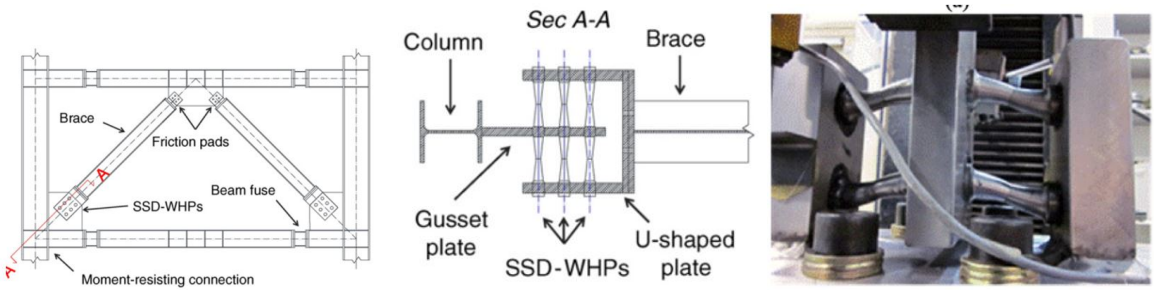

(a) (b) (c)

Figure A.4.3: (a) Concentric braced moment frame with SSD-WHP connections, (b) section through the SSD-WHP connection and (c) experimental tests on the WHPs (Baiguera et al., 2016)

Baiguera et al. (2016) showed through push over analysis of the frame, that the integrated WHP fuse sections reduced the base shear and horizontal drifts. However, more tests should be undertaken to take into account the specific boundary conditions which may affect the performance of the WHPs. Baiguera et al. (2016). concluded that the proposed dual frame shown in Figure A.4.3a allowed plastic deformations to be concentrated in the fuses. The WHPs give the system a much higher post yield stiffness. Results showed that the combination of both the WHPs and bracing drastically reduced the maximum residual drift. The WHPs have been designed to have large yield displacements in order to minimize the likelihood of fracture and prevent collapse.

A.4.3 Sliding controlled coupled beam module

A novel sliding controlled self-centring coupled beam module adopted by Lin (2015), shown in Figure A.4.4, was adopted for a global frame analysis of a steel frame. The module consists of two wide flange beams are mounted on top of each other with a number of post tensioned stands between them. Energy dissipation devices are also located between the wide flanged beams consisting of friction bolts, steel plates and tee sections to dissipate the energy. Lin (2015) investigated the performance of the new self-centring couple beam system using OpenSees (a finite element dynamic package). A non-linear model was created and a static pushover analysis was used to verify its behaviour. A dynamic time history analysis was performed in order to investigate how the frame responded to 44 different ground motion records.

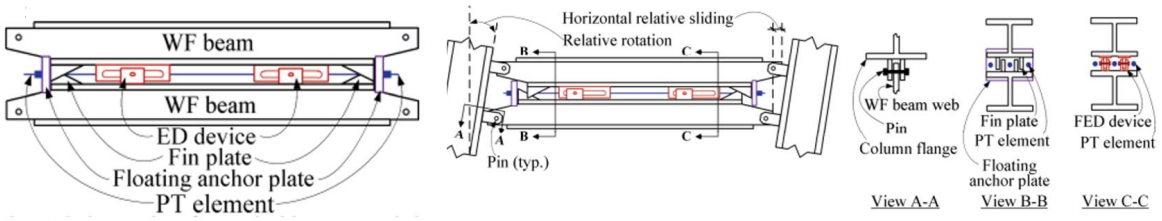

Figure A.4.4: Sliding controlled coupled beam used in the frame analysis (Lin, 2015)

From the static push over analysis Lin (2015) showed that the sliding couple beam system achieved the expected limit states with some column base yielding which consequently reduced the moment-rotation stiffness. The peak story drifts indicated that the couple beam system could reduce the damage to displacement-sensitive elements of a building. In addition, the minimal residual story drifts of about 0.0002% also showed that minimal residual damage of the building frame would occur compared to a frame without the coupling module. Finally, the ground floor accelerations were also very small, suggesting very little damage would occur to acceleration-sensitive building elements.

A.4.4 Weld free cast steel energy dissipation connections

Two innovative weld free beam to column connections have been proposed and investigated by Tong et al. (2016). The cast steel connections shown in Figure A.4.5a were labelled as C1 type connection and C2 type connection. The "C1" type dissipative device was designed for unidirectional deformation only and the "C2" type device for bidirectional deformations.

Tong et al. (2016) wanted to force the deformation and energy dissipation away from the beam (and column) and into the dissipative connection to allow easy replacement of the connection after a seismic event. Figure A.4.5b shows five different arrangements of the dissipation devices to form five connections. These consisted of a combination of the new innovative dissipation devices (C1 and C2 – shown in Figure A.4.5a) as well as shear tabs and traditional welded T-stubs (WT1 and WT2).

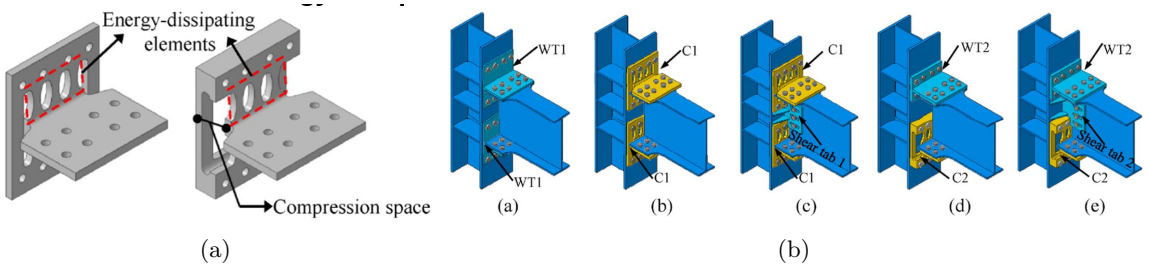

Figure A.4.5: (a) Weld free cast steel connections with "C1" type on the left and "C2" type on the right (b) Five different connection combinations investigated (Tong et al., 2016)

All of these connections tested by Tong et al. (2016) eventually failed by the fracturing of the cast steel energy dissipation devices. The traditional welded connections all failed by fracture of the T-stub along the weld line. Tong et al. (2016) concluded that the innovative cast steel devices have a good energy dissipation capacity. The shear tab did not improve the energy dissipation capacity of the connection but did increase the stiffness and strength, therefore, it was recommended that the shear tab should not be used unless large shear forces are present. A simple equation to determine the resistance of the connection and design recommendations relating to connection detailing and preliminarily design for the cast steel dampers were also proposed.

A.4.5 Slit dampers

Oh et al. (2009) developed a metallic slit damper, shown in Figure A.4.6a, that limited the plastic deformations of the connection into the damper which can easily be replaced. The slit damper actively plastics before any damage occurs in the beam-column connection, achieving suitable energy absorbing characteristics. Four different arrangements were tested: two different arrangements of slit damper geometry (shown in Figure A.4.6b), and each tested with and without a concrete slab present above a welded moment connection. The results showed that all slit damper configurations sustained rotations over $0.03rad$ with no sign of plastic deformation in any parts of the beam or column, an ultimate state was achieved at $0.04rad$ of rotation. The slit dampers absorbed on average 94% of the energy showing that the energy absorption of this connection is mainly in the dampers (more specifically the damper struts – shown in Figure A.4.6c) rather than in to the beam.

The presence of a reinforced concrete slab affects the position of the neutral axis and hence causes a larger strain on the lower flange, leading to a potential brittle fracture at the bottom flange. Oh et al. (2009) showed that the deformation capacity of a composite connection was half of that of a steel beam connection with the slit damper at the lower flange. Experimental tests were also compared to a conventional welded connection, shown in Figure A.4.6d. This welded connection sustained major local buckling, demonstrating how the slit damper can absorb most of the energy and concentrate all of the deformation to the dampers struts (Figure A.4.6c). Slit dampers are located at the lower flanges of the beam, to allow easy replacement even if a reinforced composite concrete slab is present. Oh et al. (2009) concluded that this damping system provided stable hysteretic energy absorption behaviour with the plastic rotations concentrated only in the replaceable slit dampers.

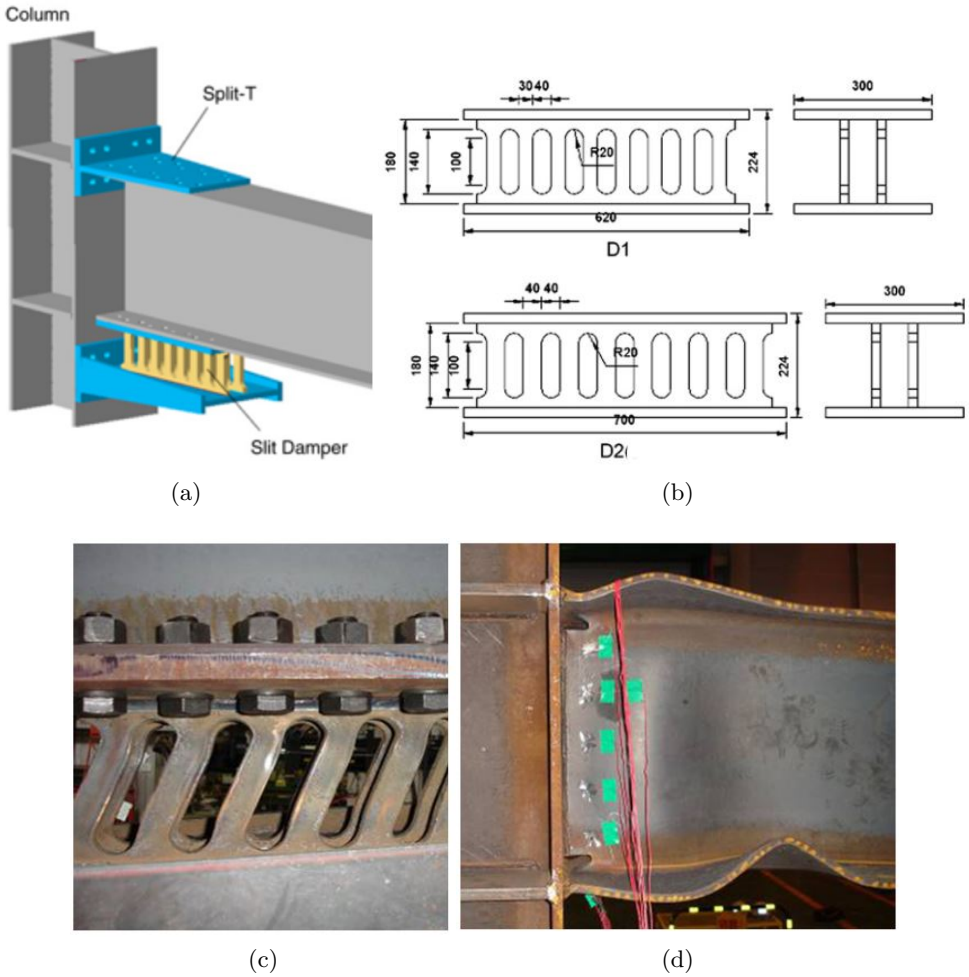

Figure A.4.6: (a) energy dissipation device connection (b) two different geometries of slit damper investigated (c) yielding of the slit damper and (d) deformations due to local buckling in cases where no slit damper is present (Oh et al., 2009)

Köken and Körolu (2015) carried out experimental studies on beam to column connections with slit dampers in order to dissipate lateral cyclic loading. The slit damper tested, shown in Figure A.4.7a allows the structure to be easily repaired. Köken and Körolu (2015) carried out three full scale experiments using two dampers (Figures A.4.7b) and one traditional extended end plate (Figure A.4.7b). They observed that for the end plate connection buckling of the lower flange of the beam occurred after $0.02rad$ but in both connections with dampers, rotations of 0.04 and 0.06 (for the two different thickness of dampers $12mm$ and $15mm$ respectively) were obtained with cracks developing in the dampers at these large rotations. Stiffeners have been added to the beam and column to help concentrate the deformation in the damper, allowing the beams to remain elastic until the ultimate state (typical arrangement of the connection shown in Figure A.4.7b). The larger (thickness) slit damper of $15mm$ carried a higher load compared to the thinner (thickness) $12mm$ slit damper. Köken and Körolu (2015) concluded that the slit dampers provide a stable hysteresis behaviour under large storey drifts.

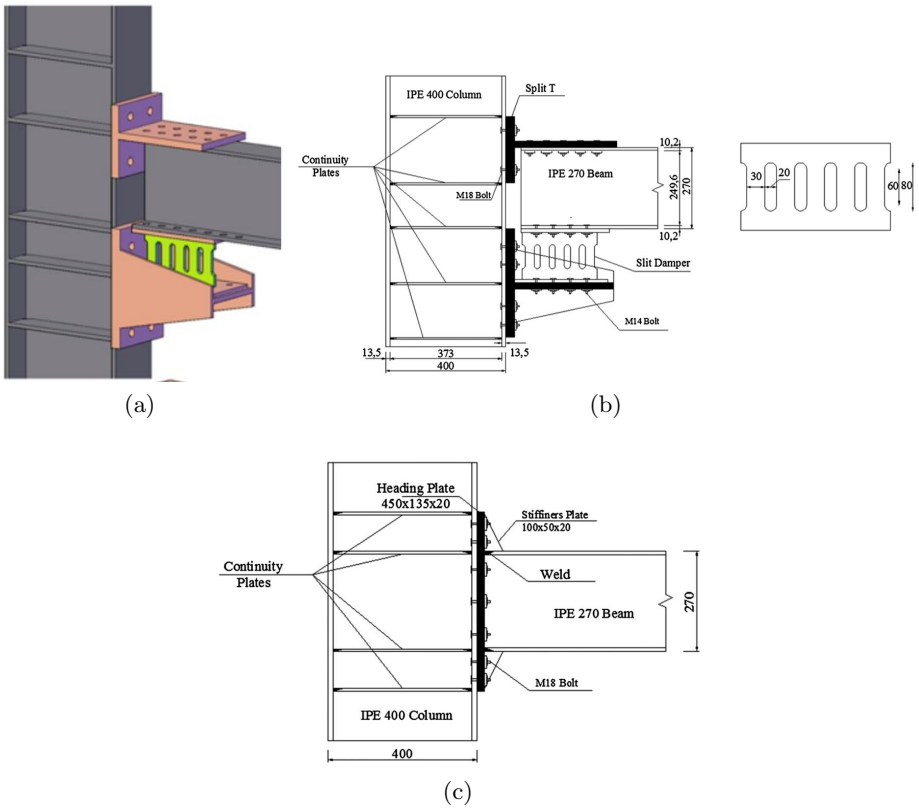

Figure A.4.7: (a) typical schematic of the slit damper tested and (b) connection details fitted with the damper (c) traditional extended end plate connection (Köken and Körolu, 2015)

A.4.6 Pi damper for weak axis connections

A new and novel connection for the weak axis of a beam-column connection shown in Figures A.4.8a and A.4.8b has been proposed by Koetaka et al. (2005). The new connection configuration consists of U-shaped steel dampers (Figure A.4.8b) which connect the beams lower flange to a continuity plate which is welded to the column. The top of the beam flange is connected by splice plates as shown in Figure A.4.8a. This novel connection was developed in order to have a stable hysteresis behaviour, large ductility capacity and a resistance to low-cycle fatigue. Koetaka et al. (2005) tested 6 different variations of the Pi damper sub assembly as shown in Figure A.4.8c.

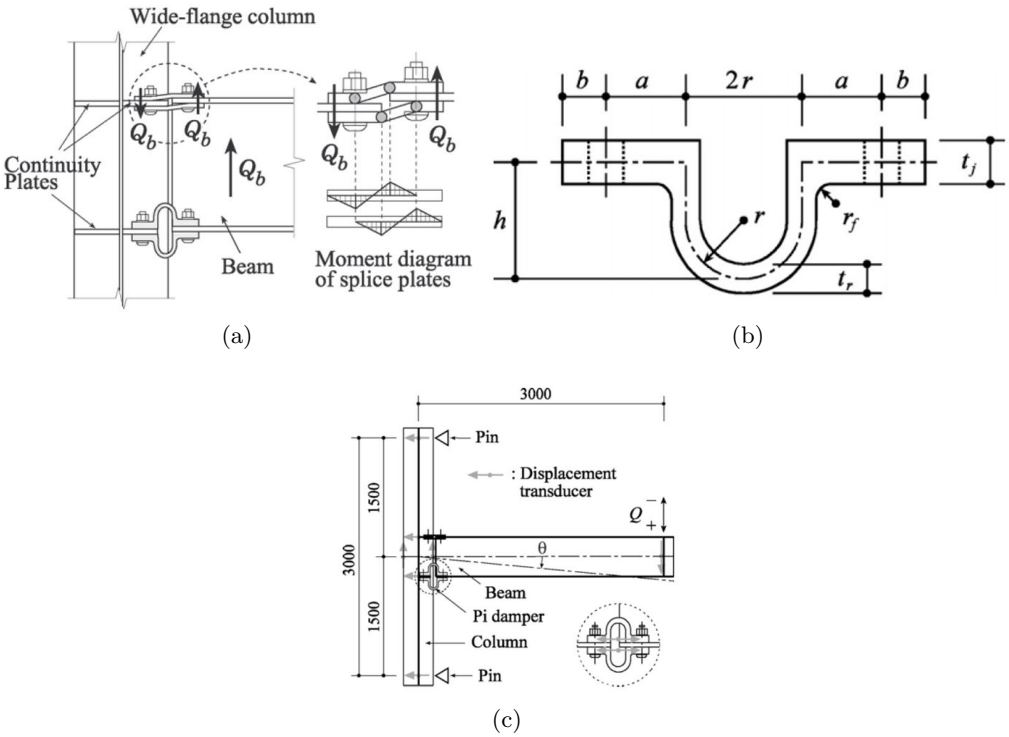

Figure A.4.8: (a) Connection showin the Pi damper with moment splice plates, (b) dimensions of the Pi damper and (c) experimental set up used (Koetaka et al., 2005)

The innovative U-shaped Pi damper could provide an effective weld free moment resistant frame by transferring the gravity loading through bending of the splice on the top flange and transferring the moment, as a couple, through the splice and U-shaper Pi damper. The simple design of the connection enabled it to be very predictable and precise design was to be possible through equations, as a result of their work a number of equations are presented in Appendix A of Koetaka et al. (2005).

A.4.7 Curved steel damper

Hsu and Halim (2017) proposed to use curved steel dampers (shown in Figure A.4.9a) as an energy dissipation device in-order to improve the strength, stiffness and energy dissipation of moment resisting steel framed buildings. Hsu and Halim (2017) performed cyclic tests on rigid, semi-rigid steel frames (without curved dampers) and semi-rigid steel frames fitted with curved dampers: examples of the frames tested are shown in Figure A.4.9b.

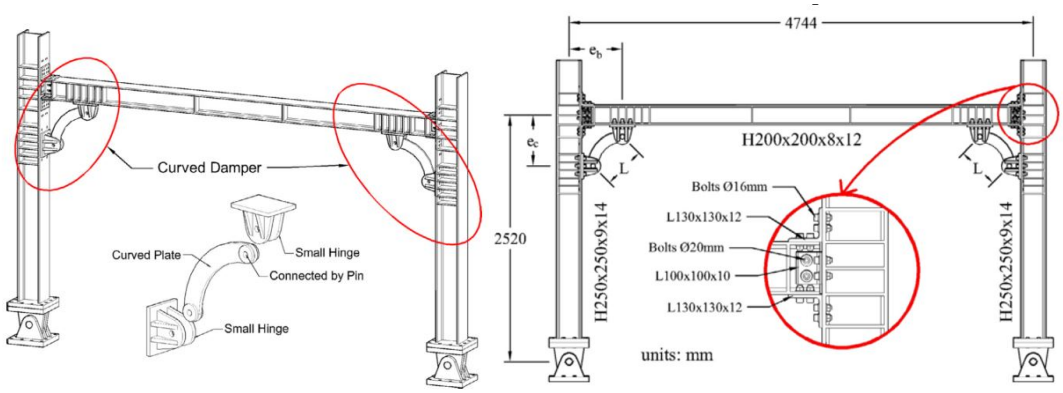

(a) (b)

Figure A.4.9: (a) Semi-rigid frame system with curved damper and (b) elevation of the frame and damper system (Sabbagh et al., 2012)

The tests showed how the stiffness of the semi-rigid frames is enhanced by using the curved dampers providing a stiffer frame compared to a semi-rigid steel frame (without curved dampers). The response of the frame due to different sized dampers was investigated and in general, larger dampers gave lower stiffness in structural frames. Although the rigid moment frame was the strongest the semi rigid moment frame with dampers fitted improved the strength compared to a semi rigid moment frame (without dampers) and the curved dampers improved the dissipation of the semi rigid moment frame significantly providing a much larger energy dissipation compared to the rigid moment frame. The curved dampers provided a stable hysteresis response as well as, significant improvements in the stiffness, strength and energy dissipation compared to semi-rigid moment frames and enhanced frame performance compared to a rigid moment frame.

A.4.8 Yielding shear panel device

Chan et al. (2009) proposed a new type of seismic energy dissipation device, which dissipates energy through the plastic shear deformation of a thin walled steel plate welded to the inside of a hollow section. A yield shear panel device (YSPD) is connected to the top of an inverted V-brace and the floor panel in a structural system (shown in Figure A.4.10a). The YSPD device is made from a short section of a square hollow section (SHS) with a steel diaphragm plate welded inside. Examples of the YSPDs are shown in Figure A.4.10b. Twelve specimens were tested under monotonic and cyclic tests with two different sized SHS and three different sizes of diaphragm plates with thickness t (refer to Figure A.4.10c). Bolt holes were drilled into the flanges of the SHS and the diaphragms were spot welded in the corners and fillet welded along the edges.

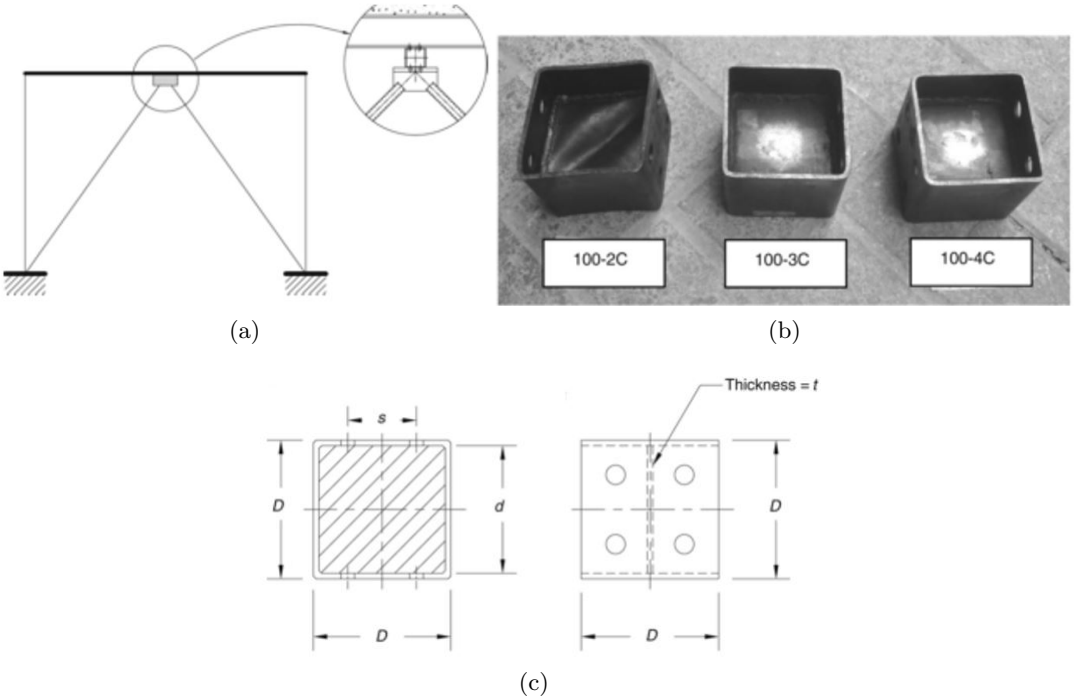

Figure A.4.10: (a) inverted V-braced frame, (b) cyclic deformations on the yield shear panel devices (YSPD) and (c) elevation (left) and plan (right) of a YSPD (Chan et al., 2009)

From the experimental cyclic tests it was observed that specimens with thick diaphragms did not buckle but produced largely pinched hysteresis loops while most others exhibited shear buckling depending on the plate slenderness. Slender diaphragms offered good energy dissipation, strength and ductility due to inelastic plate buckling whereas devices that did not buckle gave unsatisfactory strength and energy dissipation.

A.4.9 Steel plate shear walls

Dampers dissipate energy by deformation/yielding or by another means (such as fluid dampers). The simplest method and most widely adopted approach is a fuse device which is designed to yield when dissipating energy and hence needs to be replaced after an earthquake (Kurata et al., 2015).

The special steel plate shear wall, included in American standards consists of a steel panel (Figure A.4.11a) with many slits laser cut into it (referred to as links, see Figure A.4.11b and A.4.11c). Upon shear deformation, the links behave like a flexural member with the point of inflection at mid height. As the links yield, out of plane buckling occurs and energy is dissipated by the slit wall. The stiffness and strength of the slit wall can be controlled by varying the aspect ratio and thickness of the links.

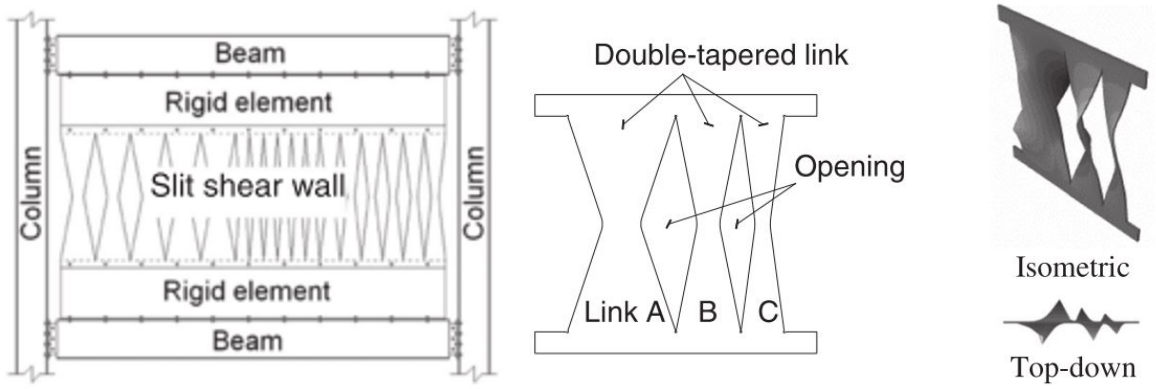

(a) (b) (c)

Figure A.4.11: (a) elevation of the slit shear wall, (b) arrangement of the openings in the slit wall and (b) isometric elevation of the openings (Kurata et al., 2015)

Kurata et al. (2015) investigated how the thickness and aspect ratio of the links affects the behaviour of the slit shear wall. A finite element (FE) model of the slit shear wall was developed and used to investigate the width-thickness ratios which control the buckling. Test results showed that the initiation and growth of torsional deformation differed depending on the thickness ratio with the smaller slits being more vulnerable to local buckling than yielding. They showed through test results that the slit shear walls could be used as an assessment of the condition of the structure. They concluded that if the links were designed to rotate at specific drift ratios in a structure, these deformed links could be used as an indicator of the maximum deformation experienced by the shear wall (and/or structure).

Steel plate shear walls have become integrated within the American design process. Previous research has shown that steel plate shear walls are good at resisting shear deformation by a tensile action after the onset of buckling of the links. Energy dissipation is provided by the yielding of laser cut links, however, shear plate walls have been noted to exhibit a pinching cyclic hysteresis behaviour.

He et al. (2016) tested four different steel shear plate walls shown in Figure A.4.12. Width to thickness ratios control the local buckling, hence, the width to thickness of the individual links in the shear walls controls the inelastic behaviour. Early local buckling reduces the energy dissipation of the links so in order to maintain the shear strength and stiffness, shorter links are required and should be arranged in rows.

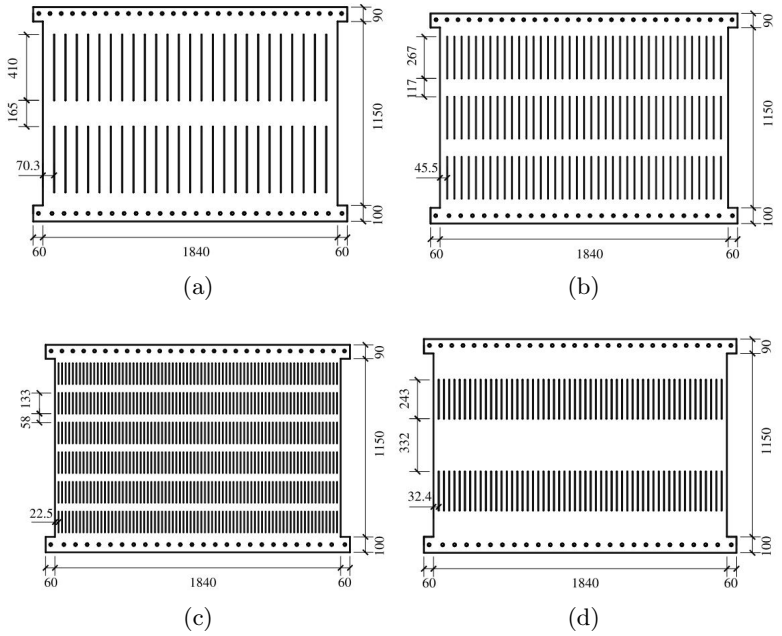

Figure A.4.12: The different shear plate walls tested refereed to as (a) Specimen 1, (b) Specimen 2, (c) Specimen 3 and (d) Specimen 4 illustrate the varying link dimensions investigated (He et al., 2016)

Experimental results showed that in specimen 1 local buckling occurred and a slight pinch in the hysteresis started from a 3.5% drift ratio. Specimen 2 and 3 exhibited a large amount of dissipation and no local buckling. Fracture of the links occurred in specimen 4 at a drift ratio of 2%. A proposed design procedure was based on the overall dimensions of the steel shear wall and also on the width to thickness ratio of the link. By changing the aspect ratio and width to thickness ratio, a specific shear strength and stiffness can be achieved while at the same time maintaining the energy dissipation.

A.4.10 Cold formed steel dissipation

Sabbagh et al. (2012) investigated the moment rotation behaviour of thin walled cold form steel sections (shown in Figures A.4.13a and A.4.13b) to identify their potential as dissipative elements in seismic design. Typically, cold form steel has a low seismic energy dissipation capacity and beam column connections develop premature local failures with low strength and stiffness. Sabbagh et al. (2012) investigated how to develop plasticity in the beams rather than yielding of the material around the bolt holes (which is usual in the relatively thin cold formed sections) and the inability of thin walled beam elements to develop plastic hinges. The moment rotation behaviour of out of plane stiffener configurations of cold formed steel beams were compared, as well as a study on the buckling and post-buckling of beams with curved flanges (see Figure A.4.13b).

Moment rotation curves are shown (Figure A.4.13b) for a range of section profiles. By increasing the number of bends in the flange the moment strength and initial stiffness is also increased. Sabbagh et al. (2012) also investigated how vertical stiffeners affected the performance of the connection (shown in Figure A.4.13c). It was noted that premature web buckling occurred in the case where no stiffeners were present, where a large force concentration was detected in the first line of bolts.

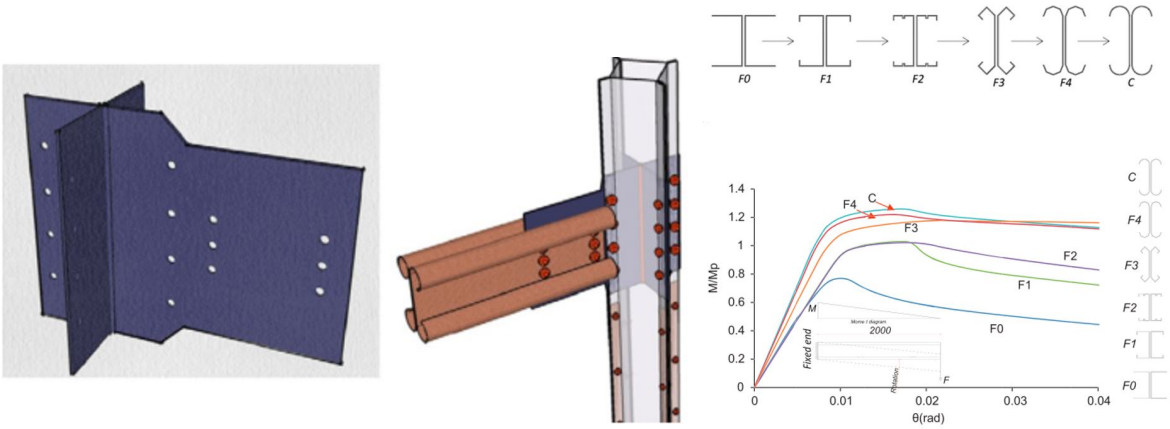

(a) (b)

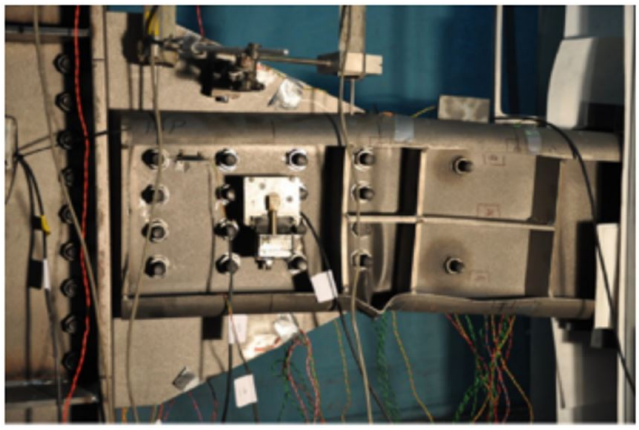

(c)

Figure A.4.13: (a) Cold formed steel connections, (b) profile of the cold formed steel sections and moment rotation curves and (c) experimental tests with additional out of plane stiffeners for increased stiffness (Sabbagh et al., 2012)

FE analysis showed that bending the flanges, increased the level of stiffness which can be achieved (with the maximum stiffness occurring when curved). FE analysis of the connection also showed that out of plane stiffeners are needed in-order to improve the bending strength and ductility of cold formed steel connections, and that the optimum configuration of stiffeners (adopted from a FE analysis) improved the moment strength, ductility and hysteretic energy dissipation capacity.

A.4.11 Retrofitted rubber dampers

Cao et al. (2016) reported on a rehabilitation project in a building where oil dampers (which were damaged due to pounding and over extending leading to significant damage beyond repair) were retrofitted with rubber bearings. A non-linear time history analysis was performed to select the appropriate retrofit strategy. The retrofitted isolators, shown in Figures A.4.14a and A.4.14b give smaller acceleration and displacement responses compared to the oil dampers under a simulated response. They are also able to accommodate large inter storey drifts and produce a stable hysteresis curve. Although the rubber isolators cannot enhance the load carrying capacity, they do however suppress the vibration responses and produce a stable hysteric response (shown in Figure A.4.14c) capable of absorbing significant energy. Cao et al. (2016) concluded that the target performance of the energy dissipation device should be set based on the building performance level for the rehabilitation

design.

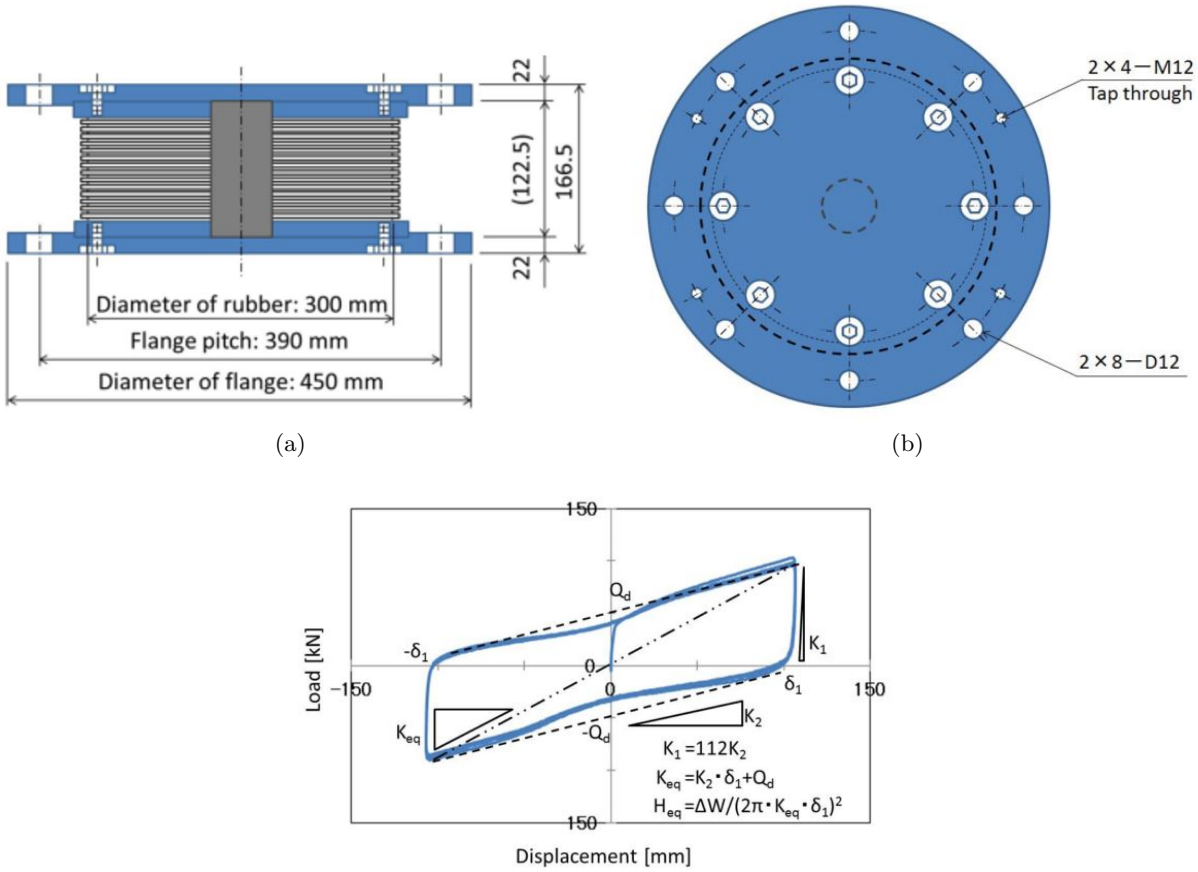

(a) (b)

(c)

Figure A.4.14: (a) section through the rubber damper, (b) plan view of the rubber damper and (c) stable cyclic hysteresis of the rubber damper (Cao et al., 2016)

A.4.12 Innovative weld free energy dissipative connections

Inoue et al. (2006) proposed a new structural system, shown in Figure A.4.15, which consists of a mechanically joined weld free arrangement with a metallic yielding damper for a beam to column joint. A weld-free system was proposed in order to avoid problems with defective welds and other detailing which could lead to brittle failure (such as backing bars and weld access holes). This research idea was to use a metallic yielding device at the beam to column joint, very high strength bolts and restraint bucking.

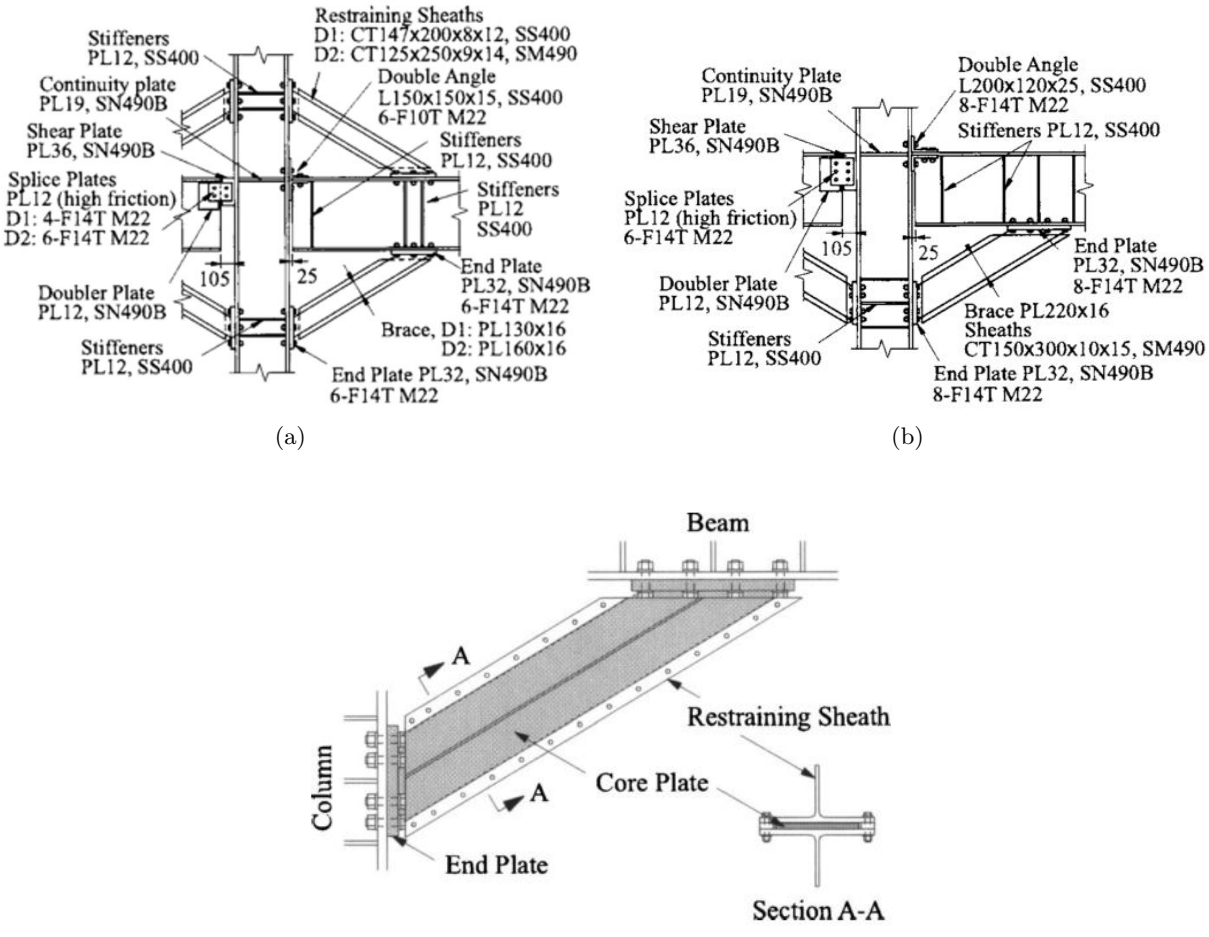

Figure A.4.15: Weld free assembly of the connection investigated with (a) double side bracing and (b) single side bracing (b) detailing and section of the bracing connection members (Inoue et al., 2006)

The top of the wide beam flange and the top of the wide column flange are bolted using shear and splice plates allowing the beams to rotate at their top flanges. Buckling braces, made of two steel tee sections, sandwich a core plate with a welded end plate at either end to provide a bolted connection to the column flange. These braces are present above and below the beam, Figure A.4.15a, and only beneath in Figure A.4.15b. Beams and columns are expected to respond in the elastic range with only significant yielding occurring in the buckling restrained braces.

The braces were designed to withstand twice the storey drift limit. The design criteria proposed assumes that yielding only occurs in the braces, the core plate axial strain must be limited and the restraining sheath in the brace must remain elastic. The lateral torsional stability of the braces have been investigated by Kawai et al. (2012) in an attempt to address these issues through experimental evaluation. The weld free set up provided a good hysteresis behaviour compared to conventional connections and moment resistant frames.

A.4.13 Improvements to double split tee connections

Latour and Rizzano (2015) proposed and developed a new concept of the double split tee stub connection. Normal tee stubs (Figure A.4.16a) are characterized by pinching and strength degradation, however, X-shaped double split tee stubs (Figure A.4.16b) have hour glass shaped flange plates to

spread the plasticization over the whole T-stub flange plate. Experimental tests (Figure A.4.16c) were conducted on a conventional double split tee connection and X-shaped double split tee connections (Figure A.4.16d) in order to compare their cyclic behaviour. The X-shaped flange has a higher dissipation capacity and does not exhibit strength degradation up to failure, which occurred in the heat-affected zone with a crack occurred in the hour glass shaped part of the flange.

(a) (b)

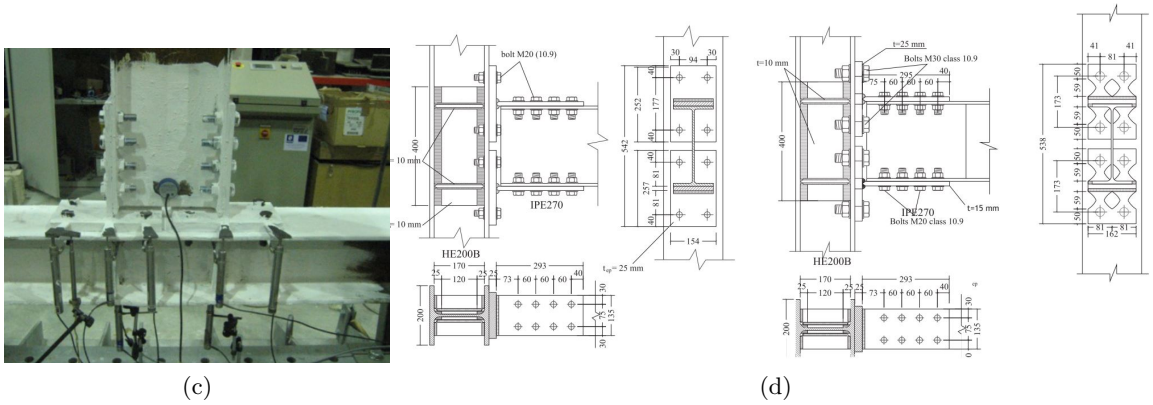

(c) (d)

Figure A.4.16: (a) Conventional double split tee, (b) X-shaped double split tee, (c) double split tee experimental testing set up and (d) the conventional double split tee connection on the left and the x-shaped double split tee connection on the right (Latour and Rizzano, 2015)

The experimental results showed that compared to a typical tee stub connection, the X-shaped tee stub connection has a much higher energy dissipation and a better strength degradation which enables it to concentrate the plasticization in the desired parts of the connection facilitating repair after seismic events. The performance of the connection could be controlled by calibrating the width and thickness of the tee stub and the distance between the bolts and the arising plastic hinge in the stem-flange connection.

Further research conducted by Latour et al. (2015) proposed the use of frictional pads integrated into double split tee connections and the effects of different types of materials (steel, brass and rubber) frictional dissipation devices using the test set up and apparatus shown in Figure A.4.17a. Classic double split tee connections with friction dampers incorporated into the joint detail are shown in Figure A.4.17b and the test set up shown in Figure A.4.17c.

Latour et al. (2015) concluded that the frictional double split tee connection is much less expensive than the traditional connections because over strength does not need to be provided in the form of

cover pates or haunches but, the damage free connections do not return to their original position after slippage occurs which suggests that large residual drifts are probable.

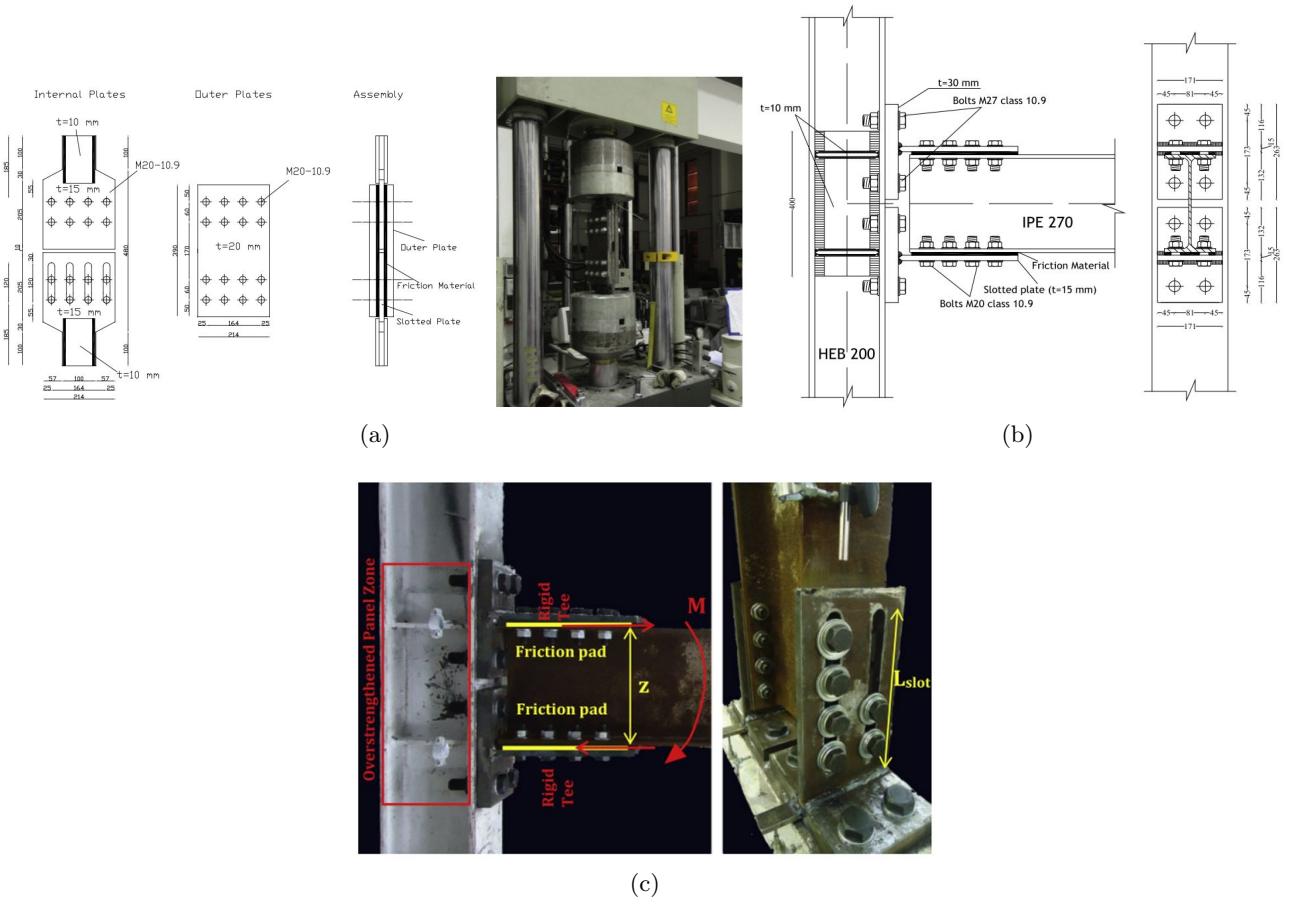

(a) (b)

(c)

Figure A.4.17: (a) Experimental arrangement and testing of the five different frictional materials, (b) double split tee connection arrangement and (c) the frictional and dynamic behaviour exhibited bt the double split tee connection during testing (Latour et al., 2015)

A.4.14 Sliding hinge joint

A sliding hinge joint, shown in Figure A.4.18, which rotates about a pin at the top of the beam flange shown as point of rotation in Figure A.4.18a was proposed by Clifton (2005). The sliding hinge joint is rigid under static loading but allows inelastic rotations under seismic or major earthquake excitations. Energy is also dissipated through an asymmetric friction connection at the bottom of the beam flange – enlarged details of the bolts, cleat and shims are shown in Figure A.4.18b. Yeung et al. (2013) conducted an experimental study in order to provide a better understanding of how the connection behaves.

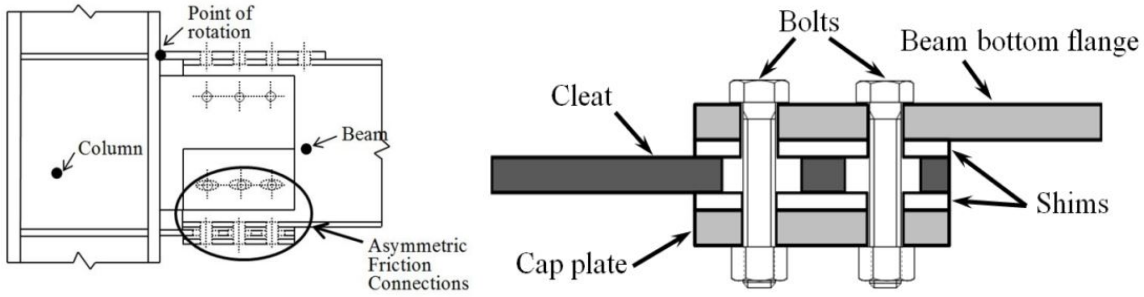

(a) (b)

Figure A.4.18: (a) Sliding hinge joint first proposed by Clifton (2005) and (b) the asymmetrical friction connection setup of the energy dissipating device in the sliding hinge joint (Yeung et al., 2013)

A.5 Replaceable fuse type connections

Most seismic design codes allow the energy from an earthquake to be dissipated in a building through inelastic deformations in the beams (or sometimes in the connections). This however leads to permanent deformations often incurring large repair costs in the building (Vargas and Bruneau, 2006). Fuse type connections consist of "links" between the beam and beam-column connection which, are usually bolted for easy replacement. Located in the position where the plastic hinge is likely to occur, these links are weaker than the beam and beam-column connection. This forces localised damage to occur in the links in order to protect the structure. Vargas and Bruneau (2006) suggest that the damage should be directed into easily replaceable fuses to allow easy replacement of these structural parts of the building. They proposed a design procedure for replaceable structural fuses based on a parametric study which considered the response of Single Degree Of Freedom (SDOF) non-linear structures under artificial ground excitations. The "upper bound" of the design procedure is controlled by an allowable storey drift, while values of the post yield stiffness ratio are chosen based on a capacity design for the type of fuse used in the connection. The ductility and post yield stiffness ratio are defined as target values. Vargas and Bruneau (2006) defined a procedure which designs an efficient frame for a specific set of design parameters which was subsequently verified using a non-linear time history analysis.

A.5.1 Dissipative devices research project

A "Dissipative Devices for Seismic-Resistant Steel Frames" (Vayas et al., 2013) investigated steel moment frames developed with dissipative fuse type connections: a bolted web and flange plate connection for a beam-column connection and dissipative pins for a shear wall assembly. The aims were to deliver a high level of ductility while at the same time providing repairable or replaceable components. A fuse type beam-column connection was developed by shown in Figures A.5.19a and A.5.19b, to control and concentrate the damage sustained during an earthquake leaving the beam and columns damage-free while at the same time being easy to replace. The stable hysteretic behaviour of the fuse allowed the damage to be concentrated in the fuse plate. A maximum rotation of $0.05rad$ was achieved by the connection and the minimum rotation capacity according to the European Design code (BS/EN 1998-3 (BSI, 2005)) was achieved.

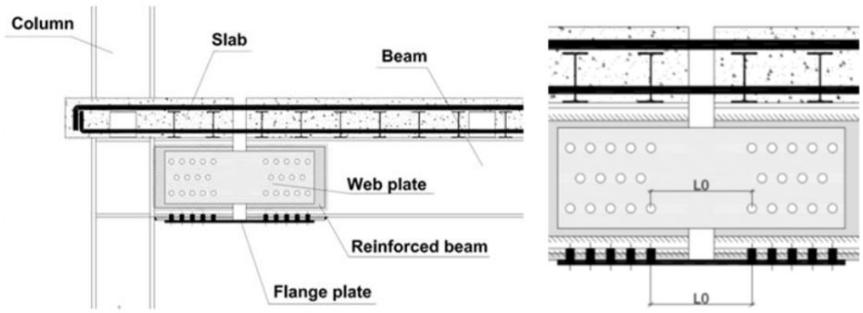

(a) (b)

Figure A.5.19: (a) Bolted fuse connection arrangement with the presence of a concrete slab and (b) elevation of the bolted fuse (Vayas et al., 2013)

A.5.2 Bolted fused web plate

Castiglioni et al. (2012b) carried out experimental testing of a bolted fuse type beam-column connection. The fuse type connection, shown in Figure A.5.20a, consists of bolted flange plates (Figure A.5.20b) and bolted web plates (Figure A.5.20c) connecting the beam to the column using high strength bolts. The energy dissipation is concentrated in these sections and are designed to develop plastic hinges so that they can be easily replaced after seismic loading.

Castiglioni et al. (2012b) conducted experimental tests (Figure A.5.20d) on four different specimens of fuse device which had varying thicknesses of the steel fuse plates. Moment rotation diagrams of the different fuses were produced, which, in general, showed a stable hysteretic behaviour with pinching due to the high strength bolts slipping and the fuse plate buckling. Energy was mainly dissipated by yielding and buckling of the plates and friction between the plates and connection surface.

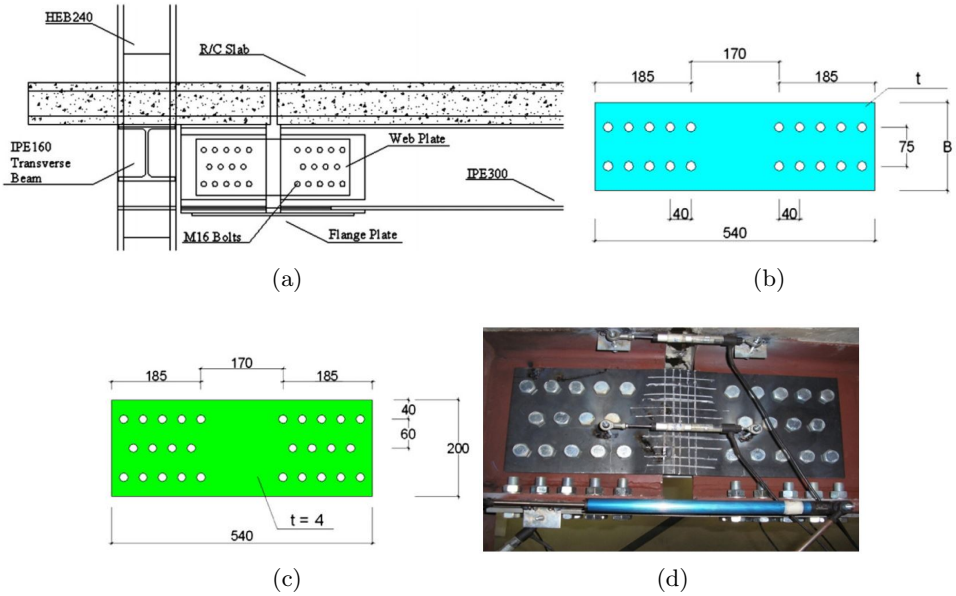

(a) (b)

(c) (d)

Figure A.5.20: (a) Bolted fuse plate connection and (b) experimental tests on the bolted fuse web and flange plates(Castiglioni et al., 2012b)

In general the beams and columns remained elastic with the inelastic behaviour being concentrated in the fuse connection. The results showed that fused connections with higher values of capacity

ratios gave better performances but connections with capacity ratios close to unity were not able to concentrate the damage to just the fuse connections.

A.5.3 Replaceable bolted steel plate

Valente et al. (2017a), carried out two experimental tests using a replaceable bolted fuse type link in a beam column connection incorporated into a composite steel and concrete set-up. The performance of the fuse device was assessed under cyclic loading. Results showed that the proposed device was easy to replace and isolated the large plastic deformations in the fuse through yielding, proving a good source of energy dissipation.

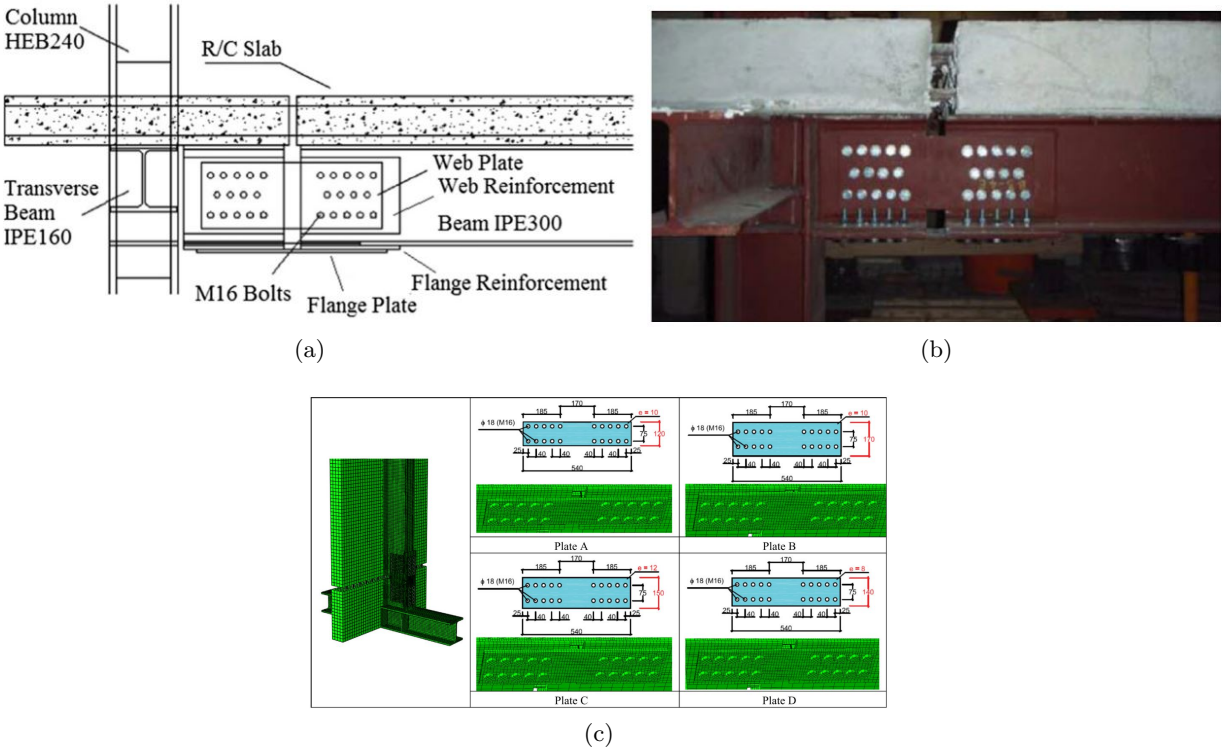

(a) (b)

(c)

Figure A.5.21: (a) Bolted fuse plate connection arrangement, (b) experimental set up of the bolted fuse plate connection and (c) FE models of the four bolted fuse plate connections assessed (Valente et al., 2017a)

Experimental tests from Valente et al. (2017a) were used to validated FE models. Four different fuses with varying slenderness, which were determined by the thickness of the fuse plate, were compared in the validated FE model. Non-linear dynamic FE analysis to assess the performance of the composite steel frames with the replaceable links using a computer code SIMQKE was also conducted. This enabled multi-storey composite steel frames to be analysed using simple numerical models calibrated from the experimental results. Results from the non-linear FE analysis of steel frames incorporating bolted fused connections lead to a reduction in the lateral stiffness and generally larger maximum displacements of upper floors, however, smaller residual drifts were noted. Higher amounts of total energy were dissipated in bolted fused frames giving a more stable plastic hinge formation under high seismic actions and gave larger ductility factors.

A.5.4 Welded fused web plate

Valente et al. (2017b) conducted a similar study but on welded fuse plates in a steel concrete composite floor system, shown in Figure A.5.22a. The fuse device consisted of steel plates welded to the web and the bottom flanges of the beam, providing a replaceable connection, allowing the plastic deformations from the stresses to be concentrated in the welded plates and hence protecting the rest of the beam, column and connection and preventing damage spreading into other parts of the structure.

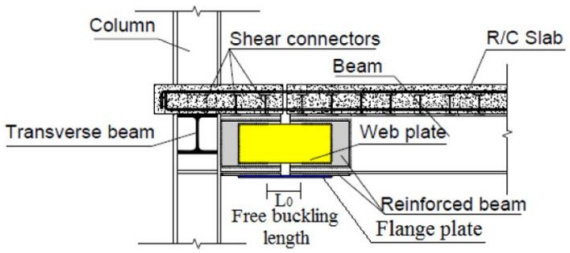

(a)

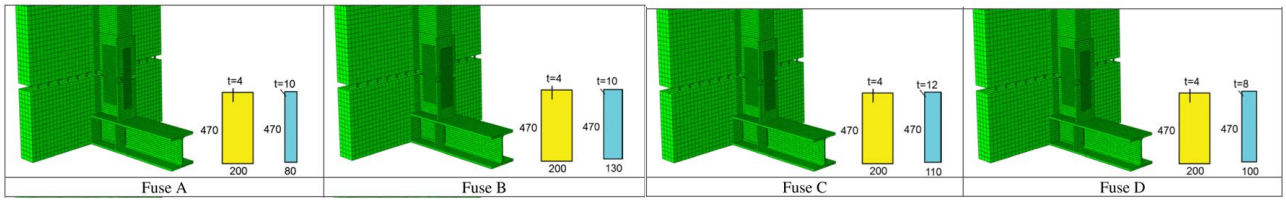

(b)

Figure A.5.22: (a) Welded fuse plate connection arrangement and (b) FE models of the four welded fuse plate connections assessed (Valente et al., 2017b)

Detailed FE models were used to analyse the response of the proposed connection – the gap between the connection was varied in order to investigate the effect of the buckling length of the steel plate on the connection; the cross section of the steel plates was also varied with four different geometries of welded fuse plate (refer to Figure A.5.22b).

Valente et al. (2017b) also investigated how steel framed multi-storey buildings with composite beam to column welded fuse plate connections responded through non-linear dynamic and static analysis. Three different steel frames with three, six and nine storeys were used and three different dynamic artificial earthquake records were applied to the steel frames through a computer code, and results were compared to conventional steel framed composite beam buildings. Generally, compared to conventional steel frames, the presence of the welded fuse plate gave larger maximum roof displacements but smaller base shears which varied depending on the resistance capacity of the welded fuse connections. The welded fuse plate frame were able to dissipate larger amounts of energy but larger maximum rotations were observed as a result of the welded fuses deforming and absorbing more energy. A collapse assessment showed that lower base shear forces were experienced for the welded fuse connection due to a reduction of the fuses bending moment capacity. Valente et al. (2017b) concluded that the position of the fuse is important and by moving the connection away from the beam column connection the top displacements of the frame could be reduced if the distance is too large plastic deformations occur in the beam or even in the column.

A.5.5 Non-linear replaceable fuse links

Shen et al. (2011) proposed two replaceable links: a W-section with bolted end plate connections (Figure A.5.23a) or back-to back channel sections with bolted web connections (Figure A.5.23a). Results indicated that frames fitted with the replaceable non-linear connection provided equivalent strength and ductility compared to conventional frames. The W-section end plate links showed a better energy dissipation capacity but a lower rotational capacity ($0.04rad$) compared to the back-to-back channel bolted web connections ($0.07rad$).

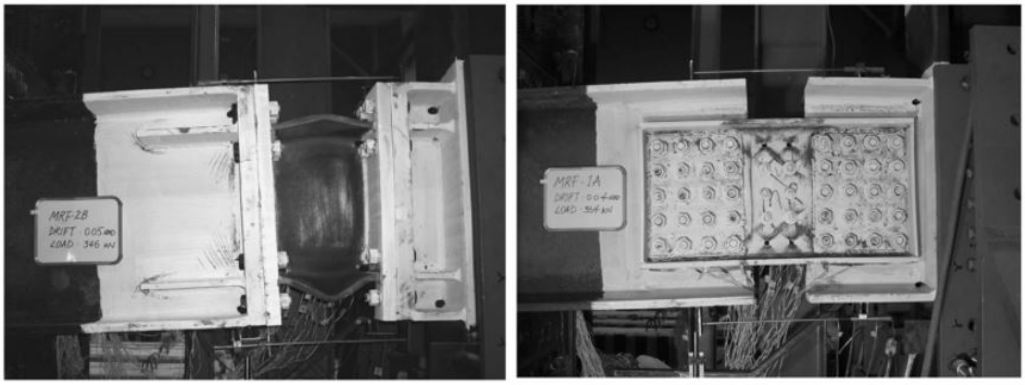

(a) (b)

Figure A.5.23: (a) W-Section replaceable fuse link and (b) back to back bolted channel section fuse link (Shen et al., 2011)

A.5.6 Removable links in braced frame

Dubina et al. (2008) attempted to direct inelastic deformations into removable links in eccentrically braced frames (shown in Figure A.5.24a) in order to allow easy repair and a reduced cost of rehabilitating a damaged building. They investigated through experimental tests (shown in Figure A.5.24b) how extended bolted end plate connections could be used as removable links. Figure A.5.24c and A.5.24d show examples of the links being tested.

Previous research by Dubina et al. (2001) showed that fillet welds, full penetration V welds (with the root at the exterior part of the beams cross-section) and the presence of a weld access hole all caused brittle failure of the beams flange during ground motions. For this reason Dubina et al. (2008) proposed the use of a full-penetration V weld with no weld access hole and a reinforcing fillet weld on the interior flanges and web. An over strength of the connection compared to the strength of the link shear resistance was adopted through a capacity design rule and the use of grade S235 steel for the link and S355 grade steel for the structure. The effect of closely and largely spaced stiffeners in the link was also investigated. Four different lengths of link connections varying between $100mm$ and $700mm$ were experimentally tested to investigate the moment to shear force ratio.

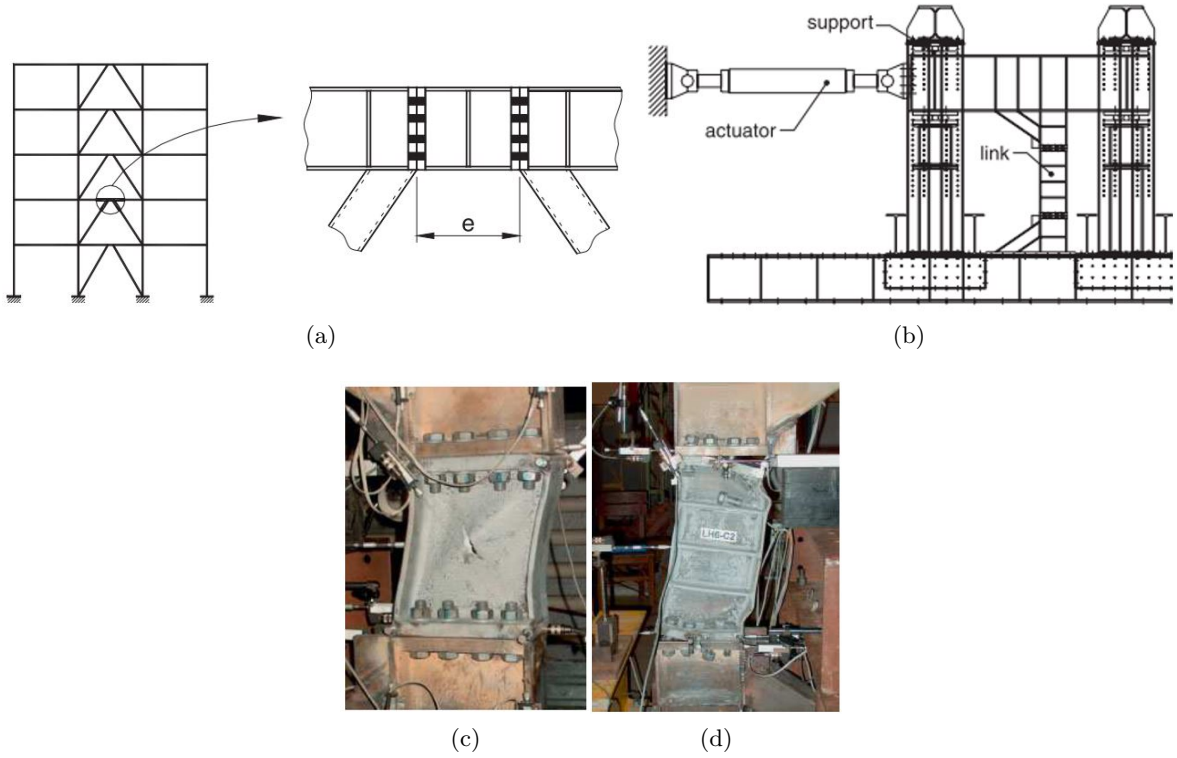

Figure A.5.24: (a) Location of the removable link in the braced frame, (b) experimental test set up, (c) short removable link and (b) long removable link with web stiffeners (Dubina et al., 2008)

Results showed that a longer link produced larger ultimate displacements with smaller links exhibiting a larger rotational capacity. Interestingly, pre-loading of the bolts did not affect the rotational capacity. The presence of the stiffeners in the links affected the deformational capacities with closely spaced stiffeners improving the deformation capacity.

Non-linear static and dynamic analyses were conducted for eccentrically braced steel framed building incorporating the replaceable link connections. The eccentrically braced frames with links exhibited larger inter-storey drifts than those without links but the links reduced the deformational demands on other members of the structure, as intended, as well as producing lower permanent inter-storey drifts.

A.5.7 Modular construction using cast beam sections

Fleischman (2013) suggested the idea of cast steel modular components in construction and showed that by casting specifically designed and engineered shapes, efficient and excellent energy dissipation, ductility and a specified reliable responses can be achieved. A superior structural performance can be achieved while improving the efficiency of structures by eliminating the need for many connection parts. The Cast Modular Ductile Brace System, aims to achieve this superior performance through a ductile mechanism, controlled by the relative flexural and axial strength of the cast components relative to the main HSS member. The main advantages of this system are a controlled buckling direction, strong bolted interface, ductile frame mechanism in the post-buckling behaviour and simple steelwork erection. Fleischman (2013) proposed the cast modular connecting concept shown in Figure A.5.25. These replaceable link elements utilize transverse or longitudinal bolts to connect the links to the rest of the frame.

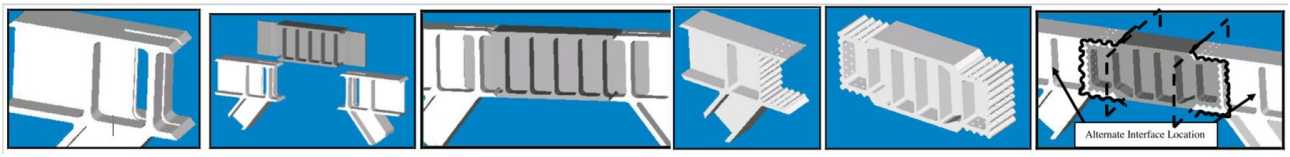

Figure A.5.25: The cast Modular Ductile Brace System proposed by Fleischman (Fleischman, 2013)

Fleischman (2013) presents two interesting concepts – a cast node connection (Figure A.5.26a) and a cast bolted plastic hinge connection (Figure A.5.26b). The cast node would eliminate a number of failure modes and reduce the need for the amount of welding and cutting of chord pieces. It also reduces the overall weight, however, this comes at an increase in fabrication cost. A cast bolted plastic hinge connection using cast connection elements consists of a reduced web section and two reduced flange sections shop welded to the beam and field bolted to the column to provide easy and fast construction. Flared geometry and smooth precise cast edges help to provide the best possible connection interface and transfer of forces between the beam and the column.

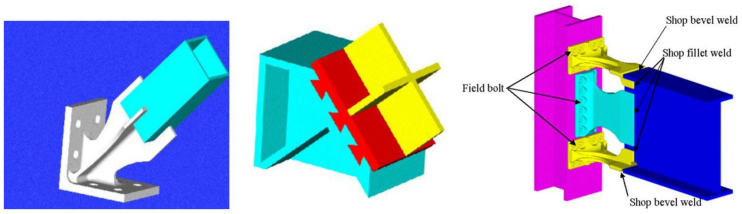

(a) (b)

Figure A.5.26: (a) Cast node connections and (b) cast bolted plastic hinge connection Fleischman (2013)

A.6 Self centring connections and frames

Self-centring moment resistant frames provide an alternative connection to the welded beam column connections (Herning et al., 2009). Post tensioned strands enable the connection to open and close during seismic excitations. The self-centring properties of these connections enable moment resisting frames to return to their original position with little, if any, residual storey drift.

A.6.1 Novel post tensioned self-centring connection

Jahangiri et al. (2016) investigated a new post-tensioned self centring connection, shown in Figure A.6.27. This connection utilizes a node which dissipates energy, while at the same time has the required stiffness, strength and ductility. Figure A.6.27b shows how the novel connection works; the post tensioned tendons pass through the column and over the yellow rigid node grooves, through the beam flanges and back over the node and return through the column. The column and beam webs require strengthening using double channel sections to prevent local buckling. Jahangiri et al. (2016) conducted monotonic experiments on this connection using a hydraulic jack to apply static monotonic loads.

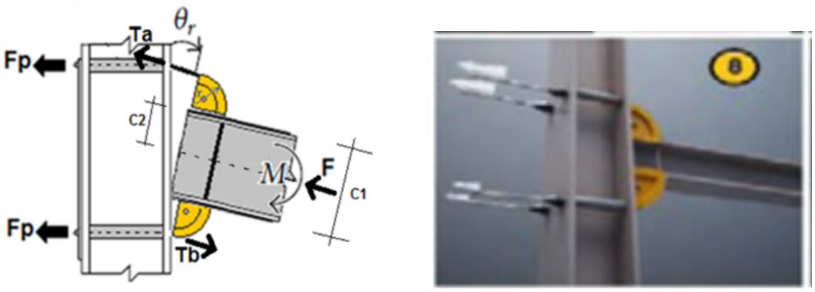

(a) (b)

Figure A.6.27: Novel self-centring connection (a) 3D view of set up and (b) cross section showing the self centring forces (Jahangiri et al., 2016)

Five test specimens with varied tendon lengths and strands were selected for experimental analysis. The post tensioned connection enabled self-centring post-testing and prevented damage to the beam and overall frame. The main advantage of this connection is the ease with which post-earthquake repairs could be carried out without welding or bolting.

A.6.2 Web friction device

Ricles et al. (2010) carried out an experimental study on a self centring moment resistant frame with web friction devices. This type of beam column connection utilises post tensioned strands to provide an opening and closing of the connection in order to allow the frame to self centre (i.e. return to its original position) after a seismic force has been applied. The addition of the web friction device allows dissipation of energy in the connection.

Figure A.6.28a shows the typical cross section of the connection tested. Two channel sections are welded to the column flange and attached to the beam by friction bolts and brass cartridge plates which provide additional friction for energy dissipation. Shim plates are also welded to the column flange to provide a large contact area. Reinforcing plates are welded to the beam flanges and to the inside column flanges (where the holes for the post tensioned strands are located) to prevent low-cycle fatigue.

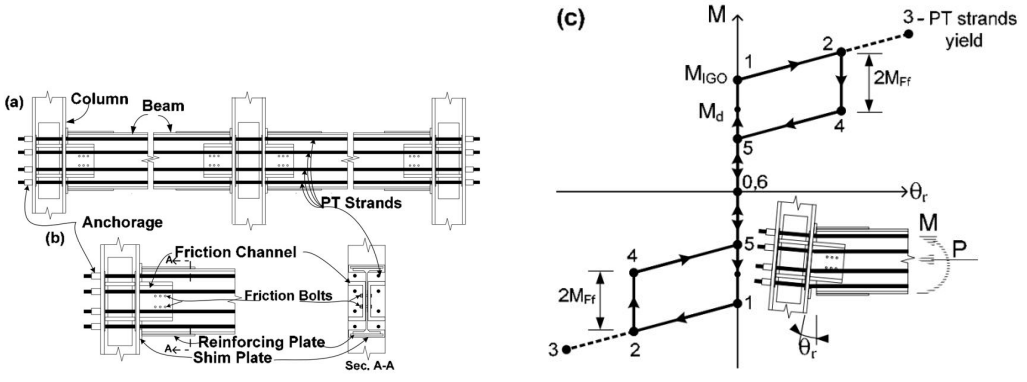

(a) (b)

Figure A.6.28: Self-centring connection showing (a) typical cross sections and (b) flag type energy dissipation concept (Ricles et al., 2010)

A typical conceptual moment rotation behaviour for a post tensioned web friction connection under cyclic loading is depicted in Figure A.6.28b (Ricles et al., 2010). Between points 1 and 2 the gap θ_r opens and energy is dissipated in the friction device. If the gap is too large, the strands yield at point 3.

A performance-based design of a steel frame incorporating these self centring devices was conducted to achieve immediate occupancy performance level under a design basis earthquake and a collapse prevention performance level after a maximum considered earthquake. The web friction device connections proved successful in self-centring the frame after design basis (immediate occupancy) and maximum considered (collapse prevention) levels of earthquake loading.

A.6.3 Bolted flange friction device

Wolski et al. (2009) carried out an similar experimental study on self centring connection utilising a bolted flange friction device. This device, shown in Figure A.6.29, dissipates additional energy through a friction device located below the lower beam flange (which helps prevent interference with the floor slab during construction). Pre-tensioned bolts with brass washers provide additional friction between the steel and brass.

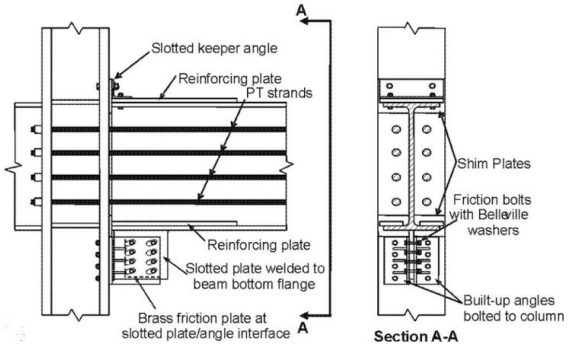

Figure A.6.29: Self centring connection with bolted flange friction device (Wolski et al., 2009)

Seven 0.6 scale tests were conducted which included both cyclic and seismic loading (Figure A.6.29). The effects of changing the level of friction, the bolt bearing, the weld details and the loading history applied to the device were investigated during the tests. The connection stayed damage free as long as the post tensioned strands remained within the elastic range. Shear failure of the friction bolts occurred after bearing on the ends of the slotted bolt holes was experienced. Furthermore, a fillet weld to connect the friction device to the bottom of the beam should be avoided as it was noted to have failed due to low cyclic fatigue and alternative complete joint penetration (CJP) weld should be used instead.

Through a performance-based design Tong et al. (2011) investigated a steel frame equipped with self centring beam column connections utilising the self centring friction device from Wolski et al. (2009). Open Systems for Earthquake Engineering Simulation (OpenSees) was used to model the frame at the global level as well as the connections at the local level. Zero length elements, based on existing experimental results in Wolski et al. (2009), were used to model the self centring connections response shown in Figure A.6.30. Compression only material properties were adopted to simulate the gap opening of the bolted flange friction device.

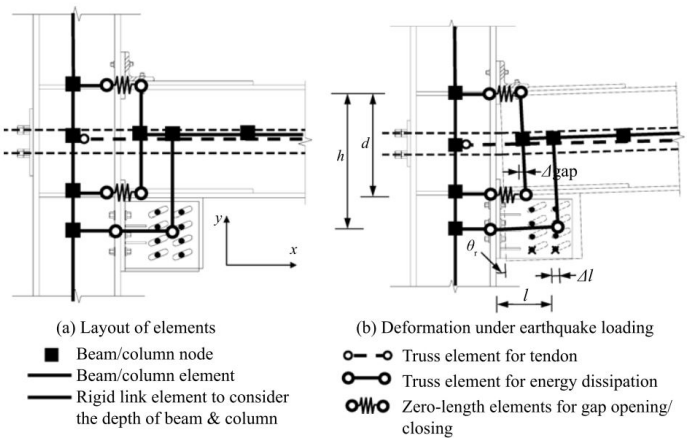

Figure A.6.30: Self centring connection with bolted flange friction device (Tong et al., 2011)

Tong et al. (2011) highlighted that a reliable performance-based design should be capable of capturing the non-linear states as well as the elastic states of the connections; many studies previously conducted in literature are limited to only the elastic analysis of the connection.

A.6.4 WHPs in self centring frames

Ductile steel moment resistant frames develop hinges in the beams in order to provide a global plastic mechanism. Although this approach has many advantages (lower floor accelerations, smaller base shear forces, collapse prevention) Vasdravellis et al. (2013a) note these plastic hinges lead to larger residual drifts and large inelastic deformations making repair difficult. To eliminate these residual deformations, flag shaped hysteresis curves need to be achieved by the connections. Vasdravellis et al. (2013a,b) used WHPs and post tension strands to help dissipate the seismic energy, shown in Figure A.6.31. This enhances the energy dissipation of the connection by isolating the damage in the WHPs, eliminating the residual inter storey drifts and any damage to the rest of the connection. The WHP pins do not interfere with the composite slab (if present), and are easy to repair without additional bolting or welding. The pins have been optimized to enhance the energy dissipation capacity and fracture capacity. The web of the beam has also been reinforced to avoid ovilasation of the WHP holes. Cyclic loading experimental tests were conducted in order to assess the energy dissipation and ductility of a post tensioned self-centring connection with integrated WHP pins. Two connections were tested one with reinforcing beam flange plates and reduced beam web sections, and one without these adjustments. The experimental tests conducted by Vasdravellis et al. (2013b) showed that WHP pins accommodate a large amount of the plastic damage and can be easily replaced without any bolting or welding.

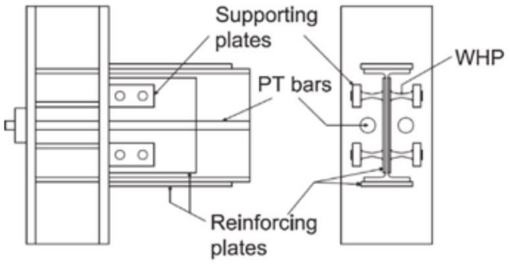

Figure A.6.31: Self centring connection with WHP pins (Vasdravellis et al., 2013b)

Experiments conducted on full scale specimens showed that the connection has a robust response to cyclic loading and can sustain damage and residual drifts of up to 6%. Repeated tests where the WHP pins were replaced, were also carried out. A finite element model was developed Vasdravellis et al. (2013a) using the results in Vasdravellis et al. (2013b). A parametric analysis of the post tensioned self centring connection characterised by the behaviour of the dissipative WHP pins was completed. Material yield strength, detailing of reinforcement in the beam (longitudinal plates and RBS) and contact plates (in the beam flange and between the beam and column faces) were all investigated in order to enhance the connection and analyse its response. The post tensioned WHP connections should be designed with RBS after the reinforcing cover plates to produce a stable plastic hinge as shown in Figure A.6.32. Additional longitudinal stiffeners and contact plates should also be used in order to help delay local yielding and prevent local buckling.

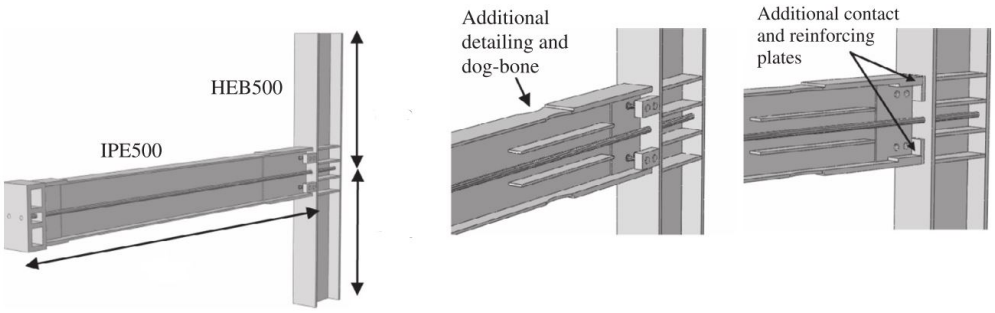

Figure A.6.32: Examples of the connection models investigated: (left) general set up (centre) additional RBS and (right) additional contact reinforcing plates (Vasdravellis et al., 2013b)

A.6.5 WHPs in self centring frames – performance-based design

Dimopoulos et al. (2013) used the work of Vasdravellis et al. (2013b,a) and incorporated their WHP pin connection in a global frame analysis using OpenSees. A simplified model, shown in Figure A.6.33 was created using zero length hysteretic springs elements to simulate connection behaviour including the gap opening phenomena. The hysteresis performance of the WHPs pins was calibrated using experimental results from Vasdravellis et al. (2013a,b).

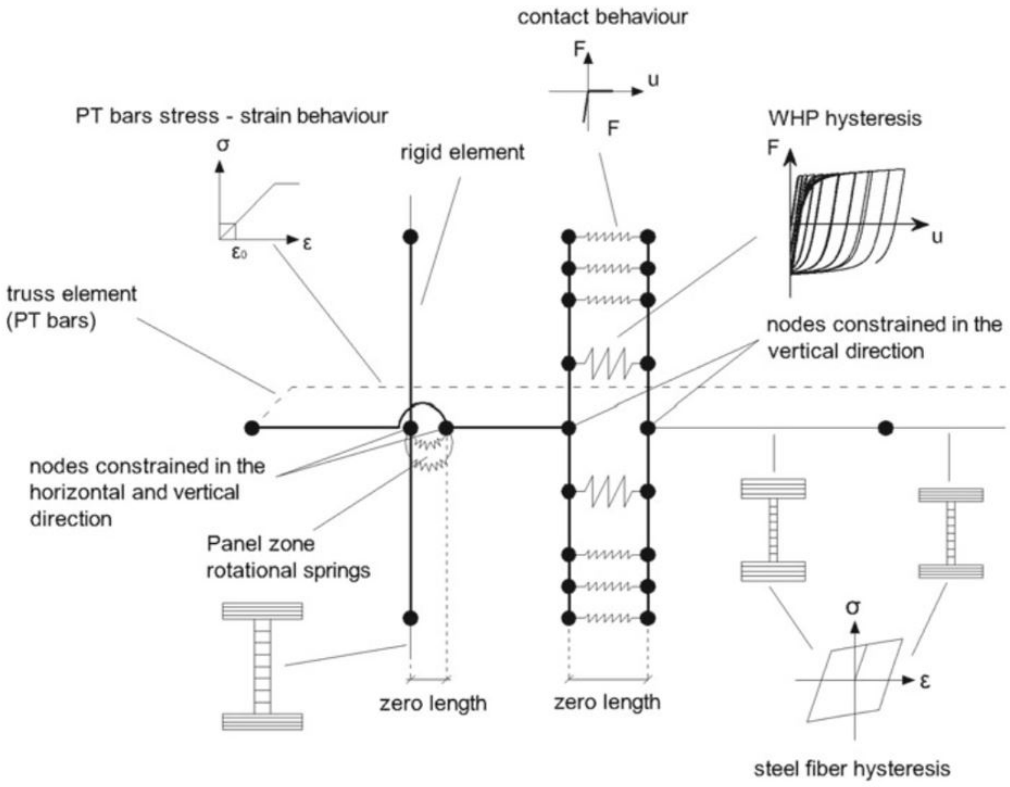

Figure A.6.33: Modelling of the self-centring devices in OpenSees (Dimopoulos et al., 2013)

Tzimas et al. (2015) investigated a self-centring moment resistant frame incorporating viscous dampers in the connection through a performance-based design. The self centring connections in the frame comprised of post tensioned connections with WHPs designed according to Dimopoulos et al. (2013) with the addition of viscous dampers. A five step performance-based procedure was suggested for the design of future self centring moment frames with or without the viscous dampers. The post tensioned connection consisted of WHP pins to absorb the inelastic deformations and keep the rest of the connection and structure damage free. The connection, in Figure A.6.31, consists of post tensioned strands to aid the self-centring ability of the connection. Four WHPs pins are aligned with drilled holes in the beams web and welded to stiff supporting plates that are in turn welded to the column flanges. The beams flanges around the WHPs contact area are reinforced using steel plates to help prevent ovalization and pinching behaviour.

A.7 Smart memory Alloys (SMA)

There are two types of of Smart Memory Alloys (SMA) which reverse the deformations: Shape Memory Effects which uses heating or Super Elastic Effects which uses unloading (Fang et al., 2015). Sultana and Youssef (2016b) investigated the use of SMA. Initially they analysed a conventional rigid connected moment resistant steel frame using a simplified pushover analysis proposed by Sultana and Youssef (2016a) and an Incremental Dynamic Analysis proposed by Luco and Cornell (1998) to identify the floors that had significant damage under the effects of a linear and dynamic analysis respectively. The failure and inter story drift limits were evaluated and used to decide where severe damage would occur. Sultana and Youssef (2016b) then incorporated SMA connections into the frames to give six different potential designs. The different designs were then analysed in terms of maximum inter storey drifts, maximum residual inter storey drifts and damage distribution. It was found that the locations of SMA affected the maximum residual inter storey drifts and that if all rigid connections were replaced

by the SMA connections maximum inter storey drifts and the level of floor damage was significantly increased compared to a rigid steel moment frame. However, if selected rigid connection locations were chosen in the frame and replaced with SMA connections then lower maximum inter storey drifts and levels of floor damage were observed. The SMA connections should be positioned at the top or bottom of the critical column in order to provide the best seismic frame response.

A.7.1 SMA within beam sections

Moradi and Alam (2015) explored the feasibility of incorporating Smart Memory Alloys (SMA) into beams (shown in Figure A.7.34) with the aim of forcing the plastic hinges to occur in the SMA so that its reshaping properties could be used to re-centre the frame and recover residual damage drifts. A 3D finite element model was used to analyse the intelligent SMA re-centring properties in order to minimize damage to buildings post-seismic excitations.

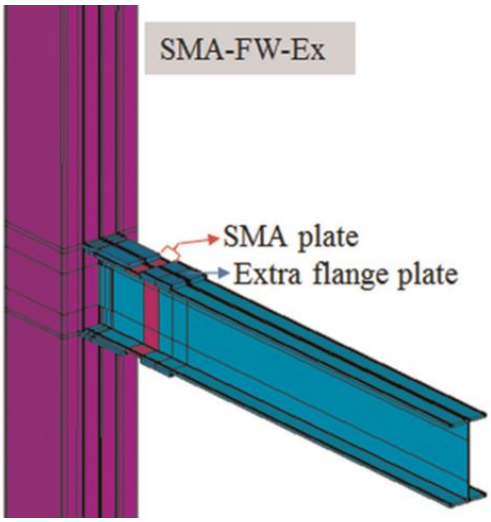

Figure A.7.34: SMA incorporated within a steel beam section (Moradi and Alam, 2015)

Four different arrangements of the SMA were investigated these included using the alloy as: part of the beam flange, part of the flange and beam and two local reinforcement arrangements of the flange plates where the plastic hinge was forced into the memory alloy and away from the steel. The SMA was assumed to be welded to the beam, with the beam also being welded to the box column. The use of SMA reduced the residual inter storey drift compared to normal steel beams and the experimental results showed that the smallest residual inter storey drift occurred in the cases where the SMA had been used in both the web and flange, (shown in Figure A.7.34). The longer the SMA was, the smaller the residual inter storey drifts remained. Yielding of the steel beams was avoided by reinforcing the steel flanges enabling better re-centring of the frame. High costs are associated with the SMA to ensure that the correct desirable properties are achieved. Also the manufacturing and welding of the SMA to the steel beam are an area which requires further research.

A.7.2 SMA bolts

Super elastic shape memory alloy bolts and end plates were investigated by Farmani and Ghassemieh (2016) as a method of re-centring the structural system. A FE model of the connection by Farmani and Ghassemieh (2016) is shown in Figure A.7.35 which was validated from a finite element model from previous experimental results and used to evaluate a number of different connection arrangements with SMA bolts.

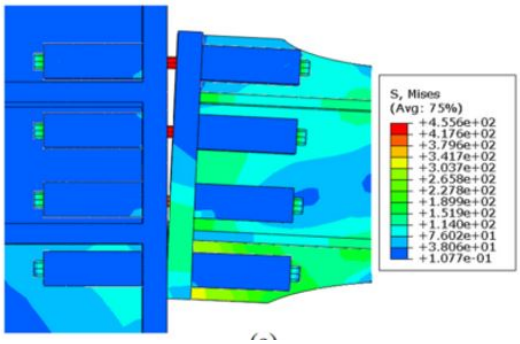

Figure A.7.35: SMA bots within a bolted end plate connection (Farmani and Ghassemieh, 2016)

Two different end plate thickness were tested in order to represent thin plate (prying) and thick plate (end plate remains elastic) failure. Different combinations of bolts were used with either 4 or 8 bolts. Normal practice allows plastic hinges to form in the beam but this study designed the bolts to limit the joint moment capacity to less than the beam. Continuity plates (plates welded in-line with the beams flange and from one column flange to the other) and doubler plates (plates flush on the column web to strengthen it) were used to strengthen parts of the beam and column connection and ensure that inelasticity was confined to the SMA bolts.

Joints with SMA bolts have similar initial stiffness but a higher drift level compared to those with high strength bolts due to the fact that the high strength bolts lose their pre-tension after a number of cyclic loadings. Flag shaped stress-strain diagrams, as a result of the super elastic nature of the SMA bolts, prevents the pretension force from reducing during increased cycles of cyclic loading.

All connections tested by Farmani and Ghassemieh (2016) achieved an inter storey drift angle of $0.04rad$ or greater with the ductility provided by the end plate and in the shanks of the SMA bolts. Higher energy dissipation in the SMA bolts compared to high strength bolts was observed as they could tolerate a higher number of loading cycles although the energy dissipation per cycle of the SMA bolts was smaller than that of the high strength bolts.

Hu et al. (2012) investigated the new connection shown in Figure A.7.36, consisting of shear tabs, clip-angles, steel shear bolts and SMA tension bolts. Two numerical models built in OpenSees were developed one using high strength bolts and the other using SMA tension bolts. The numerical models were calibrated from previous experimental results and the model was able to capture the slip and prying of the connection, as well as the bolt bearing demands.

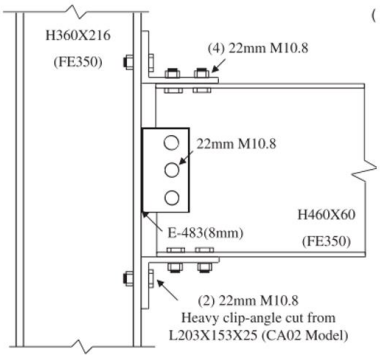

Figure A.7.36: New type of connection analysed with and without SMA bolts (Hu et al., 2012)

Compared to the connection with standard bolts, the SMA connection arrangement exhibited: 1) larger re-centring capabilities, 2) lower ultimate strength capabilities, 3) larger recoverable deformation and 4) a fatter energy dissipation curve leading to a larger energy dissipation capacity.

Fang et al. (2015) investigated the performance of using SMA bars in connections by carrying out multiple tests on SMA bars under different loading conditions. Increases of residual displacement in the experiments and in practice, leads to complex loading of tension, shear and bending on the bolt. Fang et al. (2015) suggested that because of the low shear and tensile strength of the SMA bolts (compared to high strength bolts) they should not be used to fully replace the high strength bolts. Instead they proposed a system comprising of a combination of SMA bolts and high strength bolts with spring washers, as shown in Figure A.7.37. The deformation can then be concentrated in the spring washers.

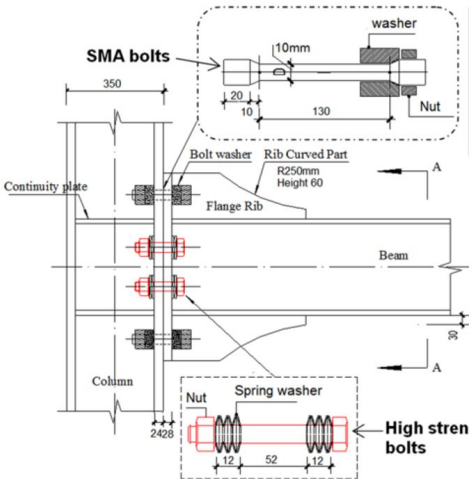

Figure A.7.37: Connection analysed using SMA bolts (Fang et al., 2015)

A FE model was developed which showed that the energy dissipation is concentrated in the bolts rows while the end plate and column flange remain elastic. They also concluded that the SMA bolts do not respond well under direct shear and do not have good tensile properties compared to high strength bolts, however, they have a reasonable energy dissipation capacity and re-centring ability. Hence, an arrangement of high strength bolts and SMA bolts was adopted.

A.7.3 SMA tendons

Wang et al. (2015) investigated the possibility of using SMA tendons and steel angles in beam to column connections, shown in Figure A.7.38. The re-centring abilities and performance of the SMA tendons was examined as well as the energy dissipative performance of the steel angle sections through experimental tests and finite element models.

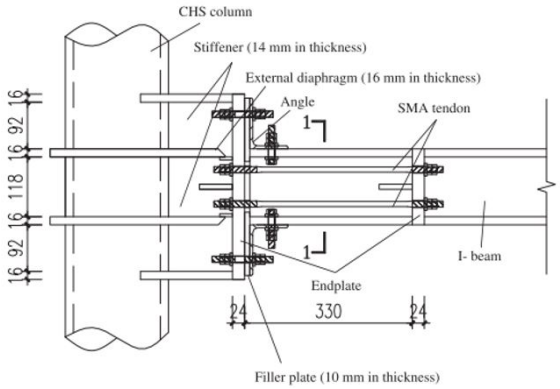

Figure A.7.38: Connection with SMA tendons (Wang et al., 2015)

SMA tendons provided a good re-centring ability of the connection and the steel angles provided good energy dissipation with thicker steel angles enhancing the energy dissipation performance of the connection.

A.7.4 Self-centring connection with SMA tendons

Two main approaches being pursued in self centring devices, consist of either post tensioned high strength steel strands or SMA tendons (Farmani and Ghassemieh, 2017). Post-tensioned devices are designed to remain elastic and not dissipate any energy under cyclic loads; additional energy dissipation devices such as frictional or yielding devices should be present in order to absorb the energy. Farmani and Ghassemieh (2017) present a detailed FE study on shear tab connections equipped with super elastic SMA tendons (see Figure A.7.39a).

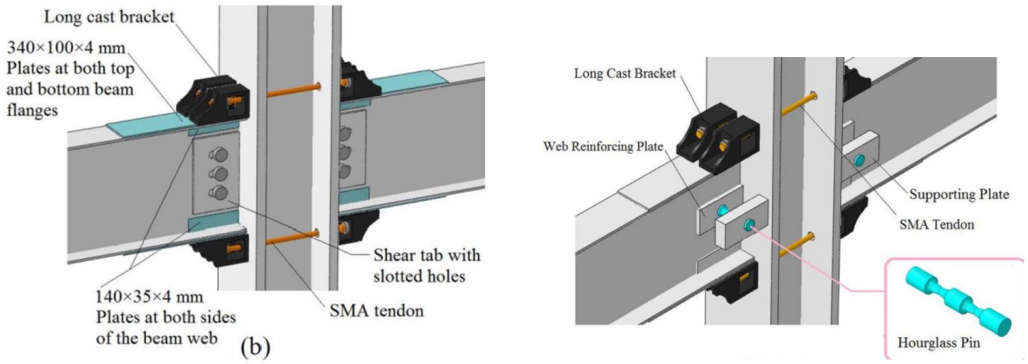

(a) (b)

Figure A.7.39: Self-centering connections with (a) SMA tendons and (b) SMA tendons with Hourglass Pins (Farmani and Ghassemieh, 2017)

A high-strength steel cast bracket (shown in Figure A.7.39a) houses a SMA tendon gives re-centring capabilities and bolted shear tabs with slotted holes allow frictional based energy dissipation. A parametric study showed that sufficient pretension of the SMA could provide a high rotational stiffness, which also enhanced the self-centring ability, and longer SMA tendons provided a higher rotational capacity.

The connection was improved by incorporating WHP pins into the web of the beam as shown in Figure A.7.39b. This provided an increase in the amount of energy dissipation, moment capacity and

initial stiffness. The WHPs were designed according to Vasdravellis et al. (2014). The connection incorporating the WHPs increased the moment capacity by 14%, initial stiffness by 17% and energy dissipation by 77% compared to the connection with a shear tab and slotted holes.Significant residual deformation of this type of connection will remain after unloading if the resisting forces induced by the WHPs exceed a specific limit. At this limit the restoring force produced from the SMA tendons will not be sufficient to restore the structure back to its initial position. Therefore, it is important to know how the pretension forces in the SMA tendons change with cyclic loading. Farmani and Ghassemieh (2017) suggested a more detailed and robust model must be produced to consider this effect in the future.

A.8 3D Printing

Additive manufacturing or 3D printing offers great potential for developing innovative beam-column connections with customised performance characteristics. 3D printing enables complex and intricate shapes and patterns to be produced in steel which would be impossible or prohibitively expensive to produce using conventional fabrication or casting techniques. These complex and intricate patterns could be developed in such a way that they absorb the energy from a seismic event.

Additive printing is founded on a layer by layer approach used to create the final design or object. Ti-6Al-7Nb and Ti-6AL-4V are the most commonly used alloys in additive manufacturing (Chlebus et al., 2011; Brenne et al., 2013). The design for the object is split into thousands of different layers in a CAD file which drives the printing equipment. Additive manufacturing machines consist of a bed of powder which is solidified using a power source, in a layer by layer fashion to build up the objects profile. The process of building up the final design object is as follows:

1. The surface is covered with a powder form of the alloy to be used in building the final design
2. The power source solidifies the powder to create the first layer of the object
3. The surface is lowered and more powder is spread on top of the surface
4. The power source solidifies the next layer of the object
5. This process is repeated until the final design of the object has been produced using a layer by layer approach

There are two common types of additive printing techniques defined by the primary source of energy for melting the powdered metal: Selective Laser Melting (SLM) and Electron Beam Melting (EBM) (Tan et al., 2016).

The mechanical properties of additively printed materials will vary depending on its method of manufacture e.g. the orientation of the layers used to build the final object. Chlebus et al. (2011) conducted investigations into the mechanical properties and microstructure of Ti-6Al-7Nb specimens in three different build directions using selective laser melting. Tensile and Compression tests were carried out to assess the mechanical properties such as: tensile yielding, ultimate strength, Young's Modulus and ultimate compressive strength. Examinations of the microstructure were also carried out.

Results showed that the properties of the materials varied depending on the build direction. The presence of pores can act as stress raisers and lead to failure under fatigue loading (Leuders et al., 2013). Internal stresses can also affect the properties of additively printed materials. The internal stress can be relieved by post heat treatment of the material or by careful monitoring of the temperature during the manufacturing process (Leuders et al., 2013).

Siddique et al. (2017) suggest that Selective Laser Melting (SLM) can produce alloys with a comparable or even better static strength than conventional manufacturing methods. This is because a denser and finer micro-structure can be produced in the additive printing process. Siddique et al. (2017) investigated the fatigue of aluminium-silicon (AlSi12) alloy under repeated cyclic loading (approximately 100 cycles per day). The microstructure and internal porosity were investigated and the fatigue behaviour carefully analysed. This level of loading is very different to the cyclic loading applied to simulate seismic excitations but does give us an insight to how micro-structures behave.

A.8.1 Future possibilities in design and manufacturing

Labonnote et al. (2016) briefly explains the different types of additive manufacturing process that are available for additive construction focusing on the forward thinking of potential construction processes. These forward thinking solutions scale up the additive manufacturing process. Potential solutions shown in Figure A.8.40 include:

a) gantry solutions a direct scaling up of a 3D printer (giant 3D printer)

b) cable-suspended solutions uses Cartesian coordinates and a suspended printer in retractable wires to control its position

c) swarm solutions uses the idea of several smaller mobile robots

d) multi-purpose robotics involves the use of a robotic arm for movement of the 3d printer

e) combination with folding (folding and self-assembly) this involves the idea of origami, printing thin layered materials to integrate a layer-based fabrication approach with appropriate folding operations

Thus there are a range of potential options that can be used to manufacture objects and structures using additive technologies. The specific technique that should be used can be decided based on the type, location and assembly technique that will be used in order to produce the specified structure.

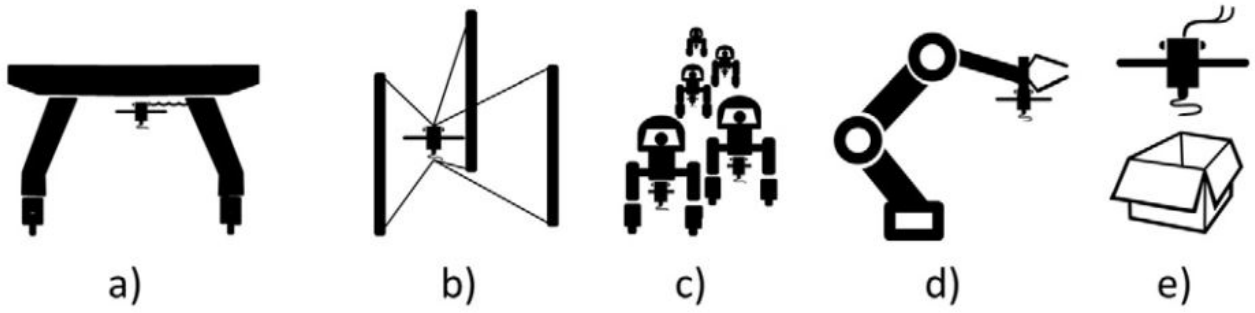

Figure A.8.40: Depictions of different 3D printing approaches (Labonnote et al., 2016)

Labonnote et al. (2016) also explores the opportunity and potential of large scale production of complex geometries at a structural scale, with advanced topologies and multi-functional building components at no extra cost and hopes that the paper will trigger movement towards additive construction with its potential to revolutionise the construction industry.

A.8.2 Lattified objects

Arisoy et al. (2015) presents a framework design engineering analysis of solids with lattice structures. This methodology takes a CAD model of the proposed solid structure and generates a lattice structure used to replace the solid surfaces. Lattified objects describe an object whose solid volume has been replaced by a lattice structure. These 3D structural lattices are then optimized to improve the structural properties and response. Additive manufacturing enables the ability to create a complex internal lattice without much fabrication process.

Lattified objects can provide an enhanced energy absorption which can be used for damping or vibration control. Previous software available takes the solid geometry from a CAD software system and transforms it into a lattice using independent software. This is generally done by removing the solid internal of a specified object and replacing it with a lattice grid of cells, shown in Figure A.8.41.

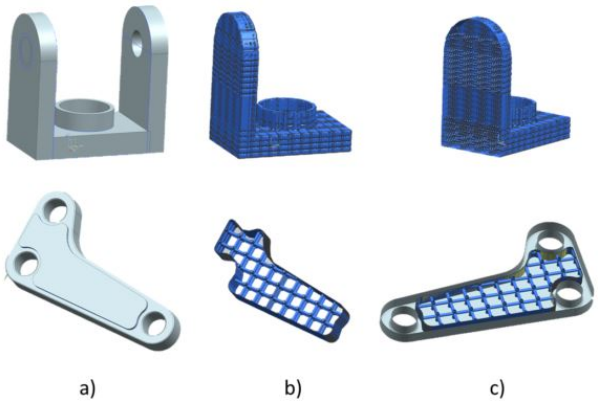

Figure A.8.41: Demonstrating how an object can be latified (Arisoy et al., 2015)

Booleans and shelling are typical methods used in software to generate lattice structures such as AutoCAD (Autodesk AutoCAD, 2019). However, these can cause many problems and require regularization in order to avoid manufacturing failures. A new method is proposed which can be used to lattify objects which is briefly described below. A new Discrete Signed Distance Field (d.s.d.f) based modelling technique is presented by Arisoy et al. (2015) in order to provide a geometrical representation of the lattice and is able to express complicated shape topology without representational complexity.

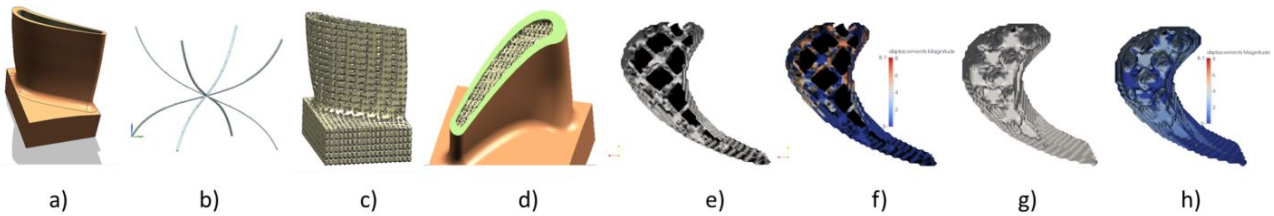

Figure A.8.42: A latified modelling process (Arisoy et al., 2015)

A typical lattifield modelling scenario is shown in Figure A.8.42 (Arisoy et al., 2015). The eight summary steps are: a) Select model, b) Create a shell, c) Select a user defined lattice template, d) Hollow the internal volume and arrange the lattice, e) Use d.s.d.f based modelling techniques, f) Carry out a FEA, g) Either send for additive printing if optimization is not required or h) Perform a topology optimization and i) Verify using FEA and send for additive printing.

Optimization enables improved lattified designs to be created in CAD modelling systems. The proposed system by Arisoy et al. (2015) can be added as a plugin to a Siemens NX CAD system (Siemens, 2013) to help optimize lattified structures and improve their structural characteristics.

A.8.3 Dynamic testing

Nishida et al. (2015) carried out dynamic compression tests on both wrought manufactured 304L stainless steel and additively manufactured 304L stainless steel using a Kolsky bar experimental set up concluding that both materials showed a similar work hardening behaviour. However, the additively manufactured specimen showed higher yield and stress flows and smaller strains but reduced when the strains went above 15%. This suggests a milder work hardening behaviour in the additively manufactured stainless steel sample. The surface of both samples were very different after the dynamic tests.

Figure A.8.43: Left shows the wrought specimen tested and right shows the additively manufactures 304L SS specimen (Nishida et al., 2015)

A.8.4 Honeycomb structures

Honeycomb structures provide excellent energy absorbing characteristics. The characteristics and properties of honeycomb structures could be incorporated into additive manufacturing and used in an innovative beam-column connection. The following sections provide a brief overview of the research that has been conducted into honeycomb and energy absorbing lattices.

A.8.5 Bending or stretching dominant structures

Deshpande et al. (2001) looked at the response of different structures under a bending or stretching dominant structural application. Figure A.8.44 shows an example of a mechanism on the left and a structure on the right. The deforming behaviour of the structure is stretch dominant, where the structure would fail as a result of stretching of the elements. If all joints in Figure A.8.44 were moment connections, this would represent most foam structures. The frame on the left would now adopt a bending dominant failure. However, the frame on the right would have practically no effect on the strength or stiffness compared to a frame with pinned connections and both the bending dominant and stretching dominant variations would have the same response.

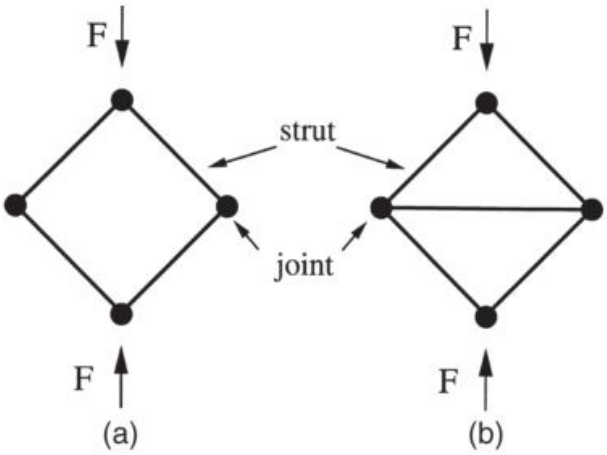

Figure A.8.44: Different frames which represent a (a) mechanism and (b) structure (Deshpande et al., 2001)

Foams that are stretching-dominated are more efficient from a weight point of view. A stretching dominated foam is 10 times as stiff and 3 times as strong as a bending-dominated foam for similar relative densities.

A.8.6 2D honeycomb mechanical behaviour

Hedayati et al. (2016) examined the mechanical behaviour of thick honeycomb structures with varying thicknesses, additively printed from polylactic acid using a 5th generation replicator desktop Markerbot 3D Printer. Analytical solutions using Euler-Bernoulli and Timoshenko beam theories were developed to predict analytical relationships of the hexagonal honeycomb structure in both major in-plane directions. Finite element models were developed which were compared to the two beam theories. The model was validated with experimental results, which showed good agreement. Four different densities of cell wall shown in Figure A.8.45 were experimentally tested under compression using a 100kN load cell at a rate of 2mm/min.

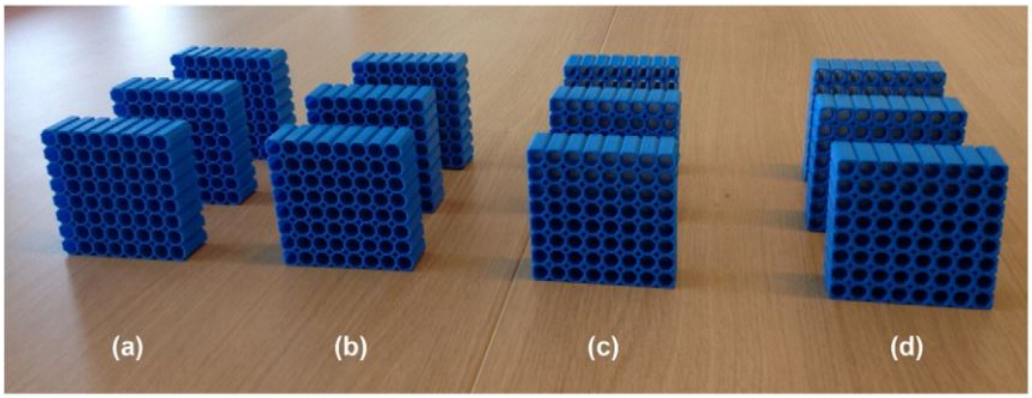

Figure A.8.45: The different Octagonal honeycomb samples with varying cell wall densities with wall thickness to length ratios of (a) 0.2727, (b) 0.4091, (c) 0.5454 and (d) 0.6817 (Hedayati et al., 2016)

The tests showed how the analytical relationships using the Euler-Bernoulli and Timoshenko beam theories were much closer to the finite element and experimental results than older models of honeycomb structural predictions.

The experimental results of the four different relative densities (created by varying the wall thickness to length ratio) showed a 45 degree failure pattern on all of the octagonal specimens with stress levels and failure loading being much higher for the specimens with higher relative densities.

Hedayati et al. (2016) compared the elastic properties of the octagonal honeycomb structure with properties of square, triangular, hexagonal, mixed diamond and Kagome shaped lattice. The octagonal and hexagonal lattices showed similar properties in terms of yield stress and elastic modulus with all other cell arrangements exhibiting much lower elastic properties.

A.8.7 Mechanical response of different types of honeycomb structure

Seven different cell types are considered by Wang and McDowell (2004) which consist of: square, hexagonal with equilateral triangles, regular hexagonal, square super-cell (mix of squares and triangles), Kagome, rectangular and diamond. These are shown respectively in Figure A.8.46.

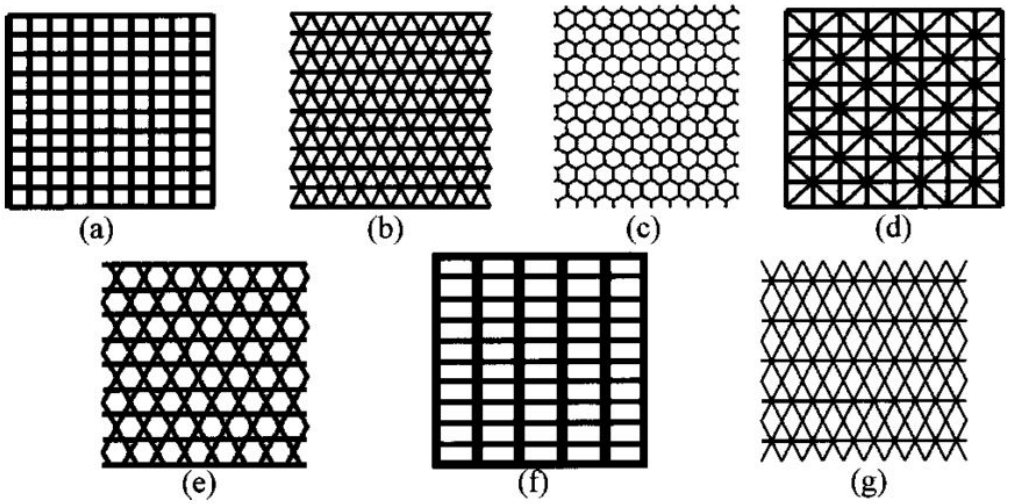

Figure A.8.46: Honeycomb structures investigated (a) square cell (b) hexagonal cell (c) regular hexagonal cell (d) square super cell (triangles and squares) (e) Kagome cell (f) rectangular cell and (g) diamond cell (Wang and McDowell, 2004)

Wang and McDowell (2004) suggest that in-plane loading of honeycomb structures is the limiting factor which induces elastic buckling and yielding prior to failure of the specimens. Metal honeycomb structures are commonly made from either strip-glued sheets or a stamping/bending process in order to provide a 2D lattice. The cell walls of the honeycomb structures exhibit either bending, axial or shear stresses. The stress-strain behaviour of typical honeycomb structures is considered to be an initial elastic regime, followed by an extended stress plateau leading to densification, finally followed by crushing of the material. The extended stress plateau occurs after the honeycomb cells begin to collapse. Densification of the material occurs as the cells have completely collapsed.

Wang and McDowell (2004) considered a practical class of extruded cell structures. Yielding and plastic flows were considered as the important failure mechanism, with this paper focusing on the cell wall yielding. The cell wall struts can be considered as smaller trusses built from a number of elements. Simple beam theories (e.g. Timoshenkos beam column theory) have been used considering shear, rotation, bending and axial stress. In-plane shear properties, Youngs moduli and compressive yield strengths of a number of honeycomb specimens were investigated. A simple truss analysis was conducted on each 2D lattice structure in-order to explore its properties.

Results showed that square cells deform by axial compression or extension hence cell wall bending under shear loading will reduce the elastic stiffness. Hexagonal cells were noted to be stretch dominant, with values of Youngs modulus, shear modulus, buckling limits and yield strength for hexagonal honeycomb similar to the widely available values in literature (Zhang and Ashby, 1992; Gibson and Ashby, 1997; Torquato et al., 1998). Equilateral triangular cell on the other hand behaved differently to square and hexagonal, the deformations of the cell wall are stretch dominated, if the structure is considered to be pinned and determinate. Mixed square/triangular cells were noted as statically indeterminate structures with the in-plane response expected to be anisotropic due to the triangle being a different size to each other. Kagome structures which are a mix of triangular and hexagonal cells produced a stretch dominated periodic structure. Rectangular cell unit walls, all deform like a fixed end column. Finally, diamond cells built from equilateral triangles and hexagonal super cells were stretch dominant. It was noted that the compressive strength and stiffness were different in both of the directions. Wang and McDowell (2004) concluded that based on simple beam theories, the cell structure plays an important role in determining the in-plane mechanical properties of the proposed 2D honeycomb lattices.

A.8.8 2D honeycomb structural response under different loading rates

Previous research has shown the deformation mode of honeycombs behave differently under varying dynamic loading. Ruan et al. (2003) used a finite element model in ABAQUS to study the deformation modes of 2D hexagonal aluminium honeycomb structures, shown in Figure A.8.47a, in both the X1 and X2 directions (defined in the figure). The parameters investigated were the cell wall thickness and the speed of impact on the deformation of the honeycomb structure. The failure mode (Figure A.8.47b) in the X1 direction produced an X shaped failure band under low impacts and a I shaped failure mode occurred at high impacts. A transitional V failure mode for moderate impacts was observed. The deformation mode or shape is also dependent on the cell wall thickness of the honeycomb. Layer by layer crushing failure of the honeycomb structure was observed in the X2 direction. Similar to the V and I mode. Lower velocities of impact allow the upper middle proportion on the structure to crush where as higher velocities of impact let the crushing start at the face of impact.

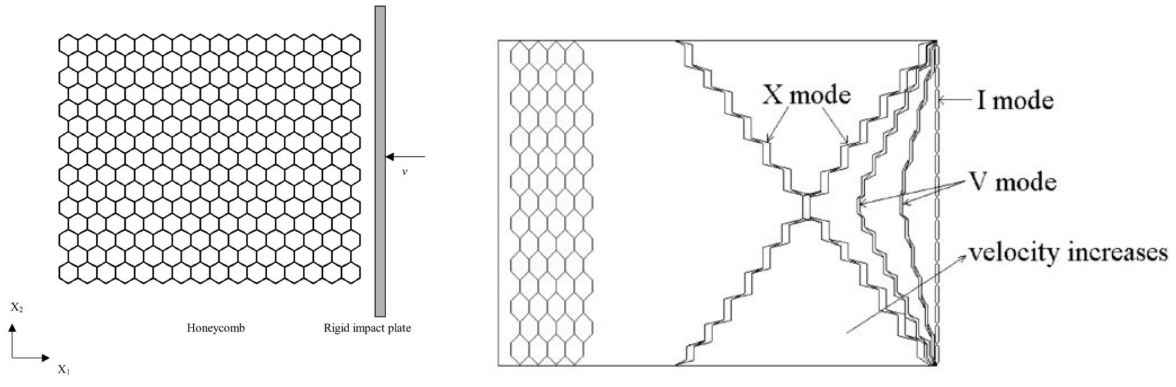

(a) (b)

Figure A.8.47: (a) the 2D hexagonal structure analysed and (b) the different failure mechanisms analysed (Ruan et al., 2003)

The cell wall thickness and size influenced the plateau stress depending on the impact velocity; in general the plateau stress in the structure increases with impact velocity.

A.8.9 Effect of the honeycomb orientation

Foo et al. (2007) created finite element models as well as experimental prototypes of Nomex Honeycomb 2D structures. Nomex is made from strip-glued sheets as shown in Figure A.8.48. Tensile tests in both the X1 and X2 direction were performed as well as compressive tests on the honeycomb cores, in order to asses the orientation of honeycomb structures.

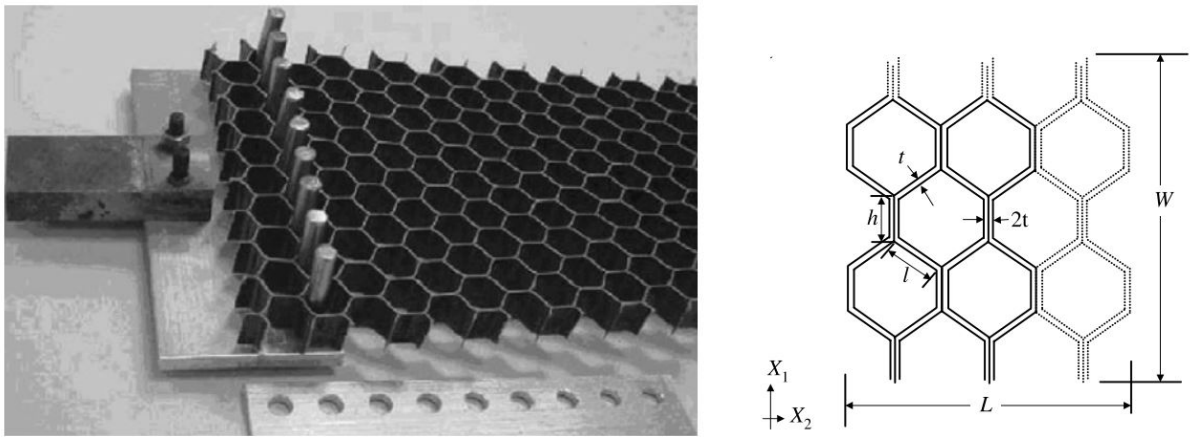

(a) (b)

Figure A.8.48: (a) 3D printed prototype (b) 2D lattice structure (Foo et al., 2007)

More load and displacement was taken in the X1 direction by the honeycomb structure in tension compared to the X2 direction. Plasticity also occurred during the tensile tests due to the de-bonding of the papers. Only static tension and compression tests were conducted and not the response of cyclic performance.

A.8.10 Analytical approach of 2D structures

Goswami (2006) explores the various effective elastic properties of a number of different forms of hexagonal honeycomb cellular structures by changing: the diagonal strut lengths, vertical strut lengths, strut angles and thicknesses of the struts. This change of cellular structure geometry, shown in Figure A.8.49, requires a complete new meshing and analysis. Goswami (2006) presents a new analytical approach which computes the effective properties of the structure in a fraction of the time. Metallic honeycomb core structures play important energy absorbing roles in super lightweight structures. Hexagonal honeycomb structures are used especially in aerospace structures due to their lightweight in sandwich structures comprising of a thick core and thin top and bottom skins.

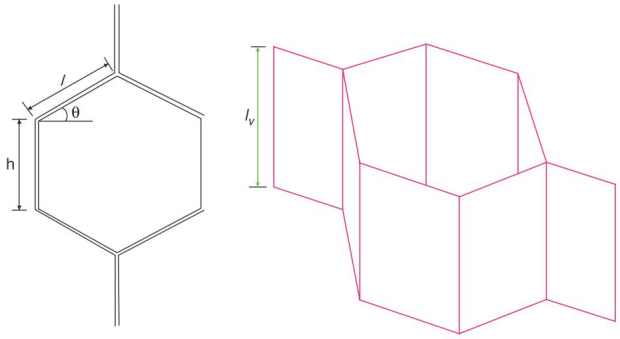

Figure A.8.49: the hexagonal core investigated (Goswami, 2006)

A unit cell from a standard hexagonal structure was taken and used in order to produce equations for the Youngs modulus in both the X1 and X2 directions. Equations for the effective elastic properties were also calculated using simple equations. These are based on a linear elastic approach and show good agreement with experimental data and other analytical approaches in literature (Goswami, 2006).

A.8.11 Crushing experiment

Papka and Kyriakides (1998) conducted experimental and numerical tests on the crushing of honeycomb structures, looking specifically at the failure mechanisms of the structures. Crushing experiments were made from sheets of Al-5052-H39 of two thicknesses which are bonded together at bond lines to make predefined assembled stacks. The honeycomb structure was then cut out from these stacks of aluminium. Good agreement was shown between the ABAQUS finite element model and the experimental results. The experimental results showed that a band of cells crushed locally under shear which spreads out throughout the specimen. Larger specimens of the honeycomb structure showed criss-cross patterns of localized crushing.

A.8.12 3D micro lattices

Ozdemir et al. (2016) considered how lattice structures on a macro scale absorbed energy under quasi-static and dynamic loading. Additively manufactured lattice structures from Electron Beam Melting techniques were used as they could produce more samples in less time as well as avoiding the need for additional treatments. Spherical grade 5 Ti6A14V powder with an ARCAM S12 EBM machine was used. The three different arrangements of lattice structures shown in Figure A.8.50 consisted of: cubic, diamond and re-entrant cubes.

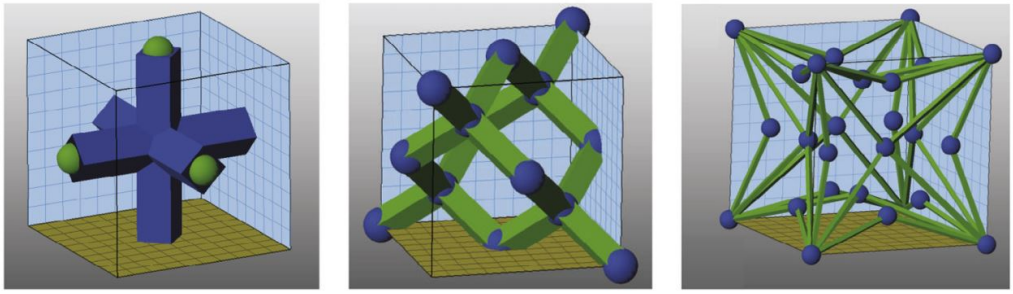

Figure A.8.50: Units cells for (a) cubic, (b) diamond and (c) re-entrant lattice (Ozdemir et al., 2016)

Two different arrangements of lattice structure consisting of single layer and multi-layer lattices were tested under quasi-static loading. The single layer lattices are shown in Figure A.8.51. Both lattices were tested in compression by either a 0.2mm/min or 0.1mm/min cross head speed actuator.

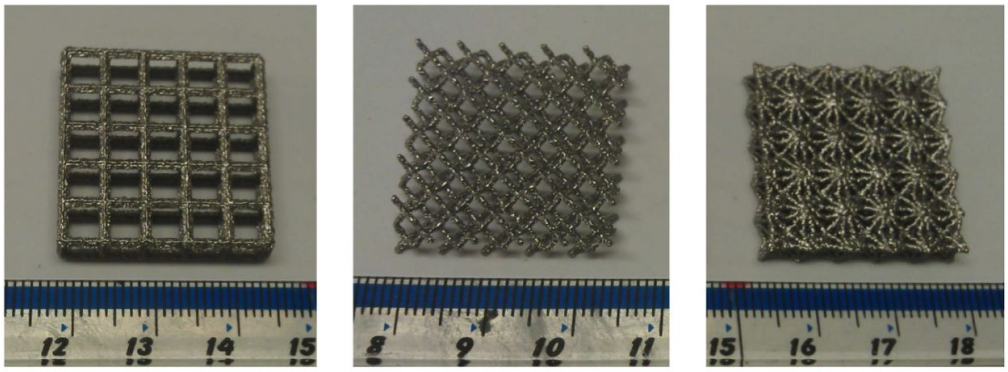

Figure A.8.51: Single layer lattices of (a) cubic, (b) diamond and (c) re-entrant lattice (Ozdemir et al., 2016)

Single-layer results showed: 1) Cubic structures give elastic response followed by brittle failure due to the lattices inability to deform plastically and 2) Diamond and re-entrant lattices produce constant initial stiffness followed by post-peak softening and later a stiffness increase due to the densification of the material

Multi-layer results showed: 1) diamond and re-entrant lattice structures demonstrate clear peaks at smaller latent displacements with smaller peaks at higher latent displacements these peaks on the stress-strain curve correspond to individual layers failing, 2) re-entrant lattice structures tend to give a more predictable response and 3) the re-entrant lattice fails layer by layer.

A.8.13 Energy absorbing micro-truss

Cellular materials such as stochastic foams and honeycombs can be a good source of energy absorption. These cellular materials absorb this energy elastically or by plastic yielding of the material. Evans et al. (2010) looked at how a hollow pyramidal truss member absorbed energy by post buckling deformation.

Figure A.8.52: The hollow Ni-micro lattice struss (Evans et al., 2010)

A shock propagation analysis of Ni Micro-Lattice structures was carried out using ABAQUS, which gave similar experimental results. Evans et al. (2010) concluded that an unusually large amount of energy was absorbed per unit mass of the hollow truss structure. Most of the energy absorption is absorbed from the buckling and kinking of the lattice members. The experimental results showed some wrinkling at the nodes which provided extra levels of energy absorption.

A.8.14 Scaffold applications

Xu Bin et al. (2012) looked at developing porous scaffolds to be used in medical purposes. Specimens were fabricated using Ti6Al4V material in an argon filled shielded environment. The fabrication quality of the additively printed scaffolds was investigated and it was noted that overhang is a major issue affecting the fabrication quality of additive manufacturing components (overhang is caused when the liquid phase material droops due to gravity and capillarity inducing a dross formation on the overhang surface).

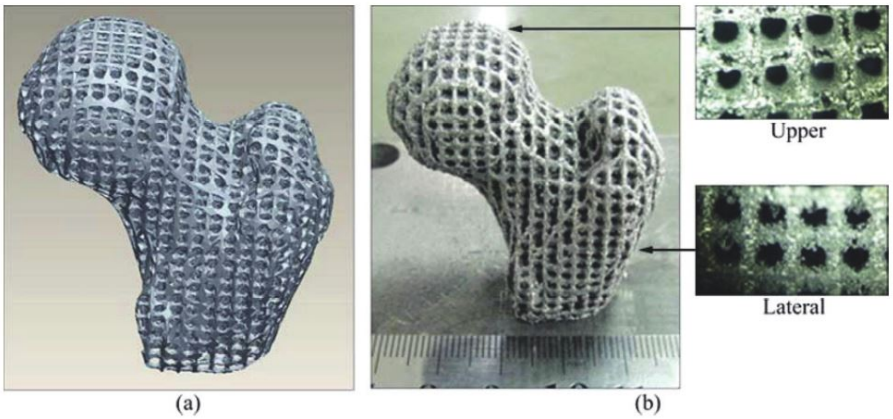

Figure A.8.53: Comparisons between (a) computer model and (b) fabricated 3D printed model (Xu Bin et al., 2012)

A.8.15 Porous scaffold

Chantarapanich et al. (2012) used selective melting additive methods in order to develop porous scaffolds. They considered 119 different polyhedrons as open or closed cell scaffolds, as well as the potential of joining different cell scaffolds together based on their contact surfaces.

Finite element analysis (Figure A.8.54a) was used on the library of scaffolds in order to evaluate the equivalent stresses under a compressive strength analysis. A sample selection of these scaffolds is shown in Figure A.8.54b. A three stage criteria was developed and used to evaluate each of the proposed polyhedrons.

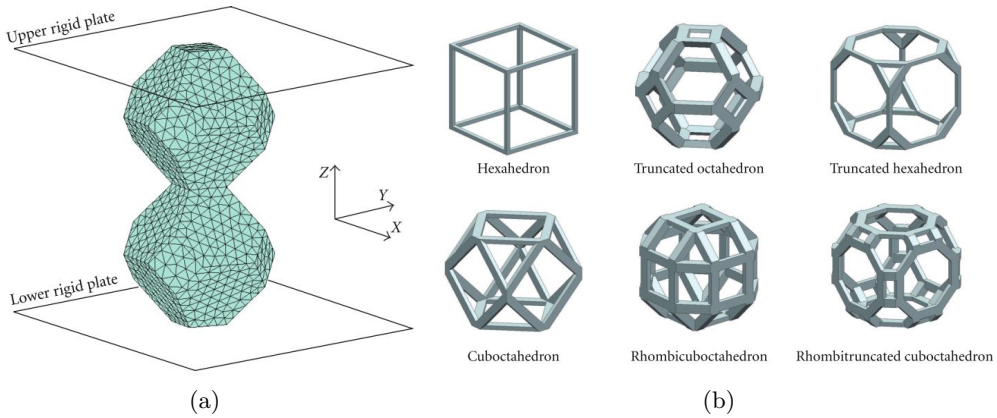

Figure A.8.54: (a) Compressive FE analysis used (b) sample selection of open-cellular structures (Chantarapanich et al., 2012)

A.8.16 Selective laser 3D lattices

Chantarapanich et al. (2014) researched the design and production of 3D honeycomb selective laser melted lattices for use in an aeronautical sandwich structure panel application. The main function of a honeycomb structure is to withstand normal load in the longitudinal axis and a shear load in the transverse axis.

Four polyhedrons shown in Figure A.8.55 which consisted of: cubic, cuboctahedron, truncated octahedron and truncated hexahedron were selected to become possible sandwich lattice structures. A finite element analysis was carried out in order to assess which structures mechanical performance was more desirable for aeronautical sandwich structure panel application. The strain energy density was used to assess how much energy the specific structure could absorb instead of transferring it to the surrounding structure. Chantarapanich et al. (2014) showed using finite element analysis that the truncated octahedron had the highest energy absorption properties.

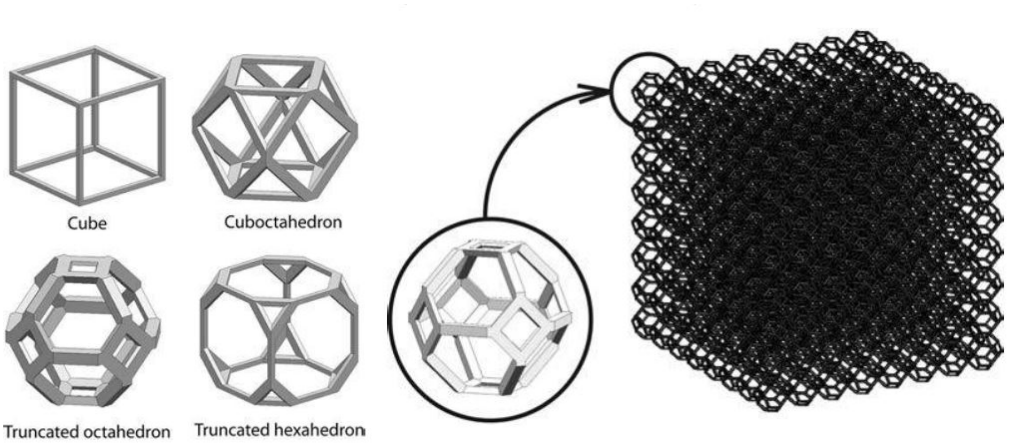

(a) (b)

Figure A.8.55: (a) The hollow Ni-micro lattice truss and (b)selected 3D honeycomb truncated octahedron tested (Chantarapanich et al., 2014)

AISA-316L stainless steel was used to produce a 3D printed truncated octahedron 3D honeycomb matrix with unit cell of 2.5m and beam thickness of 0.15mm. It was then tested under compressive loading at a rate on 3mm/min. The study showed that this type of arrangement provided the best strain energy density.

A.8.17 Mechanical properties of 3D lattices

Van Bael et al. (2012) explored how the scaffold pore size, pore shape permeability and permeability influenced 3D human periosteum-derived cell cultures. The properties of the different 3D structures could be useful in producing specific mechanical properties for use in beam-column structural connection components. Selective laser melting was used to produce six different morphological specimens made from Ti6Al4V which are described and shown in Figure A.8.56. The morphological parameters of the different geometrical selectively melted 3D structures were evaluated All of the unit cell sizes were $200\mu m$ in both planes.

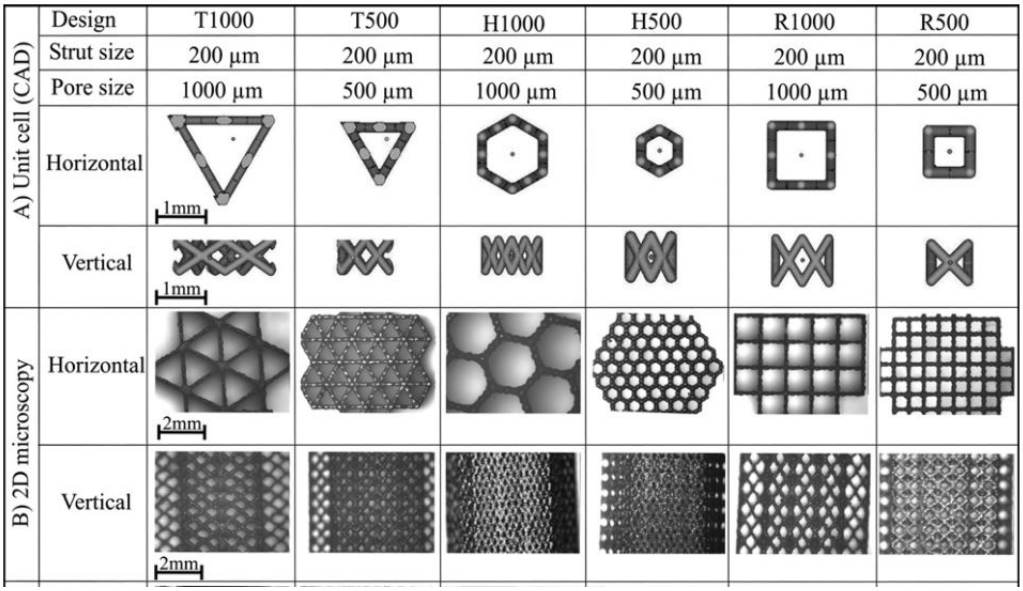

Figure A.8.56: (a) The unit cell of the 3D printed Ti6Al4V scaffolds and (b) Microscopy images of the scaffolds structure (Van Bael et al., 2012)

Mechanical properties of the different structures were deduced from a compression test using a $100kN$ load at a loading rate of 0.2 mm per min, the stiffness of each of the structures was calculated using the slope of the stress strain envelope. Hexagonal scaffold gave the highest compressive stiffness.

A.8.18 Octet truss lattice response under loading

Wendy Gu and Greer (2015) showed how the compressive strength of a laser written mesostructured Cu lattice (shown in Figure A.8.57) exhibited a stronger bulk yield strength compared to the bulk strength of a solid Cu sample. The octet structural topology and micron-sized beam thickness added to the strength of the material and gave a strength of up to 1.8 times stronger compared to the solid Cu sample. This was verified by Zheng et al. (2014). They showed how six different hollow Al2O3 and Ni-P micro lattices provide nearly a constant stiffness per unit mass density over three orders of magnitude compared to the solid Al2O3 and Ni-P samples.

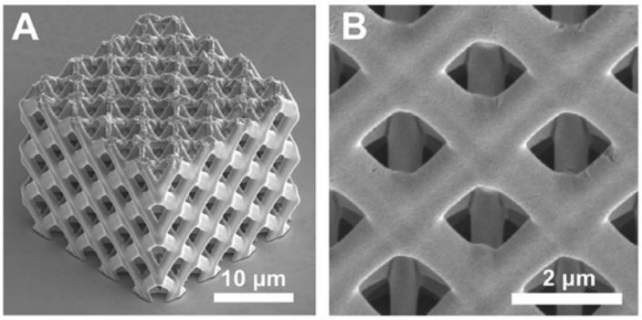

Figure A.8.57: Showing the 3D lattice structure of the truss tested (Wendy Gu and Greer, 2015)

Tancogne-Dejean et al. (2016) highlighted the benefits that micro structures can have. The mechanical responses of micro trusses can be described as either bending or stretching dominant depending on their nodal connectivity. Direct laser writing and additive manufacturing provide excellent lattice printing opportunities, enabling almost any complex geometry to be a possibility (Tancogne-Dejean et al., 2016).

Lattice structures with hollow trusses provide a high load carrying capacity per unit density compared to solid arrangements. Oct trusses with a non-circular cross sections buckle elastically and yield plastically simultaneously. Tancogne-Dejean et al. (2016) highlighted the three main factors that affect lattice structures which include: 1) The basis material, 2) The lattice geometry (tetrahedrol, octetc, cubic etc), 3) Strut shape and 4) Relative density of the lattice material.

An octect truss lattice configuration shown in Figure A.8.58, provides an isotropic elastic response which consists of two platonic tetrahedron and octahedron solids. An optimal configuration was chosen by Tancogne-Dejean et al. (2016) which aimed at maximising the lattices energy absorbing characteristics.

FE tests on 6 different relative density samples of 5x5x5 unit cells (shown in Figure A.8.58) showed stable and unstable characteristics of different lattice densities were observed.

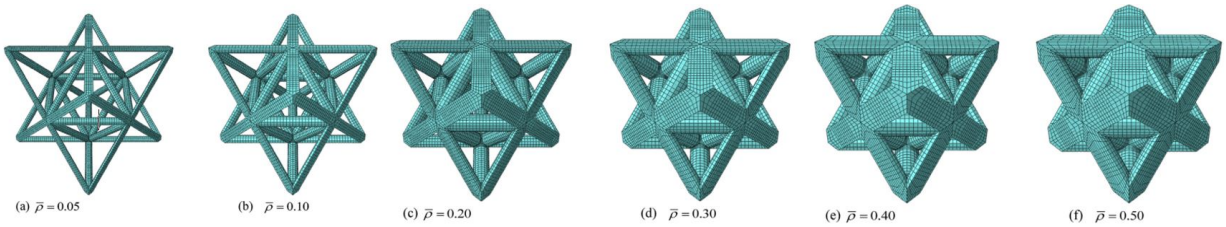

Figure A.8.58: Six FE models with varying density (Tancogne-Dejean et al., 2016)

The less dense lattices with thin slender elements tended to buckle under axial load forming plastic hinges at the centre of the struts. As the lattice is compressed further plastic deformation occurred at the centre of the slender struts producing a rigid body twisting effect. This reflects an unstable low density structure. In denser lattices, plastic hinges formed at the connecting nodes which enabled neighbouring plastic hinges to interact and a global state of plastic deformation to occur. These findings were confirmed through experimental analysis.

A.9 Application of 3D printing in future steel connections

While RBS connections may provide a safe and stable steel moment frame by absorbing the seismic energy, repairing damaged RBS connections in the frames has proved challenging. This state-of-the-art literature review has extensively reviewed a wide range of alternative connections, many of these connections utilise a replaceable type fuse type section. This replaceable section is designed to absorb the large majority of the seismic energy while leaving the rest of the connection damage free, thus enabling easy replacement of the damaged section. Many of these replaceable fuse type connections are coupled with post tensioning strands or smart memory alloys, these mechanical aids help recentre the frame following an earthquake and thus help to reduce the amount of permanent or residual damage experienced by the frame compared to connections without these self centring aids. In this review, the fuse type section of the connection is considered to be the fundamental part of the connection. However, there are many challenges faced with the manufacturing and utilisation of these fuse type sections.

Multi-storey steel moment frames require a significant amount of connections. In order to utilise the full seismic capacity of a multi storey steel frame, many of the connections in the frame may require varying seismic and energy dissipating capabilities and hence varying size and shape of the fuse type sections. The current methods and techniques used for manufacturing the existing fuse type sections of the connection reviewed in this Appendix are significantly time consuming to make, rely on a specific

jig/template or require a bespoke casting mould. This presents many obvious challenges when scaling up the fabrication process. The current methods of manufacturing these fuse type components leads to complications when a bespoke or specific seismic capability (size and shape of the fuse section) is required.

This research has shown that the arrangements and types of additively manufactured micro structure/lattices and mechanical properties which define honeycomb structures effect its energy absorbing capabilities. Thus, if appropriately designed, an additively printed structure can have any desirable capabilities. Subsequently, additive manufacturing presents a simple yet attractive solution to the problem of scaling up the production of fuse type connections, whereby, producing a fuse type component which can dissipate the seismic energy through the yielding of small components within the connection, leading to a lateral displacement (energy absorbing) method for absorbing energy. This method of manufacturing allows the designer to produce any size and shape component at no extra cost, thus allowing scaling up of hundreds of varying and bespoke components possible. Computer Aided Design (CAD) is widely used in industry for the design of structural components, additive manufacturing techniques require the input of a detailed CAD drawing in order to produce the design. This mitigates the requirement for many specific jigs, templates or casting moulds.

There is much scope for the future development of additive manufactured connections, perhaps a solution could be in a replaceable fuse type section of the connection as depicted in Figure A.9.59a. Whereby, the additivity printed connection is designed to absorb the seismic energy as a result of the design effects from a non-linear dynamic seismic analysis at each connection location. Or perhaps a modular type connection shown in Figure A.9.59b and Figure A.9.59c could be re-imagined with additively printed components that have the desirable characteristics specific to the seismic energy absorbing requirements of a steel frame and/or connection integrated within the internal structure. Currently, the idea of suggesting the scaling up of additive manufacturing for industrial structural connection capabilities may seem unrealistic due to significant high costs and complications with additively printing large scale components. However, given the current speed and rate of developing technology, additive manufacturing or 3D printing could well be at the forefront of large scale manufacturing within the coming decade.

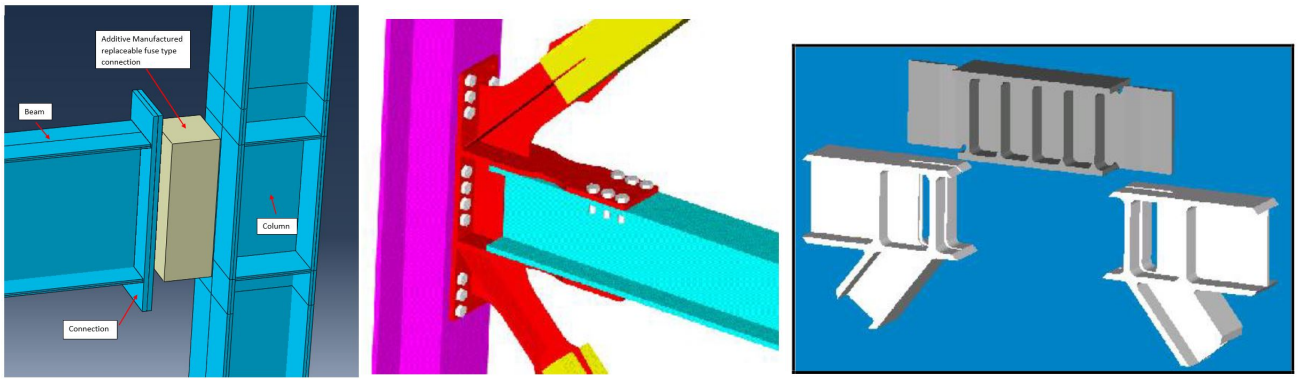

(a) (b) (c)

Figure A.9.59: (a) Additively printed fuse type section concept integrated into a steel connection (b) A modular connection arrangement (Fleischman, 2013) and (c) Modular component construction (Fleischman, 2013)

A.10 Conclusion

The widely accepted RBS method provides a practical solution for a safe and stable steel moment frame by absorbing the seismic energy and thus shifting the plastic deformations from the column and beam-column connections, into the beam. While this protects the columns in the steel frame and prevents brittle fractures in beam-column connections, there are a number of limitations to the RBS solution which include 1) large plastic deformations occur in the beam (Valente et al., 2017a; Moradi and Alam, 2017; Tong et al., 2016; Sultana and Youssef, 2016b), 2) large residual drifts may occur (Farmani and Ghassemieh, 2016; Baiguera et al., 2016; Dimopoulos et al., 2013; Valente et al., 2017b; Iqbal et al., 2016; Vasdravellis et al., 2013b; Moradi and Alam, 2017), 3) significant cost for repair (Castiglioni et al., 2012b,a; Chan et al., 2009; Lin, 2015; Banisheikholeslami et al., 2016; Priestley, 2000; Vasdravellis et al., 2013a; Farmani and Ghassemieh, 2016; Xu et al., 2016) and 4) structures may not satisfy the Immediate Occupancy (IO) criteria (Baiguera et al., 2016; Moradi and Alam, 2015, 2017; Lin, 2015; Erochko et al., 2010).

New ranges of connections and new innovative connection ideas, have been explored and discussed in this Appendix. In general, these fall into three groups: weakening sections of the beam, fuse type connections and self-centring connections. These effective methods shift the damage away from the column or beam-column-connection and into the beams or replaceable sections of the connection or beam. However, many of these methods still do not solve the problems of a) no efficient design methodology provided that can produce an efficient acceptance criteria, b) no optimal solution has been developed for steel frames where these new connections or innovative methods have been implemented and c) many of the the new connections and innovative methods discussed in this Appendix do not have the flexibility to be easily adjusted. In order to optimize steel frames with replaceable connections, the strength and stiffness (and consequently the energy dissipation) of the connection needs to be easily controlled. For optimization, a large number of the same connections with varying geometries and non-linear dynamic responses need to be produced. There is no connection that has sufficient flexibility or that can be easily changed and adjusted.

However, while many of the innovative connections explored in this Appendix successfully shift the deformation in steel framed buildings away from the column and connection and into the beam (at the RBS location) there is currently no efficient, generic or optimal frame work for a multi-criteria performance design of RBS steel frames in multi-storey steel structures, to consider the non-linear dynamic affects at the element or structural level.

Perhaps a solution to this problem lies in developing a concept and framework for an additively printed connection that can dissipate the seismic energy through the yielding of small components within the connection, leading to a lateral displacement (energy absorbing) method for absorbing energy. Additive printing provides the opportunity to produce a huge range and variety of different connections at no extra cost (Leblanc, 2014). The detailed literature review in this Appendix explores the superior behaviour of 2D and 3D additively printed lattices compared to their solid counter part sections. Stronger, more efficient and lighter shapes of additively printed lattices lead to increased energy absorption; utilising these properties opens up opportunities for connections with designed characteristics and specified performance. The ideal solution would allow additively printed beam-column connections that can be tailored to achieve different performance targets in different parts of the structure by adjusting the geometries of the connection (and consequently the stiffness and strength of the connection which effects the energy absorption characteristics of the connection). This would allow an optimal solution to be achieved which is highly flexible, where the characteristics of each connection can vary significantly.

While this idea may seem unrealistic at this current time, with the speed and rate of developing technology, advances in additive (3D) printing and leaps and bounds in the sophisticated computer technology, could the answer to the future design of optimized seismic connections lie within additive (3D) printing?

Appendix B

Review of the European and American Standards

The following three main design guidelines and standards in Europe and America specify recommendations for RBS design, Section B.0.1 reviews these methods in more detail:

- Eurocode 8 outlines a retrofitting design procedures for reduced flange sections. Firstly, the RBS design procedure should be followed and then the limit state of the required rotational capacities of the reduced beams should be then checked using table B.5 in BS/EN 1998-3 (BSI, 2005).
- ANSI/AISC 358-16 also lays down some prequalified limits on the design of RBS sections. Limits are placed on the beam and column depths (limited to W36/W920). Weight, flange thickness and span to depth ratios are also imposed on sections. The design procedure for the geometries of RBS start with trial values based on the beam width and depth (AISC, 2016b).
- FEMA 350 lays down some prequalified limits and design procedures that should be used in special and ordinary moment frame connections. Initial RBS geometries are defined based on beam properties (SAC Joint Venture, 2000a).

B.0.1 RBS in current design

Reduced Beam Section (RBS) connections have become widely adopted in the European and American design guides and standards. The following sections briefly reviews these design guides. It should be noted that there are many American Federal Emergency Management Agency (FEMA) documents which aid in seismic design and retrofitting, only a few of the prominent and most interesting guides have been summarised.

British design codes and standards

Eurocode 8 (British Standards Institute, 2005), is part of a set of standards known as the Eurocodes. The Eurocodes are the reference design codes. The Eurocodes are standards recognised by all members of the European union, they provide common structural design rules for all building types. There are 10 Eurocodes (abbreviated EN 1990 to EN 1999), each code consists of a number of parts (58 EN Eurocode parts in total). They apply to the structural design of buildings and other civil engineering works. The Eurocodes provide common rules for structural design within the European Union (Hamburger et al., 2015). These have been published by the European Committee for Standardization (CEN) to bring together the National Standardization Bodies of 34 European countries. Officially recognised by the European Union and European Free Trade Association, the CEN has the responsibility of defining voluntary standards at a European Level (CEN, 2017). BS/EN 1998 (BSI, 2004) is the British National Standard for seismic design, covering all common and basic structures.

BS/EN 1998-1: Design of Structures for Earthquake Resistance – Part 1: General rules, seismic actions and rules for buildings (BSI, 2004)

The British Standard Design Code, Eurocode 8: Design of Structures for Earthquake Resistance (BSI, 2004), applies to the design and construction of buildings and civil engineering works in seismic regions. BS/EN 1998-1 (BSI, 2004) is based on two fundamental requirements; the no-collapse requirement and damage limitation requirement.

1. The no collapse requirement of a structure in BS/EN 1998-1 (BSI, 2004) is evaluated using a design seismic action expressed as the combination of a reference probability of exceedance in 50 years (or a return period) and an importance factor (depending on the type of structure).

2. The damage limitation requirement is verified using seismic action expressed as a probability of exceedance of 10 years and a reduction factor.

BS/EN 1998-1 (BSI, 2004) uses a compliance criteria in order to satisfy the fundamental requirements for structures (previously mentioned). Ultimate limit states as well as damage limits states are checked in the compliance criteria to help ensure the fundamental requirements are met.

1. The ultimate limit state needs to verify that the structure that is being designed for has the necessary resistance and energy dissipation capacity, in order to prevent collapse or failure thus protecting public safety. The resistance and energy dissipation represents how much of a non-linear response the structure gives; which is based on the behaviour factor and class of ductility assigned to the structure. A low dissipative structure would have a low behaviour factor value and low ductility class; a highly dissipative structure would have a larger behaviour factor and high ductility class.

2. The damage limit state helps to protect structures against an unacceptable level of damage to building service requirements. This damage state is achieved by satisfying relevant limits in the code.

BS/EN 1998-3: Design of Structures for Earthquake Resistance – Part 3: Assessment and retrofitting of buildings (BSI, 2005)

Eurocode 8 Part 3 (BSI, 2005), acts as a guidance for the evaluation of seismic performance of existing buildings, selecting appropriate corrective measures and defines criteria for the retrofitting of buildings. BS/EN 1998-3 (BSI, 2005) has been developed because:

- The seismic design and resistance for many older structures have not been considered
- Evaluations on existing buildings may be required in order to indicate the need for retrofitting
- Damage caused by earthquakes may require major repairs

BS/EN 1998-3 (BSI, 2005) is intended for the evaluation and assessment of structures to check if the building will satisfy the required limit state. A performance criteria for all structures is defined in BS/EN 1998-3 (BSI, 2005) as three fundamental limit state requirements, their definitions are as follows:

- Near Collapse (NC) significant damage to the structure, low stiffness and strength of main structural members, non-structural members collapsed, large residual drifts and very unlikely to survive another earthquake.

- Significant Damage (SD) some residual stiffness and strength in structural members, non-structural members damaged, moderate permanent drifts, able to survive after shock of an earthquake and uneconomical to repair
- Damage Limitation (DL) small damage, yielding of structural elements (not much loss of strength or stiffness), non-structural components may only be slightly cracked and negligible permanent drift

A popular way of retrofitting a structure is by weakening the beams in order to improve the ductility. By weakening the beam flanges, this shifts the location of the plastic hinge away from the column and beam-column connection and into the beam. Reduced Beam Sections (RBS) are where the flanges of the beams are trimmed back to weaken the beam, table B.5 in BS/EN 1998-3 (BSI, 2005) shows the required rotation capacity of RBS dependent on the limit state required: 1) Damage Limitation (DL) $0.010rad$, 2) Significant Damage (SD) $0.025rad$ and 3) Near Collapse (NC) $0.040rad$.

If the specific design procedures in section B.5.5.4(3) of BS/EN 1998-3 (BSI, 2005) are followed, then the above capacity rotations can be achieved. Beam-to-column connection retrofitting in accordance with clause B.6.2.1(1) of BS/EN 1998-3 (BSI, 2005) aims at moving the plastic hinge location, from the column face and into the beam. Retrofitting structures in this way can be achieved by either:

- Weld replacement; by replacing the filler, removing the backing bar or adding additional stiffeners
- Weakening strategy, aimed at shifting the plastic deformations into the beam and away from the beam-column interface by using: RBS or adopting semi-rigid connections
- Strengthening strategy, which reduces the stress at the welds and forces the plastic hinge zone to occur at the ends of either the haunch or cover plate, BS/EN 1998-3 cover the design of: haunched or cover plate connections

Table B.6 in BS/EN 1998-3 (BSI, 2005) outlines the requirements of retrofitted beam-column connections. Rotational capacities of five different connections and the three limit states are specified, which can be achieved if the correct design detailing and requirements to BS/EN 1998-3 (BSI, 2005) are fulfilled.

American design codes and standards

The code requirements for structural steel design of buildings are minimum legal requirements that structures must meet. The American design requirements are contained in a set of standards or building codes that consist of:

- ASCE/SEI 7-10 (ASCE, 2010) Minimum Design Loads for Buildings and Other Structures sets basic loading criteria and drift limits for special moment steel frames
- ANSI/AISC 341-16 (AISC, 2016a) Seismic Provisions for Structural Steel Buildings this provides detailed requirements for the detailing of steel buildings
- ANSI/AISC 358-16 (AISC, 2016b) Pre-qualified Connections for special and Intermediate Steel Moment Frames for Seismic Applications Standardise the design of connections and allow these connections in structural buildings without the need for additional testing.

Other guides have been written by Federal Emergency Management Agency (FEMA) and American Society of Civil Engineers (ASCE) to assist in the clarification of the Code Requirements. Guides also include recommendations or good design and construction practice that may not be specifically required in the Code or Standard requirements. In America it is the responsibility of the local government to enforce building codes and practices. Cities, countries or states base their building codes on the International Building Code (IBC, 2015). The IBC (IBC, 2015) is regarded as the model building code and is adopted as the base code for most jurisdictions in the United States of America.

The International Code Council (ICC) develops model codes and standards for use in structural design which aim to protect the health, safety and welfare of the public. Updates to the IBC are published every three years, which adopt the latest additions of the American National Standards Institute (ANSI). The American National Standards Institutes (ANSI) oversees the development of American National Standards such as ASCE/SEI 7-10: Minimum Design Loads for Buildings and Other Structures (ASCE, 2010) by accrediting the procedures of Standard Developing Organisations (SDOs) which include committees such as the American Institute of Steel Construction (AISC), the Federal Emergency Management Agency (FEMA) and the American Society of Civil Engineering (ASCE).

The IBC (IBC, 2015) has detailed provisions and requirements relating to: fire, life safety, health and safety, construction and building design. The IBC is a tool which aims at preserving public health and safety while providing safe guards from hazards within the built environment. The IBC IBC (2015) adopts provisions for structural design which have been approved by the American National Standards Institutes (ANSI). The IBC is accepted by the Unites States as a model code. This code should be adopted in accordance with laws and procedures of the government jurisdiction. IBC volume 2 chapters 16 to 35 provide structural provisions for seismic resistant buildings.

American Institute of Steel Construction (AISC)

The American Institute of Steel Construction (AISC) provides publications and documents for design and construction of steel buildings for the United States. The AISC is accredited by the ANSI to ensure it meets their standards. An ANSI-accredited balloting process, ensures that all AISC publications are scrutinised through discussions and suggestions for improvements. The AISC has produced current standards for all types of structural buildings for the United States. Contributions to the standard by many committees in the United States include: the Building Seismic Safety Council (BSSC), the Federal Emergency Management Agency (FEMA), the National Science Foundation (NSF) and the Structural Engineers Association of California (SEAOC). The AISCs mission is to; make structural steel the material of choice (AISC, 2017).

ANSI/AISC 341-16: Seismic Provisions of Structural Steel Buildings (AISC, 2016a)

Seismic Provisions for Structural Steel buildings (AISC 341-16) (AISC, 2016a) is one of the current American Standard. The design guideline covers connection detailing and member design requirements for structural steel or composite steel and concrete systems. This design code accompanies the Specification for Structural Steel Buildings (AISC 360-16 (AISC, 2016c)) which provides general requirements for the construction and design of steel structures. AISC 341-16 (AISC, 2016a) provides the design, fabrication and erection guidelines of structural steel members and connections in seismic force-resisting systems (SFRS). It covers: additional codes, standards and specifications, for materials and design drawings.

ANSI/AISC 358-16: Pre-qualified Connections for Special and Intermediate Steel Moment frames foe Seismic Applications (AISC, 2016b)

This pre-qualified connection standard is based on chapter k of AISC 341-16 (AISC, 2016a) (Prequalification and Cyclic Qualification Testing Provisions). It specifies connections that have been pre-qualified for use in Special Moment Frames and Intermediate Moment Frames, which require no further testing. Pre-qualified connections are defined as connections that have been previously tested experimentally, if specific detailing is provided then the required connection response can be achieved.

The ten pre-qualified connections defined in AISC 358-16 (AISC, 2016b) are: Reduced Beam Sections (RBS), Bolted unstiffened extended end plate (BUEEP), Bolted stiffened extended end plate (BSEEP), Bolted flange plate (BFP), Welded unreinforced flange-welded web (WUF-W), Kaiser bolted bracket (KBB), ConXtech ConXL moment connection (ConXL), Simpson Strong-Tie String Frame moment connection and Double-tee moment connection. Refer to AISC 358-16 (AISC, 2016b) for more details of these connections.

American Society of Civil Engineers (ASCE)

The American Society of Civil Engineers (ASCE) is the worlds largest publisher of civil engineering content and is the forefront of the built environment while at the same time protecting the natural environment. The ASCE mission is to Deliver value to our members, advance civil engineering, and protect the public health, safety and welfare (ASCE, 2017b). The Structural Engineers Institute (SEI) is a technical institute within the ASCE (one of nine sub institutes within the ASCE) comprising of 30,000 members. It is responsible for developing the ASCE standards through a Consensus Standards Process. Specifically, the SEI Codes and Standards Division produces a variety of publications (including standards). This division (sometimes referred to as a committee) co-ordinates all activities of ASCE relating to the establishment, use and discontinuance of building codes and standards. The ASCE is accredited by the ANSI and hence provides technical guidelines, standards and building codes that can be adopted by the United States. The process of the ASCE are overseen by the Codes and Standards Committee (CSC). Building codes are reviewed every 5 years to ensure the latest additions are available.

ASCE/SEI 7-10: Minimum Design Loads for Buildings and Other Structures (ASCE, 2010)

Minimum design loads for buildings and other structures (ASCE/SEI 7-10) (ASCE, 2010) has been prepared by the SEI committee. The ASCE/SEI 7-10 provides minimum load requirements, design strengths, design limits, drift limits and design specifications for the structural design of buildings in the Unites States.

ASCE/SEI 31-03: Seismic Evaluation of Existing Buildings (ACSE, 2003)

In some cases, the seismic evaluation of existing buildings may be required where structures have not been initially designed to seismic provisions. This is common in old buildings or where a buildings structure has been significantly altered. This standard is used to assess buildings to determine if it has been adequately designed and constructed to resist seismic forces, and whether or not the structure needs to be seismically retrofitted. Buildings are evaluated to either Life Safety or Immediate Occupancy performance levels. The need to evaluate a building using ASCE 31-03 (ACSE, 2003) may have been prompted by the Rapid Visual Screening of Buildings for Potential Seismic Hazards (FEMA P-154) (FEMA, 2015) handbook. If a structure is deemed suitable for rehabilitation the Seismic Rehabilitation of Existing Buildings (ASCE 41-17) (ASCE, 2017a) should be consulted for information regarding retrofitting and mitigation strategies.

ASCE/SEI 41-17: Seismic Evaluation and Retrofit of Existing Buildings (ASCE, 2017a)

The Seismic Evaluation and Retrofit of Existing Buildings (ASCE 41-17) (ASCE, 2017a) standard defines deficiency-based and systematic based methods in order to evaluate and retrofit structures to withstand seismic forces. Performance-based principles underpin the methods used for evaluation. A deficiency based evaluation procedure, relies on past observations and responses of a similar building as a result of seismic events. A systematic based procedure is appropriate for any type of building, comprising of a complete methodology to evaluate the entire building. ASCE 41-17 (ASCE, 2017a) has been based on the Pre-standard and commentary for the seismic rehabilitation of buildings (FEMA 356) (FEMA, 2000). For a more extensive array of retrofitting techniques for strengthening structural elements in buildings refer to Techniques for the Seismic Rehabilitation of Existing Buildings (FEMA 547) (FEMA, 2006) for additional information.

Federal Emergency Management Agency (FEMA)

The Federal Emergency Management Agency (FEMA) is part of the United States Department of Homeland Security and is responsible for coordinating government-wide relief efforts. The FEMA brings assistance to areas in the United States affected by natural disasters, (this includes earthquakes). It also works to protect communities from hazards. FEMAs mission is to build, sustain and improve the United States capability to prepare for, protect against, respond to, recover from and mitigate all hazards (FEMA, 2017). FEMA is one of four federal agencies of the National Earthquake Hazards Reduction Program (NEHRP). NEHRP is at the forefront of the federal governments efforts to reduce the facilities, injuries and property losses caused by earthquakes. The United States governments long-term nationwide program is to reduce the risk imposed on life and property due to earthquakes; thus, NEHRP was established by the congress in the Unites States to help reduce losses due to earthquake through improved methods.

FEMA 355D: State of the Art Report on Connection Performance (SAC Joint Venture, 2000d)

The State of the Art Report on Connection Performance (FEMA 355D) (SAC Joint Venture, 2000d) is a report put together by the SAC, this is a Joint Venture comprising of three organisations:

- the Structural Engineers Association of California (SEAOC) a professional structural engineers organisation based in California which helped develop the International Building Code (IBC) (IBC, 2015) and the NEHRP recommended Seismic Provisions for new buildings and other structures (FEMA P-750) FEMA (2009)
- the Applied Technology Council (ATC) is a non-profit organisation which aims at mitigating the effects of natural hazards among civil engineering structures
- and the California Universities for Research Engineering (CUREe) a non-profit organisation which carries out earthquake hazard prevention research.

This SAC Joint Venture was formed specifically to solve intermediate and long term effects of the problems relating to steel moment connections, following the 1994 North Ridge Earthquake. Refer to Chapter 1 Section 1.2.1 for more details.

FEMA 350: Recommended Seismic Design Criteria for New Steel Moment–Frame Buildings (SAC Joint Venture, 2000a)

FEMA 350 (SAC Joint Venture, 2000a) provides specific design and performance evaluation procedures for steel framed moment resisting structures. The seismic performance-based design of steel

buildings is also considered in this report; which can be useful for a more reliable and higher building performance compared to code based designs. Detailed pre-qualified connections are presented as well as the procedure for performance and evaluation for new connections. The performance evaluation of structures using two performance levels is adopted, and an acceptance criteria has been used to assess the buildings ability to achieve the selected performance objective.

Performance evaluation in chapter 4 of FEMA 350 (SAC Joint Venture, 2000a), gives guidance on evaluating welded steel moment framed buildings. Performance objectives are defined so that structures can achieve a level of confidence for a desired performance objective. An acceptance criteria has been defined to evaluate the buildings ability to meet the desired level of confidence. Two performance levels are defined in FEMA 350 (SAC Joint Venture, 2000a) which are: Collapse Prevention (CP) and Immediate Occupancy (IO). They describe damage states for the structural elements of steel-moment framed buildings as follows:

- Collapse Prevention (CP) the structure is on the edge of total or partial collapse post earthquake and is not safe for occupancy, significant reduction in the stiffness strength and vertical load carrying capacity of the elements, large permanent deformations/drifts, possibility of collapse if another seismic event is experienced and uneconomical to repair.
  - Damage to columns some experience yielding
  - Damage to beam-column connections many fractured and loss of capacity
  - Inter storey drift large permanent
- Immediate Occupancy (IO) damage is significantly light and building inspection not necessary, vertical and lateral load resisting systems keep nearly all of their stiffness and strength, buildings likely to be safe for immediate occupancy as long as appropriate services are available.
  - Damage to columns no damage
  - Damage to beam-column connections less than 10% fractured on any one floor
  - Inter storey drift less than 1% permanent

Structural analysis is used to predict the structural responses and demands in steel frames. The four types of analysis permitted in FEMA 350 (SAC Joint Venture, 2000a) are: 1) Linear static procedure, 2) Linear dynamic procedure, 3) Non-linear static procedure and 4) Non-linear dynamic procedure. Acceptance of a structure is determined by its ability to achieve the performance objectives of either CP or IO, with a level of confidence.

FEMA P-750: NEHRP Recommended Seismic Provision for new buildings and other Structures (FEMA, 2009)

Prepared for FEMA by the Building Seismic Safety Council (BSSC). The BSSC is a voluntary body with a purpose to enhance the safety of the public by providing improved seismic safety provisions for use in the building community for planning, designing, regulation and utilization of structures. This FEMA P-750 (FEMA, 2009) references the ASCE/SEI 7-10 (ASCE, 2010) standard published by the ASCE and SEI.

FEMA P-154: Rapid Visual Screening of Buildings for Potential Seismic Hazards (FEMA, 2015)

This handbook provides you with guidance for a rapid visual screening process on existing buildings to determine if a detailed evaluation and hence potential retrofitting or rehabilitation of the structure is required; in order to provide the required seismic resistance and level of performance.

FEMA 547: Techniques for the Seismic Rehabilitation of Existing Buildings FEMA (2006)

Some buildings constructed in the United States have a poor seismic resistance to earthquakes, generally this is because there was no seismic code or standard available at the time of construction. Seismic rehabilitation, retrofitting or strengthening is the process of improving the seismic performance of existing buildings. The Techniques for seismic Rehabilitation of Existing Buildings (FEMA 547) FEMA (2006) guide has two main purposes: 1) to provide a number of appropriate and practical rehabilitation techniques for existing buildings and 2) to provide guidance on which techniques are appropriate for specific seismic deficiencies in buildings. FEMA 547 FEMA (2006) is just a retrofitting and rehabilitation guide for existing buildings and does not provide guidance, requirements or seismic engineering procedures for buildings.

FEMA 356: Pre-standard and Commentary for the Seismic Rehabilitation of Buildings (FEMA, 2000)

The Pre-standard and commentary for the seismic rehabilitation of buildings (FEMA 356) (FEMA, 2000), provides provisions for the rehabilitation of buildings and structures so that the performance and resilience to earthquakes can be improved.

Appendix C

Detailed Review of Connection and Frame Modelling

C.0.1 Modelling of connections to ASCE/SEI 41-17 (ASCE, 2017a)

There are two main types of connections, fully restrained and partially restrained. A connection is considered to be fully or partially restrained depending on the strength and stiffness of the connection assembly. Fully restrained connections are defined in ASCE/SEI 41-17 (ASCE, 2017a) in a table which depends on the type of connection used, where for example, Reduced Beam Sections (RBS) are defined as fully restrained connections. If the connection is not specified in the table, a fully restrained connection is classified where: 1) the connection deformation does not contribute to more than 10% of the total lateral deflection and 2) the connection is just as strong as the weakest member of the two connecting members of the joint.

The following sections briefly summarise the important modelling procedures specified in ASCE/SEI 41-17 (ASCE, 2017a) for linear static, linear dynamic, non-linear static and non-linear dynamic analysis of connections.

Linear Static and Linear Dynamic

Unless specified in ASCE/SEI 41-17 (ASCE, 2017a), the specifications of ANSI/AISC 360-16 (AISC, 2016c) should be followed. The panel zone modelling can be taken into account by either: 1) adding an element to model and take into account the flexibility of the panel zone – such as a spring element or 2) adjustment of the beams stiffness to take into account the flexibility of the panel zone

Direct modelling of the panel zone is not needed when either: 1) the expected shear strength of the panel zone is larger than the flexural strength of the beams at the connection or 2) the stiffness of the panel zone at least 10 times larger than the flexural stiffness of the beam. For connections (such as RBS considered in this study) where the plastic hinge is forced to occur in the beam, rigid elements can be used for the effective span of the beam.

Non-linear static

To account for the non-linear effects the following shall be taken into account: 1) elastic properties to be modelled as per Linear Static and Linear Dynamic Procedures. The flexural stiffness of the beam and column shall be modified using τ_b as specified in ANSI/AISC 360-16 (AISC, 2016c), 2) the plastification should be modelled using moment-curvature relationships and 3) the non-linear behaviour of panel zones should be taken into account using a mathematical model.

Instead of using experimental methods or analysis, the generalized load-deformation curves in ASCE/SEI 41-17 (ASCE, 2017a), shown in Figure C.0.1 can be adopted for the components in the frame. The parameters of the curve are defined in ASCE/SEI 41-17 (ASCE, 2017a) in the relevant tables depending on the type of connections. The load-deformation curves can be adjusted to take into account strain hardening by: 1) strain-hardening the elastic slope of the curve by 3% and, 2) if panel zone yielding occurs, apply a strain-hardening slope of 6% for the panel zone.

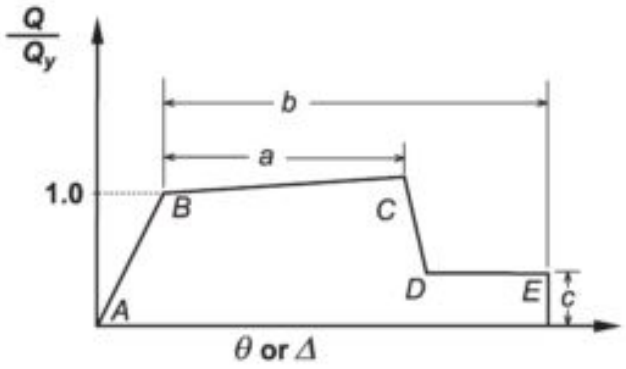

Figure C.0.1: Generalized load-deformation to be used in nonlinear dynamic analysis instead of experimental or analysis results (ASCE, 2017a)

where: Q = generalized component load, Q_y = generalized component expected strength, θ = total elastic and plastic rotation of the beam or column, θ_y = yield rotation of beam or column or the angular shear deformation for shear panels, Δ = total elastic and plastic displacement and Δ_y = yield displacement.

Non-linear Dynamic

ASCE/SEI 41-17 (ASCE, 2017a) states that the complete hysteresis behaviour of the connection should be taken into account from experimental results or using other appropriate methods approved from jurisdictions. This research focuses on the modelling of RBS connections for implementation in the non-linear dynamic analysis of steel structures.

C.0.2 Modelling the hysteretic behaviour of connections

There are a wide range of different methods available which are capable of modelling and representing the non-linear behaviour of connections. In this research the modified-Ibarra-Krawinkler model has been used. The following sections provide some background and introduction into this model. Refer to Chapter 3, Section 3.2.3 and Chapter 4 Section 4.2.3 for an in-depth literature review of this method.

Background to the Ibarra-Krawinkler model

According to Ibarra et al. (2005), it is necessary to have a simplified model in order to represent the seismic demand on elements or sub-assemblies. Ibarra et al. (2005) first investigated this by comparing the load verses displacement of plywood shear panels under cyclic and monotonic loading. Figure C.0.2a shows that the strength has been capped followed by a negative tangent stiffness. The results clearly shown the strength of the plywood shear panel during the hysteretic response, deteriorate with an increase in the the number of loading cycles. According to previous work carried out by Ibarra et al. (2005), the hysteretic behaviour of existing models do not incorporate the important strength degradation properties.

Figure C.0.2b shows a backbone curve which is used to simplify the hysteretic plot. It represents a monotonically increasing deformation representation of the hysteretic response. The main parameters used to define this backbone curve are: K_e = elastic stiffness, F_y = yield strength, K_s = strain hardening stiffness, δ_y = yield deformation, δ_c = capping deformation, δ_r = residual deformation F_c = peak strength, K_c = post-capping stiffness and F_r = residual strength. These parameters can have different values in the positive and negative regions if necessary. Parameters: α_c, δ_c/δ_y, α_s and λ are all obtained from either analytical predictions or from experimental calibration results.

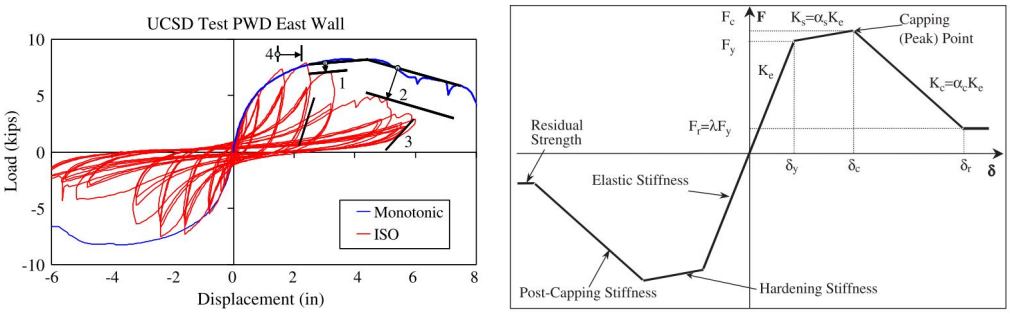

(a) (b)

Figure C.0.2: (a) Comparisons of monotonic and hysteretic models and (b)Backbone curve representing the deformation against force for the simplified model of the hysteresis plot (Ibarra et al., 2005)

There are three types of basic model by Ibarra et al. (2005) which are capable of capturing the cyclic deterioration. These are bilinear model, peak-oriented model and pinching model (models shown in Figure C.0.3). Different rules which define the hysteresis, are bound by the backbone curve of the basic Krawlinkler curve shown in Figure C.0.2b.

Figure C.0.3a shows the standard bilinear hysteretic rules with kinematic strain hardening. A strength limit should be introduced to the model to prevent the strength increase in the loading path at later stages of the model. The strength limit corresponds to the smallest strength in the non-linear range. Figure C.0.3b shows the peak-oriented hysteretic model. The backbone model is changed to include strength capping and residual strength. The reloading of the curve always targets the previous maximum displacements. Figure C.0.3c shows the pinching hysteretic model. Reloading of this model is of two parts: the $K_{rel,g}$ and $K_{rel,b}$. Reloading of the model is initially directed towards a break point (which is a function of the maximum permanent deformation and the maximum load experienced in the direction of loading).

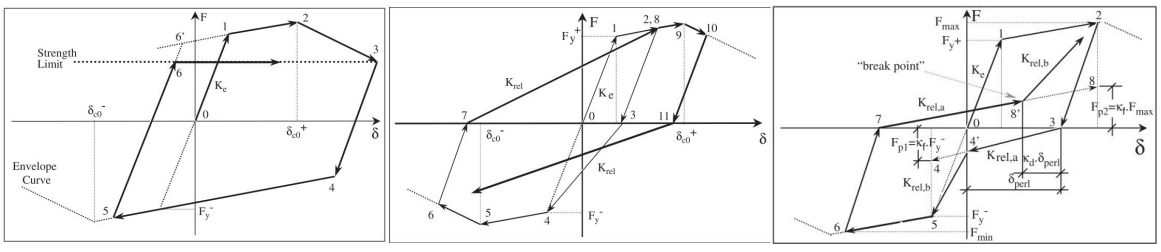

(a) (b) (c)

Figure C.0.3: (a) Bilinear hysteretic model, (b) Peak-orientated model and (c) Pinching model (Ibarra et al., 2005)

Modifications by Ibarra et al. (2005) take into account strength degradation by predefined rules which govern the cyclic loading. There are up to four different modes of deterioration that can be activated once a yield point has been surpassed in either direction, refer to Figure C.0.4 for these four modes. A defined parameter ($\gamma_{s,c,a,k}$) controls the rate of these deteriorations. The basic strength deterioration has two strength deterioration parts. Firstly, Figure C.0.4a shows how the branch between the yield strength F_y and the peak strength F_c is translated towards (0,0) by reducing the yield strength of the cycle which is of interest. Secondly, the strain hardening stiffness K_s is reduced. Figure C.0.4b, which defines post capping strength deterioration, shows how the post capping branch (which is the backbone branch defined between F_c and F_r) is translated towards (0,0) by reducing the reference strength of the peak strength F_c. Figure C.0.4c shows how the unloading stiffness deteriorates, this is similar to the deterioration of the strain hardening stiffness. Finally, the accelerated reloading stiffness is shown in Figure C.0.4d. This deterioration only applies to the peak oriented model, in general, the location of the target displacement (which is based on the maximum previous cycle) is moved by a specific amount along the backbone curve. the distance the target displacement is moved along the backbone curve depends on the amount of energy dissipated in the previous cycle.

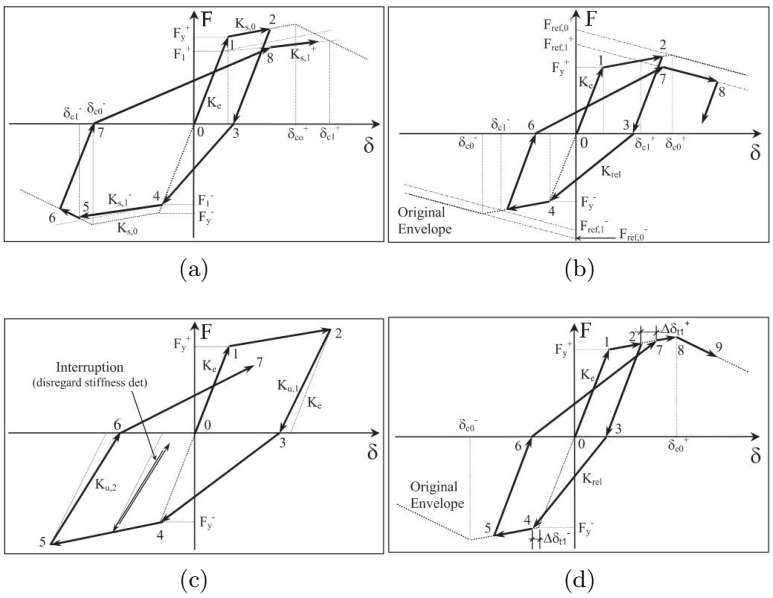

Figure C.0.4: Examples of (a) Basic strength deterioration, (b) post-capping strength deterioration, (c) unloading stiffness deterioration and (c) accelerated reloading deterioration for a peak orientated model (Ibarra et al., 2005)

As explained previously, the rate of these deterioration modes is controlled by the parameter ($\gamma_{s,c,a,k}$) which is associated with a β_i parameter. The energy deterioration parameter which controls the rate of deterioration is β_i defined in Equation C.1. The cyclic deterioration of the model is based on a hysteretic energy rule developed by Rahnama and Krawinkler (1993) which considers the energy dissipation under cyclic loading of the element.

The energy deterioration parameter is defined as:

$$\beta_i = \left(\frac{E_i}{E_t - \sum_{j=1}^{i-1} E_j} \right)^c \tag{C.1}$$

where E_i is the hysteretic energy dissipation during the i^{th} excursion, $\sum E_j$ is the total energy from previous excursions, E_t is the reference energy and c is an empricial parameter (taken as 1.0

in Lignos and Krawinkler (2011)). Different rates of deterioration can be defined in the positive and negative direction – see Ibarra et al. (2005) and Lignos and Krawinkler (2012) for more details.

For the bilinear hysterisis response the strength deterioration and postcapping strength deterioration (basic strength deterioration) is modeled by translating the strength bounds towards the origin at the rate:

$$F_i = (1 - \beta_i) \cdot F_{i-1} \tag{C.2}$$

where i is the extrusion where energy is dissipated, F_i is the reference strength value on each backbone curve and β_i is the energy deterioration parameter.

The stiffness deterioration for the bilinear hysterisis per i^{th} excursion is modeled using:

$$K_i = (1 - \beta_i) \cdot K_{i-1} \tag{C.3}$$

where K_i is the stiffness of the i^{th} excursion and β_i is the energy based excursion parameter of the i^{th} cycle and K_{i-1} is the stiffness of the previous excursion.

The modified-Ibarra-Krawinkler (mIK) model

An improved model, first proposed by Lignos and Krawinkler (2007), is an improvement on the original Krawlinkler model by Ibarra et al. (2005). The differences in the models are due to differences between determining the parameters that define the backbone curve. More detailed information on the modified Ibarra-Krawlinker models can be found in: Lignos (2008), Ibarra and Krawinkler (2005), Lignos and Krawinkler (2007) and Lignos and Krawinkler (2012). The differences between the Ibarra-Krawlinker and modified Ibarra-Krawlinker model are as follows:

1. The relation of post yielding stiffness to initial stiffness by the strain hardening ratio results in an unreliable prediction of the cap strength F_c. The post strength ratio results in an unreliable prediction of the cap strength F_c. The post yield strength ratio of F_c/F_y (1.05 for bare RBS steel connections) is a much more reliable for post yield behaviour.

2. δ_c/δ_y (shown in Figure C.0.2b) has been previously used to define plastic deformation capacity. θ_p is better to describe the deformation capacity of steel components. θ_{pc} (the post capping plastic hinge deformation) defines the post-capping strength deterioration. Figure C.0.5a shows the definition of these new parameters.

3. Λ_s, Λ_c, Λ_a and Λ_k (which are the reference cumulative plastic rotation parameters for strength deterioration, post-capping deterioration, accelerated reloading deterioration and unloading stiffness deterioration respectively) are used opposed to γ_s, γ_c, γ_a and γ_k. These parameters are used to describe the cyclic deterioration as a function of the cumulative deformation capacity of the component, where $\Lambda_{s,c,a,k} = E_t/F_y = \lambda_{s,c,a,k} \cdot \theta_p$. Refer to Lignos and Krawinkler (2011) for more details.

The model has strength bounds established by a backbone curve shown in Figure C.0.5a. A set of new parameters to define this backbone curve are slightly different to the original Ibarra-Krawlinker curve. This curve is defined by three strength parameters and four deformation parameters, these are as follows: effective yield moment M_y, capping moment strength M_c, residual moment $M_r = \kappa \cdot M_y$, yield rotation θ_y, pre-capping plastic rotation θ_p, post capping plastic rotation θ_{pc} and ultimate rotation capacity θ_u. Similarly, the same set of rules define the bilinear, peak-oriented or pinching hysteretic behaviour.

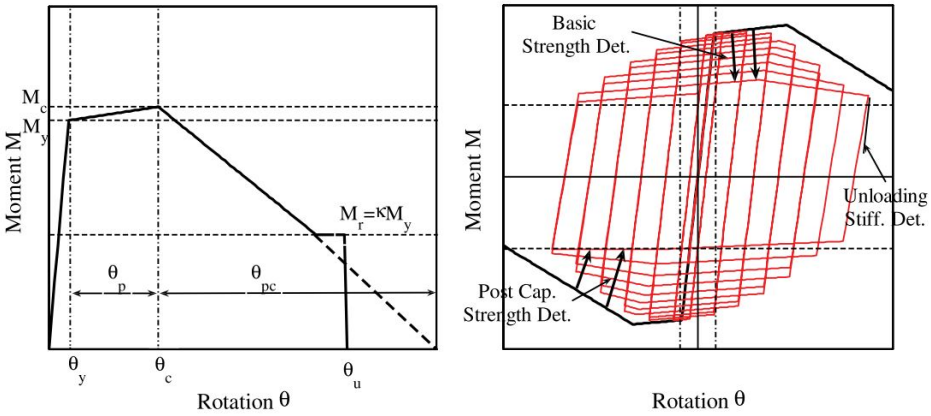

Figure C.0.5: (a) The new improved back bone curve used to define the bounds of the hysteresis and (b) the three main deterioration modes that can be activated in the bilinear model (Lignos and Krawinkler, 2011)

Refer to Chapter 3 Section 3.3.1 and Chapter 4 Section 4.3.2 for more information on the parameters which define the behaviour of the mIK model.

Parameters used to define the mIK

Lignos and Krawinkler (2007) highlighted that the effects of residual strength in RBS connections are significantly important and should be incorporated into the hysteretic response of the connection. In order to determine the appropriate parameters for these deterioration models Lignos and Krawinkler (2007) first developed a database of cyclic hysteretic responses from experimental results. The database produced by Lignos and Krawinkler (2007) has over 200 steel specimens, with half of them being RBS connections.

Lignos (2008) looked at both composite (mainly consisting of W36 beam sections) and non-composite (bare steel beam sections) beam column connections. From the data collected in literature, there was not enough data or range of sections for multivariable regression analysis to be carried out on composite beam column connections. However, there was a large enough range of data in current literature to carry out mulivariable regression analysis on steel connections. These connections were split into three main groups:

- Beams other than RBS connections
- Hollow square tube sections
- Beams with RBS connections

Lignos (2008) concluded that there was not a large enough range of connections in the current literature to specifically define the type of connection for other than RBS connection (such as bolted or welded connection etc). Therefore, Lignos (2008) combined all other than RBS steel connections into one data set for analysis. Hollow square tube sections are widely used in Japanese practice. Hollow square sections from 113 HHS column connections were taken from literature in order to determine multi variable regressional equations.

As this study focuses on RBS connections, only the multi variable regression analysis of RBS connections will be covered in detail here, for more information refer to (Lignos and Krawinkler, 2007; Lignos, 2008). In the RBS connection case, there was enough data from previous experimental results to create a separate set of connections. In the RBS connection data set, the depth d of all beams to be considered using the multi variable regressional equations has to be larger than $21''$ ($d \geq 533mm$), no connection with a depth smaller than $18''$ was considered in the data set.

Using the 42 RBS test results from the database Lignos and Krawinkler (2007) carried out a study in order to define relationships for the parameters: plastic rotation capacity, post capping plastic rotation and cumulative plastic rotation parameter. A Matlab tool was produced by Lignos and Krawinkler (2007) which calibrated the experimental results against the deterioration models in order to obtain the parameters required to define the deterioration model. Information to calculate the backbone curve for the modified Ibarra-Krawinkler model can be found using the following link: `http://dimitrios-lignos.research.mcgill.ca/databases/component/`.

Equations to predict these three strength parameters (θ_p), post capping plastic rotational capacity (θ_{pc}) and cumulative plastic rotation (Λ) were developed through regression analysis based on the local web and flange buckling and lateral torsional buckling of the steel beams. The multivariable regression equations are only valid for a specific range of parameters. The general non-linear regression model proposed by Lignos and Krawinkler (2007) is as follows (RP defines the response parameter θ_p, θ_{pc} or Λ):

$$RP = a_1 \cdot \left(\frac{d}{t_w}\right)^{a_2} \cdot \left(\frac{b_f}{2 \cdot t_f}\right)^{a_3} \cdot \left(\frac{L_b}{r_y}\right)^{a_4} \cdot (F_{y,f})^{a_5} \tag{C.4}$$

Lignos and Krawinkler (2011) discussed in detail and presented regression equation for determining the values of θ_p, θ_{pc} and Λ. Values for M_y, M_c/M_y, κ and θ_u are discussed in Lignos and Krawinkler (2011) and values have been suggested based on experimental statistics from the database and data interpretation. A summary of these four predictive equations for RBS connections with beam sections with a $d \geq 533mm$ are presented in Table C.0.1

Symbol	Prediction for RBS connections
θ_p	$\theta_p = 0.19 \cdot (\frac{h}{t_w})^{-0.314} \cdot (\frac{b_f}{2 \cdot t_f})^{-0.100} \cdot (\frac{L_b}{r_y})^{-0.185} \cdot (\frac{L}{d})^{0.113} \cdot (\frac{c^1_{unit} \cdot d}{533})^{-0.760} \cdot (\frac{c^2_{unit} \cdot F_y}{355})^{-0.0700}$
θ_{pc}	$\theta_{pc} = 9.52 \cdot (\frac{h}{t_w})^{-0.513} \cdot (\frac{b_f}{2 \cdot t_f})^{-0.863} \cdot (\frac{L_b}{r_y})^{-0.108} \cdot (\frac{c^2_{unit} \cdot F_y}{355})^{-0.360}$
Λ	$\Lambda = (\frac{E_t}{M_y}) = 585 \cdot (\frac{h}{t_w})^{-1.14} \cdot (\frac{b_f}{2 \cdot t_f})^{-0.632} \cdot (\frac{L_b}{r_y})^{-0.205} \cdot (\frac{c^2_{unit} \cdot F_y}{355})^{-0.391}$
M_y	$M_y/M_{y,p} = 1.06$
M_c/M_y	$M_c/M_y = 1.09$

Table C.0.1: Equations and ratios used to estimate the parameters for the modified Ibarra-Krawlinker models from Lignos and Krawinkler (2011) for cases where $d \geq 533mm$. $M_{y,p}$ is the predictive yield strength, defined using the RBS properties

C.0.3 Importance of connections in modelling of steel frames

The behaviour of steel moment frames are controlled by the detailing and hence type of connection. Therefore, it is necessary to accurately represent the performance and hysteretic response of all connections in a frame analysis. Refer to Chapter 3 Section 3.2.1 and Chapter 4 Section 4.2.1 for a detailed literature review of RBS frame analysis.

Performance Based Design (PBD) is a new modern method for the seismic design of structures. This method attempts to predict the performance of a building based on a design earthquake, thus designing the structure to be able to resits an appropriate level earthquake with an acceptable level of damage (Naeim et al., 2001). The three main performance levels in which structures are designed for in PBD are; Immediate Occupancy (IO), Life Safety (LS) or Collapse Prevention (CP). The American Society of Engineers has incorporated PBD into ASCE/SEI 41-17 (ASCE, 2017a). Other design recommendations, such as FEMA 350 (SAC Joint Venture, 2000a) and FEMA 273/274 (BSSC et al., 1997), have also included PBD in their recommendations also.

The level of damage in PBD is quantified in terms of an acceptable level of force or damage. Deformation-controlled or force-controlled actions are used in PBD, where the structures deformations or forces are compared to an acceptable criteria depending on the performance level selected. ASCE/SEI 41-17 (ASCE, 2017a) provides an acceptance criteria which specifies the allowed and permitted drifts and rotations of the frames. ASCE/SEI 41-17 (ASCE, 2017a) is a displacement based design and in general uses drift demands to compare frames to acceptable levels of drift or displacement.

All analysis methods must compare the performance of a frame to an acceptance criteria which can be either force controlled or deformation controlled:

1. Deformation Controlled actions are defined as Q_{CE} and taken as expected strengths from experimental or derived from principles. The expected strength is the average resistance expected over a specific deformation range which the element or component is expected to be subjected to.

2. Force Controlled actions are defined as Q_{CL} there are lower bound strengths taken from experimental results or derived from principles. Lower bound strengths are defined as the average strength take away one standard deviation.

Linear static and linear dynamic

ASCE/SEI 41-17 (ASCE, 2017a) defines different actions and acceptance criteria for beams, columns, panel zones and beam-column connections. For beams the deformation controlled actions of flexural and shear of steel elements should be considered for acceptance criteria. For columns, deformation controlled will be considered for flexural behaviour and force controlled for compressive behaviour. For shear panels the shear behaviour shall be considered deformation controlled. Finally for beam column connections fully restrained connections shall be considered deformation controlled.

Non-linear static and Non-linear dynamic

The actions of components under nonlinear actions must satisfy maximum deformations taken from tables in ASCE/SEI 41-17 (ASCE, 2017a). Maximum permissible rotations are defined for: Beams, Columns, Fully restrained connection panel zones and Fully restrained beam-column connections. For beams the flexural actions should be considered to be deformation controlled with maximum plastic rotations defined in ASCE/SEI 41-17 (ASCE, 2017a).

For columns the axial compressive loading shall be considered force controlled where the lower bound capacity P_{CL} is calculated according to ASCE/SEI 41-17 (ASCE, 2017a). The flexural loading of the columns with axial loads at the target displacement that are 50% less than P_{CL} shall be considered to be deformation controlled with the acceptance criteria for rotations defined in ASCE/SEI 41-17 (ASCE, 2017a). Where the flexural loading of the columns with axial loads at the target displacement

that are 50% grater than P_{CL} force controlled shall be considered. Panel zone plastic rotations shall be considered using the acceptance criteria in ASCE/SEI 41-17 (ASCE, 2017a).

The beam column connections (specific ones identified in ASCE/SEI 41-17 (ASCE, 2017a)) should be considered deformation controlled. Acceptance criteria are determined from ASCE/SEI 41-17 (ASCE, 2017a). The acceptance of the connection is dependent on: the detailing of the connection continuity plates, strength of the panel zones, the beam span to depth ratio, the slenderness of the beam web and the slenderness of the beam flanges. If the connection does not meet a number of conditions laid down in ASCE/SEI 41-17 (ASCE, 2017a) then the tabulated plastic rotations in ASCE/SEI 41-17 (ASCE, 2017a) will be multiplied by specified factors.

There are four criteria for non-linear modelling procedures in ASCE/SEI 41-17 (ASCE, 2017a), these are:

1. *Unacceptable response for nonlinear dynamic procedures:* this underpins the nonlinear dynamic methods of modelling. For a nonlinear model of a structure to be acceptable it must 1) converge 2) deformation controlled elements must not exceed the elements valid range 3) demands in force controlled elements must not exceed the elements capacity and 4) deformation demands on elements must not exceed the deformation limits of members to which they can no longer carry the applied gravity loadings. Where a buildings performance level is modelled as life safety (or lower) no more than one in eleven ground motions are allowed to fail the acceptance criteria.

2. *Acceptance criteria for deformation controlled actions:* the maximum deformation demands in the structure (such as under the target displacement) must not be more than the elements deformation capacities. In addition, the demands of the structure must be within the selected acceptance criteria of the structure.

3. *Acceptance criteria for force controlled actions:* force controlled components of the model must comply with equations specified in section 7.5.2.3. of ASCE/SEI 41-17 (ASCE, 2017a)

4. *Verification of modelling assumptions:* plastic hinges cannot form away from the ends of elements or element components unless they are specifically modelled (plastic rotations springs are accepatble [reference here needed])

According to Table 9-5 section 9.4.2. in ASCE/SEI 41-17 (ASCE, 2017a), steel moment frames with RBS connections can be modelled as fully restrained. Table 9-7.2 in ASCE/SEI 41-17 (ASCE, 2017a) provides the acceptance criteria under non-linear procedures for flexural and shear actions for steel components other than beams and columns. Table C.0.2 shows an extract (from Table 9-7.2) for the acceptance criteria of four common steel moment frame connections.

	Acceptance criteria		
Fully restrained moment connection	**IO**	**LS**	**CP**
WUF	$0.026 - 0.00065d$	$0.0323 - 0.00045d$	$0.043 - 0.00060d$
Improved WUF - bolted web	$0.010 - 0.00015d$	$0.0375 - 0.00045d$	$0.050 - 0.00060d$
Improved WUF - welded web	0.02	0.041	0.054
Reduced Beam Section	$0.025 - 0.00015d$	$0.0525 - 0.00023d$	$0.07 - 0.00030d$

Table C.0.2: Acceptance criteria from ASCE/SEI 41-17 (ASCE, 2017a) for PBD criteria where d = the depth of the beam

Appendix D

American Wide Flange Beams used for the Database

Table D.0.1: The 148 American Wide Flange beams selected for the parametric analysis, where d is the depth of the beam, b_f is the width of the beam flange, t_f is the thickness of the beam flange and t_w is the thickness of the beam web

American Wide Flange Section ID (in inches)	Section Dimensions (mm)			
	d	b_f	t_f	t_w
W 8 x 8 x 31	203	203	7.2	11
W 8 x 8 x 35	206	204	7.9	12.6
W 8 x 8 x 40	210	205	9.1	14.2
W 8 x 8 x 48	216	206	10.2	17.4
W 8 x 8 x 58	222	209	13	20.6
W 8 x 8 x 67	229	210	14.5	23.7
W 10 x 5.75 x 22	258	146	6.1	9.1
W 10 x 5.75 x 26	262	147	6.6	11.2
W 10 x 5.75 x 30	266	148	7.6	13
W 10 x 8 x 33	247	202	7.4	11
W 10 x 8 x 39	252	203	8	13.5
W 10 x 8 x 45	257	204	8.9	15.7
W 10 x 10 x 49	253	254	8.6	14.2
W 10 x 10 x 54	256	255	9.4	15.6
W 10 x 10 x 60	260	256	10.7	17.3
W 10 x 10 x 68	264	257	11.9	19.6
W 10 x 10 x 77	269	259	13.5	22.1
W 10 x 10 x 88	275	261	15.4	25.1
W 10 x 10 x 100	282	263	17.3	28.4
W 10 x 10 x 112	289	265	19.2	31.8
W 12 x 6.5 x 26	310	165	5.8	9.7
W 12 x 6.5 x 30	313	166	6.6	11.2
W 12 x 6.5 x 35	317	167	7.6	13.2
W 12 x 8 x 40	303	203	7.5	13.1
W 12 x 10 x 53	306	254	8.8	14.6
W 12 x 10 x 58	310	254	9.1	16.3
W 12 x 12 x 65	308	305	9.9	15.4
W 12 x 12 x 72	311	306	10.9	17
W 12 x 12 x 79	314	307	11.9	18.7
W 12 x 12 x 87	318	308	13.1	20.6
W 12 x 12 x 96	323	309	14	22.9
W 12 x 12 x 106	327	310	15.5	25.1
W 12 x 12 x 120	333	313	18	28.1
W 12 x 12 x 136	341	315	20.1	31.8
W 12 x 12 x 152	348	317	22.1	35.6
W 12 x 12 x 170	356	319	24.4	39.6
W 12 x 12 x 190	365	322	26.9	44.1

Continued on next page ...

Table D.0.1 continued...

American Wide Flange Section ID (in inches)	Section Dimensions (mm) d	b_f	t_f	t_w
W 12 x 12 x 210	374	325	30	48.3
W 12 x 12 x 230	382	328	32.6	52.6
W 14 x 5 x 22	349	127	5.8	8.5
W 14 x 5 x 26	353	128	6.5	10.7
W 14 x 6.75 x 34	355	171	7.2	11.6
W 14 x 6.75 x 38	358	172	7.9	13.1
W 14 x 8 x 43	347	203	7.7	13.5
W 14 x 8 x 48	350	204	8.6	15.1
W 14 x 8 x 53	354	205	9.4	16.8
W 14 x 10 x 68	357	255	10.5	18.3
W 14 x 10 x 74	360	256	11.4	19.9
W 14 x 10 x 82	363	257	13	21.7
W 14 x 14.5 x 99	360	370	12.3	19.8
W 14 x 14.5 x 109	364	371	13.3	21.8
W 14 x 14.5 x 120	368	373	15	23.9
W 14 x 14.5 x 132	372	374	16.4	26.2
W 14 x 16 x 145	375	394	17.3	27.7
W 14 x 16 x 159	380	395	18.9	30.2
W 14 x 16 x 176	387	398	21.1	33.3
W 14 x 16 x 193	393	399	22.6	36.6
W 14 x 16 x 211	399	401	24.9	39.6
W 14 x 16 x 233	407	404	27.2	43.7
W 14 x 16 x 283	425	409	32.8	52.6
W 14 x 16 x 311	435	412	35.8	57.4
W 14 x 16 x 370	455	418	42	67.6
W 14 x 16 x 398	465	421	45	72.3
W 14 x 16 x 426	474	424	47.6	77.1
W 16 x 5.5 x 26	399	140	6.4	8.8
W 16 x 5.5 x 31	403	140	7	11.2
W 16 x 7 x 36	403	177	7.5	10.9
W 16 x 7 x 40	407	178	7.7	12.8
W 16 x 7 x 45	410	179	8.8	14.4
W 16 x 7 x 50	413	180	9.7	16
W 16 x 7 x 57	417	181	10.9	18.2
W 16 x 10.25 x 67	415	260	10	16.9
W 16 x 10.25 x 77	420	261	11.6	19.3
W 16 x 10.25 x 89	425	263	13.3	22.2
W 16 x 10.25 x 100	431	265	14.9	25
W 18 x 6 x 35	450	152	7.6	10.8
W 18 x 6 x 46	459	154	9.1	15.4
W 18 x 7.5 x 50	457	190	9	14.5
W 18 x 7.5 x 55	460	191	9.9	16
W 18 x 7.5 x 60	463	192	10.5	17.7
W 18 x 7.5 x 65	466	193	11.4	19
W 18 x 7.5 x 71	469	194	12.6	20.6
W 18 x 11 x 76	463	280	10.8	17.3
W 18 x 11 x 86	467	282	12.2	19.6
W 18 x 11 x 97	472	283	13.6	22.1
W 18 x 11 x 106	476	284	15	23.9
W 18 x 11 x 119	482	286	16.6	26.9
W 18 x 11 x 130	489	283	17	30.5
W 18 x 11 x 143	495	285	18.5	33.5
W 18 x 11 x 158	501	287	20.6	36.6
W 18 x 11 x 175	509	289	22.6	40.4
W 21 x 6.5 x 44	525	165	8.9	11.4
W 21 x 6.5 x 50	529	166	9.7	13.6
W 21 x 6.5 x 57	535	166	10.3	16.5
W 21 x 8.25 x 62	533	209	10.2	15.6
W 21 x 8.25 x 68	537	210	10.9	17.4
W 21 x 8.25 x 73	539	211	11.6	18.8
W 21 x 8.25 x 83	544	212	13.1	21.2
W 21 x 8.25 x 93	549	214	14.7	23.6

Continued on next page ...

Table D.0.1 continued...

American Wide Flange Section ID (in inches)	Section Dimensions (mm) d	b_f	t_f	t_w
W 24 x 7 x 55	599	178	10	12.8
W 24 x 7 x 62	603	179	10.9	15
W 24 x 9 x 84	612	229	11.9	19.6
W 24 x 9 x 94	617	230	13.1	22.2
W 24 x 9 x 103	623	229	14	24.9
W 24 x 12.75 x 117	616	325	14	21.6
W 24 x 12.75 x 131	622	327	15.4	24.4
W 24 x 12.75 x 146	628	328	16.5	27.7
W 24 x 12.75 x 162	635	329	17.9	31
W 24 x 12.75 x 176	641	327	19	34
W 24 x 12.75 x 192	647	329	20.6	37.1
W 24 x 12.75 x 229	661	333	24.4	43.9
W 27 x 10 x 84	678	253	11.7	16.3
W 27 x 10 x 94	684	254	12.4	18.9
W 27 x 10 x 102	688	254	13.1	21.1
W 27 x 10 x 114	693	256	14.5	23.6
W 27 x 10 x 129	702	254	15.5	27.9
W 30 x 10.5 x 99	753	265	13.2	17
W 30 x 10.5 x 108	758	266	13.8	19.3
W 30 x 10.5 x 116	762	267	14.4	21.6
W 30 x 10.5 x 124	766	267	14.9	23.6
W 30 x 10.5 x 132	770	268	15.6	25.4
W 30 x 10.5 x 148	779	266	16.5	30
W 33 x 11.5 x 118	835	292	14	18.8
W 33 x 11.5 x 130	840	292	14.7	21.7
W 33 x 11.5 x 141	846	293	15.4	24.4
W 33 x 11.5 x 152	851	294	16.1	26.8
W 33 x 11.5 x 169	859	292	17	31
W 36 x 12 x 160	915	305	16.5	25.9
W 36 x 12 x 170	919	306	17.3	27.9
W 36 x 12 x 182	923	307	18.4	30
W 36 x 12 x 194	927	308	19.4	32
W 36 x 12 x 210	932	309	21.1	34.5
W 36 x 16.5 x 230	912	418	19.3	32
W 36 x 16.5 x 300	933	423	24	42.7
W 36 x 16.5 x 328	942	422	25.9	47
W 36 x 16.5 x 247	931	419	20.3	34.3
W 36 x 16.5 x 262	936	420	21.3	36.6
W 36 x 16.5 x 302	948	423	24	42.7
W 36 x 16.5 x 330	957	422	25.9	47
W 40 x 12 x 149	970	300	16	21.1
W 40 x 12 x 167	980	300	16.5	26
W 40 x 12 x 183	990	300	16.5	31
W 40 x 12 x 211	1000	300	19.1	35.9
W 40 x 12 x 235	1008	302	21.1	40
W 40 x 12 x 264	1016	303	24.4	43.9
W 40 x 12 x 278	1020	304	26	46
W 40 x 12 x 294	1026	305	26.9	49
W 40 x 12 x 327	1036	308	30	54.1